

HIGH-EFFICIENCY SOLAR DESALINATION AND SUPERHEATED STEAM  
GENERATION USING CONTACTLESS INFRARED HEATING

TAHZINUL ISLAM

A THESIS SUBMITTED TO  
THE FACULTY OF GRADUATE STUDIES  
IN PARTIAL FULFILLMENT OF THE REQUIREMENTS  
FOR THE DEGREE OF  
MASTER OF APPLIED SCIENCE

GRADUATE PROGRAM IN MECHANICAL ENGINEERING

YORK UNIVERSITY  
TORONTO, ONTARIO

MAY 2022

© Tahzinul Islam, 2022

## **Abstract**

The present study has investigated a novel configuration of a Contactless Solar Evaporation Structure (CSES), which has been prototyped over 41 experiments and 4 design iterations. The final design is able to utilize ~20% of solar energy (under 1 sun) to radiatively boil water for purposes of desalination (i.e. clean drinking water). The device can further reach boiling temperatures (water at 100 °C) as well as superheat steam to ~ 115 °C using a ~120 °C solar absorber as heat exchanger. A transient numerical model was developed and matched to the experimental results. This model was parameterized to predict trends of the device configuration to any scale, material, or solar irradiance. Secondary results include optical properties of key components of the solar still, design evolution over 41 experiments, innovation details for small-scale solar desalination devices, evaporation rates for 6 conventional solar still configurations, and a novel solar flux mapping procedure.

## Dedication

*This work is dedicated to  
my grandmother, Hazera  
and my daughter, Ayla*

## Acknowledgements

I would like to begin by thanking God for enabling me to complete this thesis in good health.

My sincerest gratitude goes out to Prof. Thomas Cooper, my supervisor, for the continual inspiration into the fields I chose to study during my Masters'. Solar Energy, Desalination, Radiative Heat Transfer, Optics, Astronomy, Statistics, Mass Energy & Momentum Transfer and Chemistry of Materials are fields of study which will stay close to my heart for the rest of my life.

I recall my high school years spent in Saudi Arabia, where I observed that the per litre cost of water (we would have delivered to us in large 5-gallon water cannisters, as tap water was not safe to drink) was more twice as expensive as petroleum! A 1 L bottle of water cost ~ \$0.40 CAD whereas the per-litre gasoline price was ~ \$0.20 CAD (today, due to the Russian Invasion in 2022, the oil prices have shot up to \$0.60 CAD which is highly abnormal) [1].

Today, I have the privilege of understanding this strange phenomenon, in the context of global water resources and the energy cost of water with regards to desalination powered by oil. In fact, I have found recently that Saudi Arabia and other Middle Eastern Gulf countries are the top adopters of desalination, enabling rapid urban expansion and sprawling megacities in the past half-century as well as recently. I also know that without the money from oil, many of these regions would simply not have been habitable without large-scale desalination measures.

Historically, many parts of the world have been reliant on availability of water for settlement, and this, I can say, is especially true for desert nations, where scarcity of water regularly leads to fatal dehydration and heat strokes. Moreover, given that many coastal nations do not have the capital resources to set up large desalination plants (e.g., Bangladesh) this affects tens of millions of water-starved people, living in highly unsanitary conditions, whom I have a strong drive to help. On that last point, I feel empowered to not only know the water crisis from a personal level, but also to engineer solutions to such crucial global problems for both urban and especially marginalized, rural communities worldwide amidst the current and future global water crises.

For that inspiration, knowledge, guidance, and empowerment, I cannot thank you enough. I also really appreciate your valuable advice on Engineering Education throughout, as I greatly respect your teaching expertise and aspire to become one who teaches as passionately and effectively as you do.

I would also like to thank my committee member, Prof. Marina Freire-Gormaly, for your valuable comments and support throughout the program.

I want to thank everyone who's helped me on this journey, including professors Prof. Roger Kempers, Prof. Jeffrey Harris and Prof. Solomon Boadkye-Yiadom, Prof. Stephanie Gora, colleagues, staff and personnel at the Lassonde School of Engineering and York University by extension.



Special thanks goes out to Prof. Hossam Sadek for flexibly teaching me ENG 6000 – Engineering Ethics, under exceptional circumstances. I sincerely appreciate your knowledge and expertise in the field of Ethics and Engineering. Especially as I prepare for the Engineer-in-Training (EIT) professional engineering & ethics exam this January 2023.

I would also like to thank Lassonde for providing a safe and warm environment for studying (both offline and online). This is not something easy to achieve, but I feel that with the honest effort of all staff, and especially during the pandemic, this was made possible.

My gratitude also goes out to Prof. Rezai, Huy and Emma for their constant support and advice of protocol throughout my Masters'. I must admit I am not the most adept when it comes to documentation, but my skills in this area have improved significantly, I feel, since I began in January, 2020.

I would not have been able to complete this thesis without the love and support of my family and friends. I would like to start by thanking my wife, Prokriti, who has constantly been by my side, even during difficult times. I would also like to thank my mother, whose constant support has pushed me forward. Finally, my deepest gratitude goes to my father. As a professor of mechanical engineering specializing in wind engineering & CFD modelling, he has constantly kept my passion for thermofluids burning. I would also like to thank my grandparents from both sides, who have inspired me as brilliant scientists in their field.

I would also like to thank colleagues at CooperLab. I always enjoyed learning through conversations and heated discussions. Special thanks to Prof. Cooper for hosting such great weekly lab sessions. I would like to thank Kourosh and Theresa for getting me set up in heat transfer as well as for numerous practical advice throughout.

We acknowledge the support of the Natural Sciences and Engineering Research Council of Canada (NSERC) for the Discovery Grant funding the research and development of the next generation of CSEs, readily deployable in coming years for a market of hundreds of millions of humans (refugees, indigenous communities, rural regions and other marginalized communities) who live under water stress, a fundamental violation of their human right to health, sanitation and safety.

# Table of Contents

Abstract .....	ii
Dedication .....	iii
Acknowledgements .....	iv
Table of Contents .....	vi
List of Figures.....	x
List of Tables.....	xviii
1 Introduction.....	1
1.1 Project background	1
1.2 Motivation	5
1.3 Scope of project	10
1.4 Goals & objectives	11
1.5 Outline of thesis	11
2 Theory & Background.....	12
2.1 Overview	12
2.2 Heat transfer fundamentals	12
2.2.1 Conduction	13
2.2.2 Convection	14
2.2.3 Radiation	18
2.2.4 Comparing among modes of heat transfer	24
2.2.5 Thermal resistance circuits	25
2.2.6 Heat exchanger analysis	26
2.3 Properties of water & steam	27
2.3.1 Molecular properties	28
2.3.2 Thermal properties	30
2.3.3 Optical properties	35
2.3.4 Salinity properties	36

2.4	Desalination systems	38
2.4.1	Brief history of desalination	40
2.4.2	Fundamentals and working principle	42
2.4.3	Thermally-driven desalination	43
2.4.4	Mechanically-driven desalination	50
2.4.5	Contactless Solar Evaporation Structures (CSES)	54
2.5	Solar energy	58
2.5.1	Sun-Earth geometry	58
2.5.2	Available power from the sun ( $q_{solar}$ )	60
2.5.3	LED solar simulators	62
2.5.4	Solar Selective Absorber (SSA)	63
2.5.5	Solar-to-thermal & optical efficiency	64
2.6	Summary	65
3	Methodology .....	66
3.1	Overview	66
3.2	Design	66
3.2.1	Thermal layout	67
3.2.2	Materials & dimensions	68
3.2.3	Prototype building	69
3.3	Experiment	83
3.3.1	Instrumentation	84
3.3.2	Experimentation	89
3.3.3	Preliminary experimental characterization	92
3.3.4	Design evolution (41 experiments)	106
3.4	Model	137
3.4.1	Solar Input	138
3.4.2	Enclosure	139
3.4.3	Side Losses & Solidworks Thermal Study	139
3.4.4	Top Losses	142

3.4.5	Bottom Losses	142
3.4.6	Heat Exchanger	144
3.4.7	Parameter study	145
4	Results & Analysis.....	148
4.1	Preliminary experimental characterization	148
4.1.1	Optical properties of 6 materials used	148
4.1.2	Optical efficiency using reflective sidewalls	150
4.1.3	Flux mapping	151
4.1.4	Evaporation rates for conventional solar stills	155
4.2	Overview of main experimental performance assessment	159
4.2.1	Absorber temperatures (~0.75 to ~1.4 suns)	160
4.2.2	Solar-to-thermal efficiency (~0.75 to ~1.4 suns)	162
4.3	Experimental results	164
4.3.1	Experiment 40 (keynote)	164
4.3.2	Experiment 39 (without cloth)	167
4.3.3	Experiment 39 (without cloth) vs. 40 (cloth)	169
4.3.4	Experiment 38 (seawater) vs. Experiment 40 (tap water)	170
4.3.5	Experiment 41 (Irradiance from ~0.75 Suns to ~1.4 suns)	173
4.3.6	Experiment 28 (first successful run)	176
4.3.7	Experiment 35 (2 thermocouples)	178
4.4	Numerical results	180
4.4.1	Water & absorber temperatures vs. irradiance	181
4.4.2	Solar-to-thermal efficiency vs. irradiance	182
4.4.3	Heat-up time vs. irradiance	183
4.4.4	Heat-up time vs. water mass	184
4.4.5	Absorber temperature vs. receiver area	185
4.4.6	Heat-up time vs. receiver area	186
4.4.7	Parameter study	187
4.5	Discussion Points	190

5	Conclusion & Recommendations .....	196
5.1	Summary of Project & Innovations	196
5.2	Conclusion	198
5.3	Recommendations for future work	199
	References.....	201

## List of Figures

Figure 1-1: Regions with water shortage ranging from 500 m <sup>3</sup> to 1700 m <sup>3</sup> per capita [34].	8
Figure 1-2: Global Horizontal Irradiation (GHI) over the world map, illustrating available energy for solar-powered desalination systems to harness over the globe (source: Global Solar Atlas).	8
Figure 1-3: Global coastal map of urban populations as of 2010, illustrating potential harms caused due to imminent rising sea levels due to climate change (source: ResourceWatch).	9
Figure 2-1: Conduction schematic.	13
Figure 2-2: Thermal conductivity of different materials, adapted from [38].	14
Figure 2-3: Convection schematic.	15
Figure 2-4: Radiation heat transfer using the proportionality constant, or Stefan-Boltzmann constant ( $\sigma$ ) and view factor ( $F$ ) applied to the simplified case of water boiling.	19
Figure 2-5: Surface radiation interactions and emission from hot surfaces [37].	20
Figure 2-6: EM wave spectrum (for radiation traveling through vacuum, with index of refraction, $n = 1$ ).	21
Figure 2-7: Three modes of heat transfer (not including evaporation) inside enclosure of CSES.	24
Figure 2-8: Water cycle, with details on molecular structure of water, mass transfer modes between water-air interface, condensation into clouds and finally delivery of water through precipitation making way finally to natural water reservoirs.	31
Figure 2-9: Transmission spectra of solar radiation through water [3].	35
Figure 2-10: Classification of Desalination Methods according to fundamental driving mechanism [53].	39
Figure 2-11: Desalination growth in last 3 decades [58].	41
Figure 2-12: Schematic diagram of a work-driven desalination system [20].	42
Figure 2-13: Losses occur due to radiation emitted from water, evaporative cooling and convective cooling from ambient air.	44
Figure 2-14: Working principle of Multi-Effect Distillation (MED) . [71].	47

Figure 2-15: Working principle of Multi-Stage Flash Distillation (MSFD), adapted from [71]	48
Figure 2-16: Working principle of Thermal Vapor Compression (TVC), adapted from [72].	49
Figure 2-17: Working Principle of Reverse Osmosis (RO) with regards to (a) working principle of osmosis, (b) osmotic equilibrium and (c) working principle of RO. Adapted from [73].	50
Figure 2-18: Working principle of Forward Osmosis (left) compared to Reverse Osmosis (right) [85].	52
Figure 2-19: Working principle of (a) Mechanical Vapor Compression (MVC) compared to (b) Thermal Vapor Compression (TVC) [86].	53
Figure 2-20: First generation prototype of CSES tested under real-sun [3].	54
Figure 2-21: Working principle of (a) Contact heating versus (b) Contactless heating.	55
Figure 2-22: Types of solar-driven interfacial evaporation [7].	56
Figure 2-23: Visualization of solar radiation impinging on a CSES receiver with two angles outlined: Zenith angle and Azimuthal angle.	59
Figure 2-24: Typical solar irradiance for a day in November [3] in Massachusetts, USA.	60
Figure 2-25: Schematic diagrams of five typical solar absorber coatings to achieve high solar absorptivity: (a) Intrinsic absorber, (b) Semiconductor absorber, (c) Multilayer interference stacks, (d) Cermet absorber, and (e) Textured surface [92].	63
Figure 2-26: Schematic of a typical solar thermal energy conversion system. Sunlight incident on absorber ( $Q_{in}$ ) is delivered to the thermal system, where desired output (steam evaporation) is produced ( $Q_{useful}$ ). Heat losses reduce the potential output of the system ( $Q_{losses}$ ). Adapted from [93].	64
Figure 3-1: Energy balance diagram of CSES with regards to heat and mass transfer modes.	67
Figure 3-2: Material components and dimensions of CSES.	69
Figure 3-3: Preparation of polyisocyanurate foam blocks. The raw boards (a) are cut to size (b), and sectioned out for selected blocks (c). Reflective tape is applied on all sectioned out blocks (d).	71
Figure 3-4: (a) Water inside FEP-folded basin showing hydrophobic interaction, (b) warranting the use of a hydrophilic layer, or cloth, to enhance basin performance.	72

Figure 3-5: Preparation of the basin by (a) first constructing hollow foam blocks, (b) making cuts for outlet tube with a groove to accommodate screws, and (c) FEP plastic sheet origami-folded into the basin. 73

Figure 3-6: Preparation of glazing system using a taping technique at 3 points on each side (12 tapes in total). Afterwards, each side is taped over with a long 24 inch stretch of tape to protect tightening tapes. The glazing system in 3 steps is shown for FEP on a ½ inch polyisocyanurate block with: (a) no tape, (b) short strips of tape applied at all corners, and (c) the final long tape along all sides. (d) FEP from nearly a year of usage and experimentation showing structural resilience for CSES. 75

Figure 3-7: (a) Close-up of closed-cell (i.e. pores not connected), and (b) silicone gasket as well as its placement on CSES. 76

Figure 3-8: (a) Large roll of solar selective absorber to be cut and uncurled. (b) After cutting an 18 inch x 18 inch piece, selective surface is uncurled, sanded and masking taped at sides to avoid epoxy spillage on absorbing side. (c) Finally, it is spray painted. 78

Figure 3-9: (a) Preparing and Applying epoxy to bond SSA to polyisocyanurate ½ inch block. (b) Wood panels are used to clamp the SSA for a complete and proper epoxy cure around corners. (c) Wet absorber after a test is shown. 79

Figure 3-10: Steps in the preparation of clamber: (a) cutting aluminum angle with Mitre box; (b) punching tapholes for drilling onto clammers; (c) ends of clamber filed; (d) clamber taped to cutting mate and 90 degree angles aligned and (e) holes marked with red pen. (f) Close-up of holes marked using the 90 degree angle as template are shown with jam nut arrangement at the four corners of bottom clamber. 81

Figure 3-11: (a) Top and (b) bottom clammers (identical and placed in reverse with holes aligned to accommodate threaded rod). 82

Figure 3-12: (a) Experimental Setup of CSES with schematic and (b) real-world setup. The Lambertian target and Pyranometer is not shown in the real-world setup. 83

Figure 3-13: Working principle of thermocouples [97]. 86

Figure 3-14: (a) K-type thermocouple from Omega Engineering; and (b) dismantled K-type Thermocouple using a precision screwdriver, showing interior components, including: two screws, bearing, thermocouple wire made of chromel/alumel (nickel alloys of the respective metals) with grommet. 87

Figure 3-15: Final Thermocouple setup on CB15 Expansion Board of Labjack U3-HV. The thermistor (barely visible) is set up in flexible Analog/Digital inputs (FI07 to FI06). A female thermocouple connector (white) is



also set in FI04 to FI05 to accept pyranometer (whose wires are to be attached to a male connector attached to the thermocouple during flux mapping procedure). 88

Figure 3-16: Scaling equation within LabJack's LJLogUD software for logging voltage signals from sensors. Touch test of thermocouple illustrates good response. 89

Figure 3-17: (a) Poor alignment of CSES relative to solar simulator, compared to (b) proper alignment viewed from the sides, and (c) from the front. 93

Figure 3-18: CM4 Pyranometer by Kipp & Zonen (mounted). 94

Figure 3-19: (a) Lambertian target placed on an xy-plane on the same y-height as CSES absorber. (b) Receiver area (meter image) plotted on target with blue circle for the 6 inch simulator height reading. This meter reading is then scaled over the area of the ROI on the target when irradiated with solar simulator. 95

Figure 3-20: Two Images taken for flux mapping: (a) meter image and (b) target image. 96

A note is made on obtaining the error for flux mapping (i.e. the maximum and minimum range of deviation) with regards to irradiance). To this regard, the 18 inch x 18 inch ROI was plotted over the 24 inch x 24 inch target plane and compared to the ROI touching corners (Figure 3-21). The only reading this is highly inaccurate for is the 6 inch height, where the proximity from the absorber leads to much human lower error than predicted. The error found from the method was ~20%, whereas in reality it would be ~10% or the nominal error throughout all ranges. 97

Figure 3-22: Care must be taken with shutter speeds to not overexpose images. Shutter speeds displayed from (a) 1/32,000 s, (b) 1/16,000 s and (c) 1/8000 s. 98

Figure 3-23: Camera histogram used to ensure properly exposed photographs during flux map images taken. 98

Figure 3-24: Error taken with (a) center average flux as upper limit and (b) corner average flux as lower limit. For example, center reading reads ~ 982 W/m<sup>2</sup> while bottom-right reads ~882 W/m<sup>2</sup>. Thus the minimum to maximum limit of error is 882 – 982 W/m<sup>2</sup>. 99

Figure 3-25: Pictures of 6 samples used for optical testing. 100

Figure 3-26: (a) UV-2600 Uv-Vis and (b) VERTEX 70 FTIR used for optical testing. 101

Figure 3-27: (a) Optical efficiency test with the overall setup, (b) the pyranometer position as viewed from eye-level, (c) pyranometer reading taken at center, (b) side edge (bottom-center) and (c) diagonal edge.	102
Figure 3-28: Pictures from the experiment. With mass readings taken of (a) tap water, which was mixed with 45 g of salt and then mixed into basin (b). (c-d) A reading was taken after 200 ml evaporated showing higher salinity. (e) No fouling spotted on absorber.	103
Figure 3-29: Two configurations tested for evaporation rates and absorber temperature details. (a) Experiment 36 was run without a cloth, using the water as the solar absorber itself as a form of bulk heating. (b) Experiment 37 was run with a cloth acting as the solar absorber.	104
Figure 3-30: Picture of OHAUS Scout Mass Balance connected to a USB logger (logged to OHAUS software on computer).	105
Figure 3-31: Design evolution overview: 4 design iterations were constructed throughout improvements over 33 experiments.	106
Figure 3-32: Overview of sections within thermal circuit, with enclosure thermal circuit highlighted with connecting nodes to custom functions for solar input, top losses, bottom losses, side losses (including Solidworks Thermal Study), water evaporation and steam superheating using hot emitter.	137
Figure 3-33: Thermal Circuit representation of Solar Input providing heat flux to CSES.	138
Figure 3-34: Thermal Circuit representation of Heat Transfer inside Enclosure boiling water.	139
Figure 3-35: Thermal Circuit representation of heat losses through CSES side insulation.	140
Figure 3-36: Side Loss Study run to integrate 3D effects into the 1D thermal circuit. (a) Run for scales from 6 inches to 72 inches of CSES basin length, (b) with temperatures set for typical absorber temperature of 140 °C and boiling water of 100 °C as boundary conditions for simulation and (c) plotted as a function to be scaled.	141
Figure 3-37: Thermal Circuit representation of heat losses through CSES top insulation.	142
Figure 3-38: Thermal Circuit representation of heat losses through CSES bottom insulation.	143
Figure 3-39: Thermal Circuit representation of heat exchange between emitter and steam at 100 °C from boiling water.	144

Figure 3-40: 10 Parameters defined in sensitivity analyzer. 7 were run with respect to materials, geometry and ambient conditions parametrized in the model; and 3 were run for the parameter. (a) 3000 random samples were generated to observe effects on (b) two requirements.	147
Figure 4-1: Spectral reflectivity data for 6 used materials.	148
Figure 4-2: Spectral transmission data for FEP (used in two thicknesses for both basin and glazing).	149
Figure 4-3: Pyranometer flux readings for optical efficiency test.	150
Figure 4-4: Irradiance from: point-measurement, center, corner and over plane. Plotted as a function of solar simulator height (inches) with correlation given. Minimum, maximum and center efficiency points are shown, with center efficiency taken for the present study.	153
Figure 4-5: Average solar heat flux mapped over CSES aperture. Simulator height and corresponding average solar flux at center: (a) 6 inches – 1390 W/m <sup>2</sup> , (b) 7.5 inches – 1311 W/m <sup>2</sup> , (c) 9 inches – 1112 W/m <sup>2</sup> , (d) 10.5 inches – 982 W/m <sup>2</sup> , (e) 12 inches – 903 W/m <sup>2</sup> , and (f) 13.5 inches – 735 W/m <sup>2</sup> .	154
Figure 4-6: Evaporation curves for Experiment 36 (cloth) and Experiment 37 (no cloth).	156
Figure 4-7: Temperature behavior of Experiment 36 (top) using cloth as solar absorber and Experiment 37 (bottom) using the water itself as solar absorber with regards to water, steam tube and ambient temperature.	157
Figure 4-8: Evaporation curve for CSES left for 22 hours with closed top. Only a total of ~ 9 grams evaporated within the 22 hour time period (~0.4 g/hr).	158
Figure 4-9: Maximum absorber temperature (center reading) achieved between 0.75 – 1.4 suns (38 experiments shown out of 41 experiments conducted). The asterisk (*) denotes experiments conducted without hydrophilic cloth. The (^) denotes temperatures of absorber after water dries, or leaks in the very early experiments (1-5).	161
Figure 4-10: Solar-to-thermal efficiency for all experiments from ~0.75 to ~1.4 suns (18 results displayed of 41 experiments conducted). The asterisk (*) indicates which experiments conducted without the hydrophilic cloth.	163
Figure 4-11: Numerical model vs. Experimental results for Experiment 40. Tuning parameters include optical efficiency (64.5%), heat exchanging effectiveness (60%) and side loss factor (3.2) (top) and close-up of steam thermocouple fluctuations due to condensation effects at outlet tube.	165

Figure 4-12: Pictures from Experiment 40 with (a) cloth, (b) setup and (c) steam thermocouple slightly bent into a spacer and also used in Experiments 35-41.	166
Figure 4-13: Experiment 39 with cloth, with incorrect heat-up temperature.	167
Figure 4-14: Pictures from Experiment 39 with no cloth with (a) SSA lifted showing CSES interior, and (b) steam thermocouple placement (bent into spacer).	168
Figure 4-15: Experiment 39 (cloth) vs. Experiment 40 (without cloth).	169
Figure -16: Experiment 38 using simulated seawater (~35,000 ppm).	170
Figure 4-17: Experiment 38 (seawater) vs Experiment 40 (tapwater).	171
Figure 4-18: Pictures from Experiment 38 conducted with simulated seawater (~35,000 ppm). (a) Saltwater on cloth is shown, with (b) CSES operating and salt used to simulate seawater.	172
Figure 4-19: Experiment 41 adjusting the solar simulator height from 13.5 inches (~0.75 suns) down to 6 inches (~1.4 suns). The 13.5 inches height was kept for ~ 7 hours. The data labels at top indicate the irradiance (in suns, with 1 sun = 1000 W/m <sup>2</sup> ) kept for ~ 1 hour at each steady-state absorber temperature.	173
Figure 4-20: Solar-to-thermal efficiency (left y-axis) and absorber temperature (right y-axis) vs. Irradiance for Experiment 41.	174
Figure 4-21: (a) Experiment 41 viewed with 6" solar simulator, with (b) close-up of steam outlet tube. Steam is transparent in the visible spectrum, so water is shown in the bottom are tiny condensed water droplets. This experiment under ~ 1.4 suns achieved steam at 136°C.	175
Figure 4-22: Experiment 28 was the first successful test with relatively smooth thermocouple readings, although under ~1.1 suns.	176
Figure 4-23: (a) Superheated steam (~115 °C) flow out of tube. (b) Condensation on the absorber after test. (c) The setup without the top (open-top). (d) Experiment 28 operating under 1 sun when viewed from standing height.	177
Figure 4-24: Experiment 35 was the first test using 2 absorber thermocouples (center and diagonal edge).	178
Figure 4-25: Experiment 35 run with (a) extra thermocouple and hydrophilic cloth. (b) Experiment 35 setup.	179

Figure 4-26: Irradiance vs. Temperatures (water and absorber reading at center).	181
Figure 4-27: Solar-to-thermal efficiency vs. Irradiance.	182
Figure 4-28: Heat-up time vs. Irradiance.	183
Figure 4-29: Heat-up time vs. Water mass.	184
Figure 4-30: Effect of increasing receiver area ( $m^2$ ) on absorber temperature.	185
Figure 4-31: Effect of higher receiver areas on heat-up time (to steady-state boiling state).	186
Figure 4-32: (a) Results from the sensitivity analysis of 3000 plotted design points. The red rectangle indicates the range of absorber temperature and mass evaporated by CSES experimentally. (b) Correlation matrix showing influence of 7 parameters on 2 requirements.	188
Figure 4-33: Effect of tuning parameters on maximum absorber temperature and evaporated mass (corresponding linearly to higher solar-to-thermal efficiencies).	189

## List of Tables

Table 2-1: Radiative property functional dependence and terminology.	21
Table 2-2: Definitions and notations of reflectivity for both spectral and total reflectivity.	22
Table 2-3: Selected physical properties of water.	29
Table 2-4: Analogy between quantities appearing in the formulation and solution of heat convection and mass convection.	34
Table 2-5: Representative ion concentrations for standard seawater, high and low salinity, brackish water, and a municipal water supply (nr = not reported), as adapted from [20].	37
Table 2-6: Overview of Desalination technologies [19].	39
Table 2-7: Comparison of energy requirements for water of different salinities and mineral content.	41
Table 3-1: Summary of 38 experiments over 4 design iterations. Key findings are outlined, with errors corrected for next experimental run. Corresponding pictures are given for visualization of experiments.	107
Table 3-2: 3,000 simulation runs taking ~ 13 hours to complete (15 seconds per thermal circuit run).	145
Table 4-1: Three potential solar-to-thermal efficiency based on irradiance point taken: maximum efficiency point, center efficiency point and minimum efficiency point (Experiment 40).	152
Table 4-2: Evaporation for different configurations of CSES.	155
Table 5-1: Summary of innovations.	197

# 1 Introduction

## 1.1 Project background

The need for desalination is made apparent by the lack of global freshwater to supply the drinking, sanitation, agricultural, and living needs of nearly 8 billion people as of 2021, with nearly a third currently without access to safe drinking water and 6% of mortality rates in underdeveloped nations being due to drinking water scarcity [2]. To augment the global water crisis, climate change and overpopulation are two major driving factors towards achieving clean water for everyone, a basic human right under Article 25 of the UN Declaration of Human Rights (1948). The UN Development Programme 6 predicts that by 2050, 1 in 4 people will suffer from the water crises due to increasing drought and desertification of Earth's Regions.

Incidentally, many water-starved nations lie in desert regions by coastal water bodies of high salinity. Examples of such desert regions (in ranking of land area without including Antarctic and Arctic deserts) include the Sahara (subtropical) desert in North Africa, Arabian (subtropical) desert spanning Saudi Arabia and Gulf neighbors, Gobi (cold winter) desert in China/Mongolia, Patagonian Desert in Argentina, Great Victoria (subtropical) desert in Australia, Great Basin Desert in North America. This leads to a further motivation to desalinate seawater into drinkable, agriculture-friendly and sanitary freshwater.

Desalination, however, comes with its own caveats made apparent in recent years, including brine disposal damaging marine ecosystems and financial investment concerns. Tropical and/or coastal regions also face regular natural disasters such as floods (particularly in the 'Ring of Fire' geographical regions), making installation of desalination plants in these regions to be technically and financially challenging.

The last factor is of particular interest in the light of low-capacity, personalized solar desalination devices, which may be of tremendous interest to refugees, rural communities and indigenous communities worldwide, who would benefit from a personalized desalination device driven by an energy source present in nearly all urban populations – solar energy. With recent developments in solar-thermal concentration, this is made even more viable for regions with receiving less average annual solar power, such as European and North American regions.

Once desalination is considered, the next step is to implement the desalination system powered by a cost-effective and sustainable energy source. Put simply, this system needs to be able to supply the clean water needs for a population at both reasonable setup costs as well as low operating costs. Also crucially, the life cycle assessment of the entire product or plant needs to be considered. To this regard, there is currently ongoing debate about popular desalination systems such as Reverse Osmosis (RO) which is able to produce clean drinking water at typically 50 cents per 1000 L (suited for urban populations), but at the environmental cost of brine disposal in marine eco-systems (with around 1.5 litre of brine produced per 1 litre of water desalinated). The cost of RO scales exponentially according to salinity of the water, with brackish water requiring significantly less capital to desalinate than brine water. Cost of thermal

desalination, however, is not a function of salinity, being able to distill water at over 99% purity. Moreover, top adopters of desalination globally are middle-income to high-income nations with either crude oil capital or exporters of another valuable commodity such as coffee, natural gas, gold, wheat, cotton, corn, or sugar (the most traded commodities globally). Lower-income nations, many of which are coastal and face annual disasters such as floods, are at greater risk of water scarcity driven primarily by growing populations and climate change.

The present study has considered using solar energy to supply the energy needs of a small-scale, low-cost desalination system – Contactless Solar Evaporation Structure (CSES). This innovative system may be visualized as an insulated box containing saline water. Sunlight is absorbed at the top of a solar absorber, which is then emitted (via emissive paint coated on the other side) to a thin layer of water. The solar absorber is a solar selective surface, meant to reduce radiative heat losses to ambient. Plastic sheets are placed above the solar absorber to trap air and reduce convective heat losses to the ambient. The present study is in the 2<sup>nd</sup> Generation (to be published), with a scale of 18 inch x 18 inch collector area, corresponding to the CSES aperture, absorber area and basin area. The 1st generation proof-of-concept prototype was demonstrated by Cooper et al. [3]. The device proved that under ambient conditions of 1 sun, water can be boiled. Moreover, superheated steam can be produced. In the study, a 6 inch x 6 inch lab prototype achieved steam temperatures of ~124 °C and distillate output of ~ 2.5 L/m<sup>2</sup>/day. The solar-to-thermal efficiency (at utilizing solar heat for evaporation) of this prototype was ~25%.

The solar device has potential to not only be a viable solution the world's clean water needs, small-scale power generation and steam sterilization, but also may be used as an experimental rig to investigate the effects of solar-driven interfacial phenomenon – the cutting-edge research of present times [4]. Moreover, boiling water by radiation enables de-coupling of the absorber to water body, which opens avenues not only for superheating of water but also bypassing one of desalination's most pressing problems, explored by several researchers, particularly from Professor Gang Chen's group in MIT: fouling [3]–[9].

In the fight against global water scarcity, CSES demonstrates a potential to be built anywhere in the globe by various marginalized stakeholders: rural regions where families regularly cross uncomfortable terrains and hills to water sources, disaster-stricken regions, military aid, conflict states with water supplies cut off (common military tactic), disaster relief and isolated regions where electricity is expensive due to land constraints for power generation (e.g. Solomon Islands, Togo and other Pacific Ocean Islands).

From a social well-being perspective, being able to utilize solar radiation as an energy source for desalination is a great option, as many regions of the Earth with urgent water crises lie in desert regions receiving some of the highest solar radiation on Earth, including: Australia, South Africa, Chile, Mexico, Algeria, Libya, Egypt, Namibia, Botswana and Zimbabwe [10]. These regions have access to a large reservoir of undrinkable, saline water, which may be readily desalinated with the sun at low costs. Furthermore, this enables decentralization of water resources, which is of tremendous interest globally.



In fact, for the past few decades, large-scale solar projects in the desert have been tested, including Masdar City in UAE and the more recent 'The Line' project under development by the company NEOM [11] in Saudi Arabia, with projected costs estimated at ~ 500 Billion USD. This project is marketed as a stretch of 'oasis' with feedwater from the highly saline Red Sea into the deserts of Saudi Arabia. These large projects illustrate the potential for solar-thermal applications in the 21<sup>st</sup> Century, particularly for desalination.

Moreover, even coastal regions with ample rain (not deserts, as geographically defined per annual rainfall) such as the 'Ring of Fire' countries either are unable to afford RO plants, or face the regular problem of floods, leading to a further need to distance residences from coastal regions, which may often be dangerous, particularly during monsoon seasons [12]–[14]. Even if RO plants could be installed at these remote village locations, or water arranged for delivery from a nearby RO plant via water pipes, there are technological challenges in projects such as these. To illustrate this, since the 1960s when RO desalination plants started being built in the wealthier oil nations, even with over 21,000 desalination plants globally, coastal regions within low-income nations constitute a very small percentage. To combat these issues, however, recently there have development of smaller-scale mechanically-driven desalination for rural communities, such as solar-powered RO at a competitive cost of roughly \$0.50 for 1000 L (or 1 cubic meter, m<sup>3</sup>).

This leads to more motivation for a solar device which can be scaled from 1 m<sup>2</sup> (half the drinking needs of a person) to as large as 10 m<sup>2</sup> (enough to supply a 5-person rural family household) to supply rural community water needs. As of 2022 in Canada, there are currently issues surrounding clean water delivery to indigenous reserves, with the reasons for the high number of contamination events being only mentioned by Awume et al. [15] as the lack of community management, water distribution systems, inadequate technology, lack of federal funding, and land use activities that affect source water quality. Latchmore et al. [16] goes on further to detail indigenous perspective on water, including its spirituality and connection with land. More broadly, transportation of clean water through pipes and over long distances presents challenges in general regarding water treatment and delivery systems worldwide.

From a technical perspective, approximately 2,300,000 Joules of energy is needed to desalinate 1 litre of water if using thermally-driven desalination methods [17]. Alternatively, water has a very cohesive molecular structure, leading to mechanically-driven desalination methods to be also quite challenging, especially at larger capacities given setup and maintenance considerations [18]. In fact, the high viscosity and specific heat properties of water warrant immense investigations to find novel ways of desalinating water efficiently given finite energy sources. These two broad characteristics of water illustrate the high costs of desalination, whether through thermal or mechanical means of separating salts from water.

Currently, the most popular method of desalination globally by far is reverse osmosis (RO), with 69% of desalination plants globally using this mechanically-driven desalination method [19]. RO plants are able to desalinate water at a cost of 50 cents per 1000 L of water [20]. Furthermore, they have a very large daily output capacities of billions of Litres per day. The most notable problem, however, in RO plants is in the

massive scale of such plants. This inherently requires initial capital investment, maintenance by locals, and stable governments to ensure that water is delivered safely to its residents. Unfortunately, for many water-starved and/or conflict nations (where cutting off water sources is a popular military tactic), these are all luxuries which a sizeable portion of the global population simply cannot afford.

This highlights the need for new devices and methods which are scalable, low cost and equitable. The CSES proposed in the present study is one such device and method at achieving clean, de-centralized drinking water, as well as other useful applications such as steam sterilization, power generation, space heating and other applications involving a hot absorber at temperatures of around  $\sim 120$  °C under one sun, which may be boosted to  $\sim 135$  °C. Moreover, the first generation proof of concept [3] provides a solid foundation for numerical modelling, experimentation and prototyping in the second generation of the device. Since then, no other studies have attempted to utilize the same configuration for solar desalination.

CSES in the present project (2<sup>nd</sup> generation) was found to be able to boil the water at 100 °C with an absorber  $\sim 120$  °C hot, and further superheat it by steam convection with the emitter side (which serves a dual function to radiatively heat the water as well as convectively heat the rising steam) to temperatures  $\sim 115$  °C. The resulting optical efficiency and heat exchanging effectiveness were found to be  $\sim 65\%$  and  $60\%$ , respectively. However, the side loss model developed was found to be a factor of 3 off, leading to further investigations of this aspect of CSES and some others, discussed in Chapter 4.

Thus, in the 2<sup>nd</sup> generation of CSES, an 18" by 18" scaled-up prototype was built and tested indoors under a solar simulator, achieving a distillate output of  $\sim 65$  grams per hour. The theoretical maximum is  $\sim 330$  g/hr for a  $0.2 \text{ m}^2$  collector area under 1 sun, which roughly equates to a solar-to-thermal efficiency of  $\sim 20\%$ . The prototype was continually improved over 4 iterations, ultimately leading to a design costing  $\sim 100$  \$USD for the basic functional cost and  $\sim 500$  \$USD for prototype costs. The lightweight build along with its foam insulation build enables future iterations to easily accommodate a floating CSES (widely useful for deployment on open saline oceans). Furthermore, recyclable and junk materials may be used to construct CSES (and solar stills in general), making the prototype costs irrelevant in a global context.

## 1.2 Motivation

The present section will detail the motivation for the study in the context of social and technological perspectives.

With regards to social perspective, solar-thermal evaporation devices in general are very cheap to build (low-cost), scalable and are typically de-centralized from reliance on any electricity. This makes such devices to be particularly useful for marginalized communities, such as rural, indigenous and refugee populations.

Thus, the over-arching motivation for desalination itself comes from the lack of freshwater reserves on Earth, whereby only 3% of earth's water is fresh while 97% is saline. Of this fraction, nearly 2.5% is locked up in polar ice caps, glaciers and the atmosphere, leaving about 0.5% of water accessible to human needs in the form of river water and groundwater [21].

Mountains also play an important role in the natural freshwater cycle, essentially acting as 'water towers' supplying lowlands with freshwater for irrigation, food production, industrial usage and domestic needs of increasing populations [22]. Many conflict regions intentionally cut off rural communities from these essential freshwater sources, leading to a reliance on an alternative water source. To this regard, RO plants are simply not able to be funded by governments in conflict zones, leading to mass water scarcity in rural communities and deaths. The International Committee of the Red Cross illustrates examples of such conflict zones with cut-off water resources, including Examples of such conflict zones include Syria, Palestine-Israel, the State of Jammu and Kashmir in India, and the most recent situation in Ukraine [23], all of whom suffer from dangerous water scarcity issues.

In addition to social barriers to basic water needs of populations, there also exist climate factors such as desertification and rising sea levels which will inevitably affect water resources for a growing population of 10 billion human beings as of 2050. To combat such imminent crises, renewable water structures and systems need to be researched in order to be technologically accommodated for the coming decades of severe water crisis, affecting a quarter of the global population. Such effects have already been demonstrated in a drastic event in South Africa, where vast regions became deserts and lost a large portion of the annual rainfall, which would've been collected in dams used to supply water to South Africans [24]. This led to roughly \$40 million of damages done to alleviate drought effects which have dried up watering holes, wholesale livestock deaths and crop failures, bringing financial ruin to farmers and a spike in food prices. The citizens in this situation were nationally advised to use water resources conservatively, which proved a lot of effectiveness.

By comparison, the average Canadian uses 2700 L of water per day for their total domestic (including residential, water costs of food and personal consumption), industrial and agricultural needs [25], compared to the average South African, who uses 800 L of water daily. Many Sub-Saharan African nations top the lowest daily water used per capita, with Congo, Nigeria, Ethiopia, Kenya and Mozambique using 47

L/capita/day, 216 L/capita/day, 279 L/capita/day, 225 L/capita/day and 149 L/capita/day, respectively. These water use statistics were obtained as of 2009 from the Worldometer site tracking water usage [25]. More recent statistics show much higher water use statistics, which denotes industrialization of developing nations, in particular.

With regards to residential water use, the government of Canada tracks water use statistics, including residential water use. Based on data from 2011, the average Canadian uses ~ 300 L of water per day for residential purposes [26].

African nations by the Mediterranean and Middle-East use much more, with examples being Egypt, Libya, Algeria, Morocco, Tunisia using 2202, 2541, 674, 883 and 1168, L/capita/day. Water usage of roughly 2000 L/capita/day was observed to be common among industrialized nations, whereby agricultural nations (largely comprising rural populations) used significantly less water of even less than 300 L/capita/day. These water usage statistics illustrate the need for water equity among regions, whereby each nation uses water proportionately according to their needs. Large-scale RO plants significantly correlate with water wastage and a lower socio-economic incentive to save water, as can be observed in water-stress nations. Especially relevant to the present study is the realization that all of the above-mentioned, largely desert, nations could benefit immensely from available solar radiation, constituting a maximum of 1000 W of power which can be harnessed from a 1 m<sup>2</sup> collector area at solar noon on a clear day.

In addition to desert nations, whereby ample available solar radiation warrants solar desalination, there are other stakeholders which would benefit immensely from low-capacity, personalized solar devices in general. These include, remote, rural, coastal and refugee communities to have definite needs for such personalized, solar devices for the many of the same reasons above, pertaining to marginalized (i.e. rural populations living far from cities established mostly by water bodies) and displaced communities (especially due to warfare).

With regards to solar irradiation, Tiwari et al. [27] comprehensively reviewed the availability of solar radiation over the globe as well as the design implications for desalination. Solar resource data are readily available online, such as on the National Renewable Energy Laboratory (NREL) site, Canada's solar radiation data [28] as well as the Global Solar Atlas [29] which is shown below in order to establish the link between available solar radiation and water scarcity. While solar energy may be intermittent throughout the day and season for many regions on Earth, such as Northern Canadian regions with rural indigenous populations, it is ubiquitous and available. Thus, while solar-driven desalination is energy intensive, it is widely available. Moreover, solar desalination systems such as solar stills are able to capitalize on low build costs, which may even be readily from junk materials such as clothes, wood and recycled transparent or glass elements.

Coastal regions are next on the list of water-scarcity, constituting 40% of the Earth's population. Such populations live within 100 km of coastal regions, with most megacities located along water bodies. This is especially true for settlement in desert nations such as Saudi Arabia, UAE, Iran and Australia [30]–[33].

These vast urban populations (i.e. future megacities) have a direct motivation to desalinate their water needs rather than resorting to unreliable water reservoirs (such as groundwater) or arranging for transporting water (which may be expensive, or depending on the terrain of the region, impossible, such as within hilly/mountainous rural communities).

Both of these options have energy needs of their own, and depending on the scale of the population, desalination technology may be warranted. Figure 1-1, Figure 1-2, and Figure 1-3 below summarize the correlations between available solar radiation, water stress as well as coastal regions.

In fact, many remote, coastal areas do not have resources of electric power for producing potable water using conventional desalination techniques such as multi-stage flash, reverse osmosis and vapor compression [10], common examples being the Pacific Ocean Island nations (e.g. Solomon Islands, Togo and more).

An example of a largely coastal country under imminent future threat of water starvation (primarily due to climate change and rising sea levels) is Bangladesh, where 27.5% of its current 160 million people reside (45 million people in one country alone) along the coast. It also is challenging to set up water treatment and desalination plants in many coastal regions such as Bangladesh simply because it's non-diversified, textile-driven economy (as is the case for many low-income nations relying the export of an agricultural commodity to the globe) is not able to financially warrant such large-scale engineering solutions, especially with the cost of hiring foreign engineers and project managers.

These are all concerns of grand proportions, and much work has been utilized to integrate current desalination technology to these regions. The macroscopic observations alone lay the necessity of desalinating the remainder 0.5% or so of global water.

### Global population living in water shortage

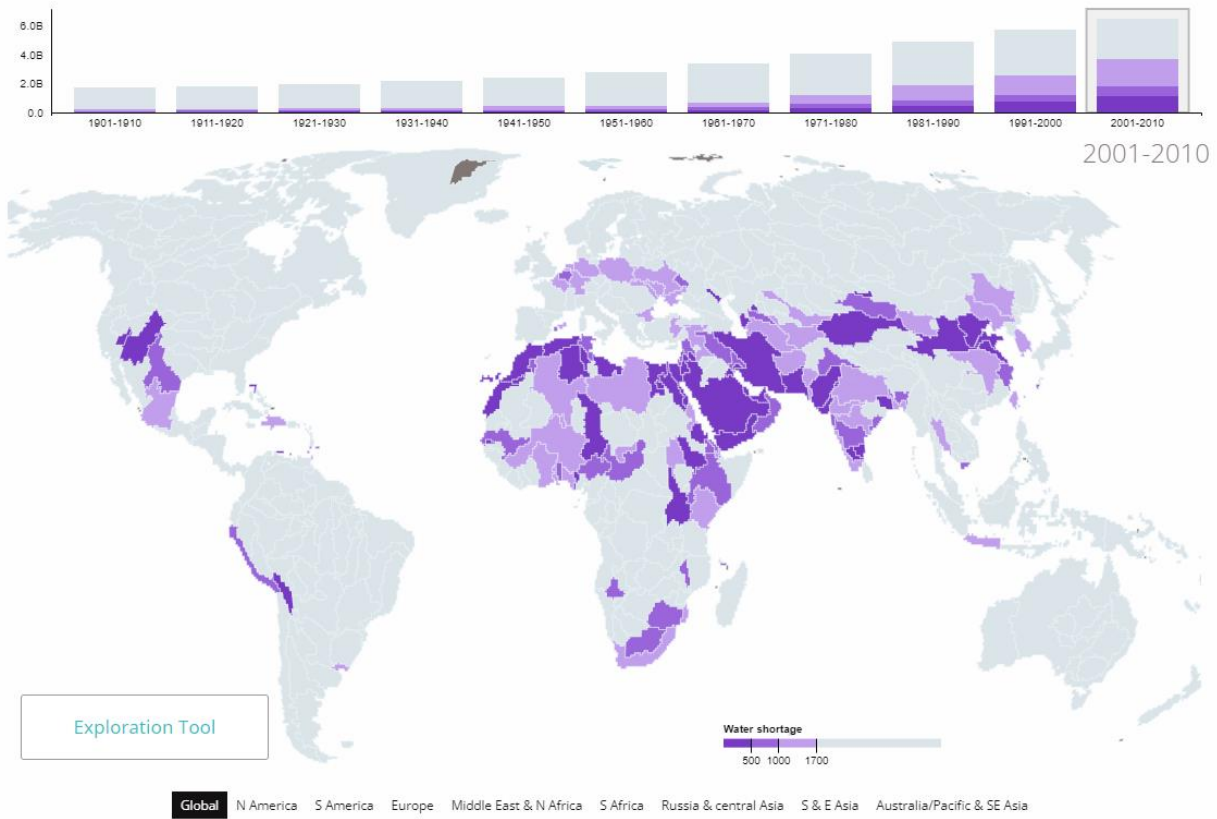


Figure 1-1: Regions with water shortage ranging from 500 m<sup>3</sup> to 1700 m<sup>3</sup> per capita [34].

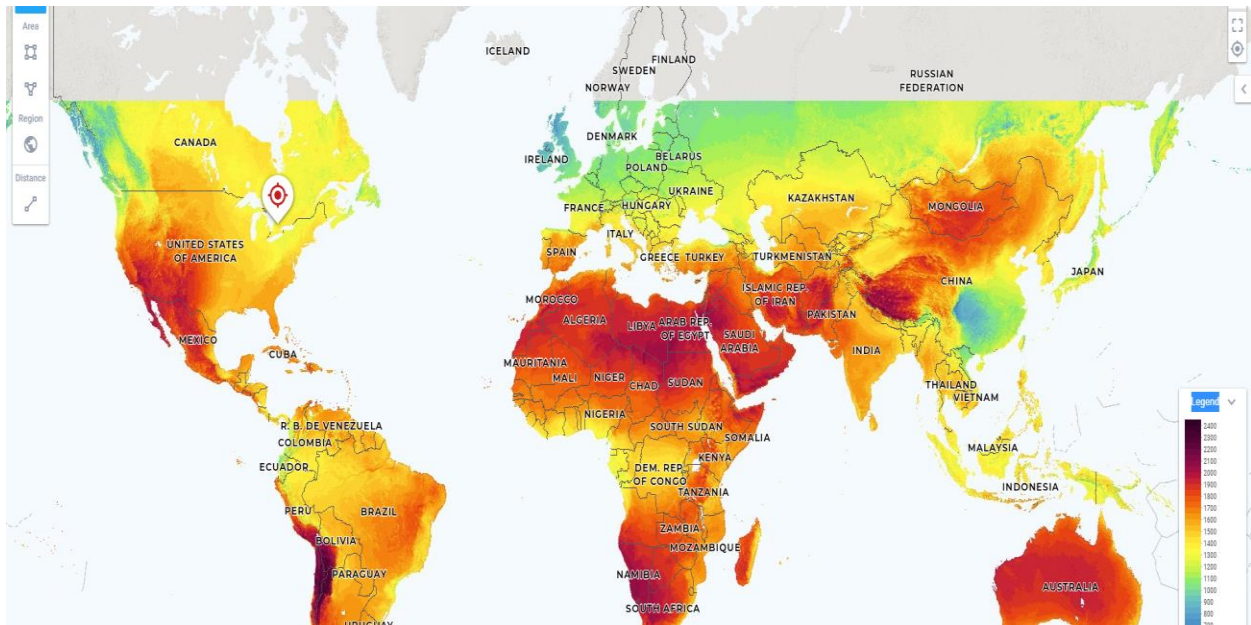


Figure 1-2: Global Horizontal Irradiation (GHI) over the world map, illustrating available energy for solar-powered desalination systems to harness over the globe (source: Global Solar Atlas).

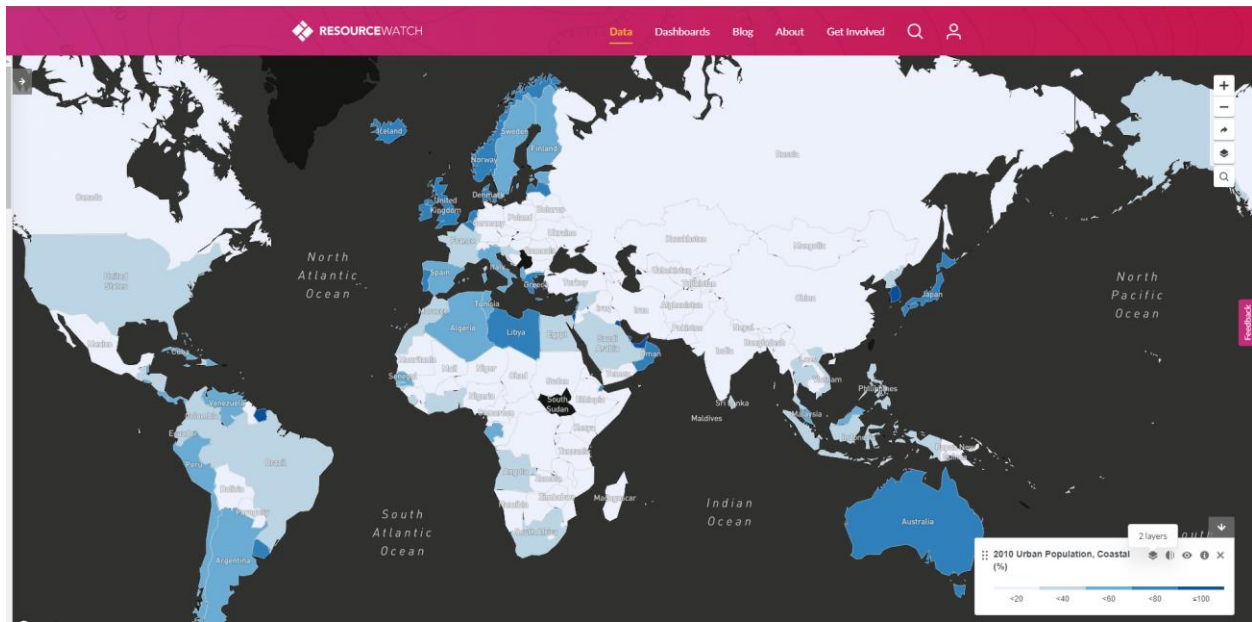


Figure 1-3: Global coastal map of urban populations as of 2010, illustrating potential harms caused due to imminent rising sea levels due to climate change (source: ResourceWatch).

### 1.3 Scope of project

The present study seeks to be innovative in the next generation of CSES, with the proof of concept established by the first generation. In order to do so, certain fields of study were prioritized to be completed within the timeframe of 2 years and 4 months, while macroscopic equations were taken from other fields.

The fields in focus include heat transfer (more particularly radiation heat transfer) and thermodynamics. The tangent fields which the present study borrows from are, in order of importance, mass transfer (for rate of evaporation and mass convection coefficient), geometric optics (concentrators and sun-earth geometry), and desalination (global water statistics, salinity of water, desalination systems).

With regards to radiative transfer and on the point of spectral nature, emitted radiation has wavelength and directional considerations to be made. This would also apply to reflectivity and absorptivity of the enclosure wall as well as the water. Diving deeper, the radiation through the water volume would need to take into consideration volume radiation properties such as absorption coefficient ( $\kappa_\lambda$ ), which has been discussed in the present study only to highlight this point, but no analysis has been made to this level of detail. To achieve the level of detail of including radiative properties (both at surface and volume levels) and geometry, one method is to use Monte Carlo Ray Tracing. This method, while very useful for investigating radiation inside the CSES enclosure more closely, could not be undertaken within time constraints of the project. Thus, the level of detail possible within the allotted time entailed a macroscopic view of the phenomenon of infrared radiation interacting with water molecules and did not dive into the microscopic (or within the micron level of detail) or molecular (particularly the interaction of photons with the structure of water molecules, including particular effects on hydrogen bonds and other weaker intermolecular bonds) levels.

Any thermal design can be improved by way of two broad characteristics: thermal layout; and material design. The present study has focused primarily on the former by way of manipulating a thermal circuit in the numerical model. No novel materials were explored in the present study. Instead, the author has experimented with a wide variety of widely available materials such as foam insulation boards used within homes to spray paint used for ovens (as emissive paint on absorber side to emit infrared radiation), and hydrophilic cloth materials used as cleaning agents in the household. Such available materials are very beneficial in the case of solar stills, where water equity entails that these personalized desalination devices be built anywhere, using anything.

Broadly, the project consisted of a prototype element (1<sup>st</sup> objective) which itself is composed of a design and experiment phase; simulation component (2<sup>nd</sup> objective) and an extension to the simulation by way of parameter tuning (3<sup>rd</sup> objective).



## 1.4 Goals & objectives

Three objectives have been proposed and investigated in the present study. These are as follows:

1. [Design and Experiment]: Experimental demonstration of a highly efficient and scaled up CSES prototype;
2. [Simulation]: Development and validation of numerical model which can accurately predict solar-to-thermal efficiency and transient temperature profiles of absorber, water and steam;
3. [Parameter Study]: Extension of the numerical model by tuning design parameters and gauging effects on evaporated mass and maximum absorber temperature.

## 1.5 Outline of thesis

The present thesis is divided into five chapters, each detailed below:

Chapter 1 begins with a background on the project, providing the motivation for not only desalination, but also desalination utilizing energy from the sun (i.e. solar desalination). Key motivations are provided for the investigation of CSES from social and technological perspectives. Finally, goals & objectives are set to complete the project. Finally, the scope of study is outlined to frame the study towards the most important physics occurring within CSES.

Chapter 2 summarizes the literature on the present topic of solar desalination by reviewing the fundamentals of heat transfer (Section 2.2) and properties of water & steam (Section 2.3). By merging the understanding from these two Sections, two further Sections on Desalination Systems and Solar Energy are outlined for a more complete understanding on Solar Desalination, including practical (other research prototypes).

Chapter 3 details the methodology in 9 steps, taking inspirations from existing engineering design methodologies. The setup of numerical model is presented (objective 2). Next, the setup of the experiment is detailed followed by a section on the construction of CSES (objective 1). Lastly, a parameter study is run to complement the numerical model and observe optimized designs with alternative parameters from the one prototyped in-lab (objective 3).

Chapter 4 delves into the results and analysis, with regards to the three objectives. Key results are broadly sub-divided into the preliminary experimental characterization, overview of main experimental performance assessment, experimental results (41 experiments) and numerical results. Lastly, discussion points are given on the design implications from the study.

Chapter 5 summarizes the findings, drawing conclusions in light of existing desalination systems. In particular, the innovations achieved with the 2<sup>nd</sup> generation CSES are summarized. Finally, the recommendations for further study are detailed.

## 2 Theory & Background

### 2.1 Overview

Understanding the process of solar thermal desalination will first require an in-depth treatment of heat transfer fundamentals (particularly the radiation mode of heat transfer) as well as the properties of the substance which is being heated (i.e. water). Thus, Sections 2.2 and 2.3 serve as review of the fundamentals required for analysis.

The marriage of Sections 2.2 and 2.3 enable us to understand the many complex configurations of systems chosen for desalination. To this end, Section 2.4 attempts to investigate solar stills in the context of the history of desalination systems and its alternatives, such as Reverse Osmosis (RO), Multi-Stage Flash Distillation (MSDF) and other desalination systems in terms of capacity, cost and water equity.

Lastly, the energy source chosen for desalination will be into consideration. To this end, the final section on Solar Energy will be vital towards understanding this energy source for the process of desalination (i.e. Solar Desalination).

### 2.2 Heat transfer fundamentals

*“Is not Fire a Body heated so hot as to emit Light copiously?*

*For what else is a red hot Iron than Fire?*

*And what else is a burning Coal than red hot Wood?”*

- Sir Isaac Newton (1704, ‘Opticks’)

Any thermal design requires an adequate understanding of the three modes of heat transfer: conduction, convection and radiation. The most complex of these three modes to understand is radiation, which will be made clear by the following sections. The mode of evaporation results in both mass reduction from water body as well as net energy leaving the water body, resulting in evaporative cooling. This very important phenomenon of evaporation covered in more detail on *Section 2.3 on Water & Steam Properties* with regards to the water cycle and the CSES.

Even though the present project concerns desalination primarily through infrared radiation, there are still effects of conduction and convection present in all thermally-driven desalination systems (and by extension, thermal systems). In order to investigate the effectiveness of desalinating via radiation, the present project has utilized techniques (outlined further in Chapter 3) to minimize conductive and convective losses.

Much of the review of heat transfer in this section are explained in-depth by books on heat transfer by Cengel [35], Lienhard [36], with an in-depth treatment of the radiation mode of heat transfer by Modest [37].

### 2.2.1 Conduction

The most basic mode of heat transfer is conduction. In this mode, heat is transferred by contact of a solid with another solid. Essentially, it refers to the transfer of internal energy by microscopic collisions of particles (molecules, atoms, and electrons) within solids.

The heat power ( $W$ ) for conduction is represented by Fourier's Law of Heat Conduction:

$$Q_{conduction} = \frac{k}{L} \cdot A \cdot (T_{hot} - T_{cold}) \quad (Eqn. 2 - 1)$$

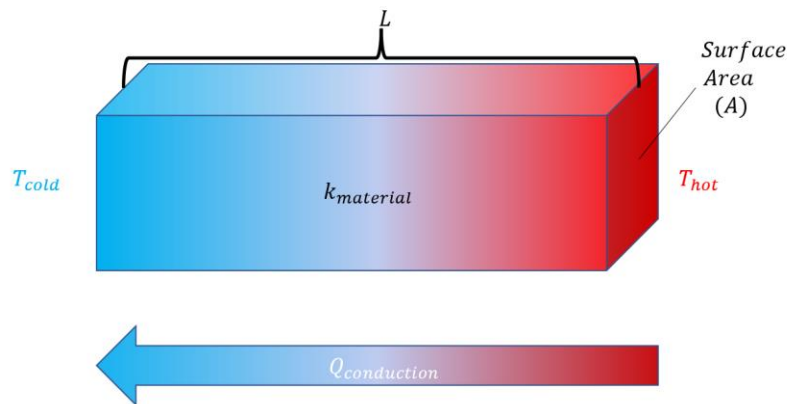


Figure 2-1: Conduction schematic.

Essentially, the equation above expresses that the rate of heat transfer between two bodies of different temperatures ( $T_{hot}$  and  $T_{cold}$ ) of certain thickness ( $L$ ) is proportional to a coefficient ( $k$ ) the thermal conductivity. The heat power ( $Q$ ) may be divided by the receiver area ( $A$ ) to obtain heat flux ( $q$ ). Thus, heat flux may be easily obtained by dividing by the receiver area ( $Q/A$ ), measured in  $W/m^2$

Thermal conductivity ( $k$ ) of materials is perhaps the most fundamental property in heat transfer and is measured according to various methods [38]. These methods include guarded hot plate ( $T < 600$  °C), heat flow meter ( $T < 200$  °C), transient hot wire/hotstrip ( $T < 200$  °C), TPS method ( $T < 900$  °C), Laser flash ( $T < 2700$  °C), Modulated DSC ( $T < 50$  °C) and 3w-method ( $T < 300$  °C). Palacios et al. [38] reviews thermal conductivity of common materials, classifying insulators starting at a thermal conductivity of  $\sim 0.03$   $W/(m \cdot K)$  corresponding to the insulation capability of stationary air (i.e. conduction heat transfer instead of convection). Figure 2-2 below summarizes the thermal conductivity of common materials [39], [40].

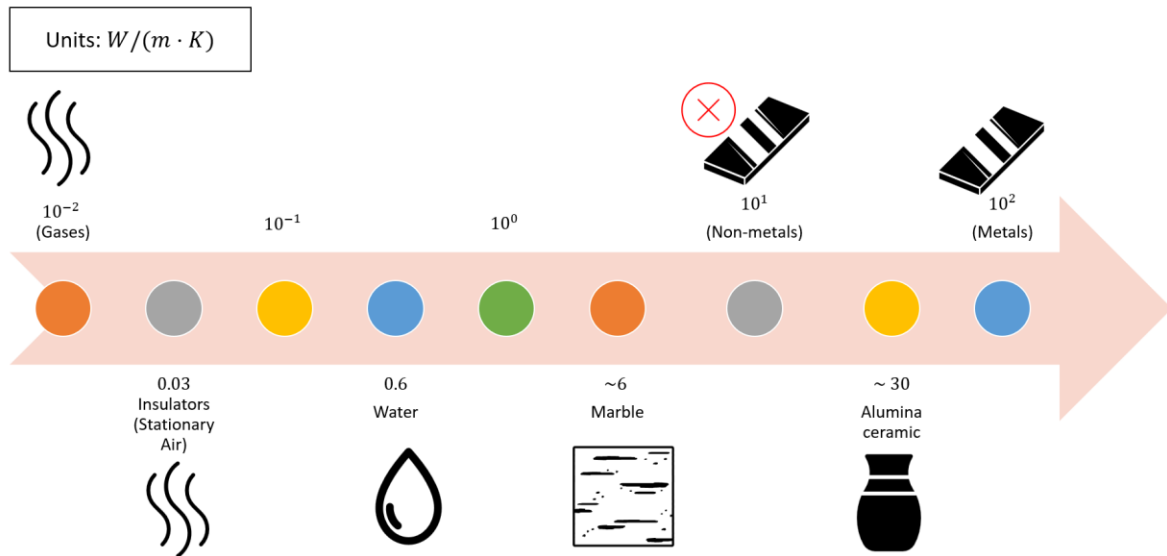


Figure 2-2: Thermal conductivity of different materials, adapted from [38].

### 2.2.2 Convection

Similar to conduction, the convection mode of heat transfer also relies on the transfer of kinetic energy by contact. In other words, convection too requires a medium to transfer heat energy. Unlike conduction, however, the medium of heat transfer in this case is a fluid. Therefore, this mode of heat transfer often requires more comprehensive fluid mechanics analyses depending on the problem and accuracy of solution required.

The present section will further demonstrate the Critical Rayleigh Number used to determine the distance between two surfaces above which convection effects would occur as the bottom surface is heated (relevant to the case of CSES and hot absorber  $\sim 140^\circ\text{C}$ ). This fluid movement, as will be demonstrated in this subsection, is due to natural convection as hot fluid rises driven by a temperature gradient caused by hot bottom surface.

The convective heat power ( $Q_{convection}$ ) is obtained from Newton's Law of Cooling:

$$Q_{convection} = h \cdot A \cdot (T_{surface} - T_{ambient}) \quad (Eqn. 2 - 2)$$

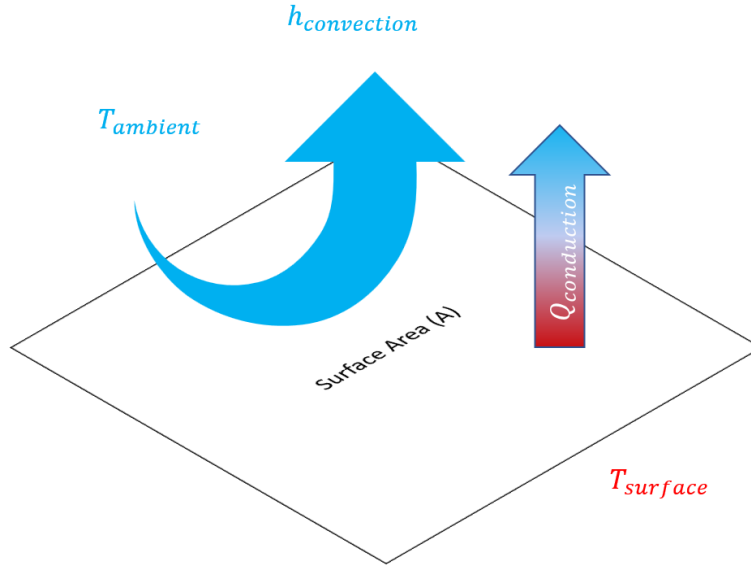


Figure 2-3: Convection schematic.

Similar to conduction, heat flux due to convection (i.e. moving fluids at ambient temperature,  $T_{ambient}$ ) over a surface of certain surface area ( $A$ ) at a given temperature ( $T_{surface}$ ) is proportional to the convection coefficient ( $h$ ). This fundamental quantity, unlike thermal conductivity above, is more difficult to account for given the inherent randomness of fluids when compared to ordered solids and lattice structures which remain relatively unchanged in their solid forms under heat. To augment this random flow of fluids, temperature effects such as a heated bottom, gives rise to natural convection.

The convection coefficient is commonly found from the Nusselt number, defined as the ratio of convective heat transfer to conductive heat transfer with the thickness of gap ( $L$ ) in conduction taken as the distance,  $D$  (i.e.  $L = K$ ):

$$Nu = \frac{q_{convection}}{q_{conduction}} = \frac{h \cdot \Delta T}{(k/L) \cdot \Delta T} = \frac{h \cdot D}{k} \quad (Eqn. 2 - 3)$$

This dimensionless number represents the contribution of conductive heat transfer to convective heat transfer. The literature [35] has reported numerous correlations of the Nusselt number as a function of its flow regime, or the Reynolds number ( $Re$ ) for a wide variety of fluid flow regimes as well as geometric scenarios (e.g. flow over a cylinder). Only the definitions are given in the present section, building up to the Rayleigh number which is relevant in the present study to calculate the thickness of the glazing system block to avoid air from circulating due to natural convection, leading to hot losses from the absorber to ambient.

Firstly, the Reynolds number is the most fundamental quantity in fluid mechanics, describing flow regime:

$$Re = \frac{\text{inertial forces}}{\text{viscous forces}} = \frac{\rho \cdot V \cdot D}{\mu} \quad (\text{Eqn. 2 - 4})$$

It is described by the ratio of inertial force (the product of density, volume, diameter of body over which the fluid flows) of a flowing fluid to the viscous forces (characterized by the dynamic viscosity  $\mu$  property of fluids). Dynamic viscosity is perhaps one of the most fundamental material properties in fluid mechanics, which is especially relevant in convection heat transfer studies.

Calculation of the Rayleigh number is also critical in the context of CSES, where glazing systems seek to eliminate moving air (i.e. convection, leading to losses, as opposed to stationary air which may be treated as an excellent insulator of  $k \sim 0.02 \text{ W/(m}^2\cdot\text{K)}$ , or comparable to aerogels). The Rayleigh number is calculated using parameters for CSES with the thickness ( $L$ ) is to be found. A Rayleigh number of  $< 1708$  denotes that the air is not moving. It is interesting to note that fluid movement leads to a phenomenon known as Rayleigh–Bénard cells, which occurs when a bottom surface is hot and the top surface is cold, leading to natural convection (or gravity-driven convection, as occurs naturally along any temperature differential with a hotter bottom surface).

The Rayleigh number is obtained by product of the Grasshoff and Prandlt numbers:

$$Ra = Gr \cdot Pr = \frac{g \cdot \beta \cdot (T_2 - T_1) \cdot L^3}{\nu^2} Pr = \frac{g \cdot \beta \cdot (T_2 - T_1) \cdot L^3}{\nu \cdot \alpha} \quad (\text{Eqn. 2 - 5})$$

Where the Prandlt number ( $\nu/\alpha$ ) represents the contribution of momentum diffusivity over the thermal diffusivity.  $\nu$  is the kinematic viscosity and  $\alpha$  is the thermal diffusivity (defined as  $k/(\rho \cdot c_p)$ ) The Grasshoff number is  $\frac{g \cdot \beta \cdot (T_2 - T_1) \cdot L^3}{\nu^2}$ , and approximates the ratio of the buoyancy to viscous force acting on a fluid.

It is also interesting to note that within the enclosure of CSES, very little convection occurs as the hot surface ( $T_H$ ) is the emitter at the top of  $\sim 140 \text{ }^\circ\text{C}$  under one sun, and water temperature of  $100 \text{ }^\circ\text{C}$ . Thus, a convection coefficient of  $\sim 0.6 \text{ W/(m}^2\cdot\text{K)}$  is utilized as obtained by Cooper et al. [3].

By contrast, the glazing experiences a hot surface at the bottom (the top of absorber as opposed to bottom with emitter side), leading to the potential of moving air leading to little parasitic convective heat losses. This may be prevented to utilizing a small layer thickness between glazing systems, leading to the calculation of the Critical Rayleigh Number at which convection occurs, which is 1708 [35].

$$Ra = \frac{g \cdot \beta \cdot (T_{\text{absorber}} - T_{\text{ambient}}) \cdot L^3}{\nu_{\text{air}} \alpha_{\text{air}}} < 1708 \quad (\text{Eqn. 2 - 6})$$

Which may be re-arranged, taking the upper limit of 1708, to solve for the thickness ( $L$ ), with air properties taken at ambient temperature (i.e.  $82.5 \text{ }^\circ\text{C}$  or  $\sim 366 \text{ K}$ ).

$$L = \left( \frac{\nu_{air} \cdot \alpha_{air} \cdot Ra}{g \cdot \beta \cdot \frac{(T_{absorber} - T_{ambient})}{2}} \right)^{\frac{1}{3}} < \quad (Eqn. 2 - 7)$$

$$\left( \frac{1.5e^{-5} \cdot 25e^{-6} \cdot 1708}{9.8 \cdot \left( \frac{1}{(413 + 298)/2} \right) \cdot \frac{413 - 298}{2}} \right)^{\frac{1}{3}} < 0.0075 \text{ m}$$

This leads to a maximum possible layer thickness of ~0.3" for the glazing system, whereas 0.5 inch boards were used. Thus, there is some expected convection within the glazing system, although it is not significant. Thus, a conduction resistance was utilized in the model instead of the little convection. Moreover, the length of conduction was set to 0.3 inch as calculated above.

In contrast to natural convection, there is also forced convection which refers to moving fluids as a result of an external force (e.g. a fan or blower).

### 2.2.3 Radiation

Before detailing the origin of radiation and its relevance in the current research, it must first be clarified that radiation in the current thesis refers exclusively to electro-magnetic radiation (as opposed to the other three types: acoustic, gravitational and particle radiation).

Electromagnetic radiation originates from the motion of charge carriers (e.g. photons, electrons) undergoing an alternating positive to negative movement. Any body with a temperature above absolute zero will emit some radiation as this denotes movement of an oscillatory movement of particles. Radiation is emitted in the form of its most elementary particle: photons. Photons, as shown in the figure below, may be represented by the Poynting Vector ( $S = E \times H$ ) which when time-averaged constitutes a ray of photons. The ray analysis is held throughout the present study as opposed to the more detailed particle and wave-particle duality definitions of photons, given the complexity of the problem encountered in the present study which, as will be shown, is accurately represented by the Stefan-Boltzmann Law. The energy of a photon was quantized by Max Planck and led to the birth of quantum physics [41]:

$$E = h \cdot f \quad (\text{Eqn. 2 - 8})$$

Where  $h$  is Planck's constant ( $6.62 \text{ e-}34 \text{ m}^2 \text{ kg s}^{-1}$ ) and  $f$  is the frequency of emitted photon.

Given that emitted radiation in the infrared wavelengths is used in the present study to heat and boil water. It is very important to understand the fundamentals of radiation and terms. We begin with the radiant heat power emitted from a surface, which is as follows.

$$Q_{\text{radiation}} = A \cdot \epsilon \cdot \sigma \cdot T^4 \quad (\text{Eqn. 2 - 9})$$

Here,  $\sigma$  is the Stephan-Boltzmann constant, the proportionality constant relating energy from radiation to the fourth power of its temperature ( $T^4$ ). Applying the equation to two surfaces as well as taking into account the surface area ( $A$ ) and emissivity ( $\epsilon$ ).

In the present study, certain assumptions were considered in the case of radiant power emitted from an emitter to water below (Figure 2-4). To this aim, assumptions are made that the water acts as a blackbody surrounding ( $\epsilon = 1$ ). Moreover, the surfaces are considered isothermal with uniform properties, gray, diffuse and planar. With these assumptions, Equation 2-10 below estimates the radiation exchange on the basis that the sidewalls used in CSES utilize reflective tape. Thus, it is assumed that all of radiation from the emitter reach the water.

$$Q_{\text{radiation,exchange}} = A \cdot \epsilon \cdot \sigma \cdot (T_{\text{emitter}}^4 - T_{\text{water}}^4) \quad (\text{Eqn. 2 - 10})$$



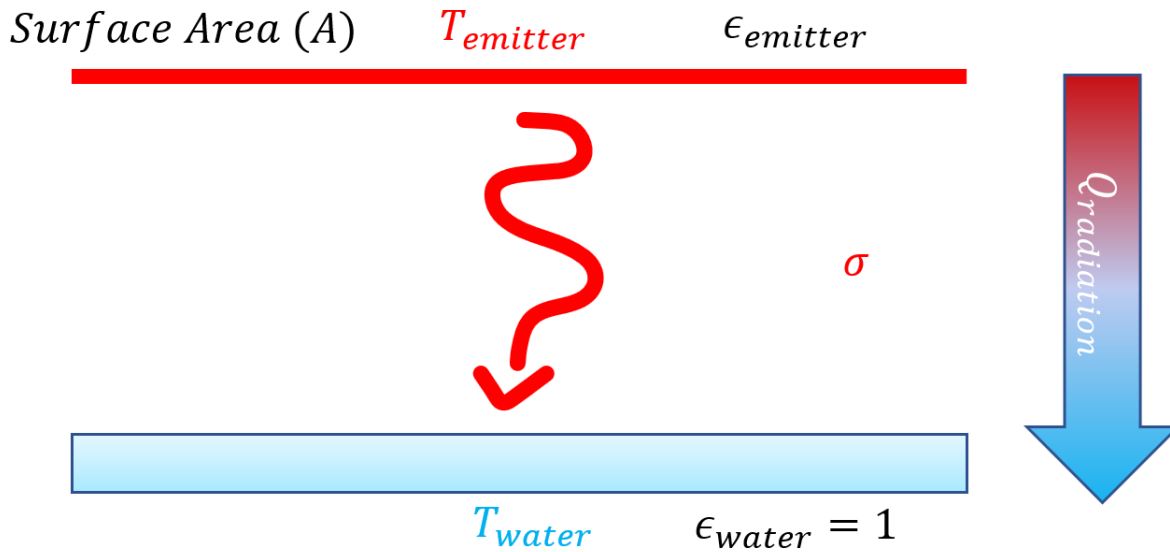


Figure 2-4: Radiation heat transfer using the proportionality constant, or Stefan-Boltzmann constant ( $\sigma$ ), applied to the simplified case of water boiling since reflective tape was used inside the CSES enclosure.

Simply, the surface area ( $A$ ), emissivity ( $\epsilon$ ) of emitter, and temperatures of emitter ( $T_{emitter}$ ) and water ( $T_{water}$ ) needs to be taken into account for both the emitter as well as the water. The emissivity ( $\epsilon_{water}$ ) of the water is considered to be 1 for the simplified case since reflective tape was used in the enclosure. Ordinarily, view factors would be taken into account for radiation surface exchange.

As will be shown in the following section on water properties, and in particular its optical properties, water turns out to be a very strong absorber in the infrared wavelengths, which coincidentally a blackbody emission evaluated at  $T_{blackbody} = 140\text{ }^{\circ}\text{C}$  matches quite well. On the other hand, water is a poor absorber below  $\sim 4$  microns of wavelength. This is realized when considering that visible sunlight may be seen in deep oceans up to  $\sim 40$  m (green light being the last color to observe). A  $\sim 140\text{ }^{\circ}\text{C}$  emitting blackbody, on the other hand, achieves radiation above 4 microns (peak wavelength at  $\sim 7$  microns using Wien's Law  $(2898\text{ }(\mu\text{m}\cdot\text{K})/(413\text{ K}))$  in which water absorbs well at a thin layer at the water surface. This leads to a new phenomenon of interfacial heating at the water-air interface which is of tremendous interest recently in the solar desalination research community.

Figure 2-5 is outlined below to provide a guide for each of the radiative properties, relations and functional dependences at the surface level (schematically shown in Figure 2-5). It must be re-iterated as in the scope of study, that only surface radiative exchange has been considered in the present study, while only considering the absorption coefficient of water (further detailed in Section 2.3) to illustrate that water is a strong absorber of infrared wavelengths, leading to a direct motivation to utilize solar-thermal collectors for

radiative heating at ambient temperatures of 140 °C and 7 microns of corresponding peak wavelength (calculation shown using Wien's Displacement below).

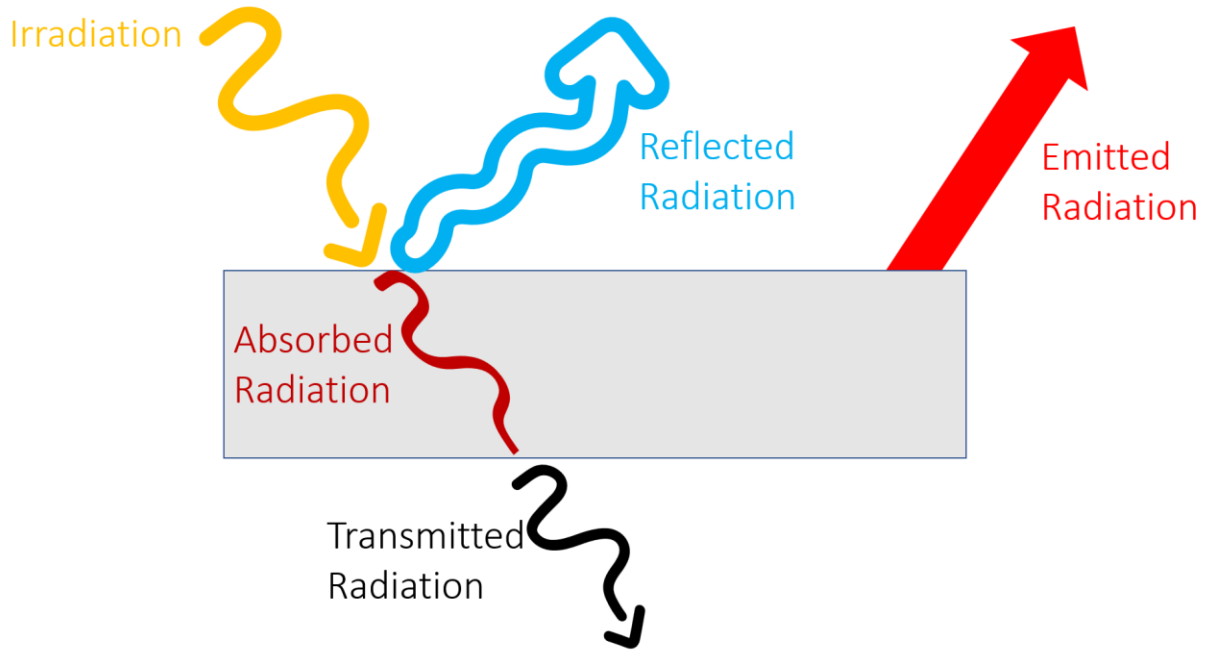


Figure 2-5: Surface radiation interactions and emission from hot surfaces [37].

A more specific definition for the emissivity listed here is the total hemispherical emissivity ( $\epsilon^{hemisphere}$ ). This parameter is a function of wavelength range ( $\lambda_1, \lambda_2$ ) and temperature obtained by:

$$\epsilon = \frac{\int_{\lambda_1}^{\omega} \epsilon_{\lambda} \cdot E_{b\lambda} \cdot d\lambda}{\sigma \cdot T^4} \quad (\text{Eqn. 2 - 11})$$

In order to better understand the wavelength nature of radiation, the EM spectrum is given in Figure 2-6 as a reference.

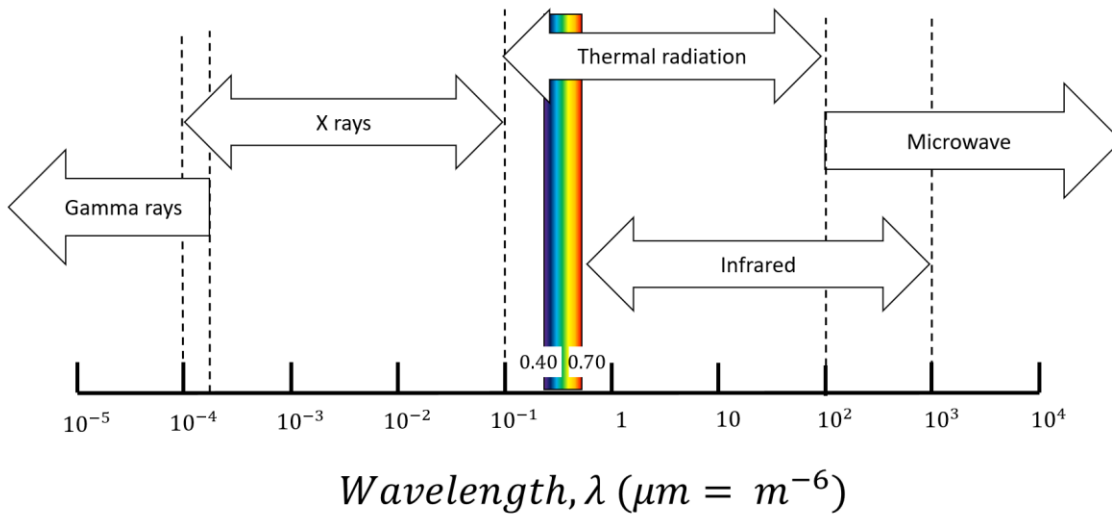


Figure 2-6: EM wave spectrum (for radiation traveling through vacuum, with index of refraction,  $n = 1$ ).

With the numerator of the emissivity now known, the denominator may easily be calculated using the Stephan-Boltzmann law for a blackbody, which is the solution to the integral of blackbody emission  $E_{b\lambda}$  over all wavelengths:

$$Q_{blackbody,radiation} = A \cdot \sigma \cdot T^4 \quad (\text{Eqn. 2 - 12})$$

With the complete definition of total hemispherical emissivity, three other optical properties will be now briefly defined as functional dependences but not delved into: total hemispherical absorptivity, total hemispherical reflectivity and transmittivity, given in the Table 2-1 below. For a more complete definition of these functions, which are not utilized in the present study, the textbook by Modest may be consulted [37].

Table 2-1: Radiative property functional dependence and terminology.

	<b>Spectral Directional</b>	<b>Spectral Hemispherical</b>	<b>Total Directional</b>	<b>Total Hemispherical</b>
Absorptivity	$\alpha'_\lambda$ $= fn(\text{direction}, \text{wavelength}, T)$	$\alpha_\lambda$ $= fn(\text{wavelength}, T)$	$\alpha'$ $= fn(\text{direction}, T)$	$\alpha = fn(T)$
Emissivity	$\epsilon'_\lambda$ $= fn(\text{direction}, \text{wavelength})$	$\epsilon_\lambda$ $= fn(\text{wavelength}, T)$	$\epsilon'$ $= fn(\text{direction}, T)$	$\epsilon = fn(T)$

For reflectivity, we extend the definition to two directions: the incoming and reflected radiation as illustrated by the equations and definitions below for reflectivity, where in Table 2-2, the superscript hemisphere denotes an integration of directional reflectivity over the hemisphere, ' superscript denotes incoming direction and '' superscript denotes incoming radiation and outgoing reflection.

*Table 2-2: Definitions and notations of reflectivity for both spectral and total reflectivity.*

	Spectral	Total
Bidirectional reflectivity	$\rho''_{\lambda}$	$\rho''$
Directional hemispherical reflectivity	$\rho_{\lambda}^{hemisphere}$	$\rho^{hemisphere}$
Hemispherical directional reflectivity	$\rho_{\lambda}^{hemisphere'}$	$\rho^{hemisphere'}$
hemispherical	$\rho_{\lambda}$	$\rho$

Reflectivity is perhaps the most fundamental of the optical properties, as it can readily be converted to absorptivity. Then, using Kirchhoff's Law of Thermal Radiation [42], absorptivity can be equated to emissivity under certain assumptions on the surface. These assumptions are on whether the radiating surface is gray (emitting on constant wavelength) and/or diffuse (emitting in all directions).

While the present study has not considered level of detail of volume exchange (restricting only to the surface properties and definitions for radiative exchange within the enclosure), one important volume property will be detailed, which is the absorption coefficient ( $\kappa_{\lambda}$ ).

This parameter, obtained as a proportionality constant for the Beer-Lambert law, which involves spectral transmission through a media, particular the infrared radiation from emitter to water volume [37].

The inverse of the absorption coefficient is known as the mean penetration depth ( $1/\kappa_{\lambda}$ ). The mean penetration depth is plotted in the Figure 2-9 using the absorption coefficient of water (Beer-Lambert Law):

$$\tau_{\lambda}(L) = \frac{I_{\lambda}(L)}{I_{\lambda,0}} = e^{-\kappa_{\lambda}L} \quad (\text{Eqn. 2 - 13})$$

We now detail Planck's Law, which is fundamental to radiation, as definitively knowing the wavelength spectra of a blackbody (an ideal radiating object which absorbs and emits all radiation) based on its temperature is a prerequisite for the derivation of fundamental optical properties of materials in comparison to blackbodies. Planck's Law is expressed as:

$$E_{b\lambda}(\lambda, T) = \frac{2 \cdot h \cdot c^2}{\lambda^5} * \frac{1}{e^{\frac{h \cdot c}{\lambda \cdot k_B \cdot T}} - 1} \quad (\text{Eqn. 2 - 14})$$

Where Blackbody Spectral Emissive Power ( $B$ ) represents the blackbody emission at given wavelength ( $\lambda$ ),  $T$  represents temperature of the radiating body and three constants:  $c$  (speed of light),  $h$  (Planck's Constant) and  $k_B$  (Boltzmann constant and not to be confused with the Stefan-Boltzmann constant  $\sigma$ ).

The peak wavelength is calculated for a blackbody at 140 °C (nominal operating temperature of solar absorber under 1 sun) using Wien's Law:

$$\lambda_{max} = \frac{C_3}{Temperature} = \frac{2898 (\mu m \cdot K)}{413 (K)} = 7 \mu m \quad (\text{Eqn. 2 - 15})$$

### 2.2.4 Comparing among modes of heat transfer

There are interesting physics at play inside CSES (Figure 2-7), which will be highlighted in the present section.

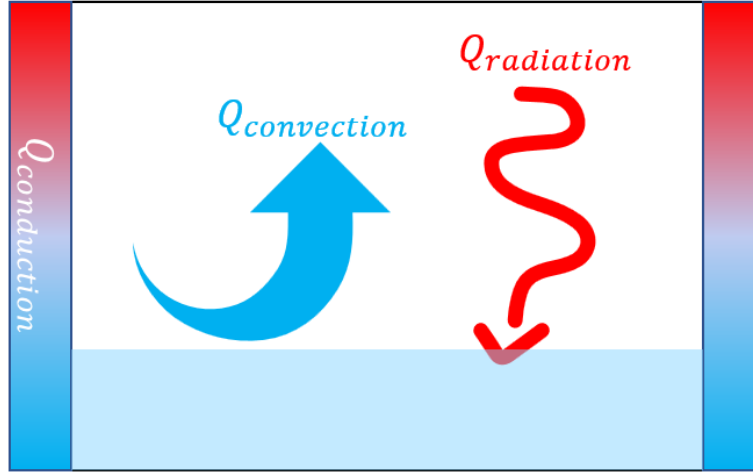


Figure 2-7: Three modes of heat transfer (not including evaporation) inside enclosure of CSES.

There is firstly conductive heat transfer from the emitter to the sidewall and then to the water by contact. Next, there is radiative heat transfer from the emitter to the water. It would be useful to be able to compare among the three modes to make important assumptions for analysis as well as to ensure that radiation is the dominant mode of heat transfer to further investigate the case of radiative boiling. It is interesting to note that there is virtually no convection inside the gas gap, as was reported by Cooper et al [3]. Nevertheless, the present section will detail convection within the context of the gas gap for purposes of comparison among the three modes of heat transfer.

Using the base definition for Newton's Law of Cooling in the case of convection, we can extend the definition of heat flux to the other two modes for a direct comparison among the three modes of heat transfer. This is done by dividing the heat flux by the area ( $A$ ) and temperature difference ( $\Delta T$ ).

$$h = \frac{Q}{A \cdot \Delta T} \quad (\text{Eqn. 2 - 16})$$

The corresponding equations for conduction, convection and radiation are:

$$h_{\text{conduction}} = \frac{Q}{A \cdot \Delta T} = \frac{(k/L) \cdot A \cdot \Delta T}{A \cdot \Delta T} = \frac{k}{L} \quad (\text{Eqn. 2 - 17})$$

$$h_{\text{convection}} = \frac{Q}{A \cdot \Delta T} = \frac{h \cdot A \cdot \Delta T}{A \cdot \Delta T} = h \quad (\text{Eqn. 2 - 18})$$

$$h_{radiation} = \frac{Q}{A \cdot \Delta T} = \frac{F \cdot A \cdot \epsilon \cdot \sigma \cdot (T_s^4 - T_{surr}^4)}{A \cdot \Delta T} = \frac{F \cdot \epsilon \cdot \sigma \cdot (T_s^4 - T_{surr}^4)}{\Delta T} \quad (Eqn. 2 - 19)$$

$$h_{radiation} = 4 \cdot \sigma \cdot \epsilon \cdot T_m^3 \quad (Eqn. 2 - 20)$$

Simplifying the above equation, we obtain the equivalent radiation coefficient in W/(m<sup>2</sup>·K) which can readily be compared to conduction and convection for similar scenarios using a mean temperature (T<sub>m</sub>).

### 2.2.5 Thermal resistance circuits

Cengel [35] details the extension of the heat conduction equation to a variety of use cases. Broadly speaking, these include steady-state, transient and numerical methods. Furthermore, specific equations are derived for a variety of 2D and 3D geometries.

While these topics are useful in their own design use case scenarios, the present study has utilized the a transient conduction method outlined by Cengel [35]. This method utilizes a thermal resistance circuit, analogous to an electrical circuit, to solve for the heat flux and temperature throughout the thermal design.

Thermal resistance circuits could be modelled with MATLAB's Simscape package, which could run 'transient' analyses by utilizing time steps, whereby after solving each steady-state circuit at a certain time, these values would then be used as boundary conditions for the next time iteration. This transient analysis utilizes a parameter for thermal storage, as excess heat from a previous iteration would stay in the real-world and translate over as initial temperature boundary conditions (based on stored thermal energy) for the next time iteration:

$$Q = \int_{T_1}^{T_2} m \cdot cp \cdot dT \quad (Eqn. 2 - 21)$$

Thermal resistances for conduction, convection and radiation are given below based on its equivalent electrical circuit as given by relating Newton's Law of Cooling ( $\Delta T = \dot{Q} R$ ) to Ohm's Law ( $\Delta V = I R$ ), is detailed below [35].

$$R_{conduction} = \frac{L}{k \cdot A} \quad (Eqn. 2 - 22)$$

$$R_{convection} = \frac{1}{h \cdot A} \quad (Eqn. 2 - 23)$$

$$R_{radiation} = \frac{1}{\epsilon \cdot \sigma \cdot A \cdot (T_s^2 + T_{surr}^2) \cdot (T_s + T_{surr})} \quad (Eqn. 2 - 24)$$

### 2.2.6 Heat exchanger analysis

In order to superheat steam, the same emitter radiatively heating the water will also convectively superheat the steam ( $\dot{Q}_{steam}$ ), as shown in Equation 2-25.

$$\dot{Q}_{steam,superheated} = f_{superheater} \cdot \dot{m}_{steam} \cdot c_{p,steam} \cdot (T_{emitter} - T_{water}) \quad (Eqn. 2 - 25)$$

Where  $\dot{Q}_{steam,superheated}$  is the heat power delivered from heat exchanger (emitter) to superheat the steam, flowing at a certain rate ( $\dot{m}_{steam}$ ) and raising its temperature according to its specific heat ( $c_{p,steam}$ ) from its initial temperature (i.e. temperature of the water, or  $T_{steam} = T_{water}$ ) up to a final temperature,  $T_{steam,superheated}$ . Of course, this process is not executed 100% effectively, leading to a heat exchanging effectiveness parameter,  $f_{superheater}$ .

After experiments, it was found that the hot emitter at ~135 °C was able to superheat steam to ~115 °C (leading to a ~40% heat exchanging effectiveness ( $f_{superheater}$ ) found experimentally. This parameter was tuned accordingly in the numerical model instead of using the  $\epsilon - NTU$  method. In contrast to the  $\epsilon - NTU$  method, there is also Log Mean Temperature Difference which may be used to obtain heat exchanging effectiveness if the temperature profiles of cold fluid and hot fluid are known [35].

In order to calculate the steam temperature within the numerical model, Equation 2-25 is re-arranged to result in the following equation modelled diagrammatically using Simscape and Simulink components in a custom Heat Exchanger block.

$$\dot{Q}_{steam,superheated} = \dot{m}_{steam} \cdot c_{p,steam} \cdot (T_{steam,superheated} - T_{water}) \quad (Eqn. 2 - 26)$$

Rearranging to solve for the superheated steam, and substituting Equation 2-25 into  $\dot{Q}_{steam,superheated}$ :

$$\begin{aligned} T_{steam,superheated} &= T_{water} + \frac{\dot{Q}_{steam,superheated}}{\dot{m}_{steam} \cdot c_{p,steam}} \\ &= T_{water} + f_{superheater} \cdot (T_{emitter} - T_{water}) \end{aligned} \quad (Eqn. 2 - 27)$$



## 2.3 Properties of water & steam

*“The sun, moving as it does,  
sets up processes of change and becoming and decay,  
and by its agency the finest and sweetest water is every day carried up and is  
dissolved into vapour and rises to the upper region, where it is condensed again by  
the cold and so returns to the earth. This, as we have said before, is the regular course of nature”*  
- Aristotle (4<sup>th</sup> Century B.C.).

Due to its unique properties, water (i.e. H<sub>2</sub>O in liquid form) has been the vital element, not only to sustain life on Planet Earth, but also to civilization on a wide variety of fundamental applications. Most notably, we rely on water either for consumption or for other purposes such as washing and sanitation, power generation, hydraulic lifts, and more. Moreover, the phases of water each have unique properties each suited to various applications.

Since the formation of the natural water cycle nearly 4.5 billion years ago (with the age of the universe currently held to be 13.7 billion years and the Earth as 4.6 billion years), water was the ultimate ingredient for the first single-celled organism to flourish (4 billion years ago), leading eventually to more complex multi-celled organisms [43]–[45]. Much later on, human settlements directly relied on the presence of water bodies, which persisted all the way up until today. Most ancient civilizations, from Ancient Mesopotamia (land between two rivers, the Euphrates and Tigris), Indus Valley civilization (named after the Indus River), Ancient Egyptians and Nubians along the Nile River, to the Ancient Greeks and Romans along the Mediterranean Sea, and the Chinese Empires along the South China Sea. The one constant to all of these ancient empires were control of water (sometimes referred to as ‘hydraulic empires’ in the literature) [46].

Even to this day, most urban mega-cities (most of which are historical capitals, administrative centers or port cities) lie along major water bodies. Presence of such water bodies enabled agriculture, naval defense, trading hubs and other bounties basic to civilizational success.

Sharp [18], in their treatment of ‘Water Structure & Properties’, also eloquently pointed out how the polar nature of water molecules as well as molecular bond structures (namely hydrogen bonds) are responsible for very subtle developments in biological evolution and adaptation. Moreover, very critical natural water cycle mechanisms rely on seemingly contradictory properties of water. For example, water in its ice form is less dense than liquid water (not the case for most matter), leading ice to float to the top of water and protect water flora and fauna while also keeping them cool by reflecting incoming solar radiation. More subtly, water

is least dense at 4 °C in its liquid form (density ~ 1000 kg/m<sup>3</sup>) in contrast to the typical density of water in liquid form at 20 °C (~ 998 kg/m<sup>3</sup>) and more drastically its ice form (~920 kg/m<sup>3</sup>) of which there are currently 18 forms known depending on solid lattice arrangements. This subtle change in density shows that in nature with ice sheets protecting water bodies, ice floats to the top and insulates water where the most dense liquid water of 4 °C floats to the bottom relative to top-layer ice sheet, preventing entire water bodies from freezing (given that ice is also a relatively good insulator with  $k \sim 2 \text{ W}/(\text{m}\cdot\text{K})$ ) and causing the death of aquatic flora and fauna below during winter seasons. It is also interesting to note that the ambient temperatures of Earth (average surface temperature being ~ 15 °C along the equator and -15 °C in polar regions) are perfectly suited to this molecule and the water cycle to sustain life.

Moreover, there are subtle details in the density of moist air (i.e. air carrying water in its vapor form), which is less dense than ambient air, leading to evaporation from oceans and other water bodies ultimately rising to the sky and condensing as clouds. The present study won't go into further detail, which may be investigated at length, such as the properties of aerosols (i.e. clouds) under solar radiation leading to more complex cases of precipitation.

Being able to manipulate water thermally requires a fundamental understanding of its molecular composition, which ultimately influence its thermal, optical and salinity properties. The present study has ignored electrical and magnetic properties of water such as dielectric constant, dipole moment and magnetic field strength [18] which may have interesting evaporation implications given the effect of a magnetic or electric force on the water-air interface [47].

Interestingly, while water is hailed as a universal solvent capable of dissolving most solutions (most notably salts and minerals), this property has undesirable effects in the context of desalination and clean drinking water. Callister [48] in an excellent materials science & engineering textbook goes on to mention all materials may be investigated from the molecular, microscopic and macroscopic levels, which may be a useful characterization for investigating water. To this end, the following sections begin with the molecular view of water, followed by a more microscopic realizations from its molecular structure with regards to thermal and optical properties. Lastly, the macroscopic interactions of water with salt (i.e. salinity of water) will be discussed.

### *2.3.1 Molecular properties*

The molecular structure of water (i.e. H<sub>2</sub>O) makes it easier to understand virtually all of its other properties, from thermal, optical to deteriorative properties in following sections. As Sharp [18] pointed out, water truly is an anomalous substance which contributes to vital functions for life on a very grand level. The quote made at the beginning the present Section illustrates this inherent understanding since time immemorial.

Water molecules are composed of two hydrogen atoms bonded with 104° of spacing between them by one oxygen atom [18]. This angle changes, with corresponding molecular arrangements changing from one state of water to another (e.g. liquid to ice, or liquid to vapor). The entire structure and properties of water

has been detailed at length and with great coherence by Sharp [18], which will be consulted as the primary literature for the present sub-section.

The resulting physical properties of water resulting from its molecular structure are further outlined by Sharp [18] in detail and adapted below in Table 2-3.

*Table 2-3: Selected physical properties of water.*

<b>Property</b>	<b>Water</b>	<b>Methanol</b>	<b>Dimethyl ether</b>
Formula	H <sub>2</sub> O	CH <sub>3</sub> OH	(CH <sub>3</sub> ) <sub>2</sub> O
Molecular weight (g mol <sup>-1</sup> )	18	32	46
Density (kg L <sup>-1</sup> )	0.998	0.7914	0.713
Boiling point (K)	373	338	248
Molecular volume (nm <sup>3</sup> )	0.0299	0.0420	0.107
Volume of fusion (nm <sup>3</sup> )	0.0027	Negative	Negative
Liquid density maximum (K)	277	None	None
Specific heat (J K <sup>-1</sup> kg <sup>-1</sup> )	4180	2530	2370
Heat of vaporization (J kg <sup>-1</sup> )	2.3e <sup>6</sup>	1.16 e <sup>6</sup>	0.40 e <sup>6</sup>
Surface tension (mN m <sup>-1</sup> )	72.8	22.6	16.4
Viscosity (μPa·s)	1002	550	233
Dielectric constant	78.6	33.6	5.0
Dipole moment (cm x 10 <sup>30</sup> ) during gas phase	6.01	5.68	4.34

Critical features of water, including its high surface tension (either measured in N/m or J/m<sup>2</sup>) may also be explained in the context of intermolecular hydrogen bonds within water. The bond between similar molecules is referred to as cohesion, with tendency to bond with dissimilar molecules being termed adhesion. Water is a very cohesive molecule, meaning that water molecules bond strongly to each other (may be thought of as 'sticky' liquid). This feature arises mainly due to hydrogen bonds among this polar molecule (oxygen being electronegative and the two hydrogen atoms being electropositive).

On the other hand, water may also be an adhesive surface, in terms of its interaction and stickiness with other molecules. Such materials attracting water and causing large droplets to form without spreading are termed 'hydrophobic'. Examples include rubber and plastics. On the other hand, surfaces over which water spreads without forming droplets are termed 'hydrophilic'. Examples include cloth, cotton, wool and other fibrous and porous surfaces.

Hydrophilic and hydrophobic materials have a lot of interesting applications in the context of desalination, such as the potential for capillary action for water feed and delivery, as well as directly using such principles as the Marangoni effect [49], which describes mass transfer between two fluids in the presence of surface tension gradients. Sharp [18], again, provides a very intuitive understanding of hydrophilicity from molecular perspective. Thus, this study is recommended on further details on hydrophilicity and hydrophobicity.

Seyfi et al. [47] illustrated the interfacial H<sub>2</sub>O bonds in their study of increasing evaporation rates using a static magnetic field perpendicular to the water-air interface. This study may be of interest to understand the top-surface water molecules with dangling bonds, resulting from the bonds among water molecules.

From a thermal-structural perspective, water is most dense at 4 °C, below which the molecular structures re-arrange to new arrangements (towards hexagonal structures in the first form of ice, which is most common for ambient temperatures of Earth) [18]. The various ice forms will not be discussed in the present study, but the vapor form is of particular interest (i.e. steam and its superheated form).

The molecular properties of water vapour closely resemble that of greenhouse gases such as methane of carbon dioxide. In fact, water is an important greenhouse gas in the atmosphere contributing to the greenhouse effect warming Earth through absorbed solar radiation in infrared wavelengths.

The distinction between evaporation and boiling here must now be made clear. Boiling is a specific type of rapid evaporation characterized by bubbles at the interface being heated. In most conventional applications (such as boiling water in a pot), this interface is a solid-liquid interface leading to bubble formation (i.e. the hottest part of the water volume). Bubbles essentially form as H<sub>2</sub>O particles at the bottom create vapor pockets that rise due to the gravitational effect of density difference, known in simpler terms as natural convection.

The density of steam is 0.6 kg/m<sup>3</sup>, which is more than 1650 less dense than its liquid form. Thus, it may be easy to visualize how spread out H<sub>2</sub>O molecules in steam (water vapour achieved by boiling) is compared to water.

### 2.3.2 *Thermal properties*

Before delving directly into thermal properties, a quick review of the water cycle is given.

Firstly, with regards to the physical phenomenon at the water body, three natural phenomenon drive mass transfer between the water-air interface (Figure 2-8): mass diffusion, mass convection and evaporation. Analogies may be made to heat transfer modes of heat diffusion and heat convection. Evaporation influences both heat and mass transfer. Where the analogy stops is in radiation, as there is no mass radiation [35].

The first is driven by a concentration gradient, while the second is driven by air flow over water molecules. The third is driven in nature by the sun, which heats water bodies, producing water vapour. Water in its gaseous form is less dense than air, leading moist air to rise to the sky where condenses into clouds. These

clouds are transported by winds, ultimately precipitating from clouds to mountains, lakes and other freshwater reserves. Water at the ground level eventually infiltrates and percolates to groundwater (i.e. aquifers), providing drinking sources for nearby populations. Moreover, rain nourishes nature, ultimately sustaining the ecosystem. detailed understanding of this process necessitates the invocation of thermodynamic principles revolving around water properties.

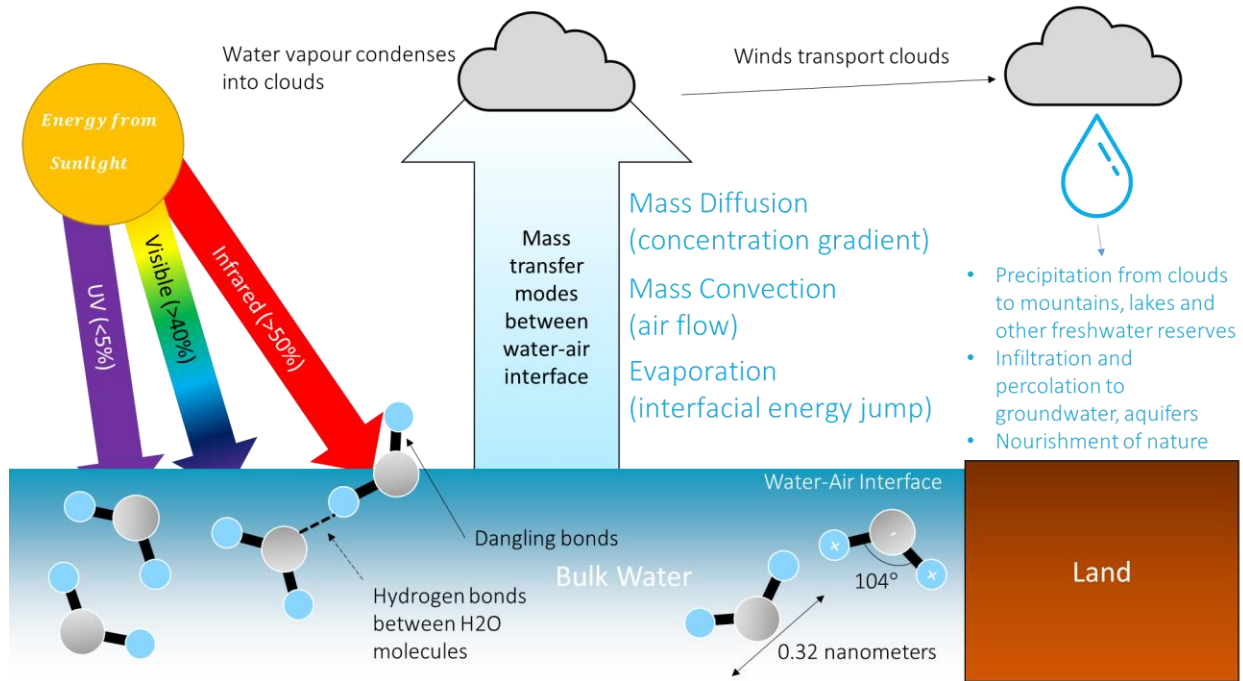


Figure 2-8: Water cycle, with details on molecular structure of water, mass transfer modes between water-air interface, condensation into clouds and finally delivery of water through precipitation making way finally to natural water reservoirs.

The most fundamental thermal property for any substance dictating its rise in temperature given a certain energy is the specific heat. It is derived from:

$$Q_{sensible} = \dot{m}_{water} \cdot c_{p,water} \cdot \Delta T \quad (Eqn. 2 - 28)$$

Re-arranging, we obtain the specific heat of water, defined as the power required to raise the temperature of a mass of water by 1 °C(measured in kJ/kg):

$$c_{p,water} = \frac{Q_{temperature,rise}}{\dot{m}_{water} \cdot \Delta T} \quad (Eqn. 2 - 29)$$

Thus, the specific heat in the case of water can be calculated if the heat transfer rate, mass of water and temperature differential values are known. Finding the specific heat of any substance is relatively straightforward with values commonly found in heat transfer and thermodynamics textbooks [35].

The specific heat of water is ~4200 J/kg (going down to ~3850 J/kg for seawater), whereas the specific heat of steam at near 100 °C is nearly half at ~ 2000 J/kg.

It must be noted that this rise in heat power may essentially be achieved by any of the three heat transfer modes discussed thus far. In the present study, we seek to maximize the radiation component of heat transfer by using infrared heating.

The fundamental parameter dictating the energy required to evaporate water is the latent heat of vaporization for water ( $h_{fg}$ ), with the  $f$  and  $g$  subscripts denoting the fluid transition to gas phase [17]. In the present study, this quantity was estimated to be 2,257,000 J/kg (or more simply, 2,257 kJ/kg). This parameter is also fundamental towards plotting Psychrometric tables for HVAC and Built Environment applications.

The sensible and latent heat terms will now be elaborated on briefly. Considering water is at its boiling point with a free surface (100 °C under atmospheric pressure of 101 kPa on Earth), any further energy delivered to the water body goes into re-arranging its molecular structure as a vapor (the same goes for the state change from liquid water to solid ice). This energy going towards state change (without a sensible rise in temperature) is known as the latent heat of vaporization (with the latent heat denoting the ‘hidden’ energy in breaking molecular bonds, or in making them in the case of the latent heat of fusion). The reverse, where there is a sensible rise in temperature (which is more intuitive from a sensory perspective), is referred to as sensible heat.

At the boiling point, there is no longer a sensible increase in temperature, and further energy put into the thermal system goes towards latent heat breaking molecular H<sub>2</sub>O bonds leading to the vapor phase.

$$Q_{evaporation} = \frac{dm_{water, evaporated}}{dt} \cdot h_{fg} \quad (Eqn. 2 - 30)$$

With key thermal properties of water covered, we may delve now into the mass transfer characteristics of water. To this regard, we begin with Fick’s first law on mass diffusion.

$$j = -D \cdot \frac{dC}{dx} \quad (Eqn. 2 - 31)$$

Where  $J$  is the mass diffusion flux, of which the dimension is amount of substance per unit area per unit time.  $D$  is the diffusion coefficient (units of area per unit time) between substances.  $C$  refers to the concentration of substance, which is the amount of substance per unit volume (units of molar mass per volume). Converting the diffusion flux to mass flow rate (kg/s), we may find an appropriate equation for modelling mass diffusion within CSES. (Eqn. 2 - 32)

$$\dot{m} = j \cdot A \cdot M = A \cdot M \cdot -D \cdot \frac{dC}{dx}$$

The diffusion coefficient ( $D$ ) is taken for the water-air interface, which is  $26e^{-6}$  m<sup>2</sup>/s. We may simplify the above equation for mass diffusion through a certain thickness ( $L$ ). The subscript 2 denotes the higher concentration of species, namely water; the subscript 1 denotes air saturated with a certain amount of water along the concentration gradient from water surface across the thickness of air (varying in concentration of water vapour molecules in air):

$$\dot{m} = A \cdot M \cdot \frac{D}{L} \cdot (C_2 - C_1) \quad (\text{Eqn. 2 - 33})$$

We define the concentration as the molar fraction per volume ( $N/V$ ) from the ideal gas law, which relates the pressure ( $P$ ), volume ( $V$ ), molar mass ( $N$ ) and temperature ( $T$ ) to a constant ( $R$ ). The ideal gas law, for review, is given by:

$$P \cdot V = N \cdot R \cdot T \quad (\text{Eqn. 2 - 34})$$

Where the concentration can be found from the vapour pressure of water at a certain temperature. The vapour pressure of water is the pressure exerted by molecules of water vapor in gaseous form (whether pure or in a mixture with other gases such as air). The saturation vapour pressure is the pressure at which water vapour is in thermodynamic equilibrium with its condensed state. At pressures higher than vapour pressure, water would condense, while at lower pressures it would evaporate or sublimate.

$$c_v = \frac{P_{\text{vapor}}}{R \cdot T} \quad (\text{Eqn. 2 - 35})$$

Substituting the above as the concentration:

$$\dot{m} = A \cdot M \cdot \frac{D}{L} \cdot \left( \left( \frac{P_2}{R \cdot T_2} \right) - \left( \frac{P_1}{R \cdot T_1} \right) \right) \quad (\text{Eqn. 2 - 36})$$

Setting  $P_2$  and  $P_1$  equal to the saturation pressure for air ( $P_{\text{saturation}}$ ).

$$\dot{m} = A \cdot M \cdot \frac{D}{L} \cdot \left( \left( \frac{P_{\text{saturation}@T_2}}{R \cdot T_2} \right) - \left( \frac{P_{\text{saturation}@T_1}}{R \cdot T_1} \right) \right) \quad (\text{Eqn. 2 - 37})$$

Taking the saturation pressure for both temperatures at the saturation pressure of  $T_1$ , the saturation pressure and ideal gas constant terms can be taken out to simplify into:

$$\dot{m} = A \cdot M \cdot \frac{D}{L} \cdot \left( \left( \frac{P_{\text{saturation}@T_1}}{R} \right) \cdot \left( \frac{1}{T_2} - \frac{1}{T_1} \right) \right) \quad (\text{Eqn. 2 - 38})$$

Finally, in the case of CSES,  $T_2$  may be taken as the water ( $T_{water}$ ) and  $T^1$  as the emitter ( $T_{emitter}$ ). This equation is the one used in the model to simulate mass diffusion in this unusual case of hot surface at top and cooler surface at bottom with saturated air in between. We also take  $h_{mass}$  as the mass transfer coefficient, which for diffusion is defined by  $D/L$ .

$$\dot{m} = A \cdot M \cdot h_{mass} \cdot \left( \left( \frac{P_{saturation@T_{emitter}}}{R} \right) \cdot \left( \frac{1}{T_{water}} - \frac{1}{T_{emitter}} \right) \right) \quad (Eqn. 2 - 39)$$

The mass transfer coefficient by convection is not used in the model but relevant in real-world scenarios with wind over water. It may be obtained from the relationship:

$$j = \dot{m} = \frac{dm}{dt} = h_{mass,convection} \cdot (\rho_{vapor} - \rho_{moist,air}) \quad (Eqn. 2 - 40)$$

Using the Chilton-Colburn analogy for special cases of  $\nu = \alpha = D_{ab}$  [35]:

$$h_{mass,convection} = \frac{h_{heat}}{cp \cdot \rho} \quad (Eqn. 2 - 41)$$

To understand the analogy between heat and mass transfer in more detail (including utilizing Reynolds, Grasshoff, Prandtl, Schmidt, Stanton, Sherwood, Nusselt numbers), the popular reference textbook by Cengel [35] may be consulted. A summary is given below in Table 2-4 below.

*Table 2-4: Analogy between quantities appearing in the formulation and solution of heat convection and mass convection.*

<b>Heat Convection</b>	<b>Mass Convection</b>
$T$	$C, y, \rho$ or $w$
$h_{convection}$	$h_{mass}$
$\delta_{convection}$	$\delta_{concentration}$
$Re = \frac{\rho \cdot V \cdot L_c}{\mu}$	$Re = \frac{\rho \cdot V \cdot L_c}{\mu}$
$Gr = \frac{g \cdot \beta \cdot (T_{surface} - T_{ambient}) \cdot L_c^3}{\nu^2}$	$Gr = \frac{g \cdot (\rho_{ambient} - \rho_{surface}) \cdot L_c^3}{\rho \cdot \nu^2}$
$Pr = \frac{\nu}{\alpha}$	$Sc = \frac{\nu}{D_{AB}}$
$St = \frac{h_{convection} \cdot L_c}{k}$	$St_{mass} = \frac{h_{mass}}{V}$
$Nu = \frac{h_{convection} \cdot L_c}{k}$	$Sh = \frac{h_{mass} \cdot L_c}{D_{AB}}$



$Nu = f(Re, Pr)$	$Sh = f(Re, Sc)$
$Nu = f(Gr, Pr)$	$Sh = f(Gr, Sc)$

### 2.3.3 Optical properties

With radiative properties defined for both surface and volume exchange problems in sub-section 2.2.3, the present section will detail the optical transmission through water, which is fundamental to understanding the reason behind utilizing infrared radiation (using a ~130 °C hot surface, i.e. the emitter) to heat water in CSES as opposed to solar wavelengths.

Plotting the penetration depth along a vertical coordinate and utilizing understanding of the mean free pathlength of photons within water before absorption ( $1/\kappa_\lambda$ ), we obtain the following plot as shown by Cooper et al [3] in Figure 2-9, showing the correlation between infrared wavelengths and absorption of photons within those wavelengths for water.

The optical properties of steam are not considered, as steam is very transparent under radiation within infrared wavelengths.

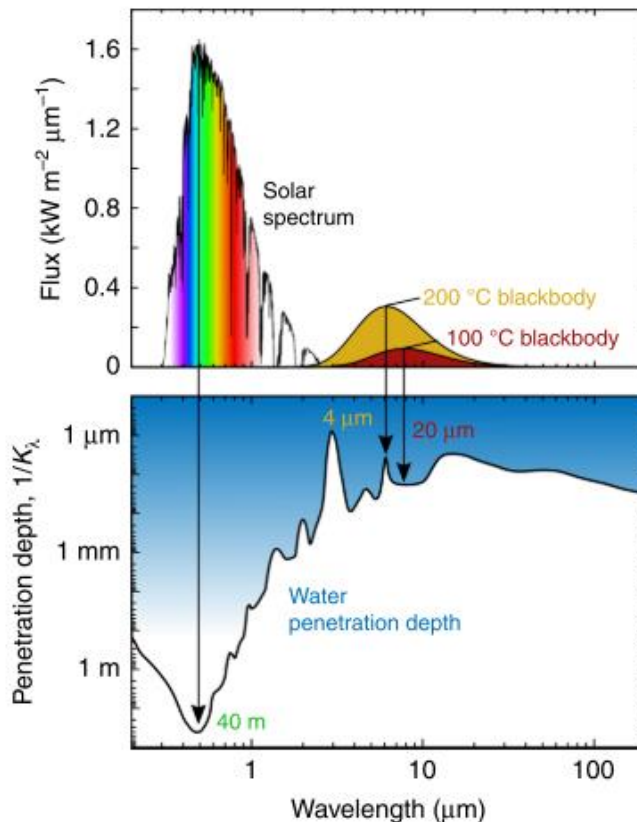


Figure 2-9: Transmission spectra of solar radiation through water [3].

#### 2.3.4 Salinity properties

The salinity properties of water discussed in the present section. It is especially relevant to fouling, which has been a critical issue in solar stills and desalination systems in general since their inception.

In general, the literature refers to the concentration of salts and minerals in water by the Total Dissolved Solids (TDS), which is measured with a sensor utilizing the electrical conductivity of saline water (as calibrated against sweet freshwater to a PPM of 0). [50].

RO systems suffer from fouling due to clogging at the semi-permeable porous membrane, effectively increasing pressure required to push saline water through it [21], [51]. In fact, the TDS of water directly affects the energy required to impart enough pressure for efficient distillate outputs.

While fouling does not increase the 'work required' for solar stills to desalinate water (which is thermally-driven and noting that distillation removes typically ~ 99% of salts and minerals from water, making this a very useful technique for chemists to obtain pure H<sub>2</sub>O), solar stills nevertheless suffer from fouling, particularly as salt degrades the performance of solar absorbers over time, leading to a need to be constantly and properly discharged and cleaned, leading to salt-rejection strategies to be a major research area of interest in coming decades [6], [49], [52].

Lienhard et al. [20] summarizes the salt and mineral content of standard seawater, high brackish water, low brackish water and drinking water content from the Massachusetts water resources authority, adapted below in Table 2-5.

Essentially, the miscibility of ionic molecules or compounds mix easily in water due to the inherently polar charge of water, which is slightly more positively charged on the side of two hydrogen atoms, and oxygen as a molecule is electronegative. This polarity causes ions such as salts (Na<sup>+</sup>Cl<sup>-</sup>) to mix really well with water [18]. In fact, water is commonly hailed as the universal solvent, due to its ability to dissolve a lot of materials. This has both benefits (such as preparation of materials), while in the present context, it is a detriment if not considering water treatment and mineralizing water for safe consumption. It is interesting to note that pure water is not recommended for human consumption (potentially being fatal), as it causes an electrolyte imbalance due to pure water (which is polar with the oxygen side being positive and the two hydrogen being negative) dissolving essential salts and electrolytes in the body. In the context of solar stills and other thermal desalination methods, which achieve purity in the range of 99%, some post-treatment with minerals and salts may be needed for safe water consumption. Steam, or water vapour, does not have deteriorative properties to speak of in terms of desalination.

Table 2-5: Representative ion concentrations for standard seawater, high and low salinity, brackish water, and a municipal water supply (nr = not reported), as adapted from [20].

Substance (amounts in mg/kg)	Standard seawater	High brackish water	Low brackish water	Massachusetts water resources authority
Sodium, Na <sup>+</sup>	10,556	1,837	90	30
Magnesium, Mg <sup>2+</sup>	1,262	130	11.7	0.8
Calcium, Ca <sup>2+</sup>	400	105	96	4.5
Potassium, K <sup>+</sup>	380	85	6.5	0.9
Strontium, Sr <sup>+</sup>	13	nr	nr	nr
Chloride, Cl <sup>-</sup>	18,980	2,970	191	21
Sulfate, SO <sub>4</sub> <sup>2-</sup>	2,649	479	159	8
Bicarbonate, HCO <sub>3</sub> <sup>-</sup>	140	250	72.6	nr
Bromide, Br <sup>-</sup>	65	nr	nr	0.016
Boric acid, B(OH) <sub>3</sub>	26	nr	nr	nr
Fluoride, F <sup>-</sup>	1	1.4	0.2	1
SiO <sub>2</sub>	1	17	24	3.3
Nitrate, NO <sub>3</sub>	nr	5.0	nr	0.11
<b>Total dissolved solids</b>	<b>34,483</b>	<b>5881</b>	<b>647</b>	<b>110</b>

## 2.4 Desalination systems

*“If we could ever competitively, at a cheap rate, get fresh water from salt water, that it would be in the long-range interests of humanity which would really dwarf any other scientific accomplishments.”*

- *President John F. Kennedy (1962)*

Desalination is a fundamental part of the natural water cycle, ultimately fuelling freshwater reserves which have kept our ancestors hydrated and alive since time immemorial. It refers to the process of removing salts (NaCl) and minerals from saline water. The by-product of desalination is brine, a high-concentration solution of salt in water. As of February 2020, there are roughly 21,000 desalination projects with roughly 17,000 installed plants worldwide with a daily capacity of roughly 100 Billion L of water [19]. The largest plant to date is in Saudi Arabia (al-Jubail) producing roughly 1.4 Billion L of water per day (more than 1% of total global installed capacity, despite at least 21,000 plants). The statistics on global projects, installed plants, daily water production capacity, energy demand and cost will all rely on the multi-criteria, comparative review by Thi et al. [19].

Broadly speaking, desalination systems may be categorized either by the energy source being used or by the fundamental driving mechanism [53]. The latter definition, sub-divided as either thermally-driven or mechanically-driven desalination systems, will be adopted in the context of the present study. Broadly speaking, 70% of desalination plants are Reverse Osmosis (RO), 20% are Multi-stage Flash Distillation (MSFD), 7% are Multi-effect Distillation (MED) plants, with the remaining 3-5% being used by methods such as Electrodialysis, or ED (a method gaining recent popularity and not falling under either thermally- or mechanically-driven, but electrically-driven desalination), nanofiltration, Membrane Distillation (MD) and Freeze Desalination (FD).

Some of the most popular desalination methods in each category are discussed below, with an overview of schematics discussed in further detail in coming sub-sections shown in Figure 2-10. Thermally-driven desalination systems (four discussed in the present study) are not widely adopted due to their high energy cost of separating salts. Thus, methods such as Membrane Distillation (MD) or Freeze Desalination (FD), are not discussed, but readers may consult the studies by Warsinger et al. [51] and Kalista et al. [54], respectively, for these methods.

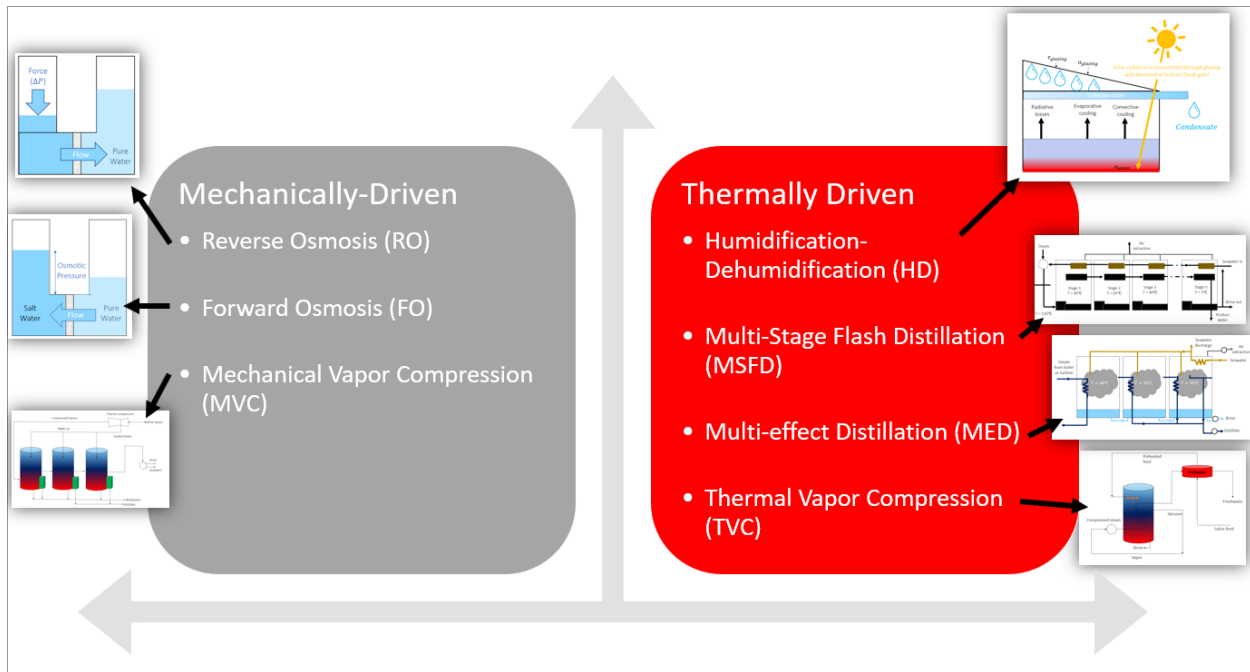


Figure 2-10: Classification of Desalination Methods according to fundamental driving mechanism [53].

Some corresponding details for each method are detailed in the Table 2-6 below based on the review of desalination technologies by Thi et al. [19].

Table 2-6: Overview of Desalination technologies [19].

Classification	Thermal	Membrane
Desalination technologies	MED, MSF, MVC, TVC	MF, UF, NF, MB, MD, ED, RO
Separation mechanism	Phase change	Diffusion
Main type of energy requirements	Thermal	Electricity
Driving force	Heat	Pressure/Electricity
Specific energy consumption	High	Low

For further information on the historical context of desalination systems as well as how they have translated to desalination system designs today, two popular references by Kalogiru may be consulted: 'Solar Energy Engineering' [55] and 'Solar Desalination Systems' [56]. Another great resource is 'Thermal Desalination Systems' by Vasilys [53]. For a more social and historical perspective, readers may consult the book on 'History of Desalination before large-scale use' by James D. Birkett or the short-yet-comprehensive journal entry by Angelakis et al. [57].

#### 2.4.1 *Brief history of desalination*

Since as early as 6000 B.C., desalination technology has been developed for both survival on the high seas by sailors, as well as during travels on ground where access to nearby water resources is limited [57]. Desert dwellers, in particular, heavily rely on novel methods of producing drinkable water from saline water for aforementioned reasons. Angelakis et al. [57], in a very comprehensive historical review of desalination technology, points out that nearly for 8000 years (6000 B.C to 1850s Industrial Revolution Era), thermally-driven desalination was the main method. Much of these methods were crucial, in terms of survival, for sailors, military expeditions and any other venture which necessitated travel in regions with unknown water reservoirs.

Bolstered by the industrial Revolution which led to development of factories and rapid urbanization, in conjunction with the scientific knowledge of thermally-driven desalination and osmosis a hundred years prior by Jean-Antoine Nollet, the first desalination plants started to be built and tested. The summary of historical achievements in the study are shown below.

Within the end of the past century, various nations without ready access to freshwater (either from groundwater, freshwater lakes, rain or mountains) have resorted to desalination plants for their water needs. The growth of desalination since the 1960s was also summarized by the UNESCO in the 2019 report [58], as shown in Figure 2-11. Key points from the report further illustrate the global water withdrawals from agriculture, industry, municipalities and reservoirs which further illustrate the motivation for desalination.

With regards to global water withdrawals, water consumption per capita and water usage per capita (including agricultural, industrial and power needs) have extensively been compiled by UNESCO. The global growth of desalination, in particular, has been compiled and reproduced from the 2019 UNESCO report (Figure ). For Canada, in particular, water data may be found on the government website for statistics [59] for the country as well as all provinces.

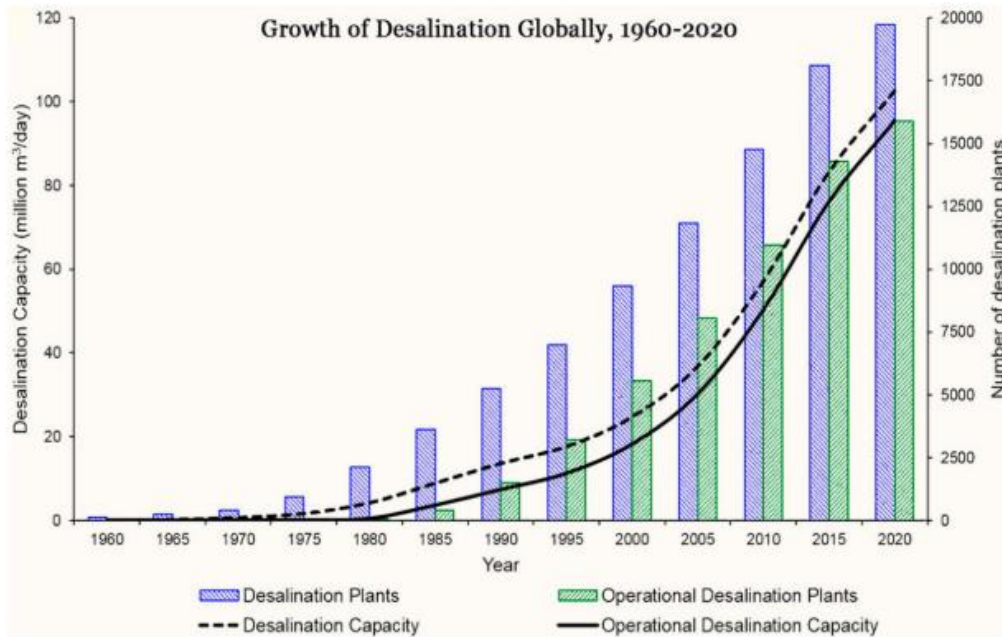


Figure 2-11: Desalination growth in last 3 decades [58].

A major motivation behind the present study is in the fact that a large number of water-starved nations (e.g. Saudi Arabia, Mexico, Australia, Morocco) receive a lot of yearly solar radiation. Furthermore, many of these regions are arid desert regions with very little annual rainfall. Coincidentally, these regions have large coastal regions full of saline water. These facts illustrate the clear motivation behind solar desalination in particular (also illustrated in Figure ). Desalination capacities outlined in further sections are summarized below using from the review by Thi et al. [19] on desalination (Table 2-7).

Due to the high energy consumption of any type of desalination, it is generally cheaper to transport from nearby freshwater reservoirs if available (Table 2-7). Holistic decisions to employ desalination methods may begin by first considering the alternatives as well as corresponding energy demand (kWh/m<sup>3</sup>) [19].

Table 2-7: Comparison of energy requirements for water of different salinities and mineral content.

Water Supply Alternative	Energy (kWh/m <sup>3</sup> )
Conventional treatment of surface water	0.20-0.40
Groundwater	0.48
Wastewater treatment	0.62-0.87
Wastewater reuse	1.00-2.50
Brackish water desalination	1.00-1.50
Seawater desalination	2.58-8.50

### 2.4.2 Fundamentals and working principle

Lienhard et al. [20] gives a great overview of all desalination systems from practical, thermal and financial perspectives. A very important part of this work was the mention of the ‘Minimum Work of Separation’, which details, from a thermodynamic point of view, the least amount of work required to desalinate water. This is done by applying the first and second laws of thermodynamics to a desalination system, summarized below in Equations 2-41 to 2-44 with accompanying schematic (Figure 2-12). This definition is extended with steps and assumptions to the least amount of separation required (i.e. the system is reversible with no entropy generated through mechanical, electrical or other means in the system components).

$$\dot{W} + \dot{Q} = (\dot{NH})_{pure} + (\dot{NH})_{brine} - (\dot{NH})_{saline} \quad (\text{Eqn. 2 - 42})$$

$$(\dot{NS})_{pure} + (\dot{NS})_{brine} = (\dot{NS})_{saline} + \frac{\dot{Q}}{T_0} + \dot{S}_{gen} \quad (\text{Eqn. 2 - 43})$$

$$\dot{W}_{least} = [(\dot{NG})_{pure} + (\dot{NG})_{brine}] - (\dot{NG})_{saline} \quad (\text{Eqn. 2 - 44})$$

$$\dot{Q}_{least} = \frac{[(\dot{NG})_{pure} + (\dot{NG})_{brine}] - (\dot{NG})_{saline}}{1 - T_0/T_H} \quad (\text{Eqn. 2 - 45})$$

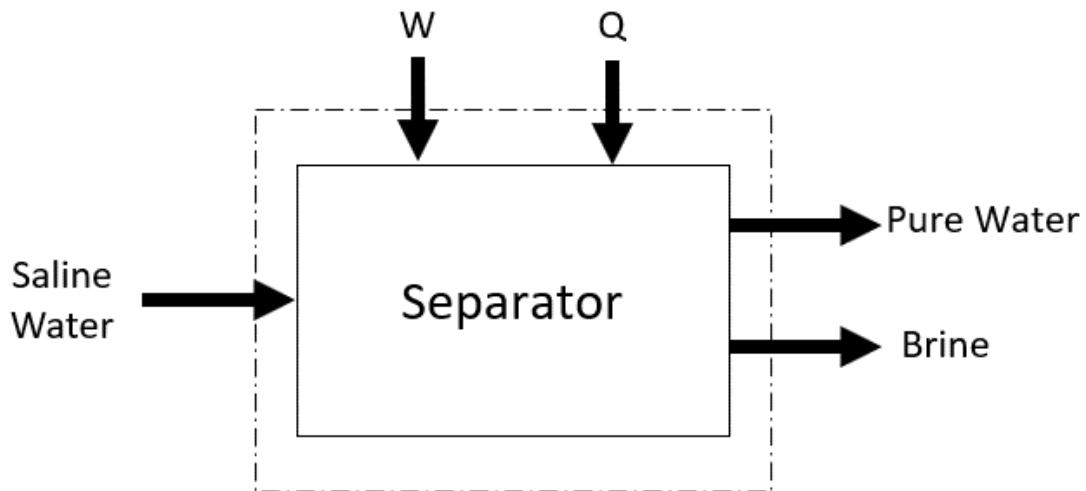


Figure 2-12: Schematic diagram of a work-driven desalination system [20].



### 2.4.3 *Thermally-driven desalination*

Thermally-driven desalination relies on the evaporation characteristics of water when heated. To this aim, high water temperatures (above 60 °C) are sought if using methods such as many HD systems, MED or TVC, or the boiling point if steam is to be produced such as in MSFD and novel HD systems which seeks to not only boil water but also to superheat its vapour form, such as CSES in the present study.

Thermally-driven desalination methods covered in this sub-section include:

- Humidification-Dehumidification (HD) systems (including solar stills and solar ponds)
- Multi-Effect Distillation (MED)
- Multi-Stage Flash Distillation (MSFD)
- Thermal Vapor Compression (TVC)

Most of the emphasis in this sub-section will be given to HD systems in the context of solar stills, as this will be the process which the present study utilizes for solar desalination.

For each method outlined, the following factors will be highlighted:

- Installed global plants and capacity
- Working principle
- Energy consumption & cost

#### 2.4.3.1 *Humidification-Dehumidification (HD) systems*

Humidification-Dehumidification (HD) systems essentially mimic the natural water cycle, but over a significantly shorter time frame and smaller scale [60]. The device which utilizes this method of desalination by using solar heat (as opposed to other heat sources) is termed a 'solar still' (i.e. a device undergoing the process of solar distillation). While there is some debate over the inter-changeable use of the terms HD and Solar Stills, the present study, for the sake of simplicity, will utilize both these terms interchangeably. Thus, a review of solar still literature will be covered in this section.

The fundamental working principle behind the solar still is illustrated with an energy balance on a typical solar still schematic which can broadly be extended to any solar still (with the energy balance on CSES formulated in sub-section 3.1.2), shown in Figure 2-13 below. Two schematics from two studies are shown for the purpose of illustrating the both the parameters and a more realistic visual of the fundamental processes behind solar distillation.

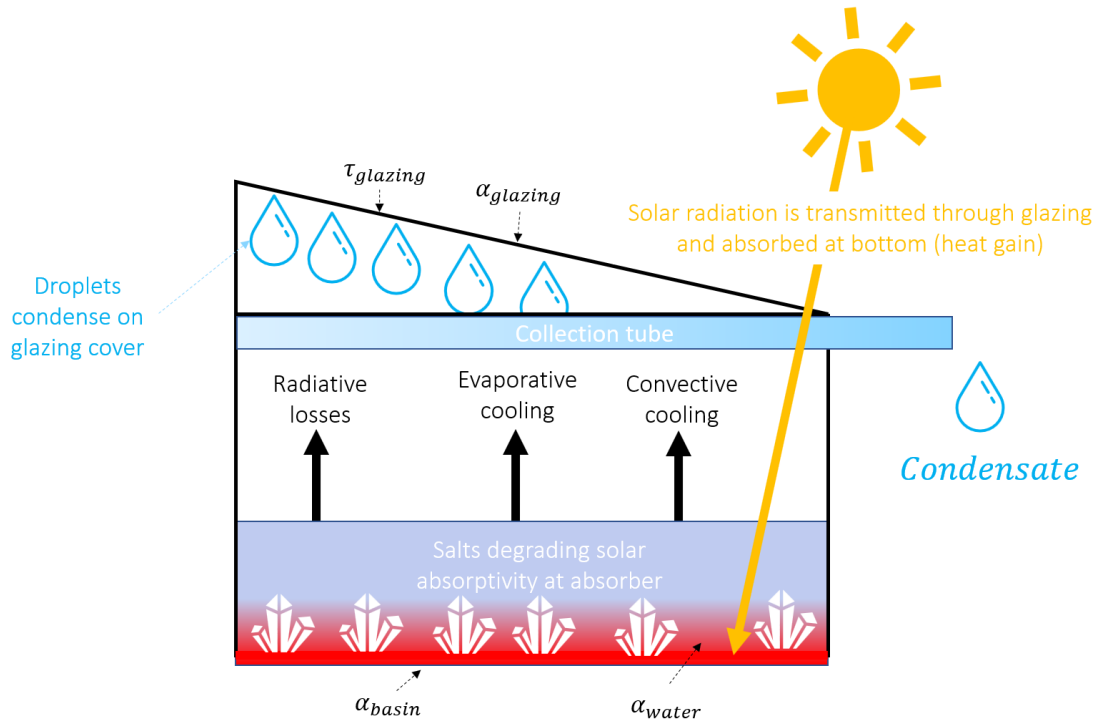


Figure 2-13: Losses occur due to radiation emitted from water, evaporative cooling and convective cooling from ambient air.

Once such an energy balance is set up, each energy loss/gain component may be observed with respect to solar irradiation throughout the day. To this aim, it would be useful to know how to gauge the productivity and performance of solar stills in relation to the energy contribution parameters discussed above. In this regard, Lienhard [20] goes on to show solar still performance in terms of the various heat flux mechanisms present.

As is apparent, solar stills are heavily reliant on the available solar energy for a particular location (discussed in more depth in Section 2.5). In this regard, all solar stills may be thought to have three distinct phases: 1) initial heat-up phase, 2) quasi-steady phase and 3) cool-down phase during the dark.

Firstly, a major limitation of HD systems are in their inherent high cost due to high latent heat of vaporization of water [18]. This point is illustrated by Kalista et al. [54]. In their study, it can be seen that HD systems have more than 4 times the typical cost for distillate outputs than do other desalination methods.

However, despite the inherently high energy cost of solar distillation may seem deceiving, as a fundamental advantage of any HD system lies in the fact they may be employed anywhere with the addition of a solar absorber or even a natural solar absorber already available. The cheap cost with which solar stills may be constructed (perhaps even for free using 'junk' materials) also contribute to their water equity. An Exergo-

economic analysis was conducted by Shoeibi et al. [61] illustrating this point, with the conclusion that despite their relatively high cost of desalinating water (and at low capacities compared to other methods), solar stills may in general be justified by their exergo-economic factors (i.e. the combination between exergy, the available energy, and cost). An enviro-economic and exergo-enviro-economic analysis was also shown in the study to justify the employment of solar stills given their very cheap building materials and environmental advantages of build materials, with a classification of different solar stills based on active collection, passive collection and geometry in light of the cost of water production, exergoeconomic, environconomic and cost-benefit ratio.

On the topic of distillate outputs, solar stills have typical yields of between 2 and 10 L/m<sup>2</sup>/day [61]. The comprehensive review by Shoeibi et al. [61] shows various configurations of the contact solar still with details on price, climatic conditions, type of solar still (e.g. pyramid, single/double slope, black steel wool fibre absorber, flat plate solar collector, sand in basin, etc.), cost of fabrication (ranging from as cheap as \$82 to \$1603), interest rate, lifetime (ranging from 8 to 50 years), annual productivity (ranging from 954 to 6099 L per year for a 1 m<sup>2</sup> receiver), and cost per litre (~\$0.01 to \$0.02 USD per litre).

This is seen by many researchers as the biggest problem plaguing solar stills, especially compared to the distillate outputs of mechanically-driven desalination methods such as Reverse Osmosis (capable of producing more than 1000 times the daily capacity at roughly 1% of the Cost per Litre (CPL)). Despite this, it is apparent from the compilation of solar stills that the cost of fabrication (i.e. low setup cost), life time and annual productivity (L/m<sup>2</sup>) may have very niche yet useful applications, particularly geared towards rural and smaller communities.

A current global topic involves the issue of water equity. Political and social turmoil in various regions of the world, particularly in impoverished nations with large rural community regions, necessitate that every household has a personalized water system, especially in emergency scenarios. In this regard, solar stills have the capability to fill this need for water equity, given the cheap and available material costs, as well as ease of building. One greenhouse company uses solar stills integrated in tandem with a greenhouse in the desert region [62]. With the imminent boom of greenhouses in urban settings in the coming decades, solar stills have a very strong potential to be integrated in this respect to not only provide desalinated water for agriculture and greenhouse applications, but also to provide nearby residents (perhaps community members) with desalinated water achieved passively and exergetically.

The issue of fouling is perhaps the more pressing concern and one which has plagued solar stills since their inception. As water evaporates and leaves salt behind, the salt accumulation effectively reduces the solar absorptivity of the absorber for solar interfacial evaporation structures, leading to a reduced efficiency throughout its operation. This time-dependent efficiency drop is one which the present study seeks to remedy by way of a CSES design (termed CSES by Cooper et al. [3]), whereby there is a gap between the solar absorber and water. This contactless configuration completely bypasses the salt accumulation on

absorber issue, as there is virtually no chance of salt interfering, unless the structure is not kept level and saline water splashes onto the emitter.

Solar stills are also crucial in the event of disasters or situations where large-scale plants cannot be practically installed. In fact, solar stills have a potential to be part of the flood rescue arsenal during disasters in some countries, with safe drinking water mentioned by researchers reviewing flood disaster management to be one of the primary concerns for flood victims [12], [13], [33], [63]. Similarly, solar stills prove to be quite useful for any marginalized, cut-off or isolated region and victims.

There is current research interest in high-efficiency, low-cost solar stills. Furthermore, these solar stills must be largely self-sufficient and automated requiring minimal maintenance typically required for solar stills due to the issue of fouling (i.e. salt accumulation in the water basin or worse, absorber, reducing its solar absorptivity).

Recent and novel designs of solar stills include designs utilizing solar ponds [64], rotating solar collector [65], floating capability [6], [66], Compound Parabolic Concentrator (CPC) [3], evacuated tube collector utilizing an antibacterial-magnetic hybrid nanofluid [67] and interfacial infrared heating explored in the present study [3].

#### *2.4.3.2 Multi-Effect Distillation (MED)*

Multi-Effect Distillation (MED), shown in Figure 2-14, operates on the principle of heating feed water in N-stages (number of stages varies highly among designs), whereby each stage heats water (commonly using steam in tubes as the heat exchanger in a counter-current arrangement) to evaporation. The heat released during condensation is recycled and used to drive the evaporation of the subsequent stage. Thus, the energy from each stage is reused with successively lower temperatures and pressures after each stage. The energy used to heat the steam may be from virtually any energy source, leading to many studies utilizing solar-driven MED [68]–[70]. Moreover, this method can operate at lower temperatures of 60 °C, which is quite easy to achieve using solar energy (flat plate collectors can heat up to above 150 °C).

As of 2019, 7% of all desalination plants utilize the MED process [19], equating to roughly 1500 plants. The total desalination capacity for this process is 6.65 billion Litres per day from all MED plants, with typical capacity per plant of 5 to 15 million Litres per day.

The energy demand is 230 to 390 kJ/kg is more than a tenth of the latent heat of vaporization of water for 1 L, leading to MED as a widely adopted (second after MSFD) thermal desalination method at more than 10 times as cheap as basic solar stills. This corresponds to a water production cost of roughly 50 cents to \$1 per 1000L of water produced (comparable to water from RO).

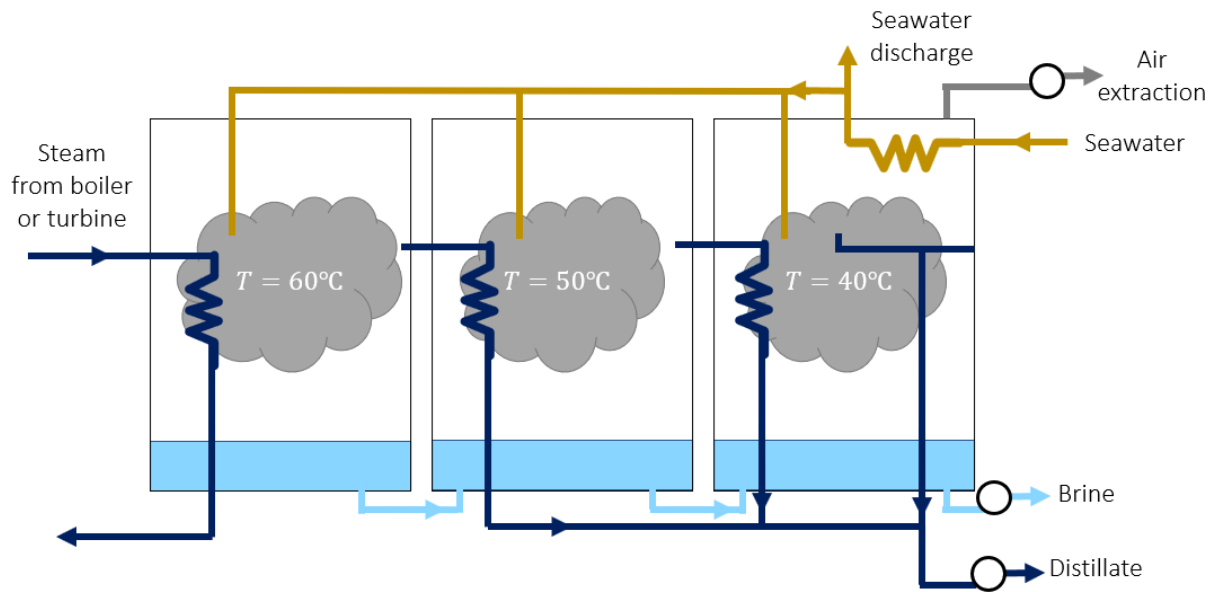


Figure 2-14: Working principle of Multi-Effect Distillation (MED) . [71].

#### 2.4.3.3 Multi-Stage Flash Distillation (MSFD)

Similar to MED, Multi-Stage Flash Distillation (MSFD), shown in *Figure 2-15*, operates on the principle of evaporating the water. This time, the fed water is flashed in multiple stages. The 'flashing' refers to flash evaporation, where water is evaporated through a reduction in pressure by passing through a throttling device. Typical operating temperatures for MSFD is 90 to 110 °C, teetering around the boiling point of water.

As of 2019, 18% of all desalination plants utilize the MSFD process [19], equating to roughly 3780 plants. MSFD is the second-most popular desalination method adopted globally after RO. In terms of thermal desalination, it is currently the cheapest option competitive with MED. The total desalination capacity for this process is 17.1 Billion Litres per day from all MED plants, with typical capacity per plant of 50-70 million Litres per day.

The energy demand is roughly 190 to 390 kJ/kg of water, within a very similar energy requirement as MED and, as before, at least 10 times cheaper than basic solar stills. It must be noted, however, that due to typically larger-capacity of units, nearly double the electricity is required compared to MED. This corresponds to a water production cost of roughly 50 cents to \$1.75 per 1000L of water produced.

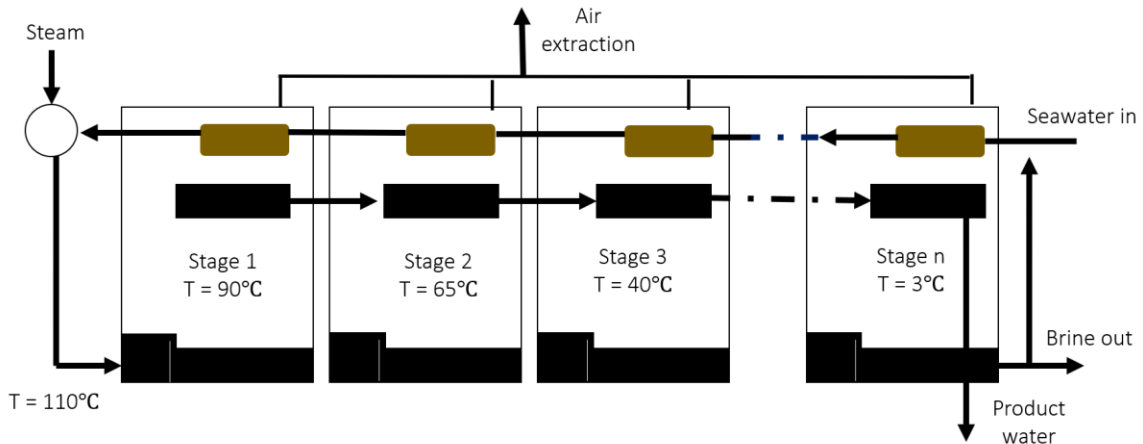


Figure 2-15: Working principle of Multi-Stage Flash Distillation (MSFD), adapted from [71]

#### 2.4.3.4 Thermal Vapor Compression (TVC)

Thermal Vapor Compression (TVC), shown in Figure 2-16, utilizes a compressor, blower or jet ejector to compress and pressurize vapor, which is then used as the heating medium for its 'mother' liquid from which water was generated using its increased condensation temperature. Without compression, the heating vapor would be at the same temperature as the 'mother' liquid without any heat transfer. Typical operating temperatures of TVC are within 63-70 °C.

As of 2019, less than 1% of all desalination plants utilize the TVC process [19]. The typical capacity per plant is 10 to 30 million Litres per day, consuming 145 to 390 kJ per kg of water heated. This translates to a water production cost of roughly 82 cents per 1000 L of water produced.

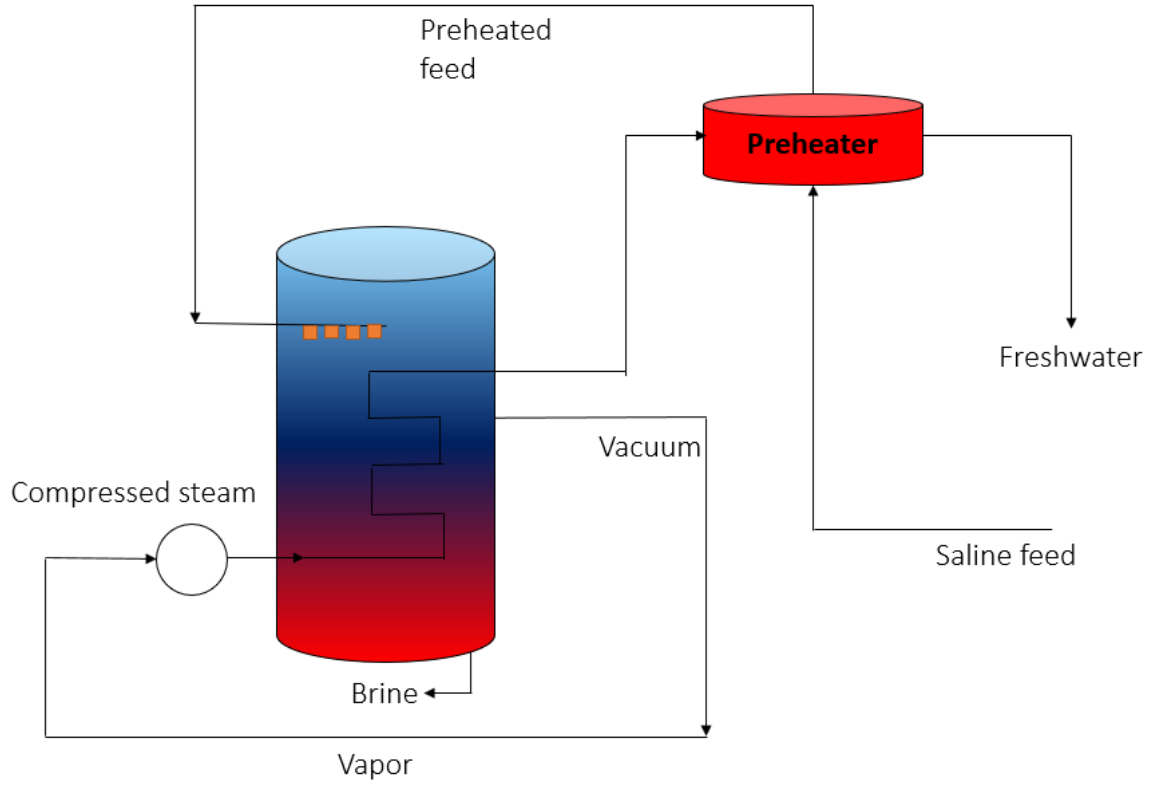


Figure 2-16: Working principle of Thermal Vapor Compression (TVC), adapted from [72].

#### 2.4.4 Mechanically-driven desalination

Mechanically-driven desalination utilizes a physical mechanical force such as a compressor (MVC) or pump to 'push' water through either a semipermeable membrane (RO and FO).

Mechanically-driven desalination methods covered in this sub-section include:

- Reverse Osmosis (RO)
- Forward Osmosis (FO)
- Mechanical Vapour Compression (MVC)

Similar to the previous sub-section, for each method outlined, the following factors will be highlighted:

- Installed global plants and capacity
- Working Principle
- Energy Consumption & Cost

##### 2.4.4.1 Reverse Osmosis (RO)

Reverse Osmosis (RO) works against osmotic pressure, a natural principle found within our bodies and studied since the 1750s [73], where water molecules spontaneously move from a solution of low solute concentration (low osmotic pressure) to one of higher solute concentration (high osmotic pressure) across a semipermeable membrane. Booming in installation since the 1950s, today there are more than 14,000 RO plants (combination planned and constructed projects) globally with a daily water capacity of roughly 24 million Litres of water per day. Salt rejection potential can be as high as 99% in most designs with a distillate quality of less than 500 ppm, but the energy demand for RO scales exponentially according to salt content of water (measured using a Total Dissolved Solids, or TDS, meter utilizing electrical conductivity of saltwater calibrated against pure water). For example, brackish water takes around 1 kWh per 1000 L of water, whereas it takes between 2 and 8 kWh for 1000 L for seawater [19].

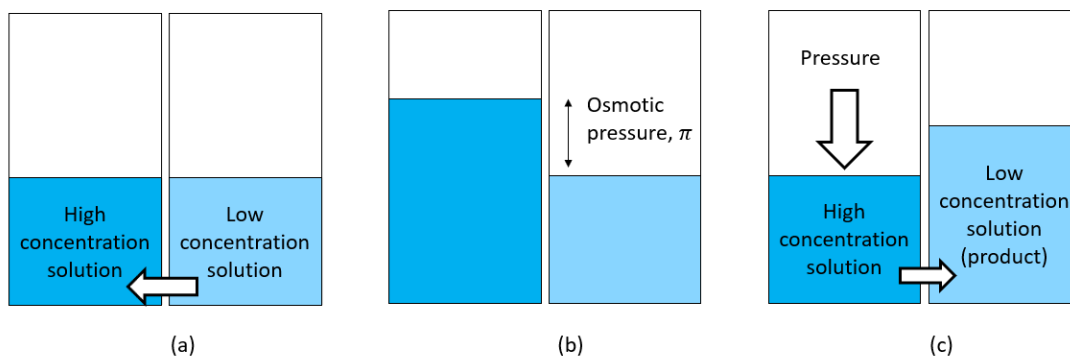


Figure 2-17: Working Principle of Reverse Osmosis (RO) with regards to (a) working principle of osmosis, (b) osmotic equilibrium and (c) working principle of RO. Adapted from [73].



For solar-powered RO systems, Shalaby [74] states that energy consumption may vary between 2.4 kWh/m<sup>3</sup> (water capacity of 1000 m<sup>3</sup> per day) up to as high as 16 kWh/m<sup>3</sup> (water capacity of 0.8 to 3 m<sup>3</sup>/day). Translating energy costs to a dollar amount, a techno-economic analysis of large-scale PV-RO (capacity of 275,000 m<sup>3</sup>/day) found that water could be produced at \$1/m<sup>3</sup> (i.e. \$1 for roughly 1000 L of water desalinated). In fact, RO systems require a lot of parts, from flocculation tanks, filter feed pumps, filters, booster pumps, suckback tank, permeate pumps, water storage tank, feed pumps, polishing units and mixed bed units [71].

Given the nature of the concentrates in RO, it is important to discuss the total dissolved solid (TDS) within solutions. Osmotic pressure for concentrations of seawater, for example, with a TDS content of 35,000 ppm would require at least 2400 kPa [75]. In reality, due to the high resistance of membranes, pressures as high as 10,000 kPa may be needed.

Without delving too much into the topic, some limitations of RO as brought up by researchers [21], [51], [76], are Pre-heating [74], Brine Disposal [74], Membrane fouling [21], [51], Plant setup, maintenance and transportation costs [77], especially important for RO adoption among low-income nations.

Novel configurations reported in the literature to combat some of these challenges include RO coupled with wave power (using natural energy processes to reduce electrical cost) [78], photovoltaics [74], [79], [80], ceramic membranes [76], ultrasonic sonification on feed channel temperature [81] and thin-film nanocomposite (TFNC) membranes [82].

#### 2.4.4.2 Forward Osmosis (FO)

Similar to RO, Forward Osmosis (FO) utilizes the principle of osmotic pressure across semi-permeable membrane, using the osmotic pressure gradient for separating brine water from purified water. The net flow of water across this gradient is driven by a draw solution of high concentration (relative to feed solution). The water must afterwards be recovered in a draw solution. By comparison, RO utilizes hydraulic pressure as the driving force for separation which serves to counteract the osmotic pressure gradient which would otherwise favor water flux from the permeate to feed. The reason for exploring FO is due to its significantly lower energy needs, energy efficiency, separation efficiency and water recovery as reviewed recently in studies [83], [84].

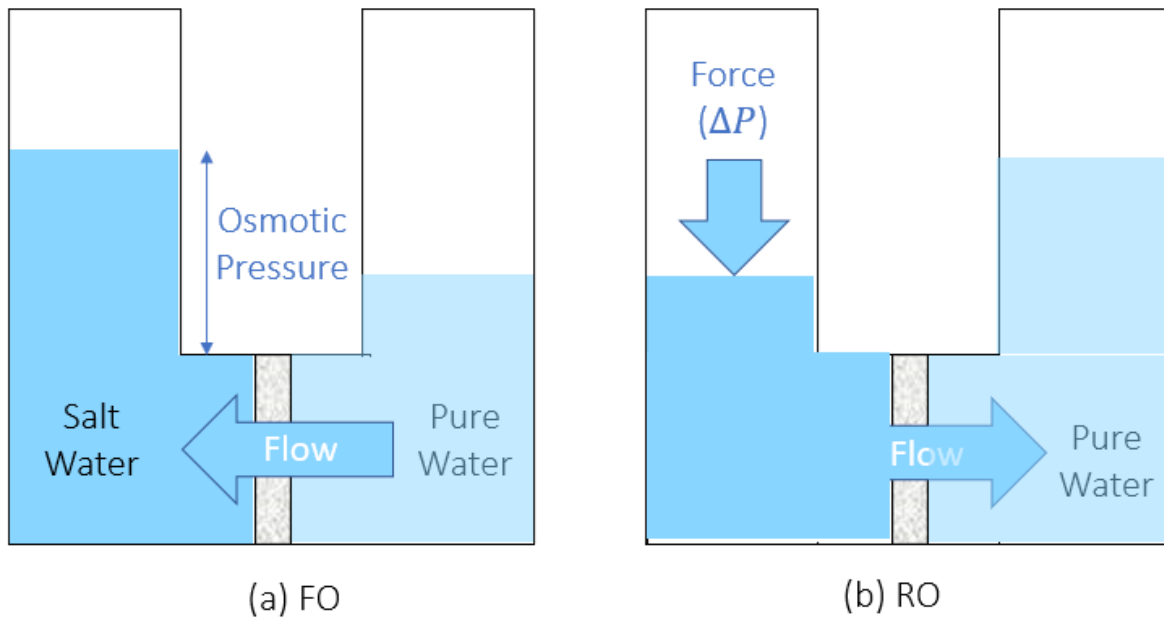


Figure 2-18: Working principle of Forward Osmosis (left) compared to Reverse Osmosis (right) [85].

2.4.4.3 Mechanical Vapor Compression (MVC)

Mechanical Vapor Compression (MVC) works on the exact working principle as TVC, with the only difference being that the energy supplied for compression is now with a mechanical compressor working using electricity instead of a thermal compressing using a steam jet ejector to create a vacuum. MVC operates at 10 times the lower capacity as TVC, at around 100,000 to 3 million Litres per day (compared to 10 million to 30 million Litres from TVC).

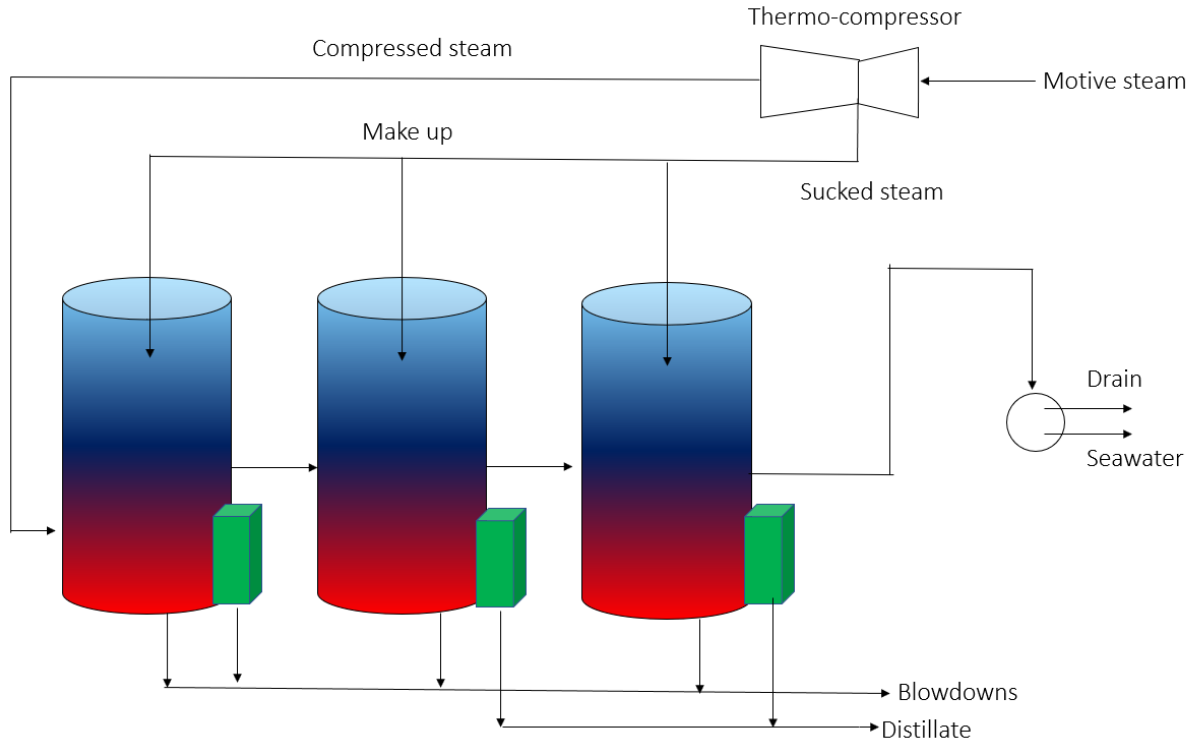


Figure 2-19: Working principle of (a) Mechanical Vapor Compression (MVC) compared to (b) Thermal Vapor Compression (TVC) [86].

#### 2.4.5 Contactless Solar Evaporation Structures (CSES)

Researchers such as Pang et al. [9] and Li et al. [2] have compiled some of the major innovations in recent solar still literature. In particular, the CSES was reviewed by both to bear tremendous potential for various heating applications, as water fundamentally absorbs better in infrared wavelengths when compared to its visible wavelength absorption spectra (leading to most HD systems, working with visible wavelengths, to have lower photon utilization whereby visible photons may be absorbed on walls of basin and lost to environment). This principle was utilized by Cooper et al. [3], who showed that water could be boiled under concentrated sunlight using infrared radiation emitted from a hot solar absorber painted with emissive paint on the side opposite absorbing side (Figure 2-20). The steam could then be convectively superheated with the same hot absorber (emitter side).

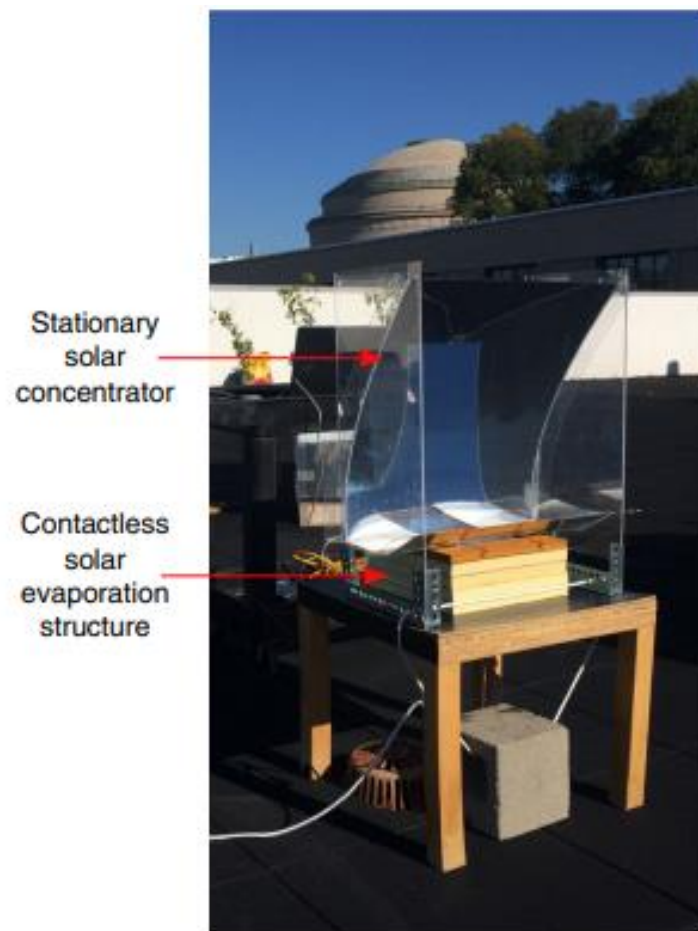


Figure 2-20: First generation prototype of CSES tested under real-sun [3].

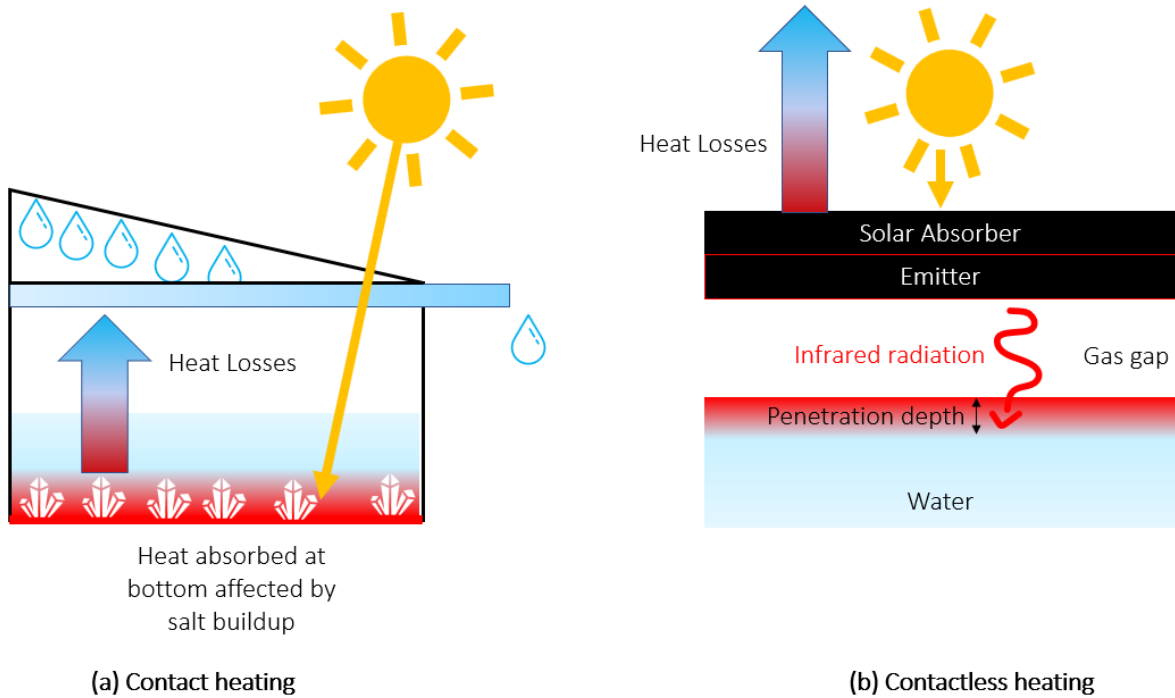


Figure 2-21: Working principle of (a) Contact heating versus (b) Contactless heating.

A later paper by Li et al. [2] summarized a few applications of infrared which have wide potential applications in everyday scenarios such as under bridges heated by the sun overpassing water bodies. These papers further illustrate the capability of HD systems to be virtually employed anywhere with clever designs involving a solar absorber and methods of conductive and convective insulation (which may be naturally available, by enclosing the thermal system somehow).

Insulation is readily available in the market, with various foam structures available. Glazing systems trap air and utilize that stationary air as insulating material (such as in windows). This is also common in solar stills to either prevent or reduce convective cooling. The thickness of such glazing systems for CSES above the absorber must be critically determined from the critical Rayleigh number, below which natural convection occurs, cooling the hot absorber from the top.

After losses are contained, the emitted energy (within infrared wavelengths with peak at 7 microns for a radiating body at ~ 150 °C) is absorbed at a very thin surface at the top of the water. There are numerous interesting physics to explore to this regard, as it is currently largely unknown what boiling effects occur during the phase change of liquid water to water vapor as infrared photons heat up local water molecules. A recent study show that infrared absorption in this regard may even exceed the thermal evaporation limit [4].

From a technological standpoint, the CSES configuration achieves superheated steam as the solar absorber is de-coupled from the water physically with a gas gap. This enables rising steam at 100 °C to

get further superheated according to the heat exchanging effectiveness of the hot emitter (acting as heat exchanger) which typically reaches 120 to 150 °C under one sun [3].

Moreover, the CSES configuration bypasses the fouling issue, present in all desalination systems discussed (either requiring cleaning for thermally-driven systems or clogging membranes for mechanically-driven systems). Salt which is left behind in the basin does not interfere with the thermal performance in any way and may be cleaned regularly as water is refilled.

The physics of the absorption of infrared radiation within water, in particular, demonstrates a lot of potentially unknown physics which is currently under investigation [3]. This includes the very nature of liquid-liquid interfacial heating within infrared wavelengths as opposed to traditional conductive heating from the bottom of water volume. More specifically, we would like to investigate how infrared photons impart energy onto water molecules within the volume (including the molecular structural links within the top surface with air-water interface to the bottom, where visible photons with high penetration depths may be absorbed). Tu et al. [7] demonstrated that within this phenomenon of liquid-liquid heating a few micrometers from the top of the water surface. This is because infrared photons within the wavelength peak of 7 microns, as readily obtained by Wien's Law for a 140 °C body, are. The interesting behavior of water volume under solar radiation is illustrated below in Figure 2-22, adapted from the excellent study by Tao et al. [7]. A direct practical implication of interfacial and bulk heating would be adjusting water depths used within solar-absorbing solar stills.

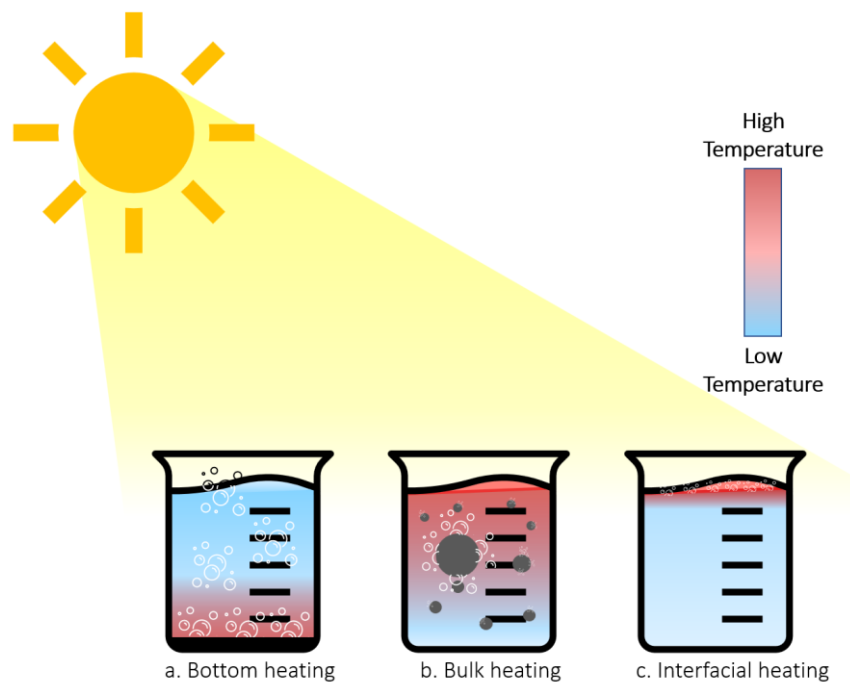


Figure 2-22: Types of solar-driven interfacial evaporation [7].

There is also interest within the research community for 'high-efficiency' solar devices which are able to utilize (often using regeneration techniques for harnessing 'waste heat') all of the incoming solar radiation. Li et al. [2] reviewed and demonstrated very high-efficient solar devices of above 90%, specifying system-level efficiency factors (further discussed in Section 2.5) for being able to fully utilize incoming solar radiation ( $q_{solar}$ ).

With regards to the technological perspective of the Contactless Solar Evaporation Structure (CSES), the present project prototyped the second generation of CSEs to utilize infrared radiation to desalinate water. This novel thermal configuration is able to avoid some key issues plaguing solar stills since time immemorial, such as fouling, inability to superheat steam, and scalability of the design to virtually any scale to accommodate any population capacity. In fact, scaling up an RO plant has its own technological challenges [53], [56], requiring expertise in setup.

## 2.5 Solar energy

*The radiation of the sun in which the planet is incessantly plunged, penetrates the air, the earth, and the waters; its elements are divided, change direction in every way, and, penetrating the mass of the globe, would raise its temperature more and more, if the heat acquired were not exactly balanced by that which escapes in rays from all points of the surface and expands through the sky.*

- J. Fourier (1822, 'The Analytical Theory of Heat')

The fundamental premise of the present study is that solar energy has the potential to power a large number of everyday applications, often linked to human survival, such as drinking water, washing and sanitation, sterilization, drying, space heating/cooling and so on. Thus, the following sections help to establish the viability of solar energy and the potential for desalination by investigating availability of solar energy given its daily intermittent nature (given Sun-Earth Geometry) as well as other meteorological factors such as clouds, time of year (season), and geographical location. These details as well as translating outdoor solar experiments to indoor lab conditions (using a Solar Simulator) are detailed. Moreover, it is important to understand the heat collecting agent, which in this scenario is the Solar Selective Absorber, which is briefly discussed.

One of the motivations of the present study is in conducting outdoor solar testing during the winter season, in particular. Given the low irradiance during winter months, especially given Canada's location along the ~45 degree latitude of the Northern Hemisphere, a stationary concentrator may be warranted. However, given the current challenges in achieving boiling temperatures (and thus high enough evaporation rates) in these regions, solutions towards water storage during summer months may be recommended. Alternatively, a novel method of heating snow to clean, potable water may also be investigated in the future.

Finally, one of the most important performance metrics for solar-thermal devices is the solar-to-thermal efficiency (sometimes called solar-to-vapor efficiency), which itself comprises component-wise efficiency considerations. These considerations, given its importance, will be discussed in the final sub-section.

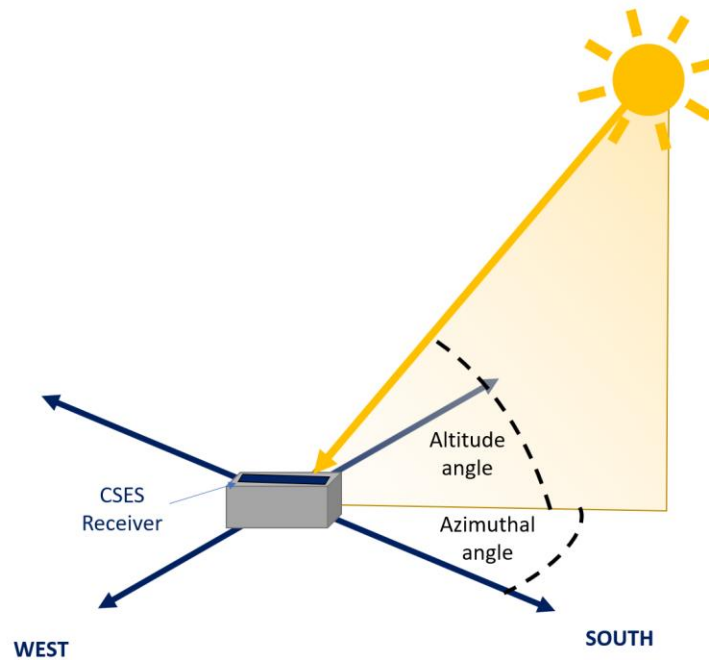
### 2.5.1 Sun-Earth geometry

Tracking the position of the sun was of fundamental importance to ancient civilizations, particularly those who ventured into naval expeditions. Many ancient civilizations even revered the Sun as a Deity due to its insurmountable power of guiding, providing a concept of time, feeding nature and sustaining the Earth [56].

While up until the 18<sup>th</sup> century, the geocentric model (i.e. placing the Earth at the center of the universe around which planets and the sun orbit) was held as the prominent model describing Sun-Earth Geometry, today, our understanding of the universe, its shape, geometry have been completely redrawn in light of the astronomical findings within the past two centuries, both in terms of research and in terms of space exploration.



Despite this, for the sake of simplicity, the geocentric model in which we observe the Sun's path from a particular geographical coordinate on Earth's surface is used for analysis purposes only as we usually consider sun relative to the observer on Earth. Usually, due to the angular nature of sun-earth geometry, spherical coordinates are commonly used instead of rectangular (Cartesian) coordinates (made apparent by Figure 2-23 below).



*Figure 2-23: Visualization of solar radiation impinging on a CSES receiver with two angles outlined: Altitude and Azimuthal angle.*

There are a few angular parameters which haven't been utilized in the present study but are important to highlight. These include the sun's altitude angle and azimuth angle. Further details on Sun-Earth Geometry (particularly the declination angle of the Earth around the Sun throughout the year, sun angle throughout the day, and latitude/longitude) are explained on the website [physicalgeography.net](http://physicalgeography.net) [87]. This level of detail is not warranted in the present study, where solar irradiance may readily be obtained with a pyranometer (if Global Horizontal Irradiance, or GHI, is needed) or pyrliometer (if Direct Normal Irradiance, or DNI, is needed).

To demonstrate a representative case of daily solar irradiance during the Fall season in the Northern Hemisphere, Figure 2-24 obtained from the original CSES study is shown [3].

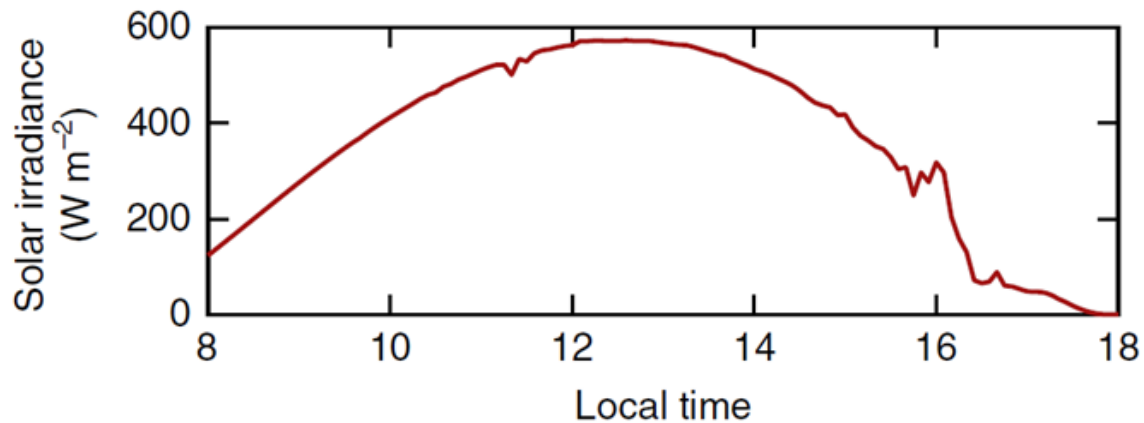


Figure 2-24: Typical solar irradiance for a day in November [3] in Massachusetts, USA.

### 2.5.2 Available power from the sun ( $q_{solar}$ )

Once geometric considerations between the sun and earth have been established, the next consideration is one of heat and energy (i.e. power considerations). Quantifying useful solar heat energy as well as how it may replace conventional energy sources (including human labor). In numerical modelling, while it is useful to know the relative position of the sun, it is often not required. Instead, the heat energy from the sun may simply be taken from an irradiance reading taken from the flat-on-the-ground planar surface under investigation (i.e. Global Horizontal Irradiance, or GHI). The GHI is the primary term used to obtain radiant flux over CSES aperture. This term itself is related to the Direct Normal Irradiance (DNI) and diffuse Horizontal Irradiance (dHI) by the following relation:

$$GHI = DNI \cos(\theta) + dHI \quad (\text{Eqn. 2 - 45})$$

In terms of measuring GHI, typically pyranometers are employed (essentially an instrument containing a convectively insulated thermopile surface), whereas DNI requires a pyrheliometer. The present study has utilized the former instrument as a concentrator was not used (which is not able to collect diffuse light, dHI).

Another important solar parameter is the solar constant, which is easily derived from the solid angle of the sun to the earth if the total radiant power from the sun (i.e. using Stefan-Boltzmann law once the temperature of the sun and its surface area are known, which are  $\sim 5780$  K and  $6e18$  m<sup>2</sup>, respectively). This constant is roughly  $1366$  W/m<sup>2</sup> outside of the Earth's atmosphere prior to attenuation. This value demonstrates the theoretical maximum solar energy available on Earth at any given point, while also providing a useful limit which may potentially be achieved by space-based solar-harvesting devices (i.e. orbiting Earth as a satellite).

Delving into a deeper level, the sun's power is commonly investigated in terms of its Electromagnetic (EM) Spectrum. There are a number of standards of the solar spectrum, which have been summarized by Tawfik et al. [88]. These standards stem from the definition of the Air Mass (AM) standards, which is lower than the blackbody radiance at 5800 K (surface temperature of Sun) [88]. Thus, the AM spectrum is useful as it details the solar irradiance after passing through the atmosphere which can be harnessed.

### 2.5.3 LED solar simulators

Tawfik et al. [88] reviews a number of solar lamps used in the solar radiation field for in-door testing as well as for other applications in photonics, radiation heat transfer and solar energy in general. These lamps include Argon arc lamps, metal halide lamps, Tungsten halogen lamps, Xenon arc lamps.

With regards to in-door solar testing with CSES, a suitable, effective, cost-effective and easy-to-use solar simulator would have to be used. With the boom in LED lighting technology in recent years, LED growlights have also ushered in a new age of in-door agriculture (i.e. greenhouses). Pattison et al. [89] reviewed this trend in lighting technology with a broader, holistic focus on light according to its 'signalling' for specific physiological responses in humans and plants; and as an efficient 'fuel' for fresh food production. The study goes on to review the evolution of lighting technology which may be useful for indoor solar testing applications.

The trends above is illustrated by the difference between luminance achieved, where chemical fuel lamps and electric incandescent lamps both utilize the principle of blackbody radiation of hot surfaces. The problem with both methods with regards to luminous efficacy within the visible EM spectrum (useful for plants and human productivity) is that a lot of radiation energy is lost by infrared radiation which is not useful in the case of luminosity. This, however, does not matter in the case of solar testing. LEDs achieve their lighting by a different principle known as electro-luminescence, where photons are emitted as a result of electric current passing through a substance (usually gallium arsenide). Other types of luminescence, not relevant in the present study, are bio-luminescence, electrochemi-luminescence, crystallo-luminescence, mechano-luminescence, photo-luminescence, radio-luminescence and thermoluminescence. The clues to each of these types of photon emission can be obtained etymologically, such as bio-luminescence emitting photons during a biochemical reaction within flora and fauna, crystallo-luminescence emitting photons during crystallization, and mechano-luminescence emitting photons during mechanical action on a solid, and thermo-luminescence emitting photons when a solid is heated (commonly observed among certain re-radiating materials such as fluorite).

To match LED lighting to the solar spectrum, an array of LEDs emitting sharply within a particular wavelength (similar to a laser but not as concentrate and with a slight spectral distribution) are piled to mimic the solar spectrum. This technology is explained in detail with regards to its emission spectra for LEDs by a popular vendor of LED array lamps: ThorLabs [90].

Thus, with regards to the current state of Solid-State Lighting such as LEDs, the present study has been motivated towards using an LED solar simulator for solar testing. To this end, it is important to calibrate the simulator to output 1 sun at a particular height from CSES aperture, or any other irradiance as desired. This is shown in more detail according to the flux mapping procedure in sub-section 3.3.7.

#### 2.5.4 Solar Selective Absorber (SSA)

In the field of Concentrated Solar Power (CSP) and, more broadly, solar-thermal energy, flat-plate collectors are commonly employed to harness solar energy, heating an absorptive surface and transferring the heat through tubular heat exchangers to air, water or another fluid.

The present study has considered a special type of solar-thermal absorber, namely the Solar Selective Absorber (SSA). The function of the SSA is to essentially absorb solar-spectrum radiation and emit radiation in the infrared spectrum obtained from Planck's Law for a surface of certain emissivity [37]. An extensive review by Kennedy [91] (2002 Technical Report from NREL) may be consulted for further details on the working principle of SSAs.

Thus, it is desired to reduce the absorptivity or emissivity (which are equal in the case of gray, diffuse, but may be slightly different for spectral and directional emissivity versus absorptivity values) within the infrared regions where heat is to be emitted. Using this principle of solar selectivity of surfaces and given that the operating temperature of the thermal system is known, solar selective absorbers have the potential (as utilized in CSES) for a wide range of solar desalination applications. Five methods of preparation of solar selective absorbers are illustrated in

Figure 2-25, adapted from a review on high-temperature SSA published in the Journal of Materiomics by Xu [92]. Similarly, a mini-review on cermet-based SSA was also conducted by Cao [93].

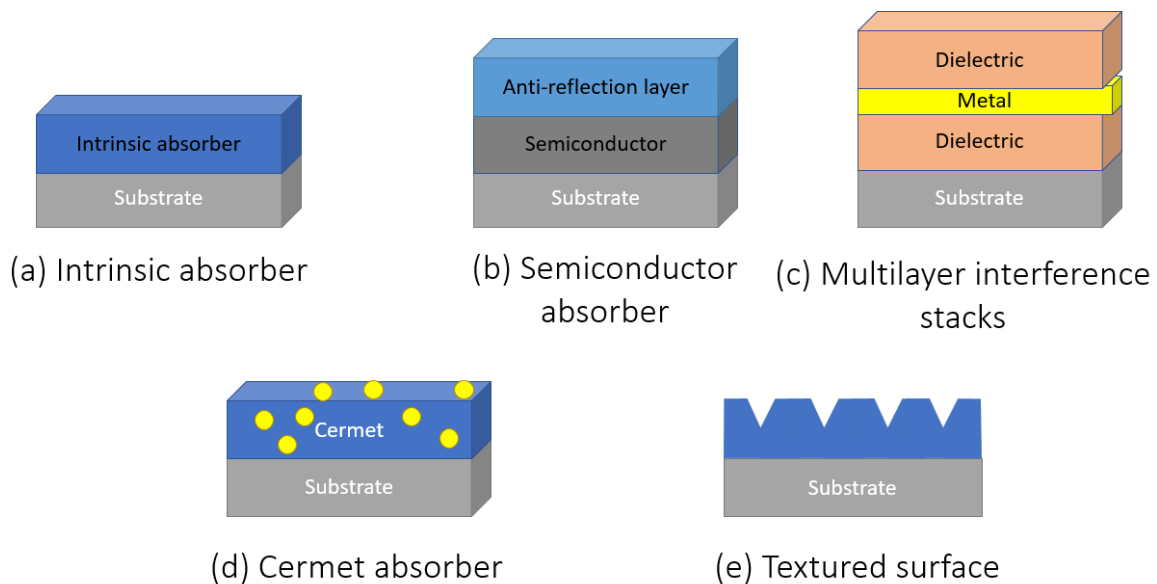


Figure 2-25: Schematic diagrams of five typical solar absorber coatings to achieve high solar absorptivity: (a) Intrinsic absorber, (b) Semiconductor absorber, (c) Multilayer interference stacks, (d) Cermet absorber, and (e) Textured surface [92].

### 2.5.5 Solar-to-thermal & optical efficiency

Solar-to-thermal efficiency is perhaps one of the most performance metrics for any solar desalination system. In the current context, this efficiency refers to the incoming solar radiation that the device can usefully use to heat and evaporate water. Thus, we may define solar-to-thermal efficiency as the mass flow rate of the water produced using the latent heat of vaporization,  $h_{fg}$  to quantify amount evaporated. Lastly, the output (numerator) is divided by the input energy from the sun ( $Q_{solar}$ ) to result in a complete definition of solar-to-thermal efficiency. Figure 2-26 may be useful to visualize this definition with regards to heat gain, heat delivered, heat losses and useful output.

$$\eta_{solar,thermal} = \frac{j \cdot h_{fg}}{Q_{solar}} = \frac{\dot{m} \cdot h_{fg}}{Q_{solar}} \quad (\text{Eqn. 2 - 46})$$

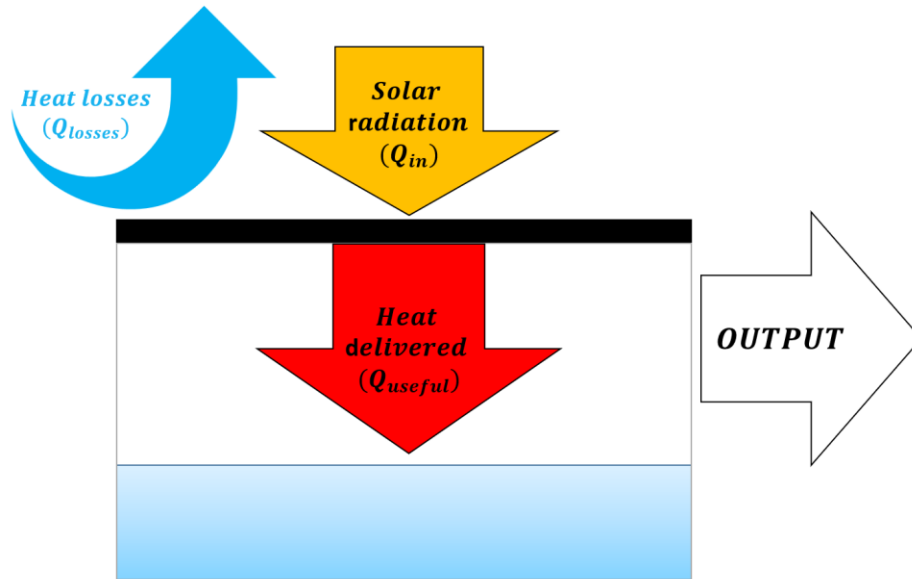


Figure 2-26: Schematic of a typical solar thermal energy conversion system. Sunlight incident on absorber ( $Q_{in}$ ) is delivered to the thermal system, where desired output (steam evaporation) is produced ( $Q_{useful}$ ). Heat losses reduce the potential output of the system ( $Q_{losses}$ ). Adapted from [93].

In real-world scenarios, optical losses would reduce the solar radiation which would ultimately make it to the absorber. Thus, optical efficiency needs to be considered. For CSES, this term comprises transmission through two transparent Fluorinated Ethylene Propylene (FEP) plastic sheets as well as the absorptivity of SSA.

$$\eta_{optical} = \tau_{FEP}^2 \cdot \alpha_{absorber} \quad (\text{Eqn. 2 - 45})$$

The heat exchanging effectiveness ( $f_{superheater}$ ) was previously highlighted in sub-subsection 2.2.6.

## 2.6 Summary

With the four sections on Properties of Water & Steam, Heat Transfer Fundamentals, Desalination Systems and Solar Energy, the methodology was formulated to achieve the objectives in the following chapter.

The Heat Transfer section reviews concepts of the modes of heat transfer, conduction, convection and radiation, which is crucial to analyzing thermal systems. The resulting thermal circuit from this section is the skeleton of the transient numerical model developed.

The Properties of Water & Steam will be utilized within numerical modelling as well as to understand the mechanisms by which water runs through the natural water cycle and within solar stills. Moreover, basic mass transfer equations are invoked to model mass diffusion and evaporation.

The Desalination Systems section enables a baseline of comparison of CSES with alternative desalination systems.

The Solar Energy section enables understanding of the energy source utilized for CSES. This energy source is the sun, and various system-level components such as the absorber, emitter, concentrator and solar simulator require direct consideration of solar energy concepts.

As a final note, the purpose of the numerical model is to guide experimentation, particularly with regards to locating where potential heat gains and losses could be within the thermal layout of CSES.

## 3 Methodology

### 3.1 Overview

The methodology section is sub-divided into three crucial components, namely a *Design* (Section 3.2) component, upon which a *Prototype* (Section 3.3). A *Model* (Section 3.4) also accompanies the prototype in order to guide its performance and understand the parameters and desired outputs (solar-to-thermal efficiency among others).

### 3.2 Design

While no specific Engineering Design methodology was adopted for the present project (which might seem strange given the project emphasis on prototyping), the 9 steps taken to complete the project are briefly outlined below. Formulation of these steps were inspired by excellent engineering design textbooks by Annacchino [94] and Ulrich et al [95]. The former is especially relevant to CSES, given that this innovative product is only in its 2<sup>nd</sup> generation, and particular care needs to be taken to shift this product to be practically and financially viable for the desalination market. In particular, CSES is suited for social benefits over capital gains, and this needs to be managed carefully in coming generations of the product. The latter resource concerns products further down the line, and especially those that have been in the market. Therefore, user experience with product and such topics are highlighted with case studies from several large product-centered companies. Such case studies may be useful for rural communities and their experience with the operation, maintenance and utilization of contactless solar stills for applications in drinking, medical sterilization, cooking, drying and other everyday tasks.

Chapter 1 and 2 have covered the first 2 steps. The present chapter (Chapter 3) builds on step 3, before formulating the methodology to achieve experimental results for steps 4 to 7. The results for these steps are discussed (Chapter 4), with the 9<sup>th</sup> and final step being summarized (Chapter 5).

1. Proof of concept & scaling considerations
2. Theory and background laying foundation for problem definition
3. Energy & mass balance leading to concept design
4. Model
5. Instrumentation
6. Experimentation
7. Parameter tuning in model
8. Data Analysis
9. Summary of innovations and path forward



### 3.2.1 Thermal layout

Understanding the operation of CSES requires a closer investigation at its thermal layout. The two paths towards improving any solar still system could be through materials improvements and thermal layout improvements, with the latter being highlighted in this sub-section and the former in the following sub-section 3.2.2. The former is achieved through both cheap and novel materials, while the latter is more concerned with geometric parameters such as basin width, gas gap height, changing or modifying layouts as would be easily visualized with a thermal resistance circuit diagram.

Prior to constructing the thermal layout via thermal resistance circuit, the heat and mass transfer mechanisms within CSES should first be understood. To this aim, Figure 3-1 below outlines these processes.

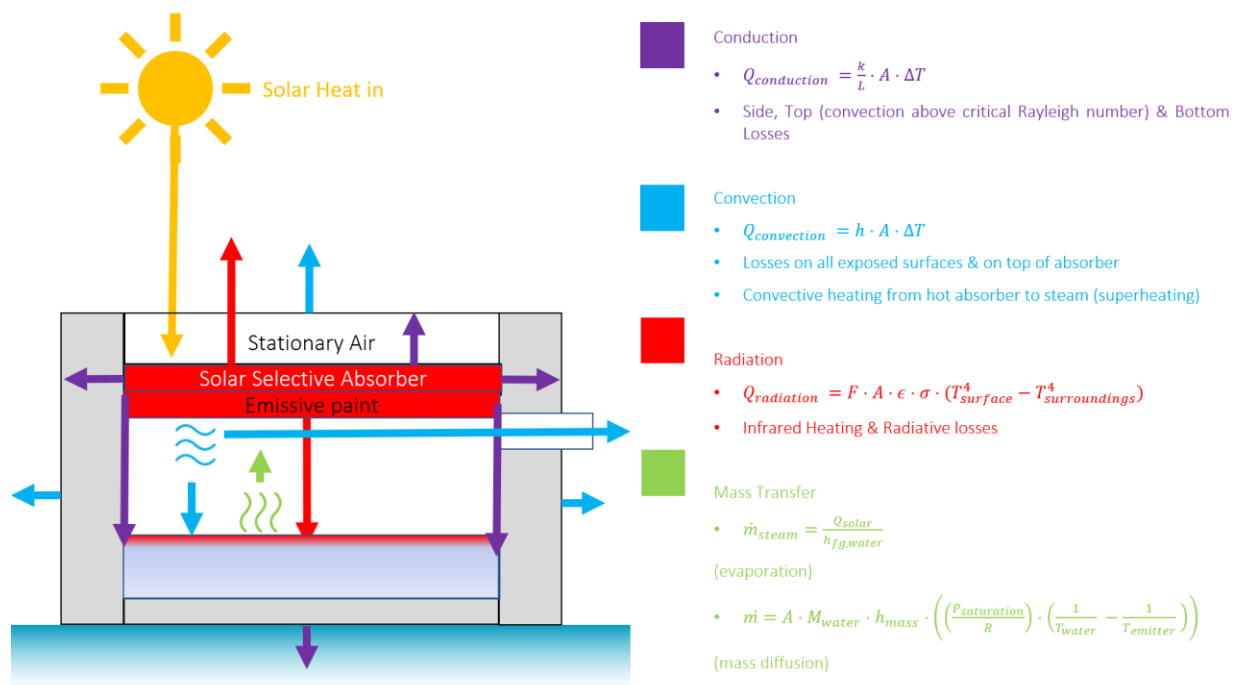


Figure 3-1: Energy balance diagram of CSES with regards to heat and mass transfer modes.

Delving more into the heat transfer aspect using the energy balance diagram, we may readily visualize the energy transfer mechanisms. In general terms, incoming solar radiation ( $q_{solar}$ ) of 1 sun ( $1000 \text{ W/m}^2$ ) heats an absorber, heating up to  $140 \text{ }^\circ\text{C}$  (validated by experiment). We utilize principles of thermal radiation and paint one side of the absorber with paint with high emissivity of at least 0.90, so that when the absorber heats up due to solar radiation, the emitter side within the CSES basin radiates heat to the water below it. It may seem strange that there exists a gap between the emitting surface and water layer, and in fact, this particular point is one of the major innovations outlined by Cooper et al. [3] with very promising future scope outlined further by researchers working on solar interfacial-evaporation [4], [6]–[8].

Given that the  $T_{abs}$  reaches  $\sim 140$  °C in the numerical model (validated by the experiment), and that the  $\epsilon_{emitter} \sim 0.90$ , we may obtain the power from infrared radiation which may be used to heat the water below (not including losses to side walls, as reflective sidewalls were used).

$$\begin{aligned} Q_{absorbed} &= A_{emitter} \cdot \epsilon_{emitter} \cdot \sigma \cdot (T_{emitter}^4 - T_{water}^4) \\ &= 0.21 \cdot 0.90 \cdot 5.67e-8 \cdot (413^4 - 373^4) = 104 \text{ W} \end{aligned} \quad (Eqn. 3 - 1)$$

This denotes that only 104 W from the incoming 210 W (1 sun for 0.21 m<sup>2</sup> receiver area corresponding to 18 inch x18 inch scale of basin proposed) is available to heat the water, with the remaining 106 W ( $\sim 50\%$  of incoming heat power from the sun,  $Q_{solar}$ ) either as parasitic heat losses to ambient (which may be computed readily from the thermal circuit or by considering any of the top layer resistances), or optical losses from reflected radiation from FEP plastic sheets, which reflect roughly 5% of irradiation per layer (2 layers in total).

### 3.2.2 Materials & dimensions

The schematic in Figure 3-2 illustrates key materials used and overall dimensions of the design. The 2<sup>nd</sup> generation of CSES was aimed to be simple in build in order to ensure its construction anywhere in the globe for clean drinking water and other applications. Moreover, manufacturing machines were minimized throughout the prototyping in order to ensure equitability of CSES construction.

The construction comprises an origami-folded FEP basin within which water would be contained. The origami-folding itself is quite innovative, as plastics can easily be moulded by hand, without complicated machinery, This basin (18 inches x 18 inches) is moulded onto the stacked polyisocyanurate blocks (for insulation). Atop this stack would sit the silicone gasket, whose function is to be compressed with a clamping force (via threaded rods and jam nut on other end). In order to spread this clamping force evenly over the edges of the aperture to ensure proper steam leak prevention, top and bottom aluminum clampers are used. Through holes in the clampers, the threaded rods would ensure structural rigidity of CSES, which is inherently very light ( $\sim 4$  kg without clampers).

A FEP outlet tube is located under the gasket through which steam would flow out of the system and into ambient. The water height within the basin is 1.25 inches, corresponding to  $\sim 1.3$  litres in the basin.

FEP glazing is used atop the Solar Selective Absorber (SSA) to utilize nearly stationary air to prevent convective heat losses to ambient. The SSA itself has low emissivity at the top, reducing radiative heat losses to ambient.

Critically, the SSA is painted with an emissive pigment at the bottom (oven paint for CSES), whose function is to emit infrared radiation from the hot SSA ( $\sim 120$  ° under one sun) to the water, boiling it.

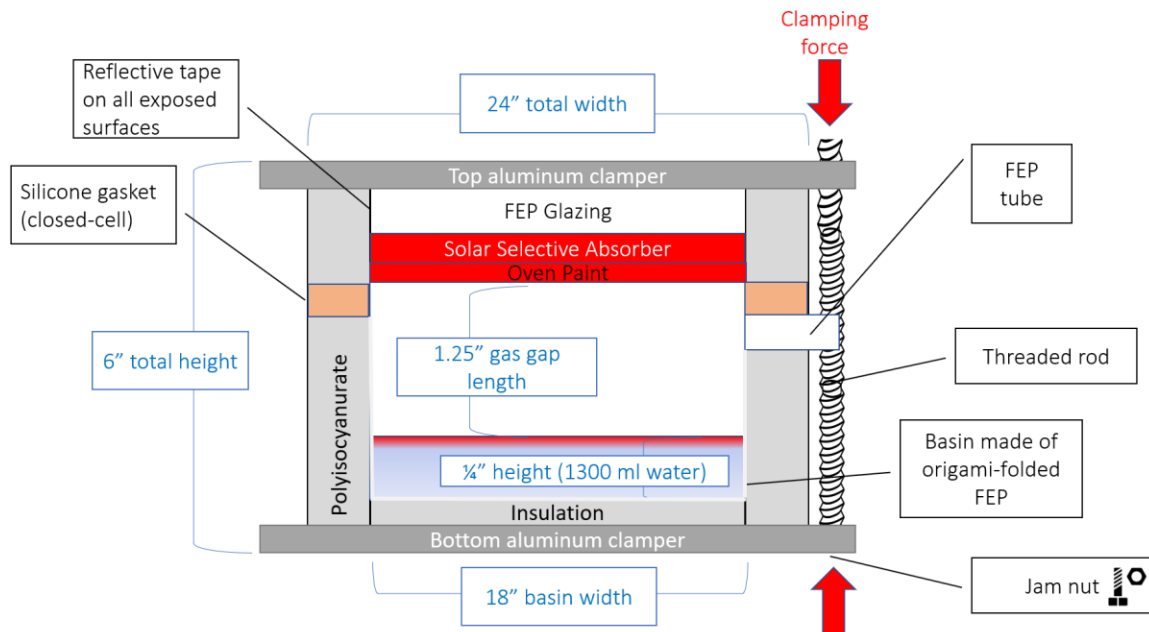


Figure 3-2: Material components and dimensions of CSES.

### 3.2.3 Prototype building

The construction of the prototype is explained in the following sub-subsections. These are explained with regards to the following 6 broad system components:

- I. Insulation blocks
- II. Basin
- III. Glazing system
- IV. Gasket
- V. Solar Selective Absorber
- VI. Clampers

Figure 3-2 may be consulted on a guide to the entire prototype.

### 3.2.3.1 *Insulation blocks*

Polyisocyanurate insulation layers (available at major hardware retailers such as Home Depot and Lowe's) were used as an integral part of the present design to reduce conductive losses to the environment. The boards were available in 4 ft. x 8 ft. sizes (48 inches x 96 inches). The surface area of the CSES prototype is 2 ft. x 2 ft. (including both collector area and insulation), and thus the boards were perfect to produce two boards with each board bought from the hardware store. Finally, reflective tape was applied on all hollowed boards, including weather-sealing gasket, as well as the faces of clamping structure facing aperture. The reflective tape would minimize radiation absorbed on the basin walls.

To this aim, 24 inches x 24 inches boards of two different thicknesses (1 inch and ½ inch) were used throughout all 4 design iterations. These boards were then processed in steps outlined in sub-sections below to prepare the basin and glazing system. The only tool required for these steps were primarily a cutting mat (blue as shown in images below), a square ruler, straight ruler and utility knife (yellow).

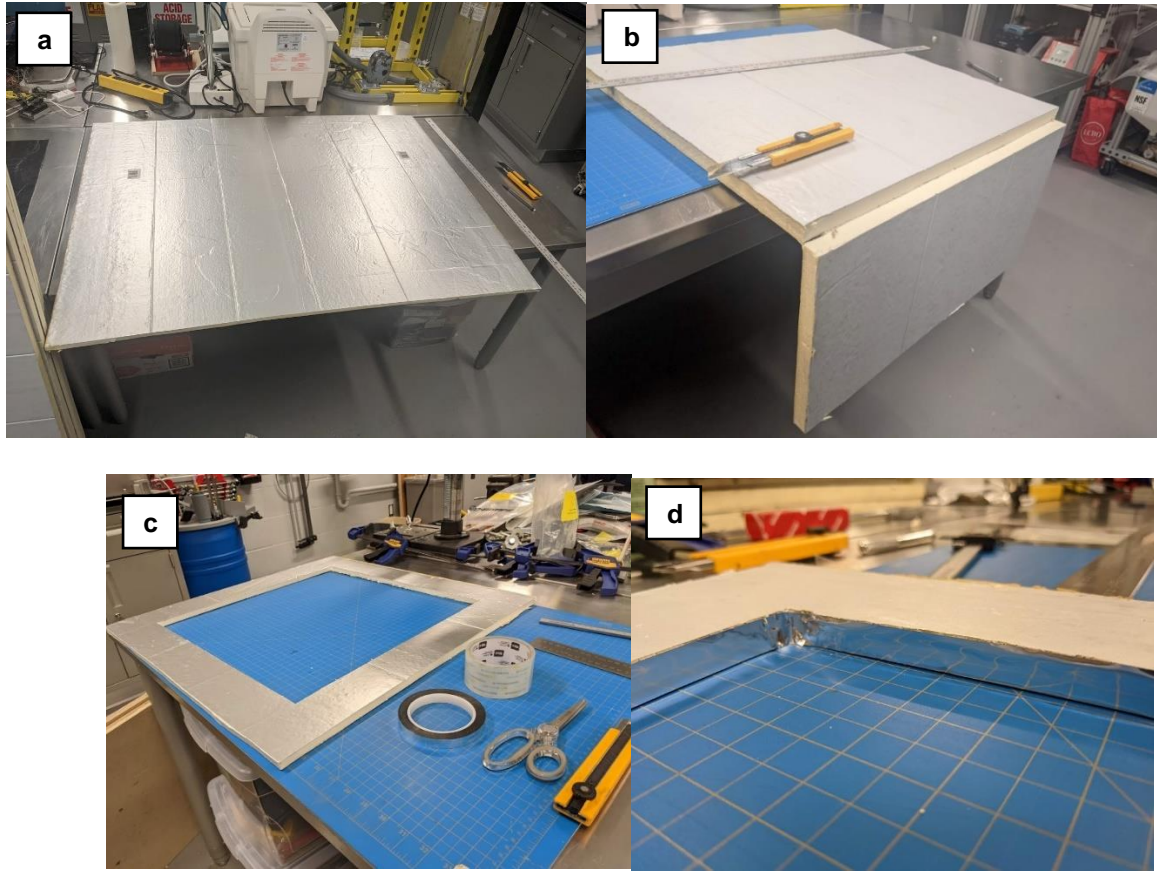


Figure 3-3: Preparation of polyisocyanurate foam blocks. The raw boards (a) are cut to size (b), and sectioned out for selected blocks (c). Reflective tape is applied on all sectioned out blocks (d).

### 3.2.3.2 Basin

The basin was prepared according to the following steps (finished version in Figure 3-4):

- i. Three 1 inch polyisocyanurate boards were stacked (but not sealed with silicone as with earlier design iterations in order for design to be more modular and flexible), with a 1 inch hollowed board followed by a ½ inch board.
- ii. Two further ½ inch hollow boards were also cut to be used as a part of the glazing system (FEP plastic sheets taped onto them as ‘windows’).
- iii. A ½ inch long cut was made in between the ½ inch board sitting atop the 1 inch. This cut would accommodate the FEP outlet tube (Figure 3-5)
- iv. A hydrophilic cloth is placed in the basin (selected tests) to enhance basin performance by preventing water pooling (reducing evaporation rates). Moreover, a cloth reduces potential for water to spill onto the emitter, fouling it by contact
- v. Lastly, a gasket was used to prevent steam leaks. This gasket would be compressed using threaded rods and a jam nut mechanism.

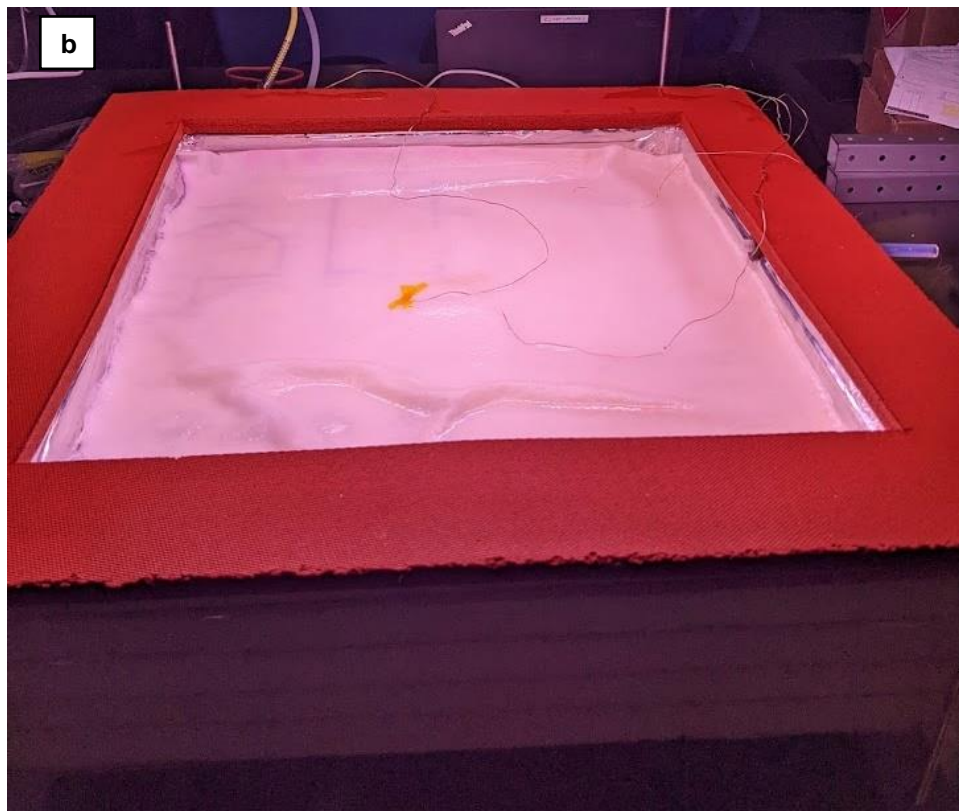
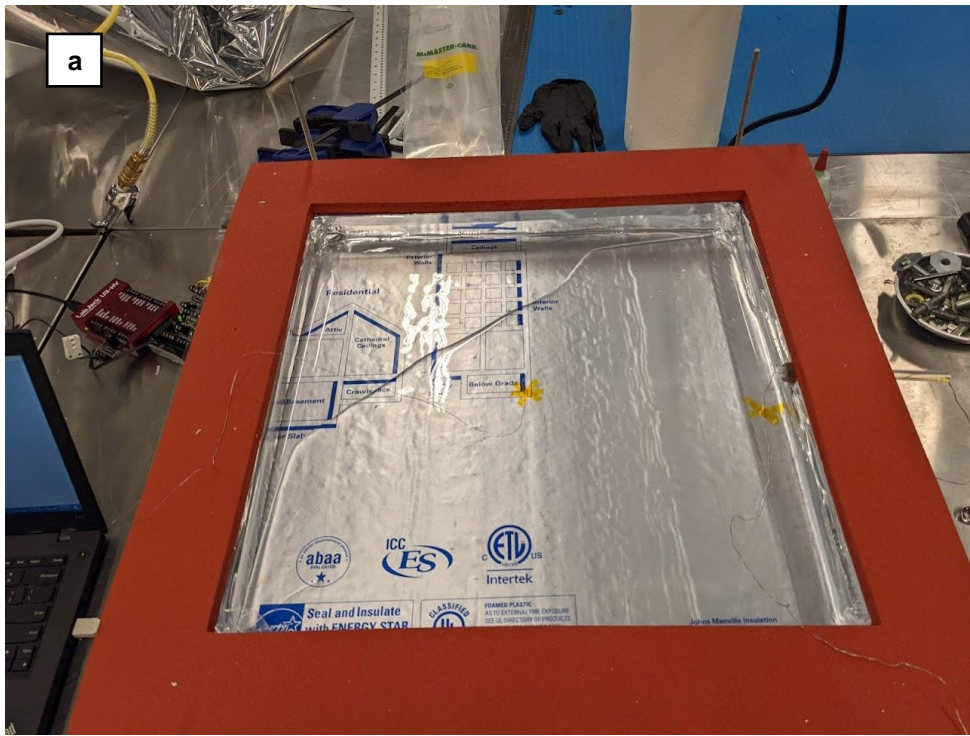


Figure 3-4: (a) Water inside FEP-folded basin showing hydrophobic interaction, (b) warranting the use of a hydrophilic layer, or cloth, to enhance basin performance.



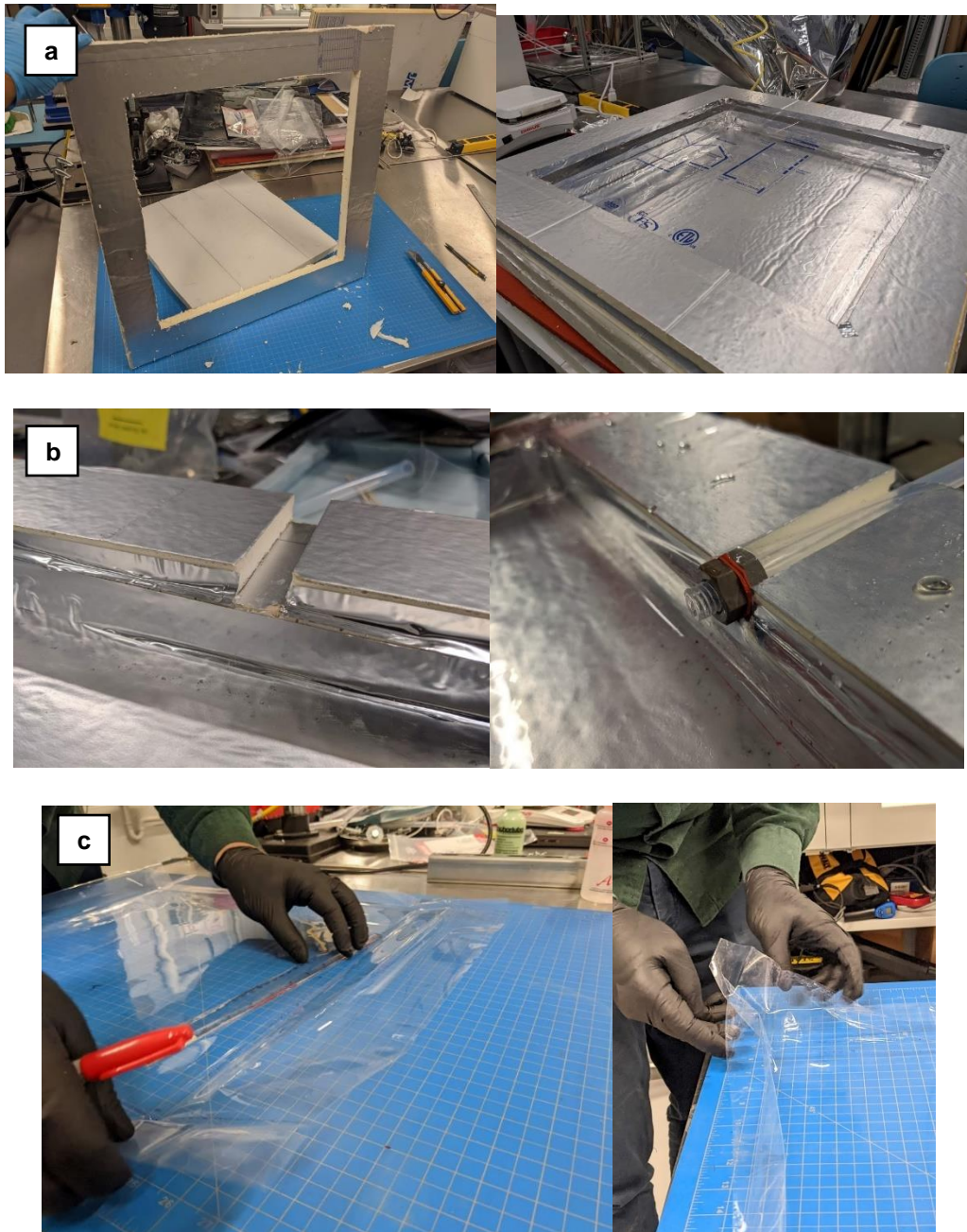


Figure 3-5: Preparation of the basin by (a) first constructing hollow foam blocks, (b) making cuts for outlet tube with a groove to accommodate screws, and (c) FEP plastic sheet origami-folded into the basin.

### 3.2.3.3 Glazing system

The glazing system is meant to insulate the hot absorber from convective heat losses to ambient. To this effect, a material which is optically transparent would have to be used, to avoid interfering with incoming solar radiation. The cheapest material to use in this case is stationary air, which could be achieved by trapping air in between two surfaces of very small thickness (determined from calculation of the Critical Rayleigh Number (or  $Ra < 1708$ ). The preparation procedure of the glazing system was undertaken in the following steps (Figure 3-6):

- i. Fluorinated ethylene propylene (FEP) film was cut into 21 inch x 21 inch size to be placed on a 24 inch x 24 inch x ½ inch polyisocyanurate board with a hollow of 18 inch x 18 inch. Two such glazing boards are to be constructed for the prototype.
- ii. Reflective tape is applied on the side walls (if not done during the insulation preparation step where it is ensured that all exposed side walls would be taped with reflective material).
- iii. Three pieces of tape (preferably tape suited for plastic bonding) of at least 3 inch strips were placed on each end, on all four ends (resulting in 12 pieces of tape in total).
- iv. A long piece of tape (at least 24 inch) was placed on each side (4 sides) to protect the 12 tapes above from losing adhesion and slowly weakening, leading to the FEP film sagging which is undesired as it could result in touching the hot absorber below and melting (or at least deforming under thermal load).
- v. Finally, pieces of tape are applied on the sides of the glazing system to prevent potential breakage
- vi. It is interesting to also note that the thin FEP films (0.005 inch thickness) used from the very 1<sup>st</sup> Design Iteration through to the 4<sup>th</sup> Iteration, really proved their rigidity and strength, not having punctured despite rough usage for over a year of testing. The author highly recommends this particular plastic sheet for such temperature ranges of between 100 to 200 °C where punctures and damage to sheets is possible.



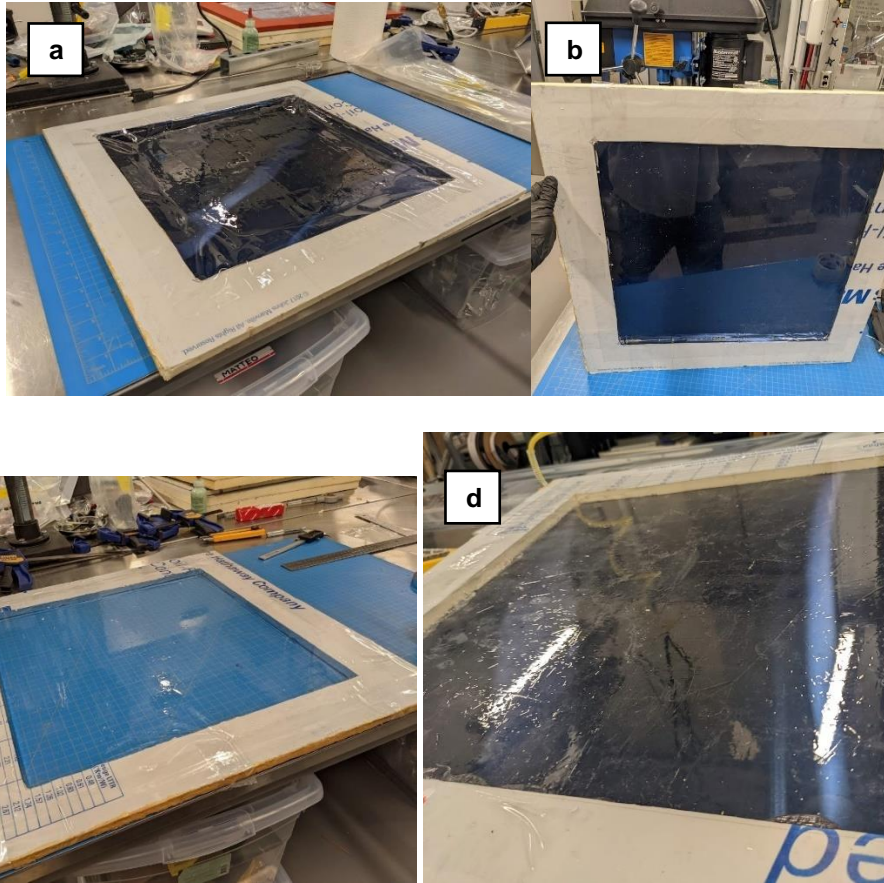


Figure 3-6: Preparation of glazing system using a taping technique at 3 points on each side (12 tapes in total). Afterwards, each side is taped over with a long 24 inch stretch of tape to protect tightening tapes. The glazing system in 3 steps is shown for FEP on a  $\frac{1}{2}$  inch polyisocyanurate block with: (a) no tape, (b) short strips of tape applied at all corners, and (c) the final long tape along all sides. (d) FEP from nearly a year of usage and experimentation showing structural resilience for CSES.

#### 3.2.3.4 Gasket

Preparing the gasket was relatively straightforward. An closed-cell [96] silicone foam of desired compressibility was utilized. The compressibility of the material was made to ensure proper gas tight seal against steam leaks within enclosure during clamping using top and bottom clampers. This 24 inch x 24 inch piece was hollowed out at the center from a 3 inch offset from edges (i.e. 18 inch x 18 inch hollow), shown in below in Figure 3-7.

Previously in the 3<sup>rd</sup> Design Iteration, a melamine gasket was used painted with flex seal (hydrophobic). This ultimately did not work as the compressibility of melamine was compromised, leading to a failure in its function to compress and provide a rigid weather seal. Various moisture leaks were observed in the first Glazing system with absorber attached to the melamine weather-sealing gasket (completely undesired, signalling steam losses).

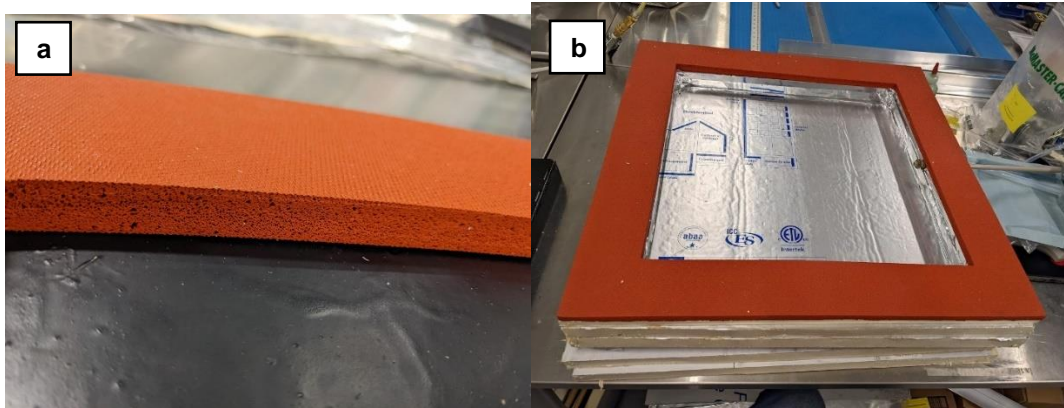


Figure 3-7: (a) Close-up of closed-cell (i.e. pores not connected), and (b) silicone gasket as well as its placement on CSES.

#### 3.2.3.5 SSA

Given the pressurized steam inside enclosure, it is of paramount importance to seal the enclosure perfectly against leaks (particularly in between the de-coupled assembly from absorber, which would be lifted to refill with water). Within the first 3 design iterations of CSES in its second generation, numerous steam leaks were observed, particularly from the corners of absorber which did not seal well with silicone initially. To remedy this, epoxy was used and a silicone weather-sealing gasket with top and bottom clampers. This subtle point of containing steam leaks is illustrated with the system components constituting a significant portion of build costs for such CSESs achieving boiling point and steam

The following steps were followed to prepare the absorber (Figure 3-8 and Figure 3-9):

- i. Absorber sheet was cut from a large roll. This malleable 'roll' resulted in some manual effort (work-hardened bending by fingers locally to avoid creases) to straighten the curvature from the manufacturer's roll.

- ii. The aluminum side of the sheet (other side being the selective surface) was sanded and cleaned to prepare for spray painting.
- iii. In order to minimize dirt or unwanted particles on potentially getting onto or scratching the absorbing side (while it has a protective plastic for this purpose) while spray painting, 6 ft. x 6ft poly sheets were used as a drop cloth to protect the surrounding area.. More importantly, the poly sheets ensure that spray paint does not escape outside of the absorber which is to be painted and damage/vandalize property. It is essential to have proper PPE such as gloves and masks (or respirators) during this process.
- iv. The sanded side was spray painted outside on a relatively windy day inside an enclave within the locality of York University. Masking tape was employed at the sides to avoid spillage of paint on the absorbing side (resulting in difficulty bonding in future steps to a polyisocyanurate block above using epoxy).
- v. Epoxy was applied at the edges and two wood pieces used along with quick clamps to apply pressure for epoxy to stick and cure without leaving any gaps for potential steam leaks.



Figure 3-8: (a) Large roll of solar selective absorber to be cut and uncurled. (b) After cutting an 18 inch x 18 inch piece, selective surface is uncurled, sanded and masking taped at sides to avoid epoxy spillage on absorbing side. (c) Finally, it is spray painted.



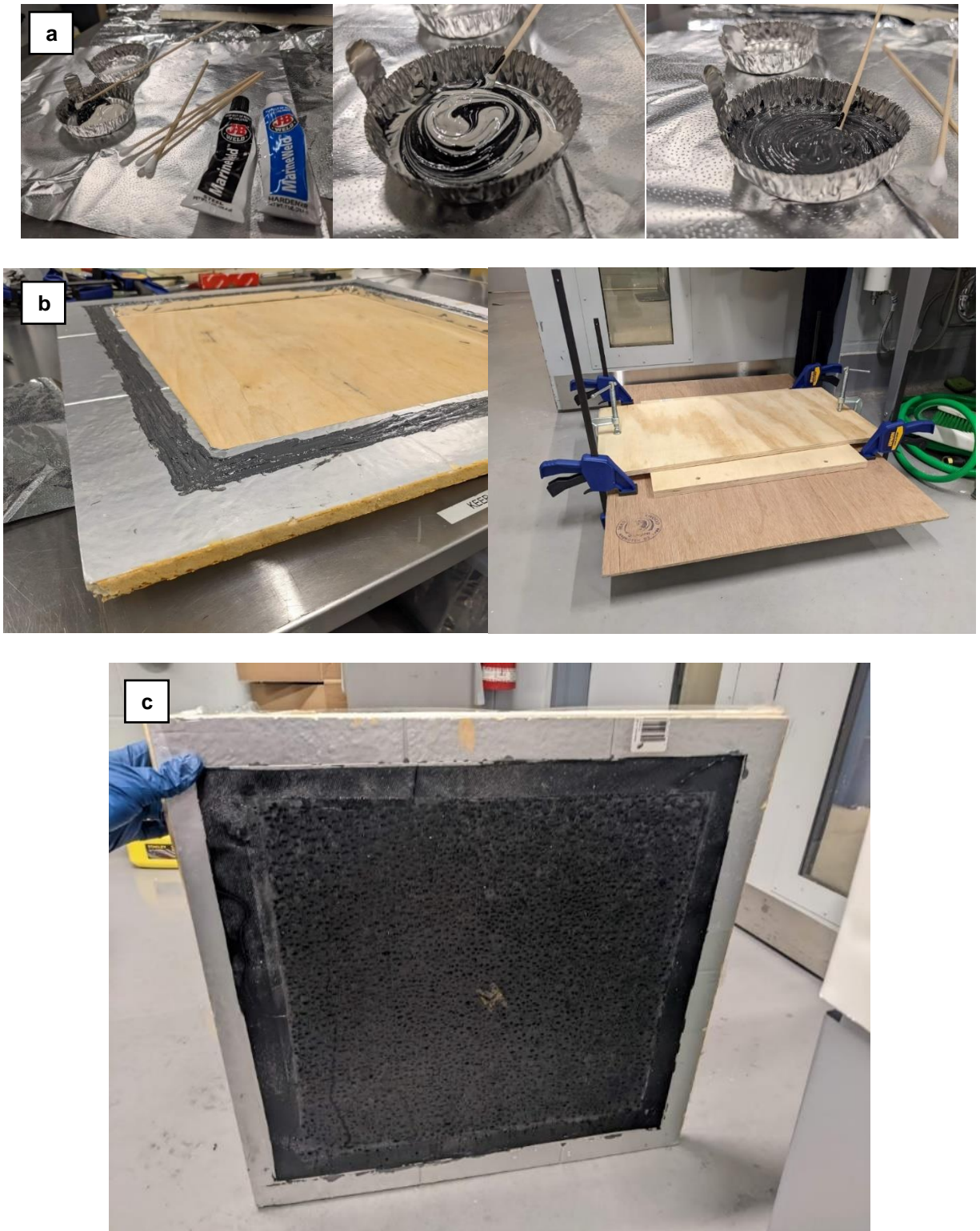


Figure 3-9: (a) Preparing and Applying epoxy to bond SSA to polyisocyanurate  $\frac{1}{2}$  inch block. (b) Wood panels are used to clamp the SSA for a complete and proper epoxy cure around corners. (c) Wet absorber after a test is shown.

#### 3.2.3.6 *Clampers*

The completed clamping structure (both top and bottom, which are identical and reversed during operations with threaded rod going through 4 corners) is shown in Figure 3-10 .

The following steps were taken for one clamper (either top or bottom, as both are identical):

- i. Aluminum angle (4ft. or 48 inches long) is cut to 18 inch so as to leave a piece ~ 30 inches. This step is repeated for another aluminum angle to yield a total of four pieces.
- ii. Drill holes (where threaded rods would be) are marked by red pen and then tap holes are punched. A Lysol wipe or disinfecting alcohol may be wiped on surfaces were red permanent marker pen is not desired.
- iii. Ends of the aluminum angles are filed to enable each piece sitting faces flush to one another.
- iv. On a measuring mat, all aluminum angles are fastened (by tape preferably) and aligned as desired. Then, 90 degree elbows, to be used as templates, are placed with drill holes (where 90 degree elbows will be fastened with screws) marked where desired.
- v. Finally, once drill holes are drilled through and all clamper pieces fastened, this is repeated for another identical clamper.
- vi. Finally, the top and bottom clampers are placed with CSES body in between and threaded rods going through 4 corners. Jam nuts on the bottom end ensure that clamping force is applied as the top screw over threaded rod is fastened.

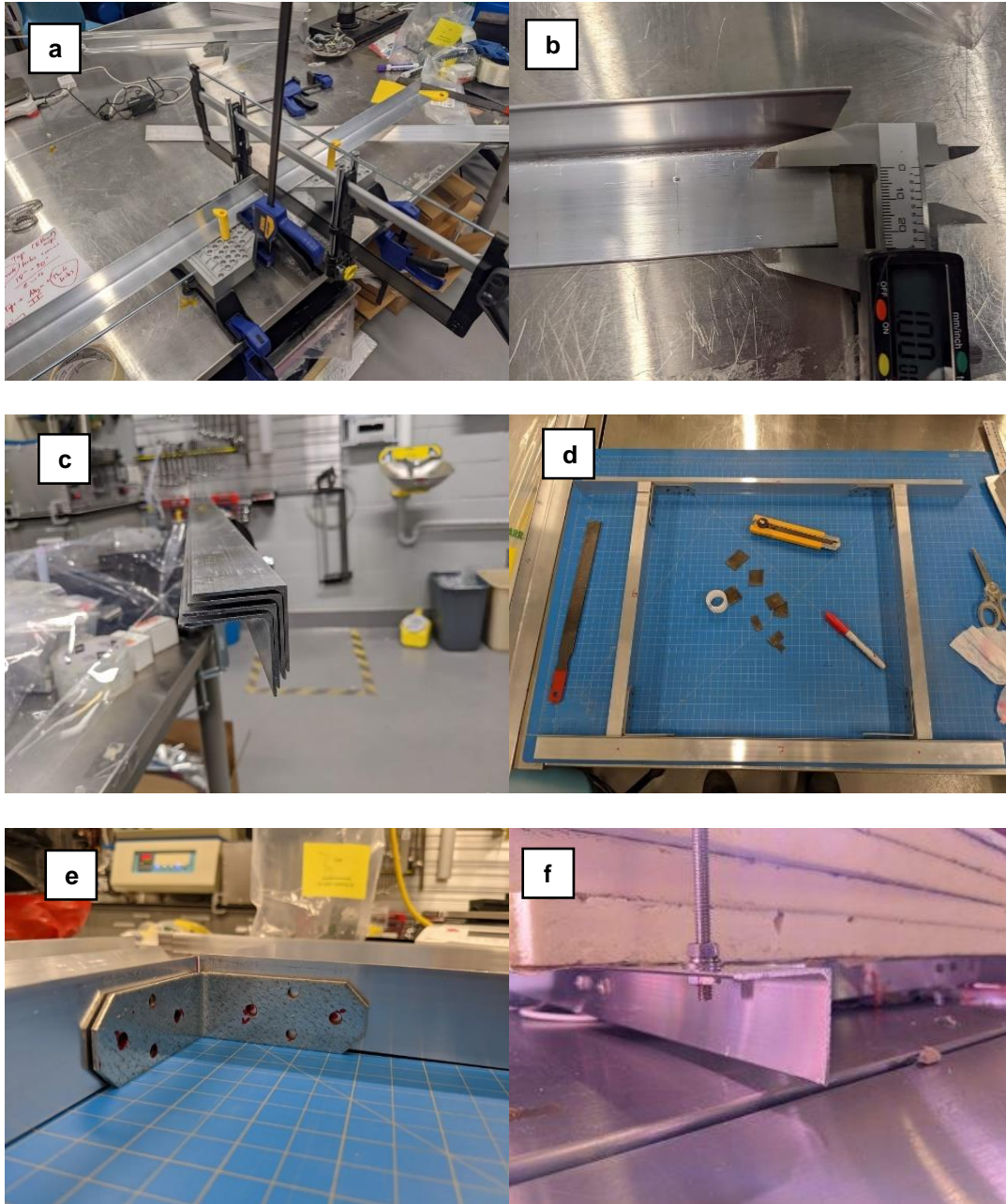


Figure 3-10: Steps in the preparation of clasper: (a) cutting aluminum angle with Mitre box; (b) punching tapholes for drilling onto claspers; (c) ends of clasper filed; (d) clasper taped to cutting mate and 90 degree angles aligned and (e) holes marked with red pen. (f) Close-up of holes marked using the 90 degree angle as template are shown with jam nut arrangement at the four corners of bottom clasper.



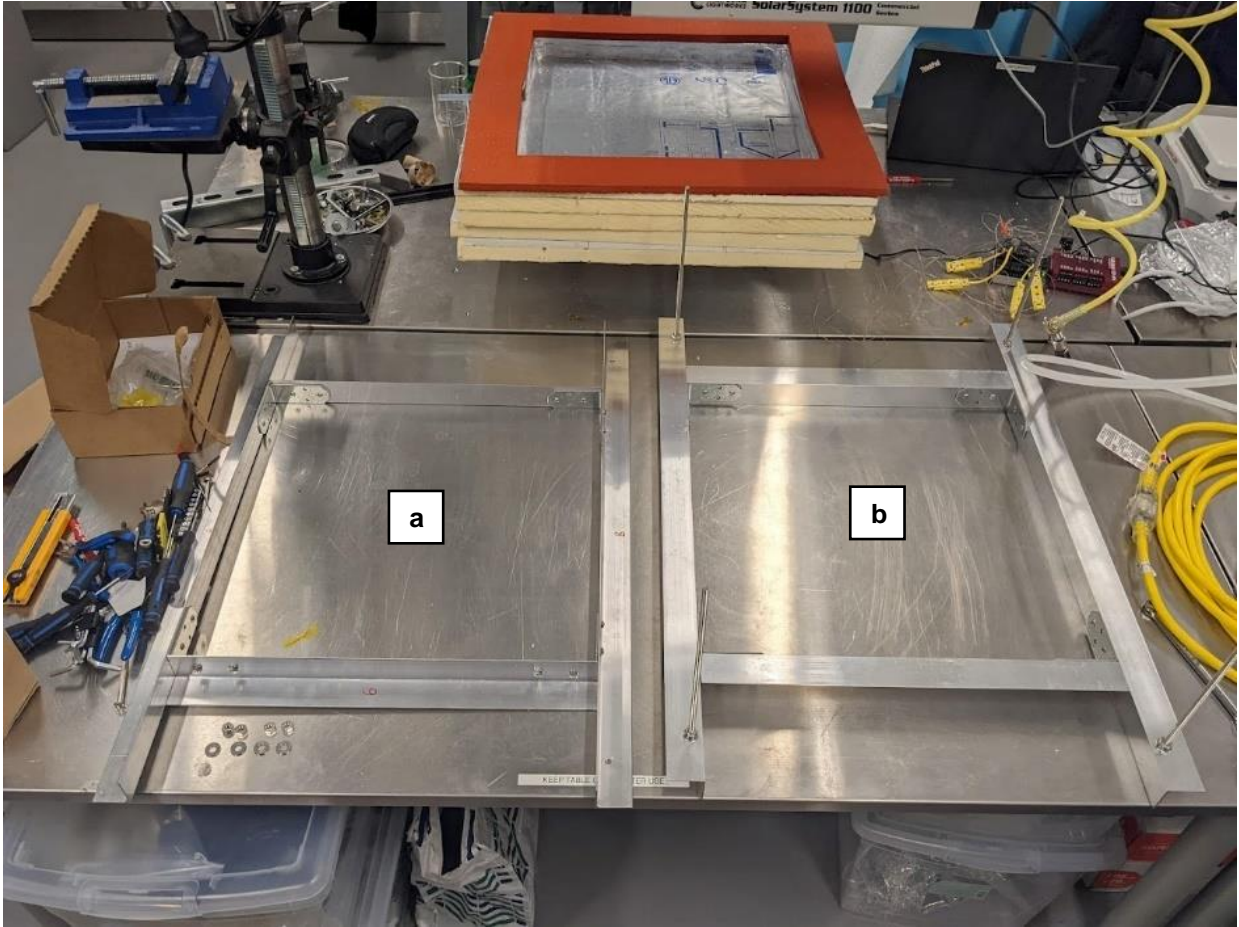


Figure 3-11: (a) Top and (b) bottom clampers (identical and placed in reverse with holes aligned to accommodate threaded rod).



### 3.3 Experiment

The experimental setup is shown in Figure 3-12.

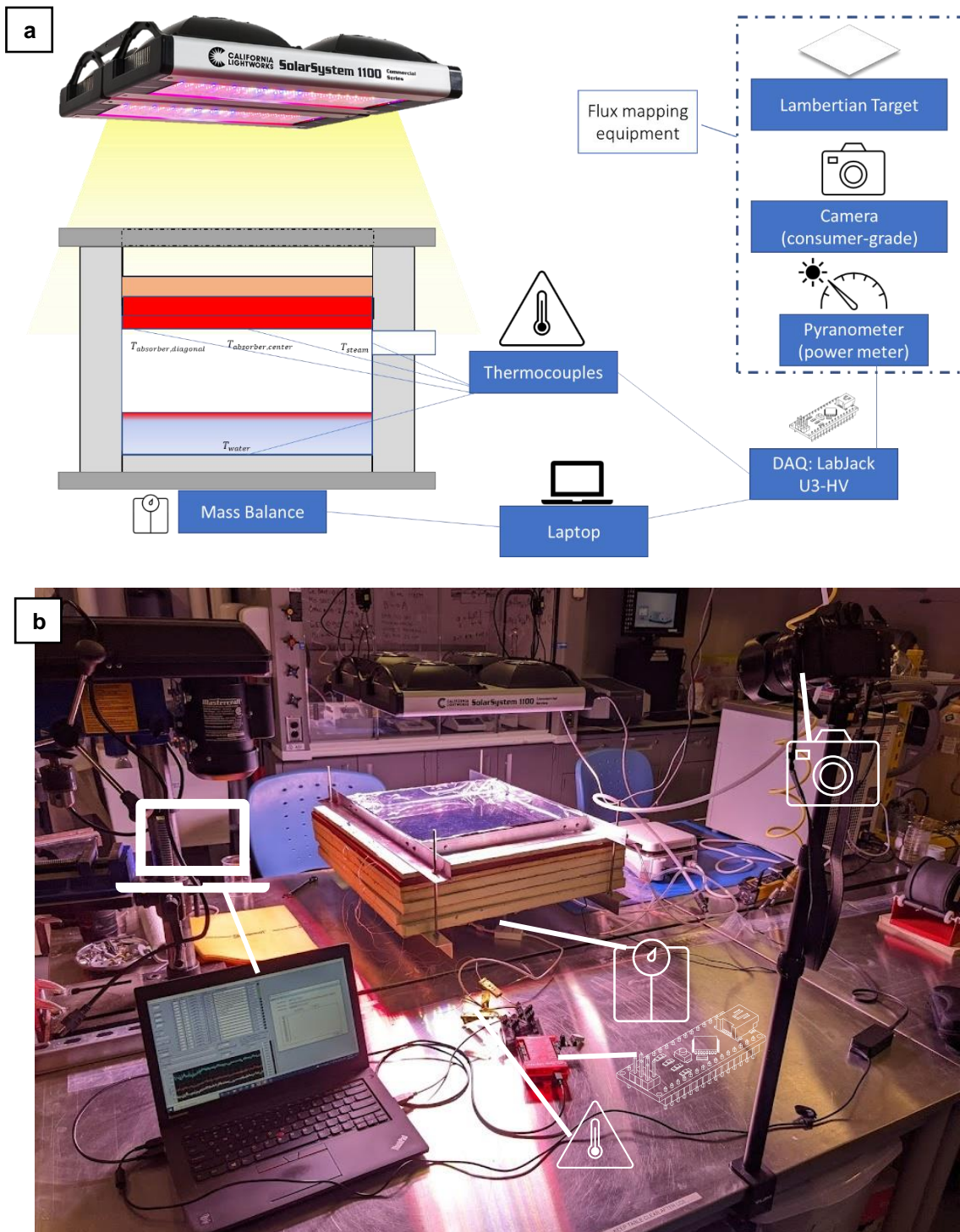


Figure 3-12: (a) Experimental Setup of CSES with schematic and (b) real-world setup. The Lambertian target and Pyranometer is not shown in the real-world setup.

With regards to the operating conditions, the experiment was undertaken indoors under lab conditions. The lab ambient temperature was found by a thermistor (LM34) to be  $\sim 25$  °C. There are no winds within the lab, letting the experimenter arbitrarily choose ambient convection coefficient of  $\sim 5$  W/(m<sup>2</sup>K), which is reasonable for a non-windy in-door environment.

### 3.3.1 Instrumentation

Five key instruments were used for the experimentation of CSES. These include, along with the respective model numbers:

- i. Mass Balance – An mass balance (OHAUS Scout) was used to measure evaporation rates from superheated steam leaving the outlet tube.
- ii. Thermocouples – K-type thermocouples (by the company Omega Engineering) was chosen to measure temperatures of absorber, water and steam.
- iii. Solar Simulator – An LED Growlight by California Lightworks (Solar System 1100) primarily designed for greenhouse application and in-door agriculture was utilized in the present study.
- iv. Pyranometer – A pyranometer (CM4 by Kipp & Zonen) was used to obtain the flux, also called irradiance for incoming radiative heat flux (W/m<sup>2</sup>), for a point chosen on the absorber heated by solar radiation. This point reading may be scaled to a flux reading (i.e. over surface area of absorber) by utilizing a Lambertian target and consumer-grade camera. More details on this ‘flux mapping method’ are given in the sub-section below on pyranometer
- v. Camera – A mirrorless camera (Fuji XS-10 with 16-80mm Fujinon lens) was utilized to take RAW pictures (i.e. the pixel values are not edited in any format in-camera or image editing software). Virtually all consumer-grade DSLR and mirrorless cameras (the difference not mattering, so long as RAW files are available) manufactured within the past decade may be used.

The Section will end by detailing the experimental testing procedure.

In order to test the mass balance (Figure 3-30), initial mass measurements were taken for open-top evaporation. This was done primarily in order to observe whether the balance can log steady values with minimal error while also obtaining a macroscopic sense of mass transfer for four useful scenarios: open-top mimicking evaporation over lakes and other open water bodies; closed-top with open outlet tube, showing capability of clamped CSES to retain moisture inside enclosure; closed-top with outlet tube taped, enabling observation of mass transfer through outlet tube in ambient conditions; and closed-top under solar irradiation (under typical ambient sunlight conditions, CSES could boil and superheat steam).

Preliminary obtained values obtained are shown below (using 1 L of water in the basin), along with steady-state evaporated mass from the irradiated test using solar simulator (elaborated further in the results section). As may be apparent immediately, the open-top configuration achieves nearly 45 times the evaporation rates of the closed-top, which only evaporates a third of a gram hourly. This illustrates the effectiveness of CSES while clamped to retain moisture (a positive). It should be noted all of these results

were obtained in lab settings under conditions outlined in the Section Summary on *Experimental Prototype and Testing*.

In order to obtain temperature curves and log them, a Labjack U3-HV was employed using K-type thermocouples, LM34CZ Thermistor (for a reference cold-junction reading), and some auxiliary parts such as K-type wires, male and female housing (yellow in Figure 3-13 below), extension K-type wires (for custom male-female housing connections for setup with LabJack), precision screwdriver and it is also very useful to have a 'holder' for the thermocouples, as small components tend to slip out of hand and require the thermocouple to be held rigidly. Given the small components, a magnifying glass may be useful for those having trouble focusing visually.

Thermocouples are dismantled and rewired so that all thermocouples are attached to a male housing as shown in Figure 3-14 to be plugged into female housing. The connections of thermocouples on the CB15 extension of the LabJack U3-HV is shown in Figure 3-15. The thermocouple equations input into the LJLogUD software in LabJack is illustrated in Figure 3-16.

Thermocouples essentially operate on the Seebeck principle, whereby a voltage is generated in the presence of heat on the thermocouple tip. The thermocouple itself is composed of two unique metallic wires (one configuration being nickel-based alloys of aluminum and chrome used in the K-type thermocouples by Omega Engineering). It must be noted that the voltage potential induced does not create a flowing current of electrons, but rather voltage difference across the 'cold-junction' or the end of the thermocouple from the tip, and the thermocouple tip where the temperature reading is to be taken as below (obtained from Omega Engineering's site [97]).

The voltage produced may be related to the temperature increase as a function of the Seebeck coefficient,  $S$ , which is a linear constant of proportionality relating voltage to temperature. This, solved in differential form, is essentially computed inside of LabJack's built-in software with one part of the integration from 0 degrees Celsius to the thermocouple tip reading. Supposing the thermocouple tip reads the temperature of a human hand at 35 °C and the thermistor at 20 °C, the equations are outlined:

$$dV = -S * dT \quad (Eqn. 3 - 1)$$

The last step after setting up the cold-junction temperature to a reliable reference temperature is to connect the thermocouples (now connected inside female housing) to a male housing connected to a LJTI A Tick-in-Amps (instrumental voltage amplifiers). This is because the voltage reading from the thermocouples are very small, and need to be amplified for accuracy.

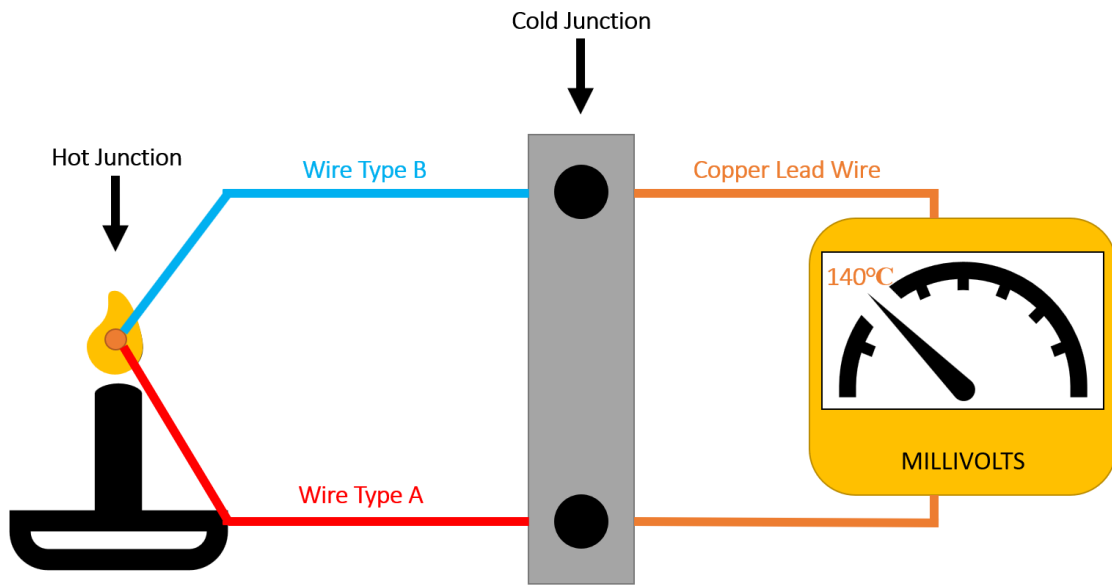
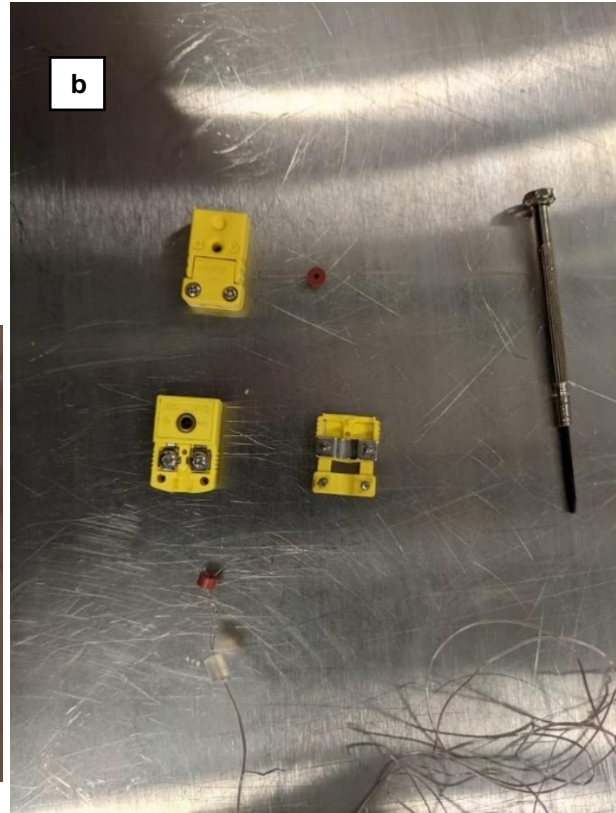
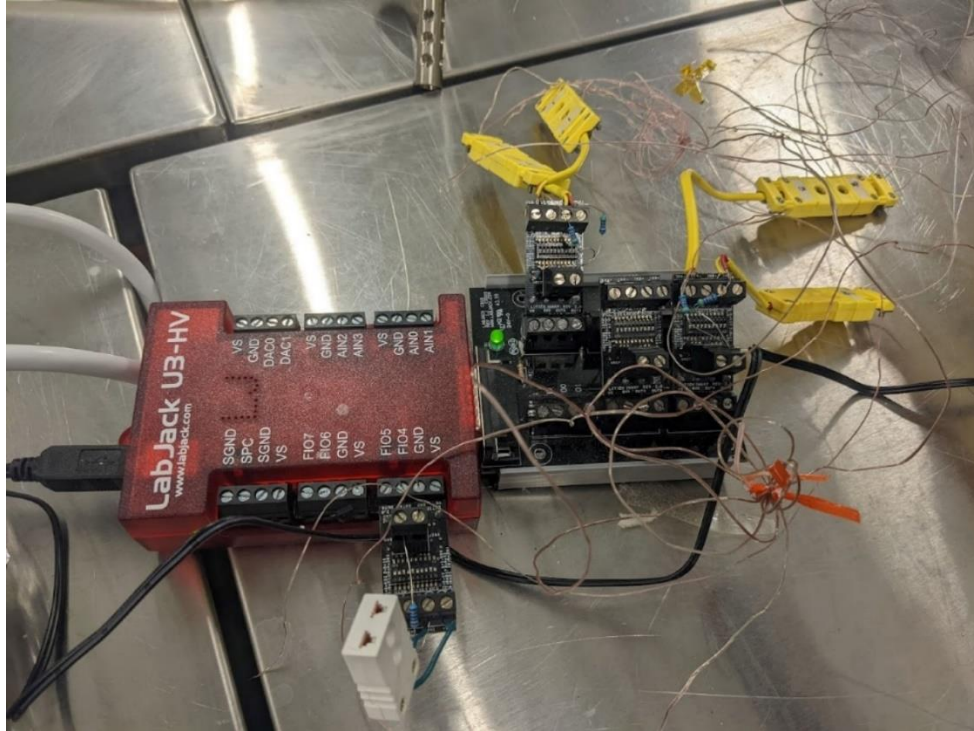


Figure 3-13: Working principle of thermocouples [97].

Historically, an ice-bath has been used as the cold-junction reference as it is relatively straightforward to keep ice at 0 degrees Celsius. In the present study, particular care was taken in ensuring an appropriate cold-junction reading, by matching the reading to a thermistor from LabJack (Model LM34CAZ). The thermistor is more accurate to use as the cold-junction reference than the built-in temperature of the LabJack module which does not accurately measure the correct cold-junction temperature.



*Figure 3-14: (a) K-type thermocouple from Omega Engineering; and (b) dismantled K-type Thermocouple using a precision screwdriver, showing interior components, including: two screws, bearing, thermocouple wire made of chromel/alumel (nickel alloys of the respective metals) with grommet.*



*Figure 3-15: Final Thermocouple setup on CB15 Expansion Board of Labjack U3-HV. The thermistor (barely visible) is set up in flexible Analog/Digital inputs (FIO7 to FIO6). A female thermocouple connector (white) is also set in FIO4 to FIO5 to accept pyranometer (whose wires are to be attached to a male connector attached to the thermocouple during flux mapping procedure).*



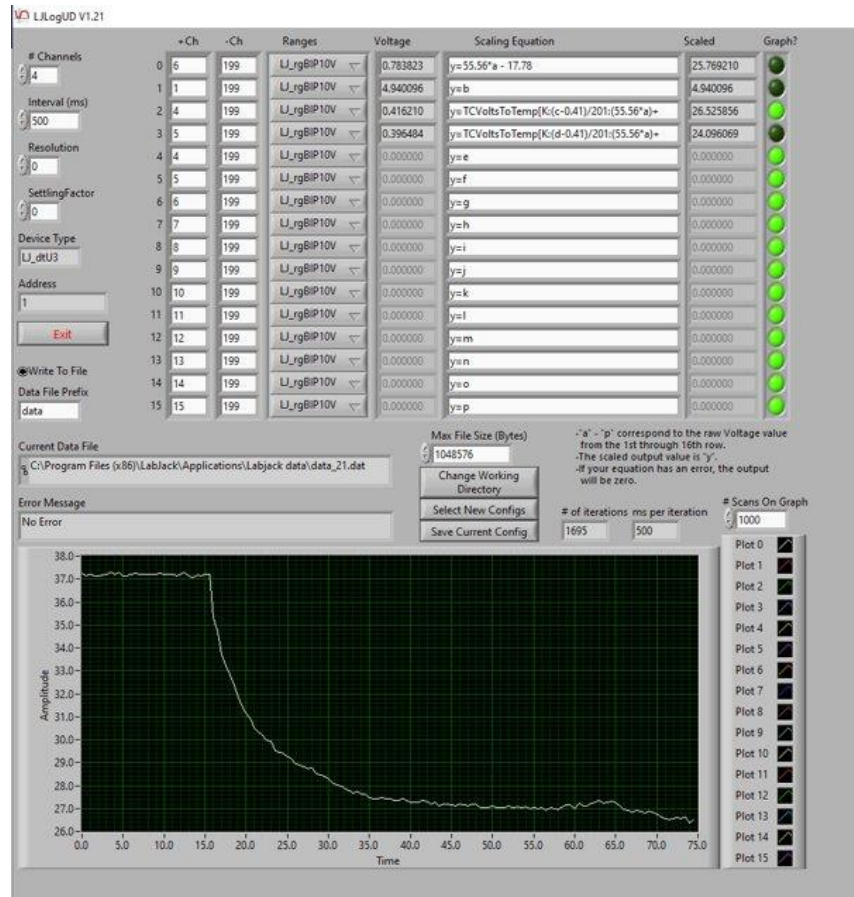


Figure 3-16: Scaling equation within LabJack's LJLogUD software for logging voltage signals from sensors. Touch test of thermocouple illustrates good response.

### 3.3.2 Experimentation

The Experimental Procedure for a typical test is detailed below with cited figures from previous sections. All of this is done after the flux mapping procedure used to obtain an area-averaged  $q_{solar}$  over the absorber plane:

- i. Firstly, if clamped, the top clamber is unscrewed
- ii. Both glazing system blocks (including the one epoxied to absorber) are removed to enable open view of the basin.
- iii. Next, the second flux map picture of pyranometer reading taken with thermopile surface at the same plane as absorber (right at the top of the orange silicone gasket) is taken. A meter reading is taken by conveniently plugging the pyranometer with male housing into the LabJack's (or whatever logger/micro-controller is used) female housing.

- iv. Lastly, the third flux map picture is taken of the Lambertian target at the same plane as absorber (measured to be 9 inches from ground) using foam (same polyisocyanurate foam used for insulation) elevation blocks as necessary.
- v. The three flux map pictures are input into the custom MATLAB code to obtain incoming solar flux ( $q_{\text{solar}}$ ). It is convenient to ensure that  $q_{\text{solar}}$  is  $\sim 1000 \text{ W/m}^2$  over the aperture of CSES, which enables easy comparison to numerical results (and manual calculations) and reporting in the literature.
- vi. It is also important to ensure that the solar simulator is level
- vii. If thermocouples are not in place, they are taped (with specialty high temperature Kapton tape made of copper) to the centre of basin, steam inlet (roughly 2 inch inside from inlet to avoid view factor from radiating emitter, leading to unwanted radiative flux to thermocouple tip), steam outlet (2" inside from the outlet), and centre of absorber. Several tapes are typically required (preferably in cross-type layouts) to ensure thermocouples don't fall or go out of place, which has commonly been observed.
- viii. CSES is placed atop mass balance, with 1 inch foam elevation block placed atop to ensure the bottom clasper doesn't touch the floor.
- ix. The balance is tared (to exclude 1 inch foam elevation block) to 0 and CSES is placed atop. It is useful to have the balance on from this moment, as the following manual tasks make it very difficult to set up thermocouples (which may be of limited length) separate from the mass balance.
- x. Basin is filled with 1350 ml of water (corresponding to a  $\frac{1}{4}$  inch height from 18 inch x 18 inch basin) using the mass balance reading as an accurate guide.
- xi. Both Glazing systems are placed atop the gasket to close the basin and clamped with top clasper.
- xii. During the clamping, it is useful to both the top and bottom ends protruding bars of the clasper to ensure a proper seal. It is crucial to ensure the clasper aperture matches the aperture of CSES, in order to avoid FEP tearing from unwanted pressure of clasper.
- xiii. The software for thermocouples (LabJack LJLog-UD) and mass balance (OHAUS) is started.
- xiv. It is very important to make sure CSES is centered relative to the solar simulator to maximize solar flux and stay consistent during tests.
- xv. The solar simulator lights are turned on, with any timer options set off (unless desired).
- xvi. Test length is almost arbitrary with some upper and lower limits. The upper limit is set by the amount of water in the basin (1350 ml), but in order to reduce thermal load on components after basin is empty, the absorber heats up to a further  $50 \text{ }^\circ\text{C}$  at least, leading to damage to components which are not made to stand  $200 \text{ }^\circ\text{C}$ . With an average mass flux rate of  $\sim 65 \text{ g/hr}$  at steady state, this sets the upper limit to 14 hours or so (heat-up evaporation rates are lower). The lower limit arises due to the heat-up phase until steady-state, which may take an hour or two. At least an hour of steady-state readings are desired, to take a wide enough time differential of mass readings. It takes approximately  $1 \frac{1}{2}$  hour to reach steady-state, leading the tester to use  $4 \frac{1}{2}$  hours with solar



simulator on, and 2 hours off (to account for cool-down time and the potential of CSES to double as a 'thermal battery', which may be augmented with radiative insulation with reflective sheet at the top, in order to 'trap' radiative losses from hot absorber to ambient), up to a total of 6 ½ hours of total testing time.

- xvii. It is now time to begin to start flux mapping, detailed in its own sub-sub-subsection in the upcoming preliminary results.

### 3.3.3 Preliminary experimental characterization

In order to gain confidence in the experiment and model, preliminary experimental characterization was conducted in order to gain confidence in the inputs of the model. The model in turn would guide understanding of the physics behind the experiment. These preliminary tests include optical testing of the materials used, optical efficiency tests of the reflective side walls, flux mapping to quantify the irradiation, and finally, the evaporation of conventional solar stills as a benchmark for CSES.

#### 3.3.3.1 Flux mapping

A novel flux mapping procedure regarding the LED solar simulator, pyranometer and camera will now be detailed. Thermocouples are one of two major contact-based temperature measurement methods (the other being Resistance Temperature Detectors (RTD)). A pyranometer (Figure 3-18) is essentially a thermopile, which are a series of thermocouples connected in series, so that when radiatively heated, a voltage output is given which can be calibrated for using a scaling coefficient with regards to temperature. Care must be taken to align the CSES aperture with center of the solar simulator (Figure 3-17).

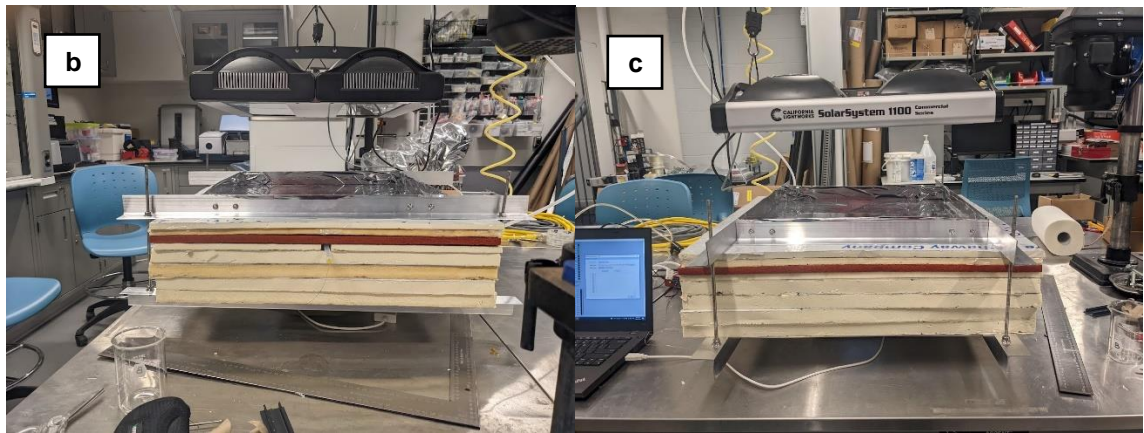


Figure 3-17: (a) Poor alignment of CSES relative to solar simulator, compared to (b) proper alignment viewed from the sides, and (c) from the front.



*Figure 3-18: CM4 Pyranometer by Kipp & Zonen (mounted).*

It is of paramount importance to accurately quantify the incoming radiation through the aperture of any solar-radiated absorber (commonly called 'receiver' in radiation literature). To this aim, a flux mapping procedure was utilized as detailed below.

Using the point reading from CM34 pyranometer and plotting it over the target plane (Figure 3-19), two pictures may be taken in any order (Figure 3-20):

- i. Picture of pyranometer spatial position on a plane matching where the absorber of CSES would be
- ii. Picture of light bouncing off a Lambertian target (utilized to reflect diffuse radiation and eliminate directional dependence of viewer camera position taking the picture)

Two pictures are shown below, with the first image being of the meter position on the same plane as receiver (i.e. absorber). The second image is of the Lambertian target (a diffuse reflector, white in color). Thus, by correlating the meter reading on a point on the target, using the relative luminance which is read as pixels in the camera, the meter reading can be scaled over the target Region of Interest (ROI). This ROI-based image processing is very useful for solar flux mapping procedures.

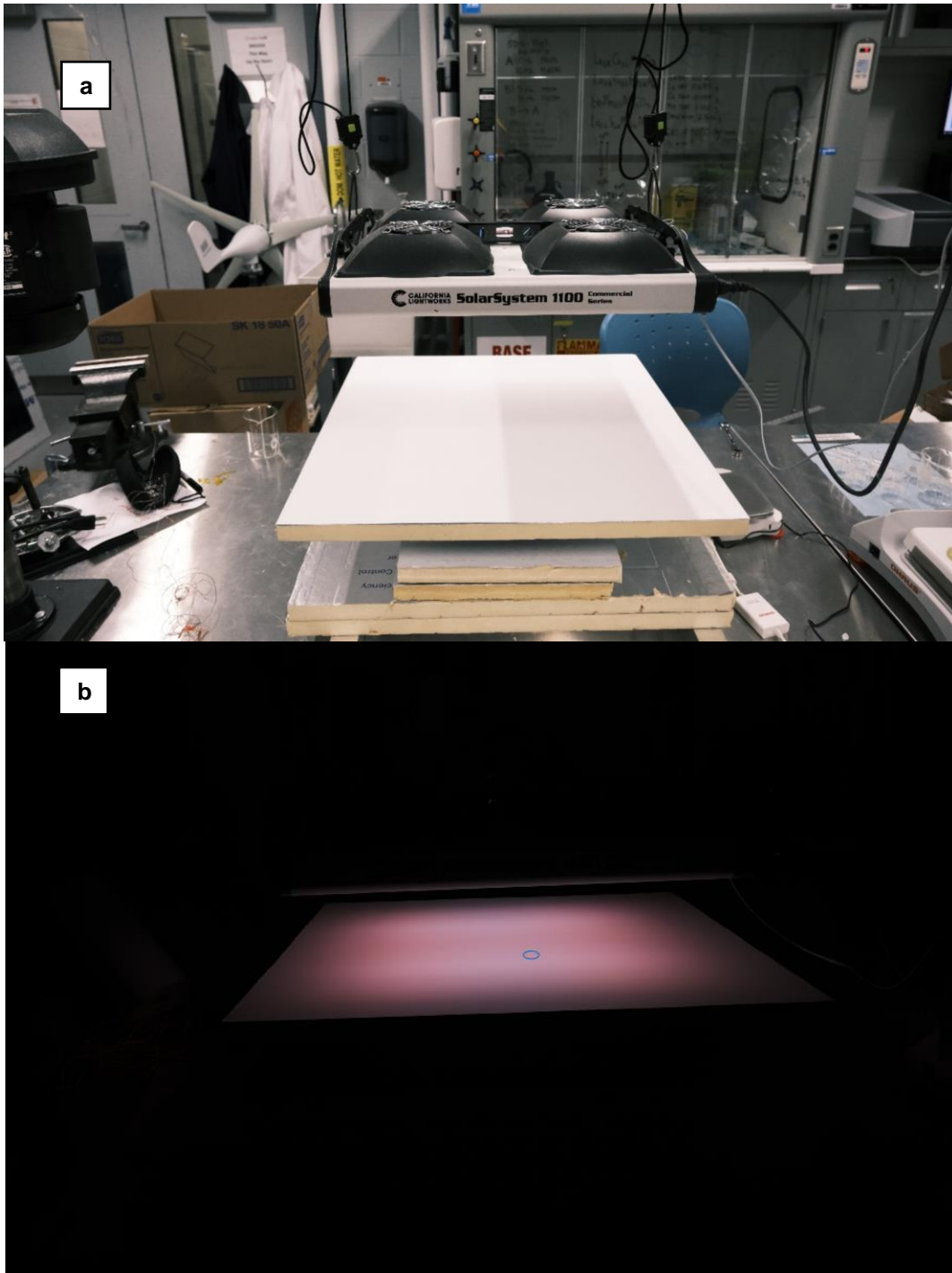


Figure 3-19: (a) Lambertian target placed on an  $xy$ -plane on the same  $y$ -height as CSES absorber. (b) Receiver area (meter image) plotted on target with blue circle for the 6 inch simulator height reading. This meter reading is then scaled over the area of the ROI on the target when irradiated with solar simulator.



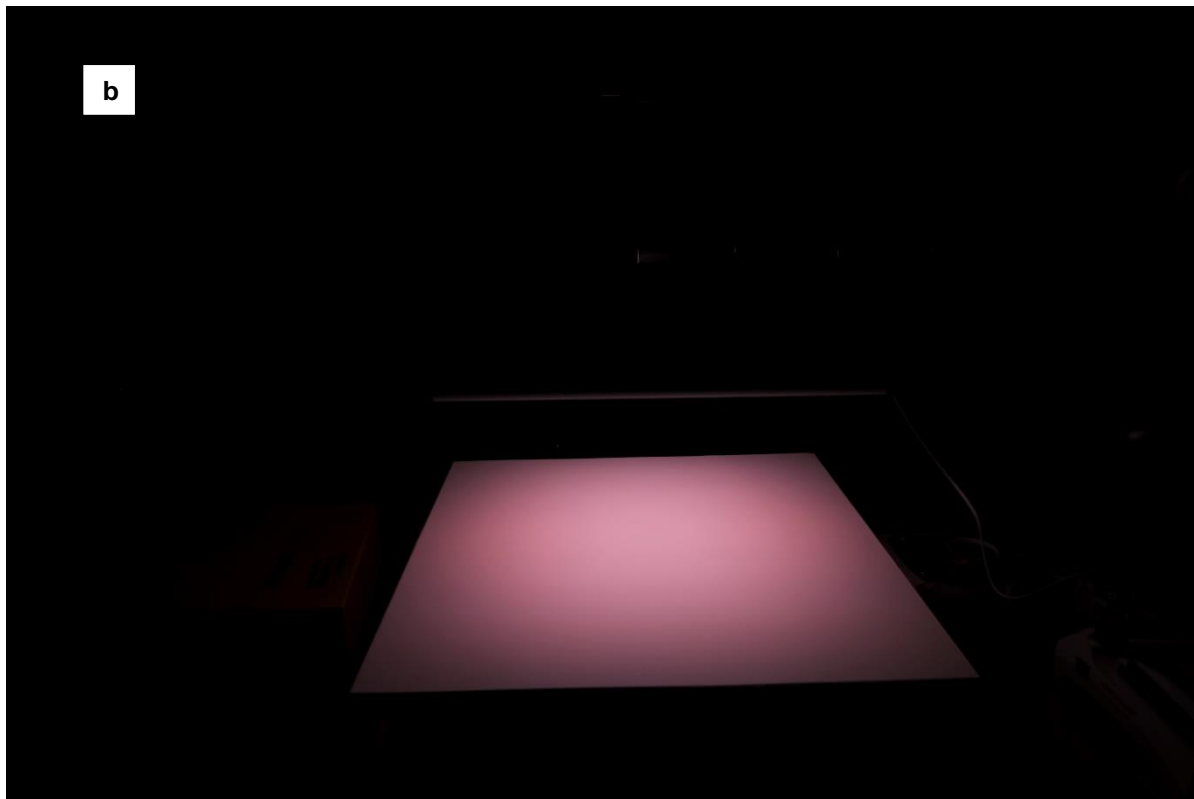
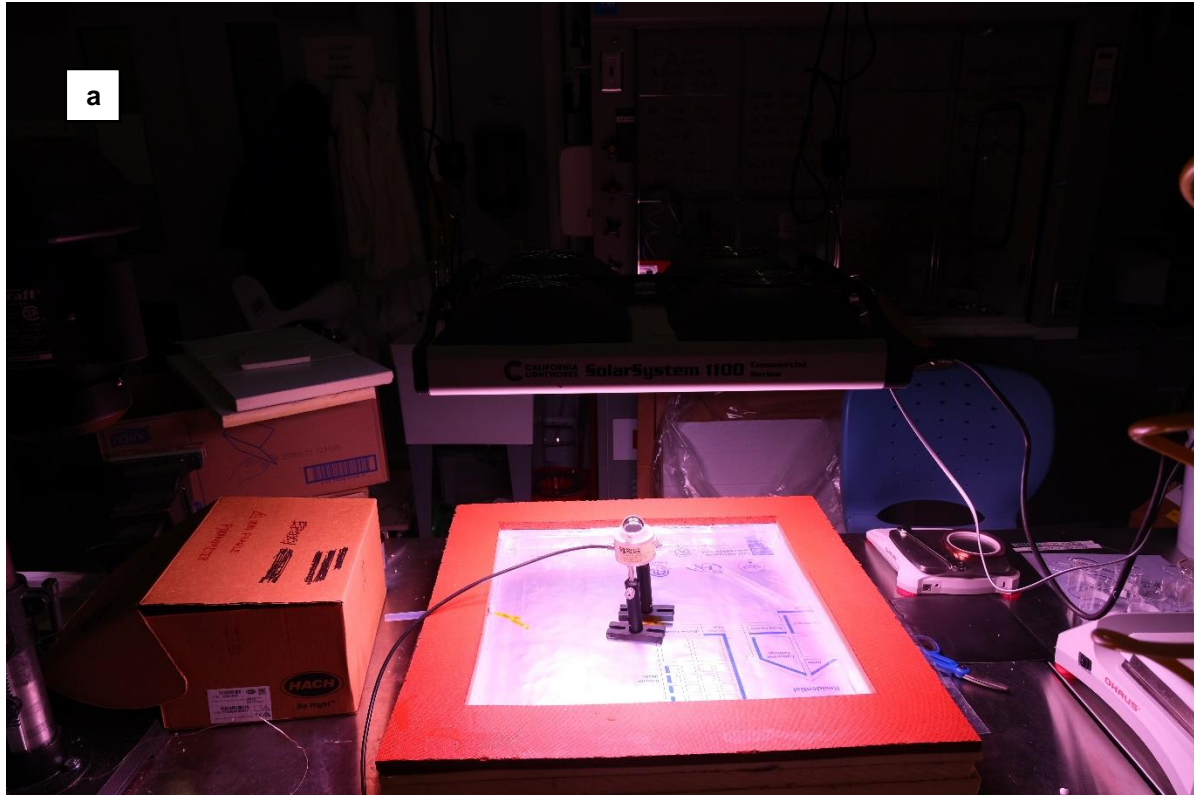


Figure 3-20: Two Images taken for flux mapping: (a) meter image and (b) target image.

Essentially, a custom code was written in MATLAB utilizing the Image Processing Toolbox and functions in order to: first obtain spatial coordinates of the pyranometer (with a point reading normalized to area of pyranometer receiver taken and recorded as well) using the first picture; second, to obtain the 'relative luminance' on the Lambertian target surface; and finally, to match the flux on the target to aperture of CSES. As may be apparent, the point reading from first picture is used and scaled to the 'relative luminance' impinging on the Lambertian target. The final average flux (i.e.  $q_{\text{solar}}$ ) is taken from an 18 inch x 18 inch ROI at the center, with error calculated from this ROI at the edges receiving the minimum solar flux possible due to human error of centering CSES as well as errors from solar simulator height. This is more apparent in the results section illustrating irradiance and solar-to-thermal efficiency being affected.

This relative illuminance, as may be apparent, essentially utilizes the fundamental working principle of not only mirrorless but also DSLR cameras (using a mirror to bounce the viewed image to an optical viewfinder). This working principle is in the photo-diode sensor within the camera body essentially counting the 'number of photons' hitting the surface. Modern CMOS camera sensors have varying degrees of dynamic range for these pixels, but the most common is 8-bit images, resulting in  $2^8$  (i.e. 256) possible pixel values.

There are a few practical concerns regarding placement of the pyranometer and geometry of the LED lights. For an LED solar simulator with a divide at the center, some care should be put into placement to avoid positional errors.

A note is made on obtaining the error for flux mapping (i.e. the maximum and minimum range of deviation) with regards to irradiance). To this regard, the 18 inch x 18 inch ROI was plotted over the 24 inch x 24 inch target plane and compared to the ROI touching corners (Figure 3-21). The only reading this is highly inaccurate for is the 6 inch height, where the proximity from the absorber leads to much human lower error than predicted. The error found from the method was ~20%, whereas in reality it would be ~10% or the nominal error throughout all ranges.

Some care needs to be given in not overexposing the image, using the lowest possible shutter speed of the camera, which is preferable to reach 1/16,000 s (most consumer-grade cameras after 2020 have this setting, with higher end models after 2015 having this feature). This is important because irradiance of 1.4 suns tends to over-expose the image with maximum pixel values reached even as of 1/8000 s (Figure 3-22). Furthermore, the shutter speed must be adjusted accordingly so as to not overexpose the image. To test whether images are over- or under-exposed, a histogram may be used in software, or in MATLAB using the Image Processing Toolbox and function 'imhist()'. The easiest option, however, available in all modern DSLR and mirrorless cameras is the 'histogram' function available in menu settings (illustrated for Fuji XS-10 in Figure 3-23 below). The histogram should be adjusted so that no pixels are over-exposed (pixel values near 256) or under-exposed (pixel values near 0).

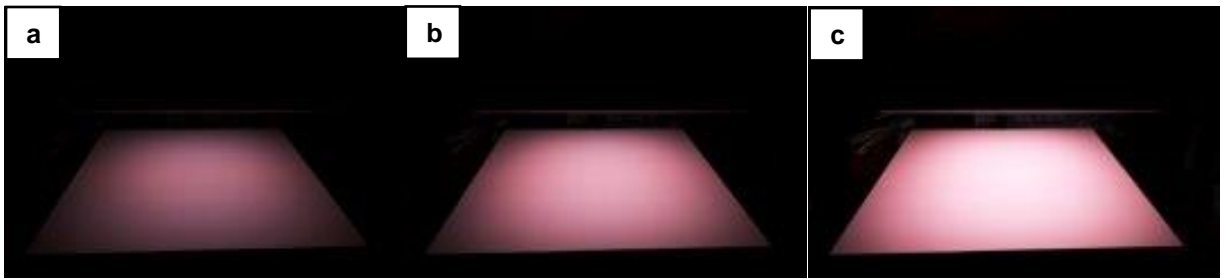


Figure 3-22: Care must be taken with shutter speeds to not overexpose images. Shutter speeds displayed from (a)  $1/32,000$  s, (b)  $1/16,000$  s and (c)  $1/8000$  s.



Figure 3-23: Camera histogram used to ensure properly exposed photographs during flux map images taken.



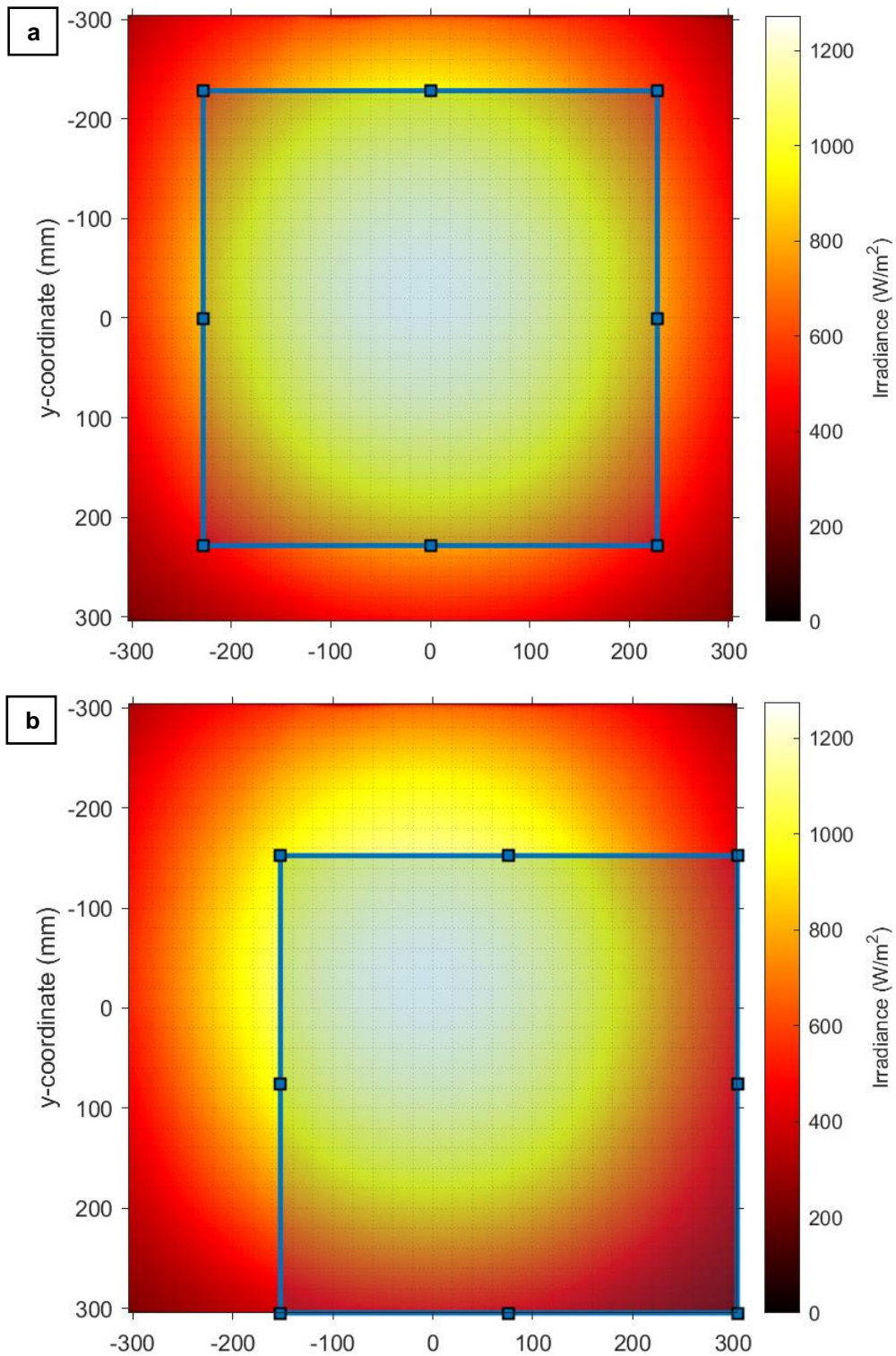


Figure 3-24: Error taken with (a) center average flux as upper limit and (b) corner average flux as lower limit. For example, center reading reads  $\sim 982 \text{ W/m}^2$  while bottom-right reads  $\sim 882 \text{ W/m}^2$ . Thus the minimum to maximum limit of error is  $882 - 982 \text{ W/m}^2$ .

3.3.3.2 *Optical properties of 6 materials used*

Six materials were tested for optical properties, namely reflectivity and transmission for the FEP sheets of two thicknesses. Two instruments were used to cover the entire wavelength spectrum for the samples, namely the UV-2600 spectrophotometer by Shimadzu and VERTEX 70 vacuum spectrometer by Bruker.

The Uv-Vis instrument measures from visible wavelengths of 220 – ~1400 nm, and the Fourier-transform infrared spectroscopy (FTIR) instrument is able to measure Near Infrared Wavelengths, NIR (820 – ~2500 nm) as well as Mid Infrared Wavelengths, MIR (1400 – ~25,000 nm). The samples comprise materials used in CSES (

Figure 3-25), with the instruments shown in Figure 3-26.

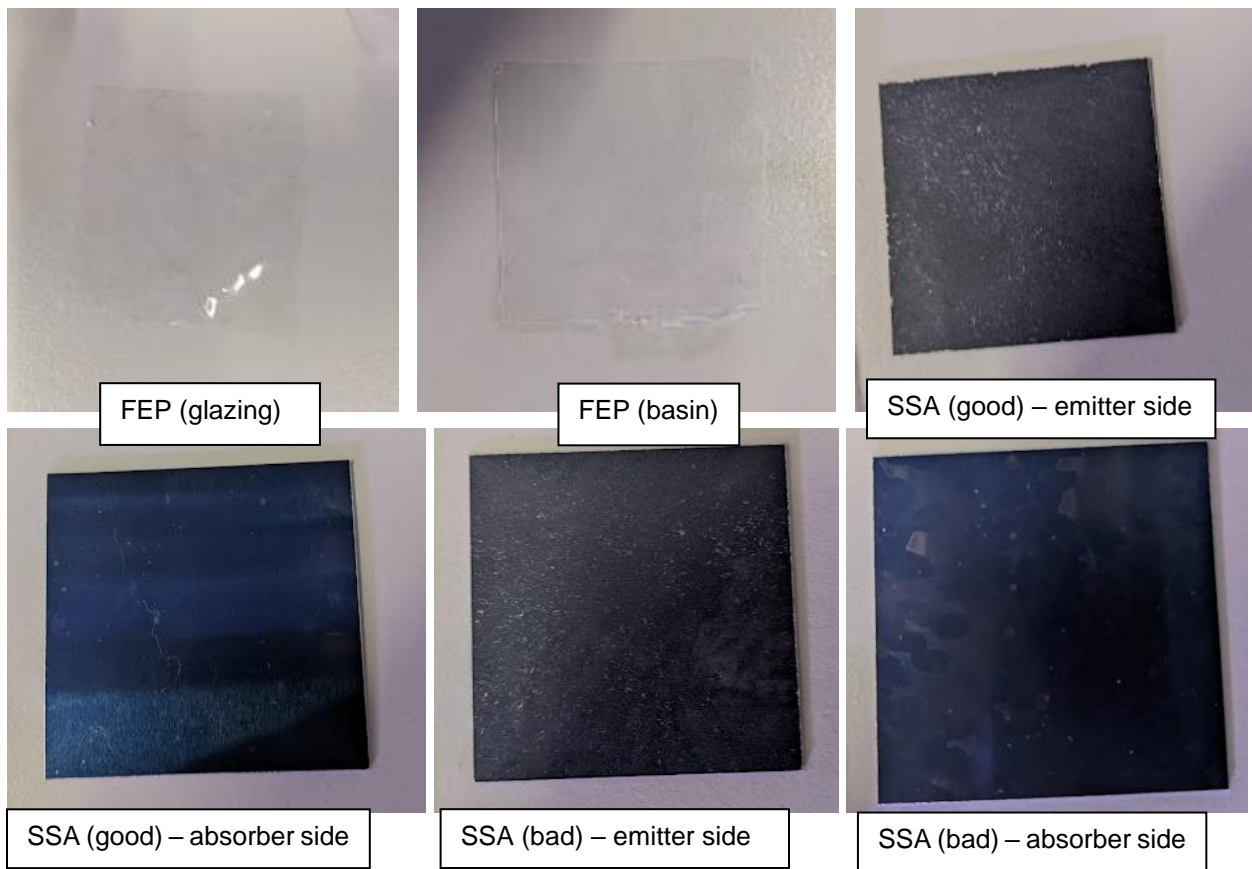


Figure 3-25: Pictures of 6 samples used for optical testing.





### 3.3.3.3 Optical efficiency test using reflective sidewalls

The setup of the optical efficiency test is outlined in Figure 3-27. Three readings were taken: center, side edge and diagonal edge. The latter two readings were taken close to the reflective walls, and thus optical efficiencies of even higher than 100% were expected.

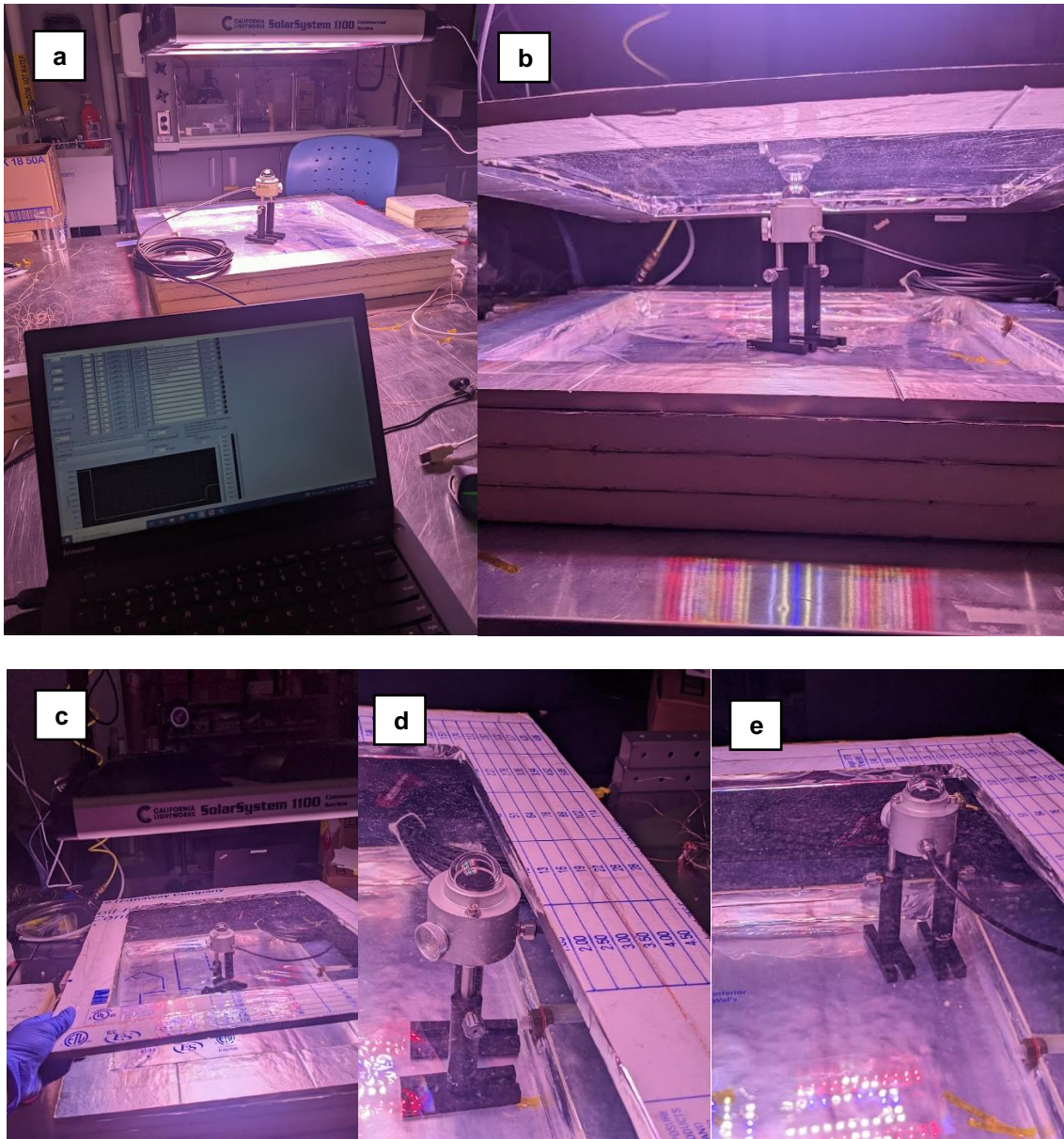


Figure 3-27: (a) Optical efficiency test with the overall setup, (b) the pyranometer position as viewed from eye-level, (c) pyranometer reading taken at center, (b) side edge (bottom-center) and (c) diagonal edge.

### 3.3.3.4 Salinity test with Experiment 38

The salinity was tested using a 200 ml beaker. Approximately 45 g of table salt was mixed in this beaker, corresponding to 35,000 ppm for 1.3 L of water in the basin. This highly saline solution was then mixed in the basin to simulate seawater. While the experiment was turned off after ~4 ½ hours, the remaining water in basin (after ~200 ml evaporated throughout the 4 ½ hours, including 2 hours of heat-up) was taken and analyzed for salinity, showing ~41,000 ppm. This was done using a mass balance and beaker. Thus, a volumetric method (litres) was used to correlate the water mass (grams) with the amount of salt increasing the weight above the reference value recorded with tapwater from lab (~100 - 500 ppm). With this test verifying CSES performance with saltwater, justification is given for all tests being conducted with freshwater (or nearly fresh tapwater). This justification is the mess caused by using salt, had it been used for the other 40 experiments. Salt would stick to surfaces and contact with absorber may foul during handling. Lastly, each experimental setup would've taken ~15 minutes longer (~10 hours for all experiments) had salt been used for all tests. Figure 3-28 below illustrates the above setup process.

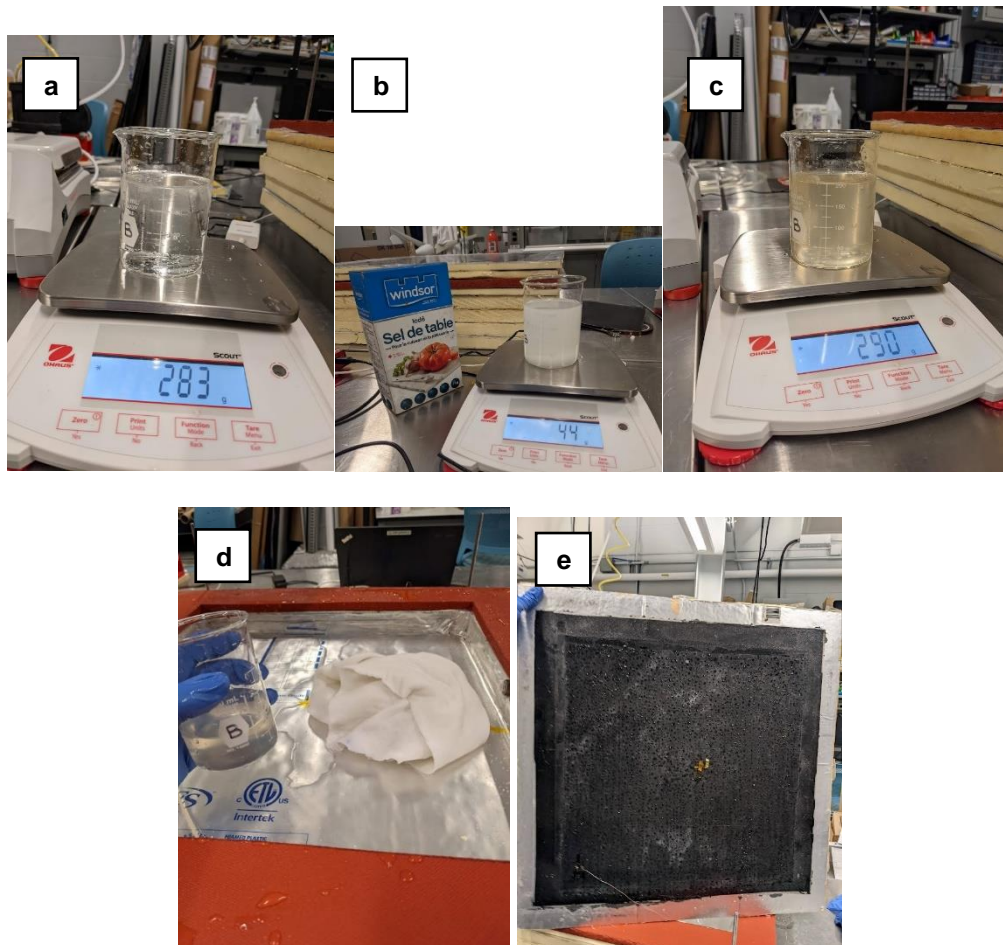


Figure 3-28: Pictures from the experiment. With mass readings taken of (a) tap water, which was mixed with 45 g of salt and then mixed into basin (b). (c-d) A reading was taken after 200 ml evaporated showing higher salinity. (e) No fouling spotted on absorber.

### 3.3.3.5 Evaporation rates for conventional solar stills

Two additional experiments were run, namely Experiment 36 and 37, to observe the evaporation rates for a solar still heating the water by conduction. This was done in Experiment 36 by using the water itself as the absorber and using a cleaning cloth (Zorb) in Experiment 37. In this way, the potential for household items, such as cleaning cloths, is illustrated experimentally using CSES itself without the solar selective absorber and convection reducers (i.e. open-top). In short, these two experiments did not use the contactless infrared heating core to the working principle of CSES. This was done to compare between CSES and its contact heating competitors in terms of energy utilized for intended purpose per cost. While evaporation rates are admirable, reported in the literature to be in the range of 2 to 4 Litres for a 1  $m^2$  receiver, per day. This is in the same range as CSES, however, the capability of CSES to superheat the steam to temperatures above 120 °C is much desired in fields such as medical sterilization, power generation, drying, cooking, and other common daily tasks requiring heat energy.

Temperature and mass details were taken for the water, summarized in the results section. Three thermocouples were placed at different locations along the basin to have more confidence in the temperature readings. The measurements were taken using the mass balance shown below (Figure 3-30).

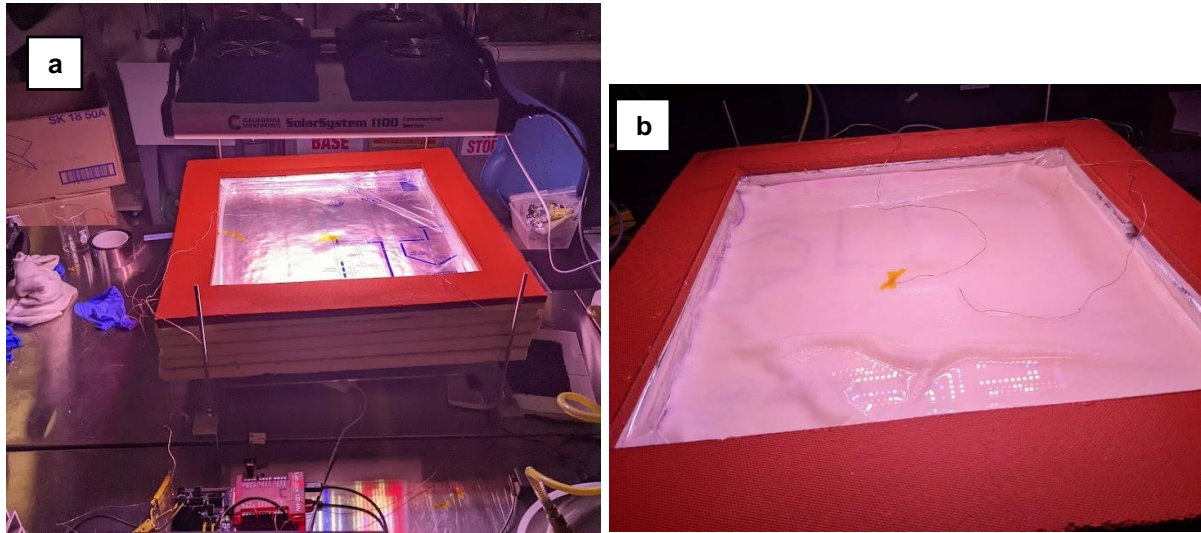


Figure 3-29: Two configurations tested for evaporation rates and absorber temperature details. (a) Experiment 36 was run without a cloth, using the water as the solar absorber itself as a form of bulk heating. (b) Experiment 37 was run with a cloth acting as the solar absorber.





*Figure 3-30: Picture of OHAUS Scout Mass Balance connected to a USB logger (logged to OHAUS software on computer).*

### 3.3.4 Design evolution (41 experiments)

Throughout the course of a year, 41 experiments have been run. Experiment 28 was the first successful experiment with smooth transient temperature and mass curves. Further experiments (35 to 38) were conducted to obtain more confidence in the values used in the model. Experiment 35, in particular, was run to confirm whether the SSA was operating isothermally (it was found that there was a sharp drop from ~130 °C to ~115 °C from center to diagonal edge). This was used to adjust for optical efficiency in the model. Moreover, Experiments 36 and 37 were run to obtain an evaporation rate and temperature comparison of contact solar stills using water and/or cloth as the solar absorber instead of the CSES configuration. Experiment 38 was run with simulated seawater (~35,000 ppm) using a mass balance instead of a Total Dissolved Solids (TDS) meter, as electrical conductivity measurements are usually not as accurate as mass measurements. Experiment 39 and 40 were conducted under 1 sun, with the former being conducted without a hydrophilic cloth and the latter with. Experiment 40 was used as the keynote results which is compared to the model in the results (Chapter 4).

These experiments are summarized (Figure 3-31 and Table 3-1), along with key findings, errors corrected for subsequent tests, and accompanying pictures for better visualization of the design evolution through 4 design iterations within 1 year (May 2021 – May 2022). The period of 1 year and a half prior to this included time for the concept design, bill of materials (BOM) and numerical model (January 2020 – June 2021) was outlined in the Gantt Chart.

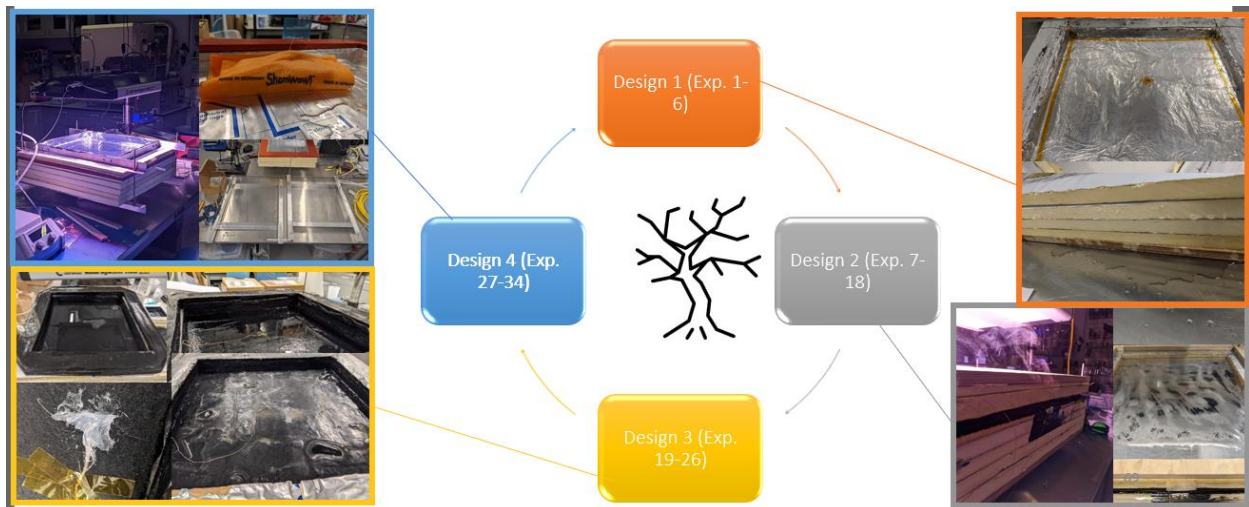
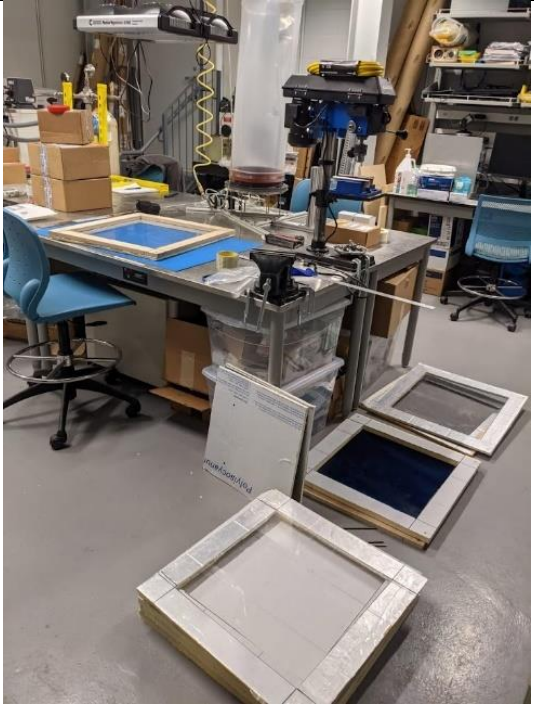
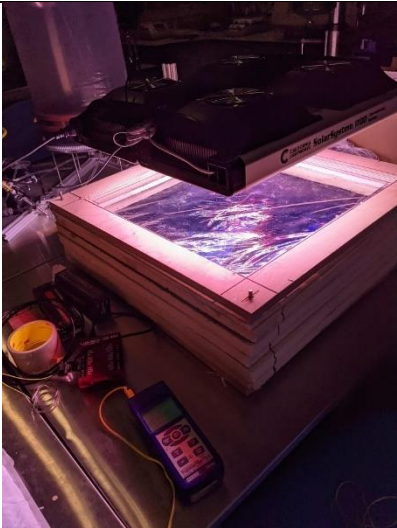
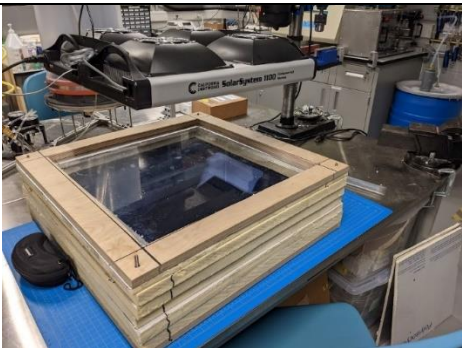


Figure 3-31: Design evolution overview: 4 design iterations were constructed throughout improvements over 33 experiments.

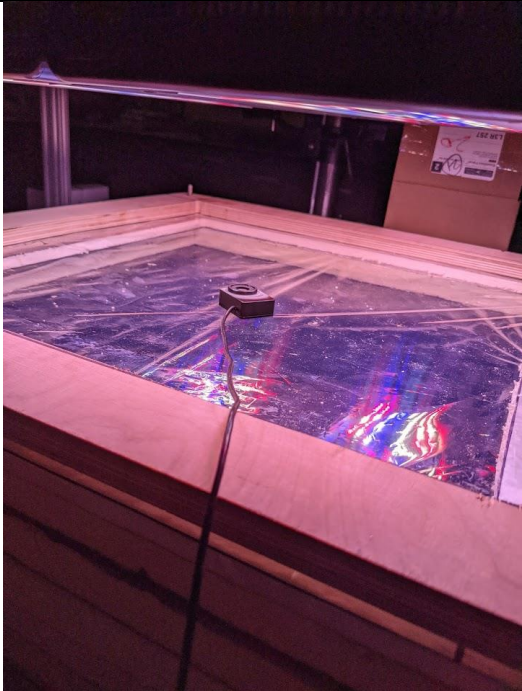
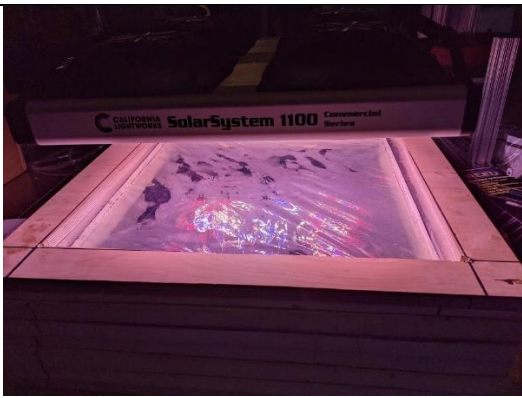




Table 3-1: Summary of 38 experiments over 4 design iterations. Key findings are outlined, with errors corrected for next experimental run. Corresponding pictures are given for visualization of experiments.


Exp no.	Maximum Absorber Temperature (°C)	Solar-to-thermal efficiency (%) for center/max./min. points	Distance from absorber (inches) -> resulting irradiance (W/m <sup>2</sup> )	Pictures	Comments
1	220.5	N/A	6 -> 1390		<p><b><u>1<sup>st</sup> design iteration.</u></b></p> <p>A series of 3 tests were conducted with water in the basin, which leaked significantly (emptying within minutes) preventing any comprehensive in-door solar testing. 650 ml, 1300 ml and 2600 ml of water was used, with 1300 ml decided for future tests.</p>

2	227.1	N/A	6 -> 1390		<p>Basin dried quickly (water leaks), letting emitter heat the basin to above 200 °C. 1300 ml of water used, draining quickly.</p>
3	136.9	N/A	6 -> 1390		<p>First test for absorber to reach a steady-state reliably within the expected range of ~135 °C under ~1.4 suns. Although, 2600 ml of water was used to obtain a quick steady-state reading before basin leaks empty.</p>

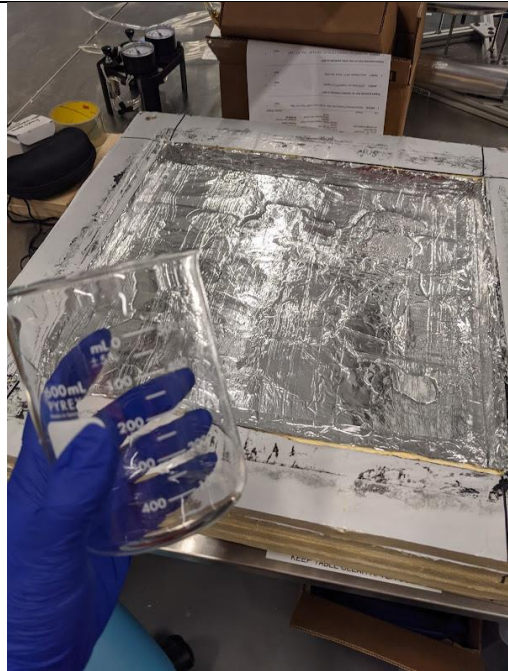
4a	138.3	N/A	6 -> 1390		<p>Thermocouples on logger setup. Test able to be run for ~ 1 hour with 1300 ml before basin empties. A spectrometer was used (ThorLabs) to quantify a range of solar flux by plotting a grid of points as is done traditionally in the solar energy field for solar flux characterization. The average solar flux found at the 6 inch distance was ~ 1 sun (5x5 points taken over the CSES aperture) based on a center reading of 1095 W/m<sup>2</sup>.</p>
----	-------	-----	-----------	--	--


4b	186	N/A	6 -> 1390		Spectrometer used to attempt quantifying average solar flux over aperture
5a	157	N/A	6 -> 1390		Top and bottom wooden clampers constructed to prevent steam and water leaks (less than an hour). New absorber block made for this experiment with improved silicone seal at sides. Significant steam leaks observed on first FEP glazing layer. The test could be run for at least ~ 2 hours before water leaks empty the basin

5b	196	N/A	6 -> 1390		<p>Significant water leaks. Test unable to run for longer than few hours without emptying and heating basin instead of water.</p>
6	162	N/A	6 -> 1390		<p>Steam outlet ran for less than an hour (water leaks prevented longer test runs). Absorber, basin and steam temperatures of ~210°C, ~196 °C and ~65 °C recorded. Temperatures logged on data logger for the first time.</p>

7	169	N/A	6 -> 1390		<p><b><u>2nd design iteration.</u></b></p> <p>New Basin, first test. This basin has been applied with lots of silicone sealant (tube) and silicone spray adhesive was tried to bond aluminum foil firmly to basin to prevent water leaks. Threaded rods were also added to provide better clamping to prevent steam leaks. Water was able to be held in this basin for at least ~4 hours (4x longer than previous tests). After water dried, absorber reached 210 °C (no water, basin at 196°C). Steam at 65 °C. Silicone spray adhesive tried to stick aluminum foil to basin and threaded rod with clamber. Excessive moisture found leaking into glazing system.</p>
---	-----	-----	-----------	---	---








8	159	N/A	6 -> 1390		<p>Steam leaks still significant. Water leaks were also observed throughout the test, emptying within ~ 4 hours as before.</p>
---	-----	-----	-----------	---	--




9	121	N/A	6 -> 1390		<p>Water emptied before reaching steady-state. New basin is brainstormed to be constructed to prevent water leaks. Water leak test showing the basin still failing to contain water.</p>
---	-----	-----	-----------	---	--

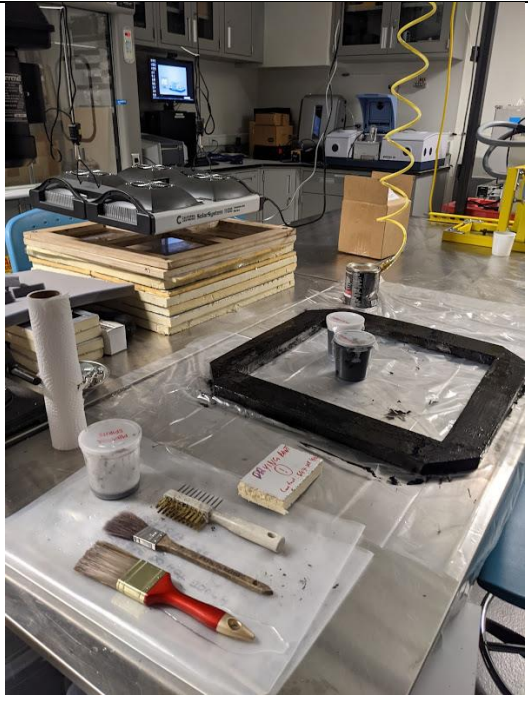
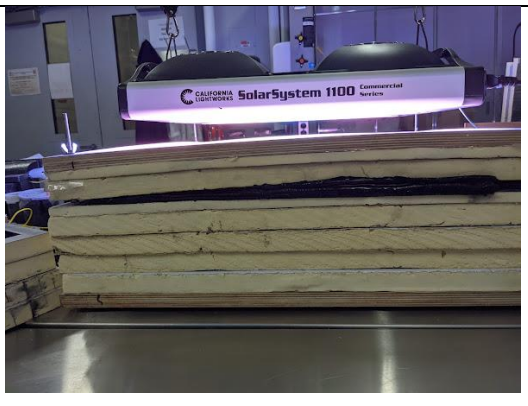
10	139	N/A	6 -> 1390		<p>Test conducted to observe radiative boiling. Most notably, the key interest was to observe bubbles appearing under contactless infrared heating. Initially, the water reached 60 °C as there were heat losses with open polyiso insulation blocks, which were slowly filled in until boiling was reached. The camera equipment and lighting was deemed too poor to observe any bubbles. 194 °C after water dries</p>
----	-----	-----	-----------	---	---



11	165	N/A	6 -> 1390		<p><b><u>3<sup>rd</sup> design iteration.</u></b></p> <p>Flex sealed basin. Water leaks significantly reduced. Test could now be run beyond a couple of hours. No observable water leaks. However, the flex sealed basin reached ~144°C, degrading it visibly.</p>
----	-----	-----	-----------	---	--

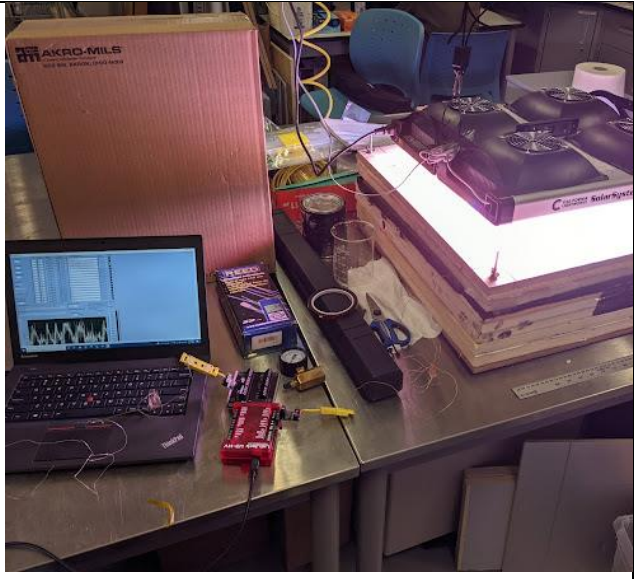
12	168	N/A	6 -> 1390		Flex seal shows excellent water leak prevention, although with visible inflated sections due heat stress.
----	-----	-----	-----------	--	---

13	162	N/A	6 -> 1390		<p>220 (water dried) with flex sealed basin at 140. Flex seal showed poor performance when irradiated to 140. Absorber block has degraded and needs to be re-sealed. However, ideas are brainstormed for effective sealing for future design iteration. Silicone found insufficient to bond absorber block to polyisocyanurate board.</p>
----	-----	-----	-----------	--	---




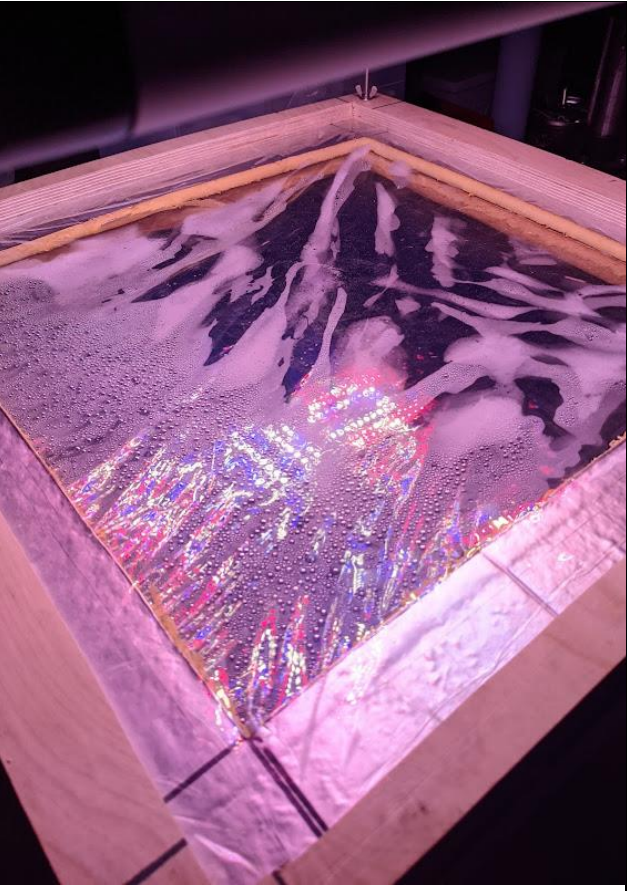
14-16	N/A	N/A	6 -> 1390		<p>Three tests are run testing the effect of gasket and clamping on moisture on FEP glazing. Melamine gasket constructed (painted with flex seal to provide hydrophobic protection against hot moisture) was found to be very effective against steam leaks. Gasket was found to reduce steam leakage to FEP glazing significantly. Melamine gasket prepared and painted with flex seal to prevent steam leaks.</p>
17	N/A	N/A	6 -> 1390		<p>New gasket is tested and compressed as much as possible to observe reduced steam leaks. Gasket performance tested with compression test (1 inch to ~0.25 inch compression).</p>


18	N/A	N/A	6 -> 1390		<p>Minor moisture (significant improvement) on first FEP glazing only after solar simulator is turned off. Moisture on FEP significantly reduced after using new gasket.</p>
19	N/A	N/A	6 -> 1390		<p><b>3rd design iteration:</b> Highly hydrophobic interaction observed with flex seal. Thus, a hydrophilic surface (felt) was implemented to reduce water pooling. Absorber readings not taken as water/steam leaks were a priority. Felt was found to absorb water well, but could be improved. New basin prepared with flex seal and laid with hydrophilic layer (felt). Wet felt and performance in holding water.</p>


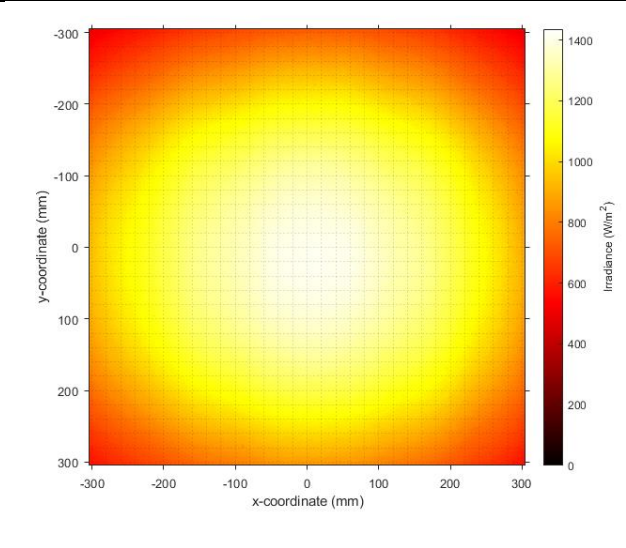
20	121	N/A	6 -> 1390		<p>Thermocouples with LabJack U3-HV (DAQ) used for the first time. Readings for this test are really abnormal given the solar flux and irradiance of ~160 in prior tests at same solar simulator height. Setup using a DAQ to record temperatures.</p>
----	-----	-----	-----------	--	--



21	159	N/A	8 -> 1244		Flux mapping is performed for the first time.
----	-----	-----	-----------	--	---



22	132	N/A	12 -> 903		<p>Steam leaks still significant. Wood bending upwards due to corner threaded rods for clamping. Excessive moisture on FEP even with current gasket and clamping mechanism.</p>
----	-----	-----	-----------	---	---

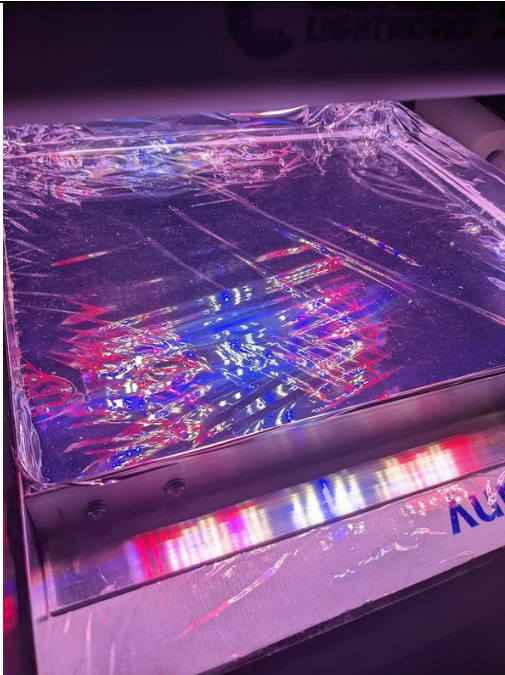

23	144	N/A	10 -> 1050		Height details for 3 <sup>rd</sup> design iteration. Aluminum foil was inserted in square tube outlet (painted with flex seal). Front view of the 3 <sup>rd</sup> design iteration
----	-----	-----	------------------	---	--


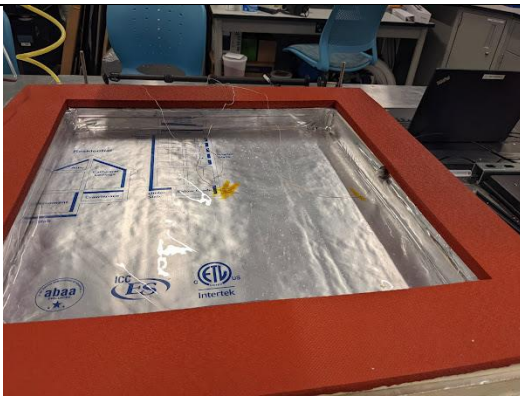
24	141	$\eta_{center} = 19.2$ $\eta_{max} = 21.88$ $\eta_{min} = 18.8$	10 -> 1050		<p>Steam recorded at 115°C, showing a correct reading for the first time. Mass balance was also used for first time to record evaporated mass. Mass balance holding CSES.</p>
25	113	$\eta_{center} = 18.4$ $\eta_{max} = 21.88$ $\eta_{min} = 18.8$	11.5 -> 917		<p>First time flux mapping with center reading 1.4 suns and 1 sun average over target. Temperature readings of wet basin at 14.4 degC, illustrating effectiveness of CSES for potential evaporative cooling. Absorber cracks noticed compromising thermal emissivity delivering heat to water (and thus impacting solar-to-thermal efficiency).</p>



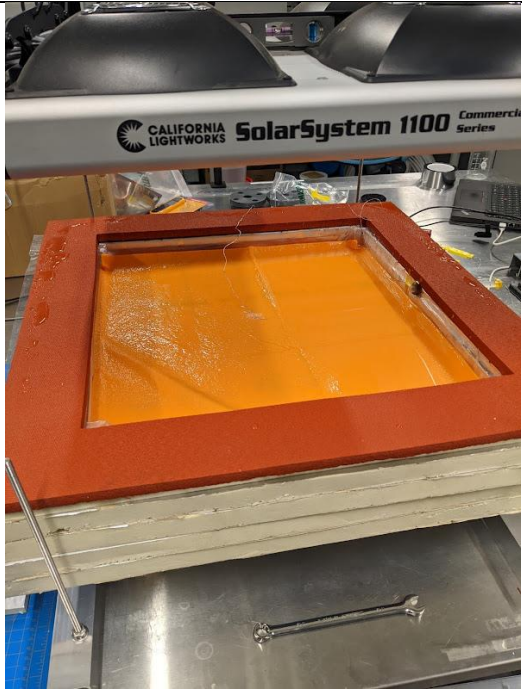



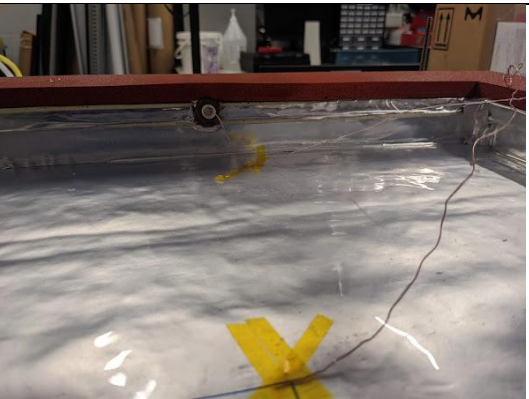
26	128	$\eta_{center} = 19.18$ $\eta_{max} = 21.72$ $\eta_{min} = 18.77$	10.5 -> 982		<p><b><u>4<sup>th</sup> design iteration.</u></b></p> <p>New design iteration with massive upgrades from previous tests (including hydrophilic layer, absorber epoxied, clampers and origami-folded FEP basin). Solar simulator lowered by 1 inches, outputting ~ 100 W/m<sup>2</sup> more flux than previous test. It was attempted to bond FEP tube to FEP thick sheet used for basin. This failed however, as 300 °C led to degradation by heat stress. Mass readings showed error due to 'mass short' as clampers were occasionally touching ground. Insulation blocks to raise CSES to not touch ground will be implemented in future tests.</p>
27	128.8	Mass short	9.5 -> 1094		<p>Due to mass short (bottom aluminum clamer touching ground), reliable mass readings could not be taken.</p>

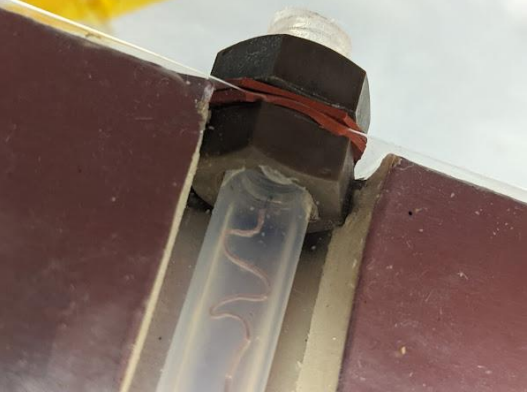
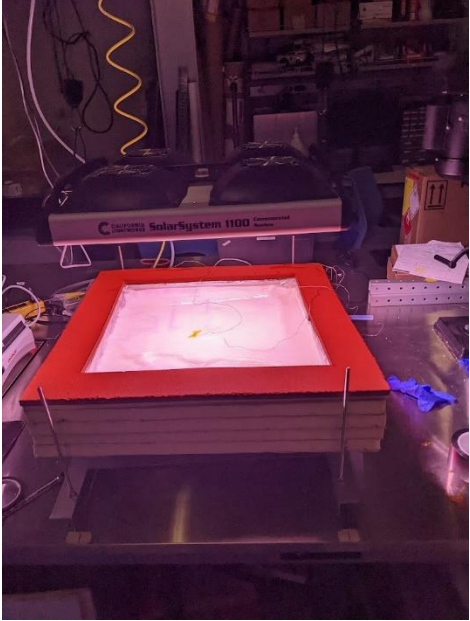
28	140	$\eta_{center} = 24.73$ $\eta_{max} = 28.06$ $\eta_{min} = 24.24$	9.5 -> 1094		<p>This and next test conducted to observe temperature discrepancies from solar simulator height based on whether 10.5 inches height (1sun) is taken from absorber plane (status quo) versus aperture (top clamber inlet). Moreover, any effects of using the hydrophilic layer are also to be observed. This is one of the experiments used as the keynote results throughout 38 experiments.</p>
29	123	$\eta_{center} = 23.12$ $\eta_{max} = 25.94$ $\eta_{min} = 24.24$	13 -> 785		<p>Test conducted without a hydrophilic layer. This and next test conducted to observe effect of adjusting simulator height 3 inches from absorber plane and inlet plane (top of clamber). The 1 sun simulator height was taken from the inlet plane (i.e. 3 inches further away from the absorber plane). The estimated 1 sun range at the time was thought to be 10 inches, but later tests confirmed the true 1 sun to be 10.5 inches of height up from absorber plane.</p>

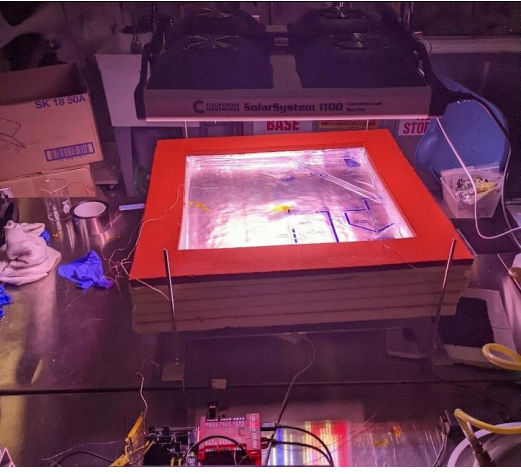

30	121	$\eta_{center} = 20.76$ $\eta_{max} = 23.65$ $\eta_{min} = 20.33$	10 -> 1060		<p>A new hydrophilic layer was used (ShamWow!™). This test was conducted with simulator taken at 1 sun height from absorber plane. Confirms that the hydrophilic layer has no effect on the absorber temperature. Interesting, the effect of adjusting the simulator height showed approximately the same absorber temperature when heights were adjusted 3 inches.</p>
31	107	N/A	13.5 -> 728		<p>Test conducted with no cloth (hydrophilic layer) this time. Strange evaporative cooling observed when left overnight. Mass reading was not taken for this experiment due to a software error which was resolved permanently after this experiment.</p>






32	104	Mass short	13.5 -> 728		Test conducted again with cloth. No observable difference found in using cloth compared to Experiment 31.
----	-----	------------	----------------	--	---

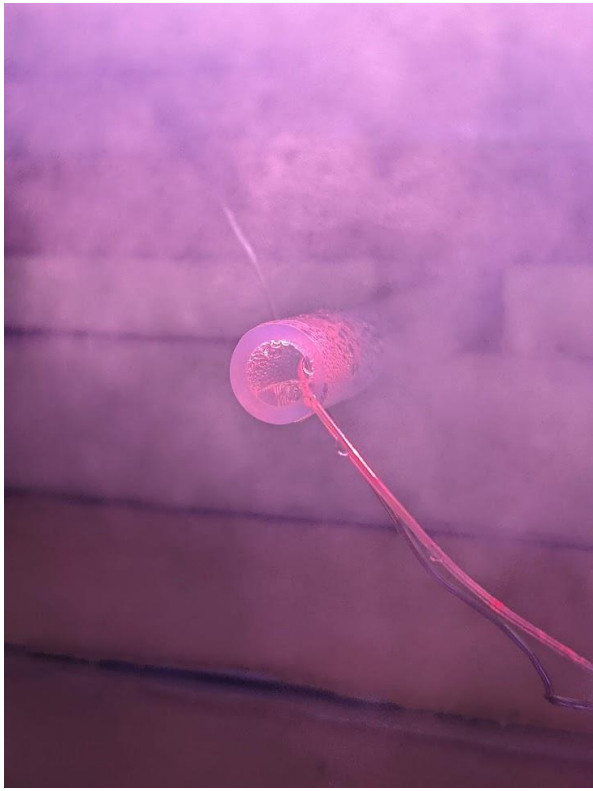
33	138	$\eta_{center} = 24.19$ $\eta_{max} = 27.39$ $\eta_{min} = 23.67$	10.5 -> 982		<p>New cotton hydrophilic layer tested with two water thermocouples tested for readings. One is silicone-encapsulated (showing 93°C) while the other is taped (showing 101°C). Incorrect steam temperature readings due to condensation collecting in FEP outlet tube.</p>
34	134	$\eta_{center} = 19.73$ $\eta_{max} = 22.34$ $\eta_{min} = 19.31$	10.5 -> 982		<p>Tested without hydrophilic layer. Incorrect steam readings again at less than 100 °C despite observable steam output</p>

35	119	$\eta_{center} = 18.69$ $\eta_{max} = 21.17$ $\eta_{min} = 18.29$	10.5 -> 982		<p>Verification testing using hydrophilic layer. Steam outlet thermocouple slightly bent into a 'spacer' to avoid touching FEP tube walls.</p>
36	~30 (no SSA)	$\eta_{center} = 24.91$ $\eta_{max} = 28.54$ $\eta_{min} = 24.56$	12 -> 903		<p>Open-top irradiated under 0.9 sun and hydrophilic layer. Evaporation rate of ~75 g/hr.</p>

37	~30 (no SSA)	$\eta_{center} = 22.84$ $\eta_{max} = 24.56$ $\eta_{min} = 19.93$	12 -> 903		<p>Same test as above (0.9 sun) except this time without a cloth. Evaporation rates of ~60 g/hr, which is 20% less than with the cloth compared to Experiment 36. The conclusions from these two experiments is clear. Using a cloth as solar absorber is highly desired, especially given the availability of cotton and other natural materials for cloth.</p>
38	125	$\eta_{center} = 19.24$ $\eta_{max} = 21.79$ $\eta_{min} = 18.83$	10.5 -> 982		<p>Final experiment run with simulated seawater (35,000 ppm) and Hydrophilic layer. Two thermocouples were placed at center and diagonal edge to confirm the temperature gradient from center to edges and decide on a final mean absorber temperature.</p>

39	128.9	$\eta_{center} = 19.2$ $\eta_{max} = 21.88$ $\eta_{min} = 18.8$	10.5 -> 982		Test run without cloth. As before, the steam thermocouple is bent into a spacer to avoid touching tube walls.
40	128.1	$\eta_{center} = 19.97$ $\eta_{max} = 22.61$ $\eta_{min} = 19.54$	10.5 -> 982		Test run with cloth. Two absorber temperatures taken as before to conclude on a suitable mean absorber temperature to model validation.

41a	117	$\eta_{center} = 11.43$ $\eta_{max} = 12.67$ $\eta_{min} = 11.01$	13.5 -> 728		<p>Comprehensive solar simulator height test irradiating receiver from ~0.75 to ~1.4 suns. Absorber temperatures, solar-to-thermal efficiency is recorded for each simulator height (therefore solar irradiance).</p> <p>This experiment may be used as a singular guide towards absorber temperatures and solar-to-thermal efficiencies achieved throughout the irradiance range. Experiments 41a to 41f achieved temperatures of 117 °C to 155.2 °C.</p> <p>Solar-to-thermal efficiencies achieved were 11.01% (41a) at the minimum efficiency point up to 45% at the maximum efficiency point (41f).</p>
41b	121	$\eta_{center} = 12.96$ $\eta_{max} = 14.84$ $\eta_{min} = 12.77$	12 -> 903		
41c	127.7	$\eta_{center} = 18.73$ $\eta_{max} = 21.20$ $\eta_{min} = 18.32$	10.5 -> 982		
41d	134.2	$\eta_{center} = 22.44$ $\eta_{max} = 25.36$ $\eta_{min} = 21.79$	9 -> 1112		
41e	147.6	$\eta_{center} = 30.20$ $\eta_{max} = 34.94$ $\eta_{min} = 29.87$	7.5 -> 1311		
41f	155.2	$\eta_{center} = 38.35$ $\eta_{max} = 45$ $\eta_{min} = 37.95$	6 -> 1390		





### 3.4 Model

The numerical model was built as a quasi-1D transient thermal circuit within Simulink's 'Simscape' package, enabling modelling of thermal circuits. The energy balance diagram (Figure 3-32) essentially captures the modes of heat transfer, evaporation and heat exchange which occurs under solar irradiation. To augment the capability of the 1D thermal circuit, side loss considerations were made with a separate Solidworks Thermal study to gauge 3D effects on side insulation from conduction within hot enclosure to ambient, as well as convection from ambient acting on all exposed surfaces of CSES. This thermal study was also run for scales of 6 inches up to 72 inches. Thus, a side loss coefficient is made available as a function of these scales, enabling the model to accommodate CSES of any geometric side length and scale. An overview of the heat transfer mechanisms within CSES are shown diagrammatically in Figure 3-32 below. The thermal circuit was segmentalized for ease of reading into the critical functions of each part. For example, the solar input is currently set to utilize irradiance data from MS Excel, which could be either from a pyranometer for outdoor solar testing, or solar similar flux under in-door lab testing. The latter was utilized in the numerical model as testing of CSES was undertaken in lab conditions.

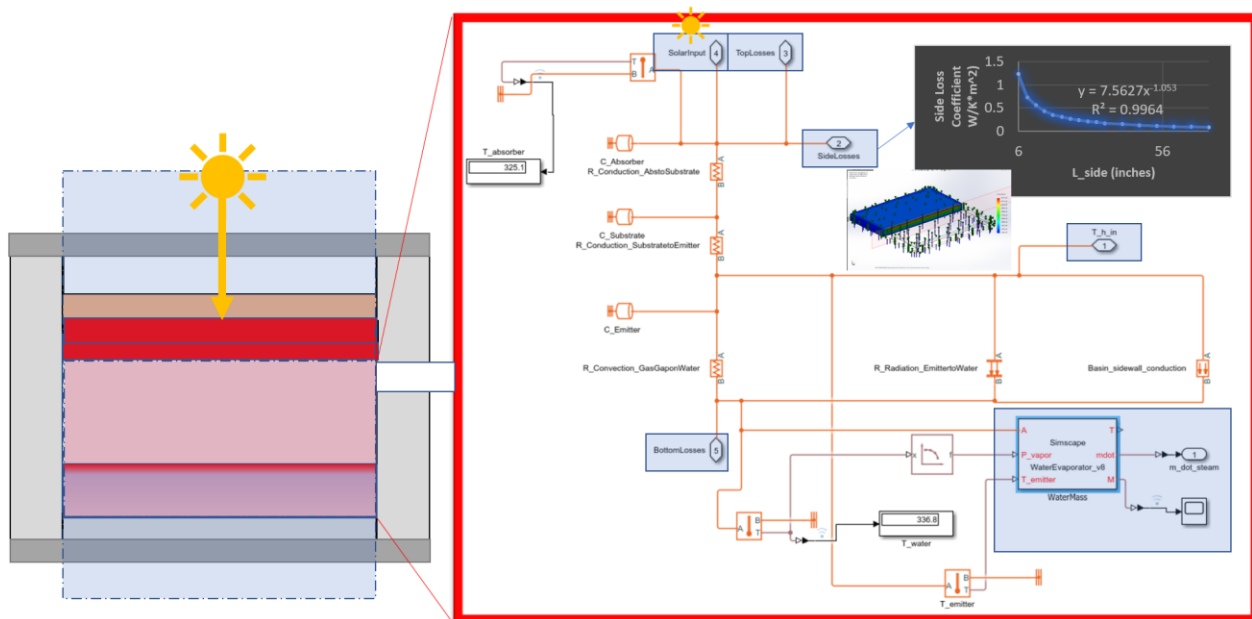


Figure 3-32: Overview of sections within thermal circuit, with enclosure thermal circuit highlighted with connecting nodes to custom functions for solar input, top losses, bottom losses, side losses (including Solidworks Thermal Study), water evaporation and steam superheating using hot emitter.

### 3.4.1 Solar Input

Figure 3-33 shows the solar irradiance input into a lookup table using the current simulation time step as an input. This lookup table multiplies irradiance input into the model (units of  $\text{W}/\text{m}^2$ ) and multiplies it by the area ( $A_{\text{aperture}}$ ), and optical efficiency losses ( $\eta_{\text{optical}}$ ). The solver block ( $f(x) = 0$ ) is required for any Simulink circuit to run.

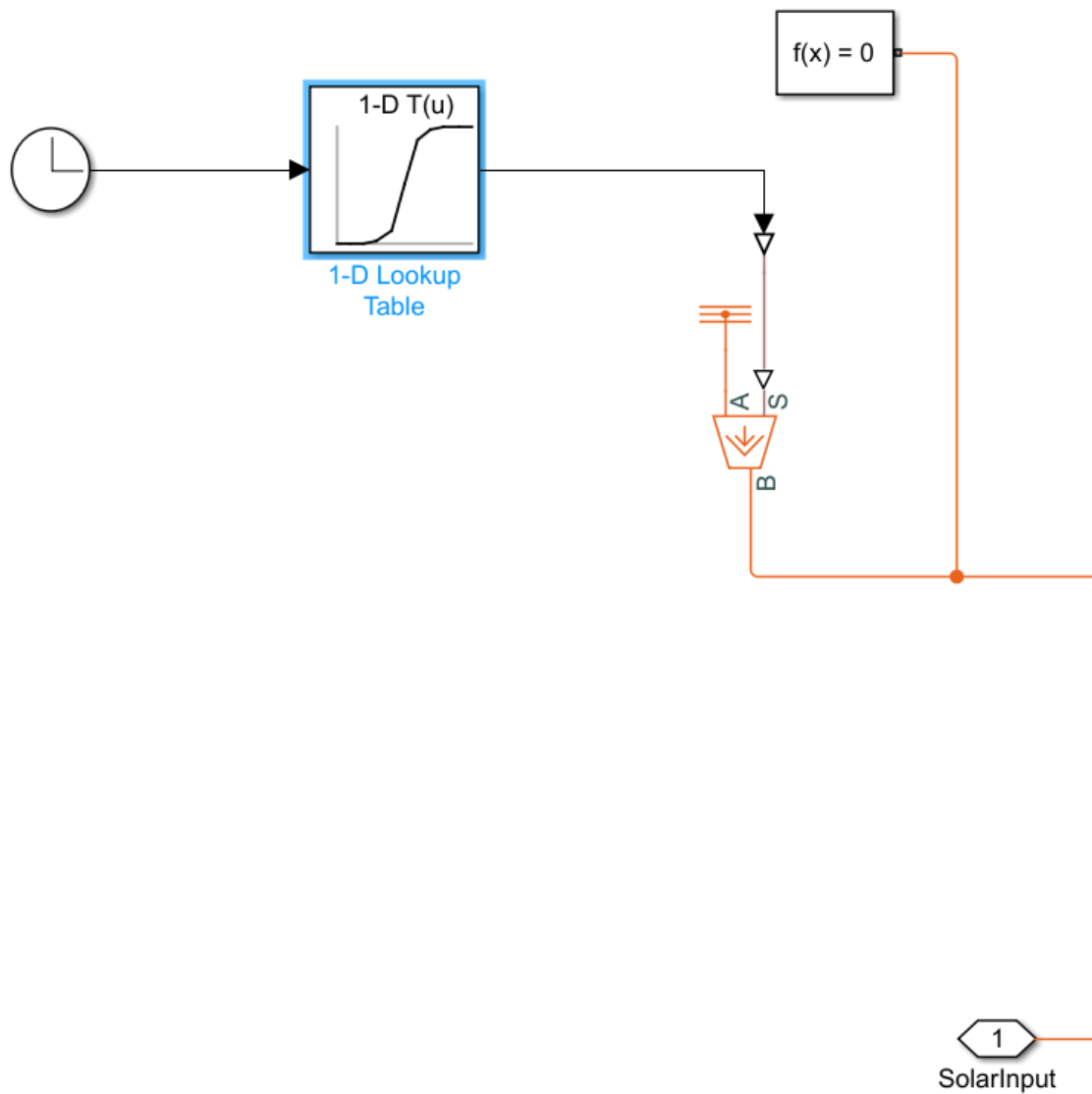


Figure 3-33: Thermal Circuit representation of Solar Input providing heat flux to CSES.



### 3.4.2 Enclosure

Figure 3-34 shows the heat transfer within the enclosure of CSES after solar irradiance is used to heat up the absorber. This heat conducts through a very thin substrate and is radiated from the emitter side to the water. It must be noted that there are also convection effects from the gas gap (mixture of water vapor and air) and conduction through basin sidewalls. The custom water block utilizes two inputs: temperature-dependent vapor pressure of water as an input; and the temperature after the three heat transfer resistances (radiation, convection and conduction) are accounted for to obtain temperature of water.

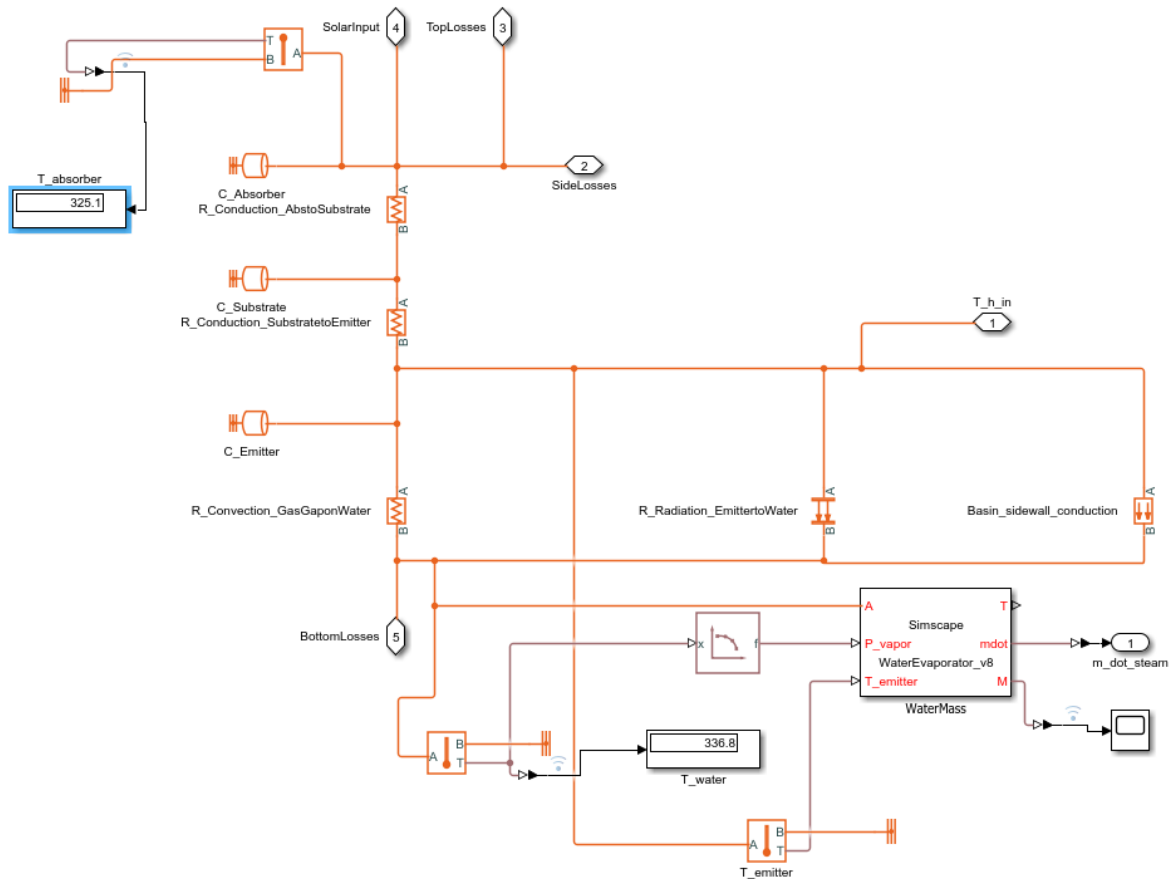


Figure 3-34: Thermal Circuit representation of Heat Transfer inside Enclosure boiling water.

### 3.4.3 Side Losses & Solidworks Thermal Study

Figure 3-35 shows the side loss resistances being divided into three layers and being the inverse of the side loss coefficient obtained from an external Solidworks thermal study. The thermal circuit detailed models 1D flow without considering 3D effects through the sides of the insulation. To resolve this issue, a side loss coefficient is computed using Finite Element Analysis (FEA) methods using the 'thermal study' option in Solidworks software (Figure 3-36). The side loss coefficient was computed and graphed as a function of side length. The useful detail from this plot is a logarithmic functional fit, the equation may then be used to

compute side losses for CSES of any geometric scale. The side lengths chosen range from 6 inches (validated against the side loss coefficient study obtained and experimentally validated by Cooper et al. [3]) to 72 inches. It was apparent from the Solidworks thermal studies that the side losses become negligible after a side length of approximately 30 inches. In order to compute the side loss coefficient, the thermal studies were run for 1D (i.e. insulation set to heat flux = 0, or adiabatic) and 3D (i.e. insulation set to thermal conductivity of polyisocyanurate insulation of  $k \sim 0.02 \text{ W}/(\text{m}\cdot\text{K})$ ).

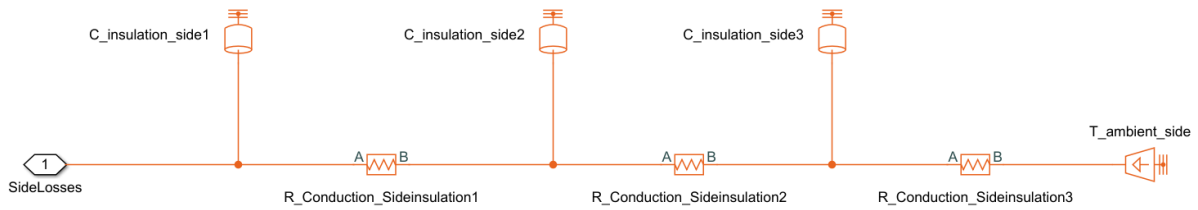


Figure 3-35: Thermal Circuit representation of heat losses through CSES side insulation.

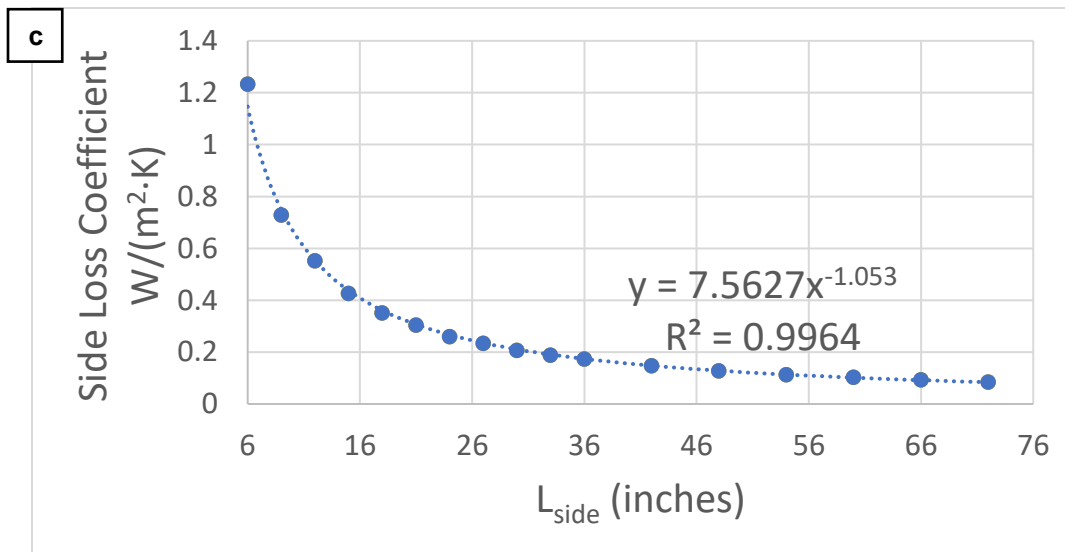
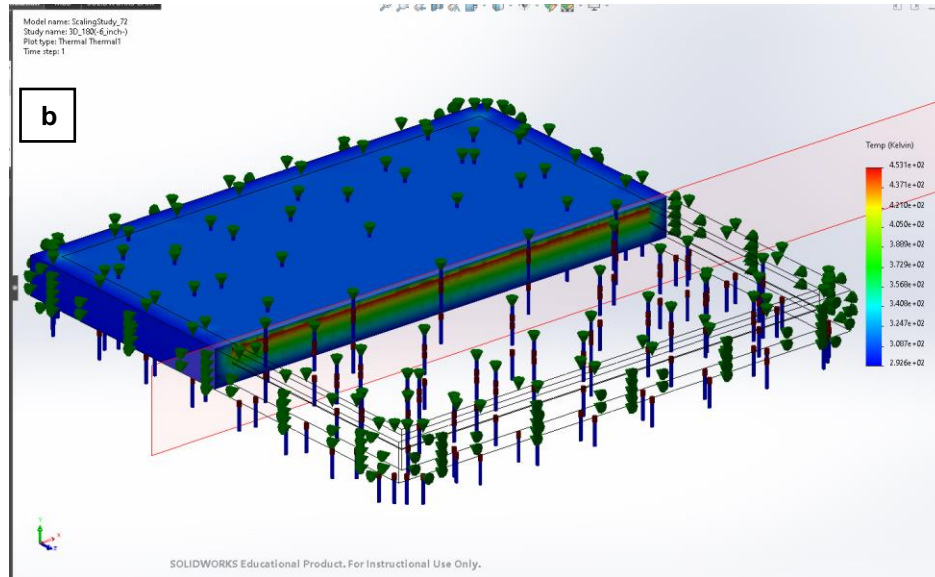
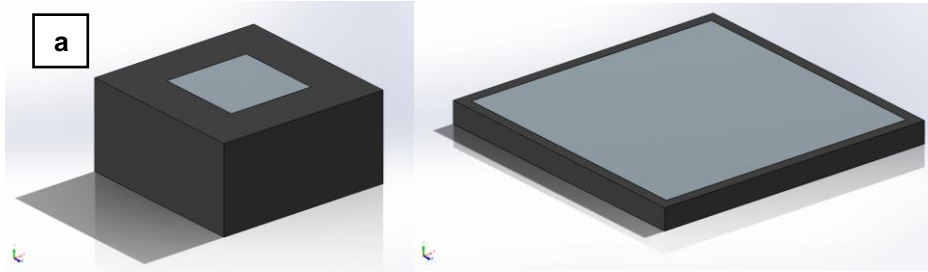


Figure 3-36: Side Loss Study run to integrate 3D effects into the 1D thermal circuit. (a) Run for scales from 6 inches to 72 inches of CSES basin length, (b) with temperatures set for typical absorber temperature of 140 °C and boiling water of 100 °C as boundary conditions for simulation and (c) plotted as a function to be scaled.

### 3.4.4 Top Losses

Figure 3-37 illustrates the top losses from hot absorber to ambient. This is accounted for by radiation from the top side of absorber (not to be confused with the bottom side emitting infrared radiation towards water) to ambient and convection of air over the absorber (driven by the temperature gradient between 140 °C absorber and ~20 °C ambient). The FEP glazing, to this aim, are modelled as conduction resistances below the critical thickness obtained from the Critical Rayleigh Number (being 0.2 inch for CSES). While the insulation thickness was 0.5 inch, there are minor convection effects which are largely ignored and modelled as stationary air with conduction instead.

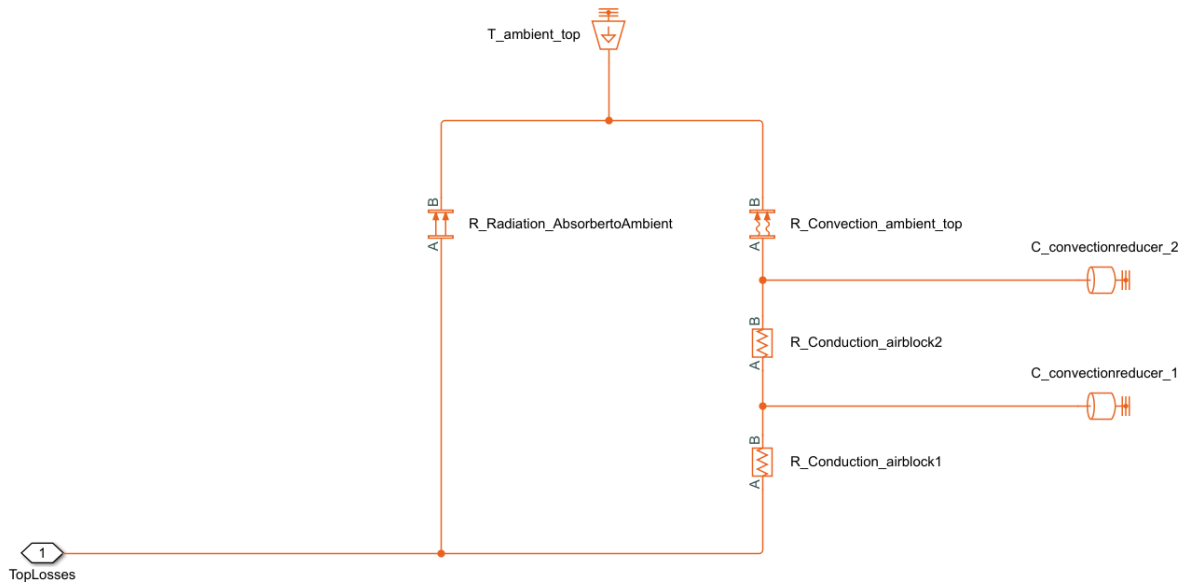


Figure 3-37: Thermal Circuit representation of heat losses through CSES top insulation.

### 3.4.5 Bottom Losses

Figure 3-38 shows the bottom resistances divided into three layers, similar to the three divisions of side resistances. Heat is conducted from water to felt and then to the FEP basin (former two conduction resistances largely negligible due to very low thickness) and finally to ambient, where convection acts on the bottom surface.

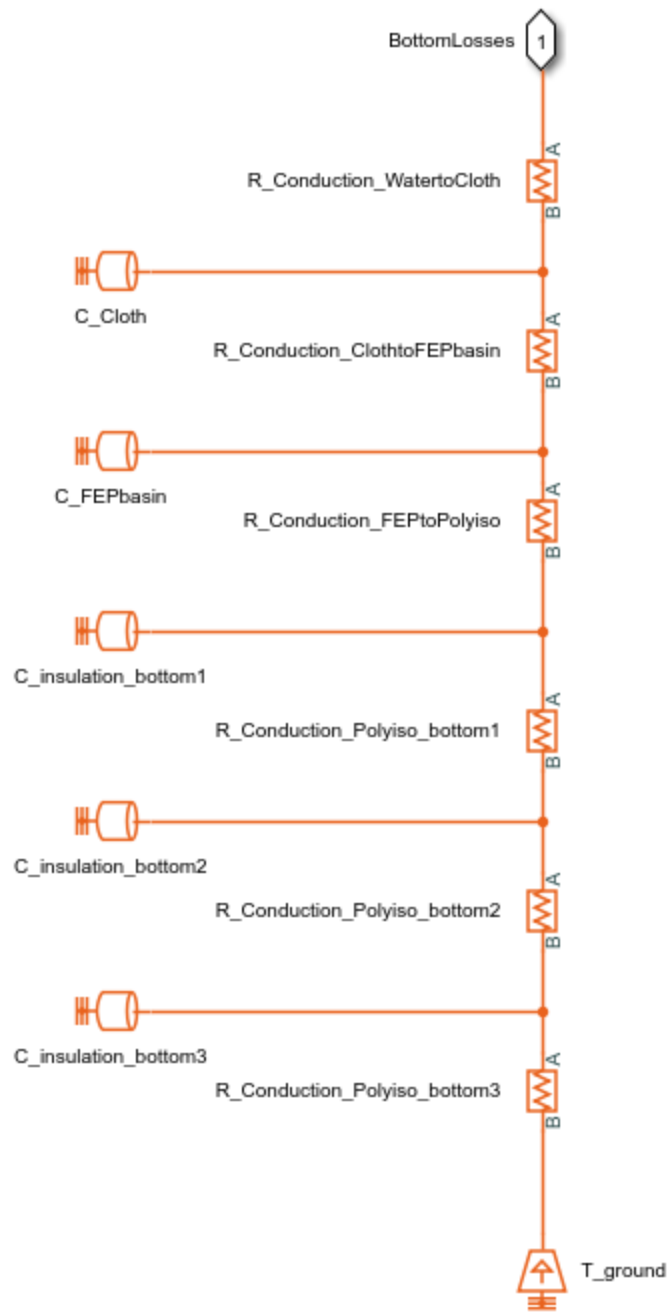


Figure 3-38: Thermal Circuit representation of heat losses through CSES bottom insulation.

### 3.4.6 Heat Exchanger

Figure 3-39 illustrates the heat exchanger being modelled from equations developed in sub-section 2.2.6. Blocks from Simscape and Simulink are utilized along with any PS-Simulink conversions made as necessary, to model the equation.

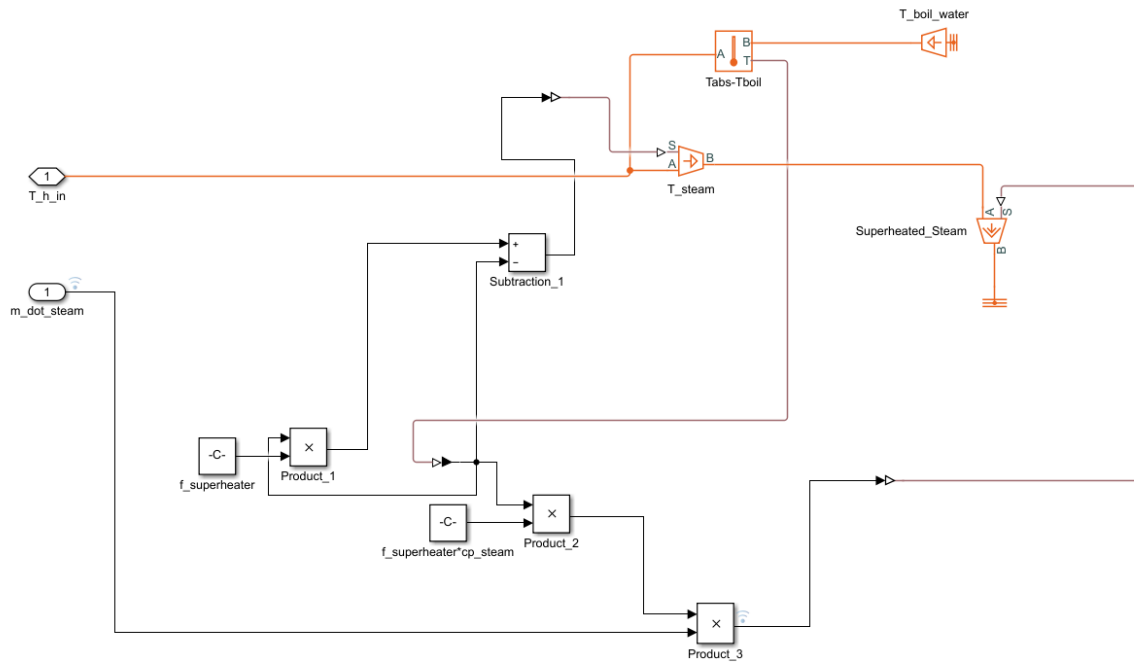


Figure 3-39: Thermal Circuit representation of heat exchange between emitter and steam at 100 °C from boiling water.

### 3.4.7 Parameter study

A parameter study was run using Simulink's 'Sensitivity Analyzer' package. The Sensitivity Analyzer generates useful statistical plots of the design points (i.e. a design made up of combinations of all 9 parameters) run within the study. These design points are plotted with regards to a defined objective function. Two crucial performance metrics were chosen to this aim: maximum absorber temperature ( $T_{abs,max}$ ) and evaporation rates using remaining water mass (grams). These were defined as 'Signal Properties' with a minimize function for a signal maximum (for maximum absorber temperature and reverse for evaporated mass to be minimized).

The model was parametrized to be run for a wide range of input parameters, broadly comprising geometric, material and ambient properties.

The software used was Simulink add-on's Sensitivity Analyzer, which conveniently runs such a useful analysis for any circuit (of any physical system) within Simulink (including the SimScape package). The purpose of the sensitivity analysis is to tune parameters within the thermal circuit (modelled using Simscape components primarily in Simulink) to more accurately match the experimental results. Furthermore, the correlation between the most important parameters may be identified with tornado plots and correlation matrices. To this end, 3000 random points were generated for 7 parameters. These design points were run in 3,000 runs of the developed numerical model, taking ~13 hours to finish (resulting in ~15 seconds per run). Each run is conducted over 8 hours, leading to the evaporated mass to be a result of heat-up and steady-state as achieved within these 8 hours.

Table 3-2 below summarizes the parameters within lower and upper limits. Rationale is given for these ranges. Figure 3-40 illustrates the parameters with respect to geometric, material and ambient properties. Moreover, 3 tuning parameters used in the model to match the experiment were tested for sensitivity to the model. Thus, 10 total parameters were run over the course of 2 simulations.

*Table 3-2: 3,000 simulation runs taking ~ 13 hours to complete (15 seconds per thermal circuit run).*

Parameter	Type	Variable	Lower limit	Upper limit	Rationale of range
<b>1<sup>st</sup> Simulation (geometric, material and ambient properties)</b>					
Thermal conductivity of insulation	Material property	$k_{insulation}$	0.02	10	Stationary air and aerogels versus mud/ground
Convection coefficient for ambient conditions	Ambient condition	$h_{ambient}$	5	40	A typical day with still air to a very windy day

Basin width	Geometry	$L_{side}$	6 inch	72 inch	The initial 6 inch x 6 inch receiver area for 1 <sup>st</sup> generation CSES prototype scaled up to 72 inch x 72 inch (3.35 m <sup>2</sup> receiver area, enough to produce ~ 6L of clean water per day)
Bottom insulation thickness	Geometry	$L_{insulation,bottom}$	1 inch	10 inch	1/3 <sup>rd</sup> of current thickness (3 inch) up to 10 inch which is practically reasonable at this scale
Ambient temperature	Ambient condition	$T_{ambient}$	-30 °C	30 °C	Typical ambient conditions in many parts of the world. In particular, the sub-zero temperature regions require viable solar desalination solutions such as CSES
Emissivity of absorber at top	Material property	$\epsilon_{absorber}$	0.05	0.5	A very low emissivity as currently used (commercially available but may be hard to find) up to widely available pigments with ~50% emissivity
Emissivity of absorber at bottom (emitting side)	Material property	$\epsilon_{emitter}$	0.3	0.95	A low bottom emissivity (~30%) up to 95% emissivity, for example with oven paint as in current study
<b>2<sup>nd</sup> Simulation: Tuning parameter study</b>					
Heat exchanging effectiveness	Tuning parameter	$f_{superheater}$	0.1	1	Range chosen from 10% to 100%. In case of side loss factor, 10 was chosen as the upper limit with 1 being the current side loss model.
Side loss factor		$side\ loss\ factor$	1	10	
Optical efficiency		$\eta_{optical}$	0.1	1	



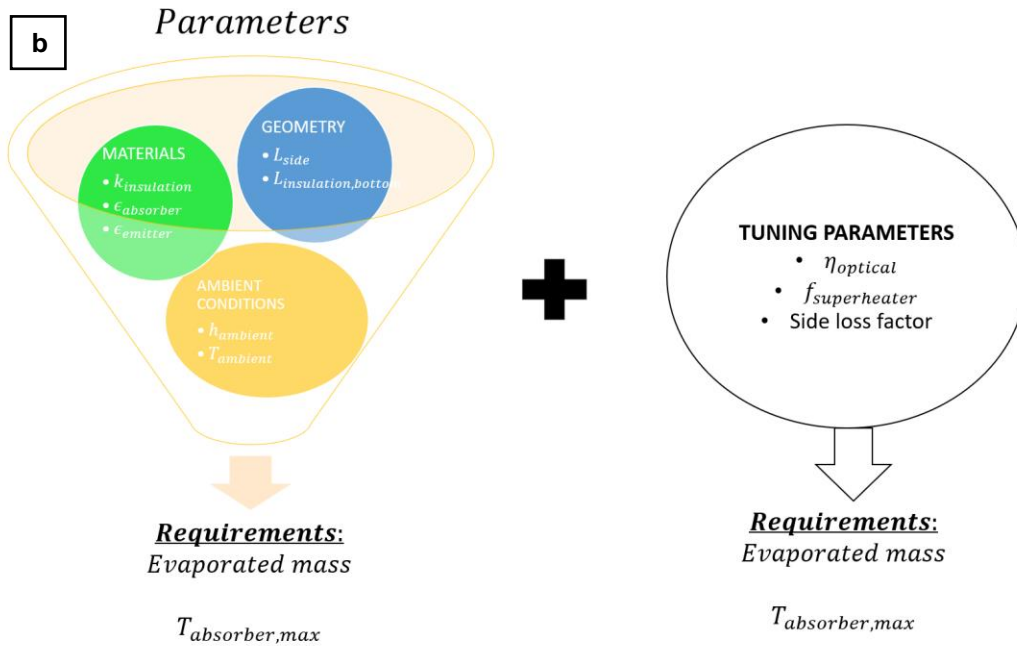
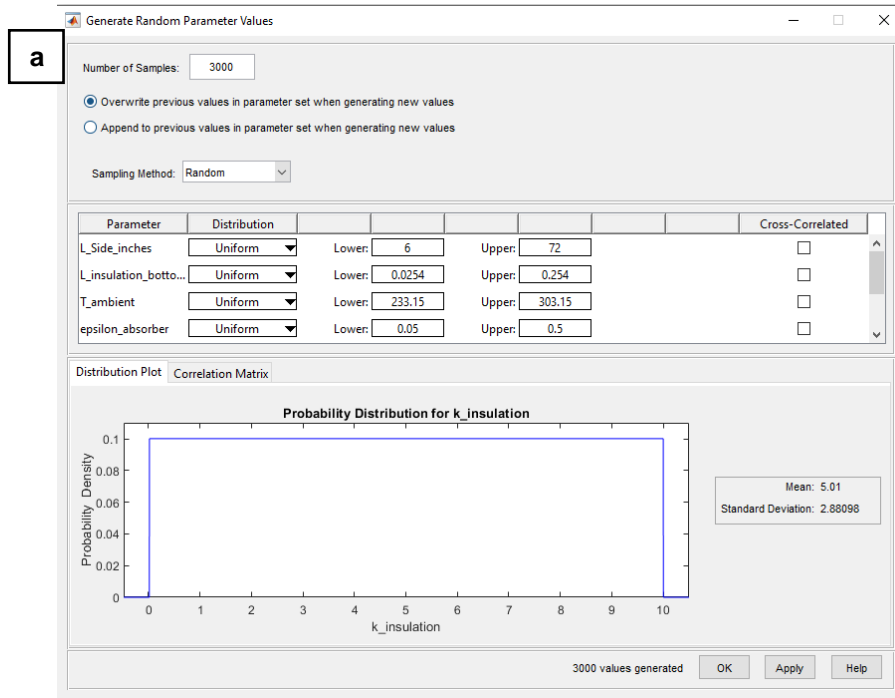


Figure 3-40: 10 Parameters defined in sensitivity analyzer. 7 were run with respect to materials, geometry and ambient conditions parametrized in the model; and 3 were run for the parameter. (a) 3000 random samples were generated to observe effects on (b) two requirements.

## 4 Results & Analysis

### 4.1 Preliminary experimental characterization

Before delving into the experimental results (Section 4.2 and 4.3) and numerical results (Section 4.4), preliminary experimental characterization was conducted to gain confidence into the material properties and parameters fed as inputs the numerical model. The model served as a guide for understanding the physics of the experiment throughout. The preliminary experimental characterization involved the following parameters:  $q_{\text{solar}}$ , optical properties (namely emissivity and absorptivity), and optical efficiency. In addition to the above, nominal evaporation rates for other configurations of CSES were also investigated. This namely involves removing the absorber and glazing, resulting in an open-top configuration.

#### 4.1.1 Optical properties of 6 materials used

The optical reflectivity data for 6 materials used for the CSES is presented. Surprisingly, the good (non-degraded) and bad (degraded) absorber/emitters showed very similar properties (blue, orange, gray and yellow). Likewise, the FEP material of two thicknesses showed similar performance (light blue and green) across the spectrum. Figure 4-1 and Figure 4-2 shows these results in log-scale. The findings demonstrate the optical resilience of FEP and the SSA used in prototyping throughout all 41 experiments.

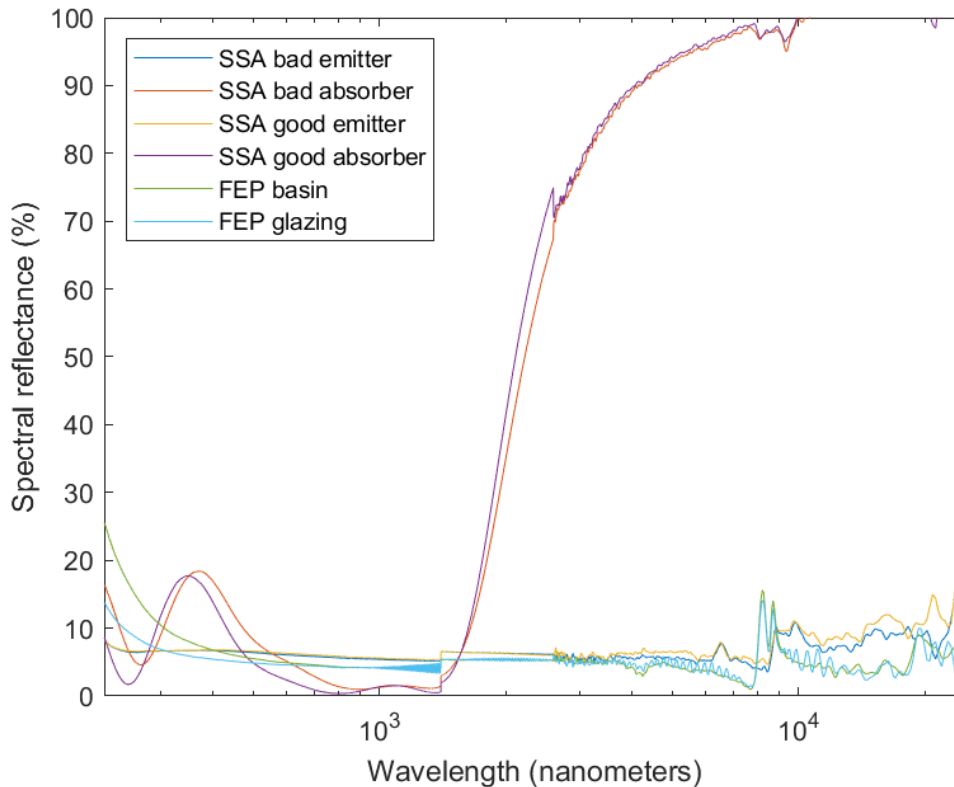


Figure 4-1: Spectral reflectivity data for 6 used materials.

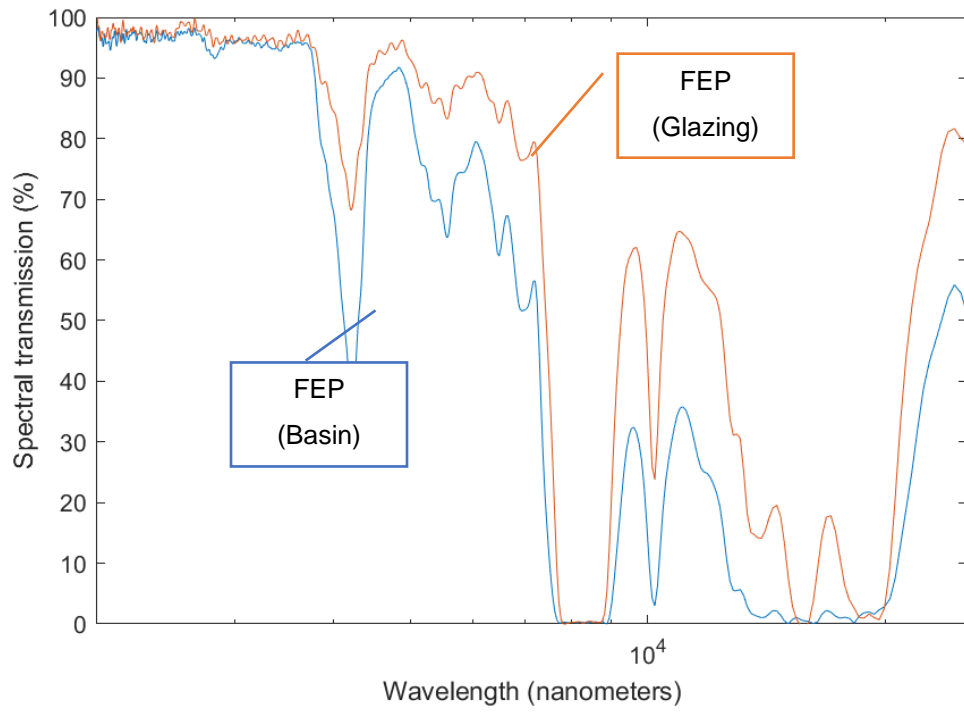


Figure 4-2: Spectral transmission data for FEP (used in two thicknesses for both basin and glazing).

#### 4.1.2 Optical efficiency using reflective sidewalls

The results from the optical efficiency show a solar heat flux of  $\sim 1180 \text{ W/m}^2$  with FEP glazing off and  $1152 \text{ W/m}^2$  with FEP glazing on (average of 5 readings taken from the graph). This illustrates low optical losses at the center. Interestingly, the optical efficiency is  $\sim 107\%$  (considering both FEP glazing blocks) for both the side and diagonal edge flux readings. For the side flux readings, the average reading with FEP glazing off was  $849 \text{ W/m}^2$  whereas it was  $877$  for FEP glazing on. This equates to an optical efficiency of  $107\%$  as previously mentioned. Both the side and diagonal edges exhibit a gain with the FEP glazing on, due to reflective walls, whose reflectivity may be  $\sim 90\%$ . For the diagonal edge reading, an optical efficiency of  $\sim 107\%$  was also found based on an average side flux of  $637 \text{ W/m}^2$  with FEP off and  $659$  with FEP on.

All the aforementioned optical efficiency values were squared. For example, the actual side and diagonal optical efficiency were  $\sim 103\%$ , and  $0.103^2 \sim 107\%$ . Despite these high values, there is little confidence in the setup, and thus these abnormally high optical efficiency values will not be considered for the present study, with a more rigorous revision needed to experimental setup needed to confirm these values.

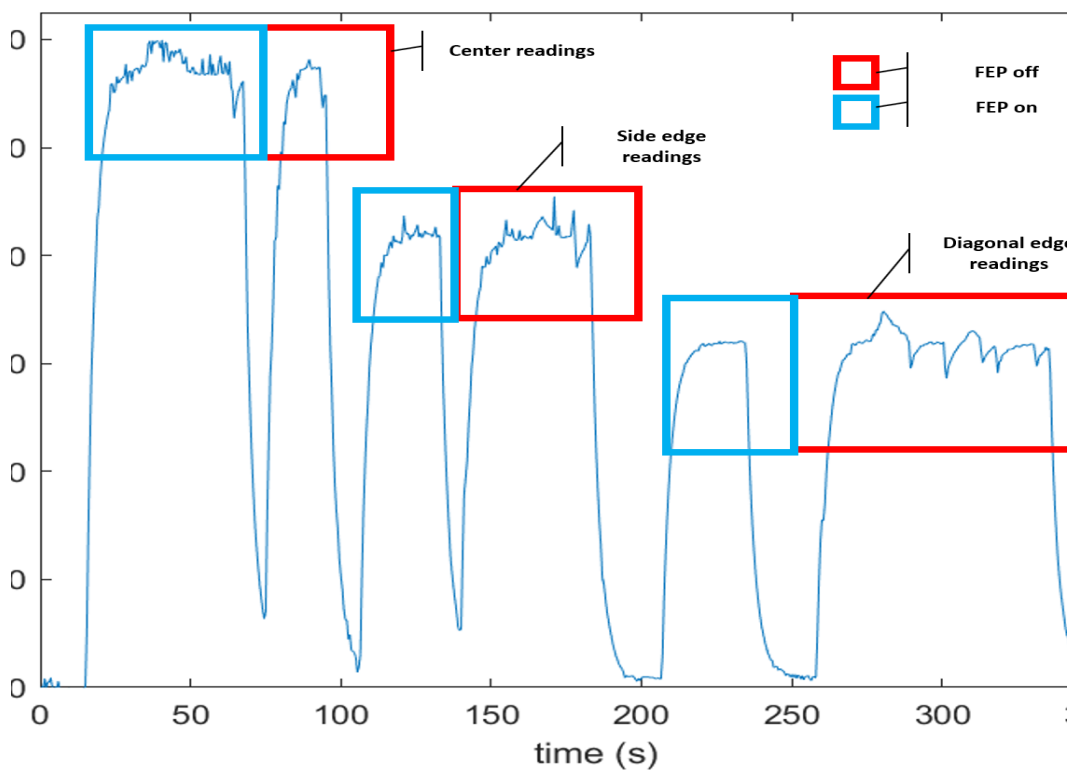


Figure 4-3: Pyranometer flux readings for optical efficiency test.

#### 4.1.3 Flux mapping

ROI-based image processing was conducted in MATLAB using the Image Processing Toolbox to find the average irradiance ( $q_{solar,average}$ ) over the 18 inches by 18 inches region of interest corresponding to CSES aperture. There is mostly a linear relationship between simulator height and irradiance, with the range of simulator height (6 inches -13.5 inches) corresponding to  $\sim 0.75$  to  $\sim 1.4$  suns. This is the mean value over the 18 inches x 18 inches CSES aperture. Four lines are displayed, in order of higher flux: point-measurement reading (pyranometer), center reading (taken as the  $q_{solar}$  input for model), corner reading and average over target plane (the 24 inch x 24 inch Lambertian target).

The center and corner readings were taken as potential x-y displacement of CSES with regards to the true center of irradiation from the solar simulator. This was taken into account in the error calculation with regards to  $q_{solar}$ , and consequently, the efficiency calculations. To this end, three points are shown in the plot: minimum efficiency point, center efficiency point, maximum efficiency point. The center value was taken to calculate solar-to-thermal efficiency which, according to Equation 2-46, displays an inverse relationship with the input flux. Thus, an error estimation as to this crucial input for efficiency calculation is needed. There is also a z- component to the displacement, which results from the simulator height, which was adjusted throughout the 41 experiments. This height was estimated to be within  $\pm 0.25$  inches due to human error in simulator setup and alignment. Figure 4-5 illustrates this x-y-z spatial error, whereby it is apparent that the x-y plane (i.e. target plane) is not at true center. Thus, with regards to CSES deviation from true center, three spatial coordinates were taken into consideration for a potential compound error.

The true solar-to-thermal efficiency is most likely higher than the reported values in the present study. This is because the center reading taken was from the center of the target plane, whereby the corner reading is lower. Taking the lower corner flux would result in a proportionally higher solar-to-thermal efficiency. As a representative example of Experiment 40 (discussed in detail in sub-section 4.3.1) and its three possible solar-to-thermal efficiency values, the following Figure 4-4 is given. In order to calculate the minimum and maximum flux points. For the irradiance upon adjusting simulator height, the center and corner values were interpolated in between for the solar simulator heights outside of the 6 data points collected for solar simulator heights (6", 7.5", 9", 10.5", 12" and 13.5"). Some of the experiments utilized solar simulator heights in between these values. For example, Experiment 29 was run under a solar simulator height of 13", but the nearest data point is 13.5". Without resorting to correlations, the very useful 'interp1()' function was used in MATLAB to interpolate between these 6 data points for an accurate point accounting for the  $\pm 0.25$  inch of the y- error. The efficiency point calculations are plotted in Table 4-1.

It is shown that for Experiment 40, while 19.97% was taken as the solar-to-thermal efficiency, based on the compound error from x-y plane (CSES alignment at true center) and y-plane (simulator height), the true solar-to-thermal efficiency may be at a lower limit of 19.54% when considering the higher flux, and 22.61% when considering the lower flux.

Table 4-1: Three potential solar-to-thermal efficiency based on irradiance point taken: maximum efficiency point, center efficiency point and minimum efficiency point (Experiment 40).

	<b>Irradiance at point – x-y error (W/m<sup>2</sup>)</b>	<b>Flux difference from simulator height – y error (%)</b>	<b>Irradiance (W/m<sup>2</sup>)</b>	<b>Evaporation rate from Experiment 40 (g/hr) / Maximum evaporation rate (g/hr)</b>	<b>Solar-to-thermal efficiency (%)</b>
<b>Maximum efficiency point</b>	879	~ -2%	867.33	65.37 / 287.17	22.61%
<b>Center efficiency point</b>	982	0	982	65.37/ 327.36	19.97%
<b>Minimum efficiency point</b>	982	~ +2.2%	1003.66	65.37/ 341.89	19.54%

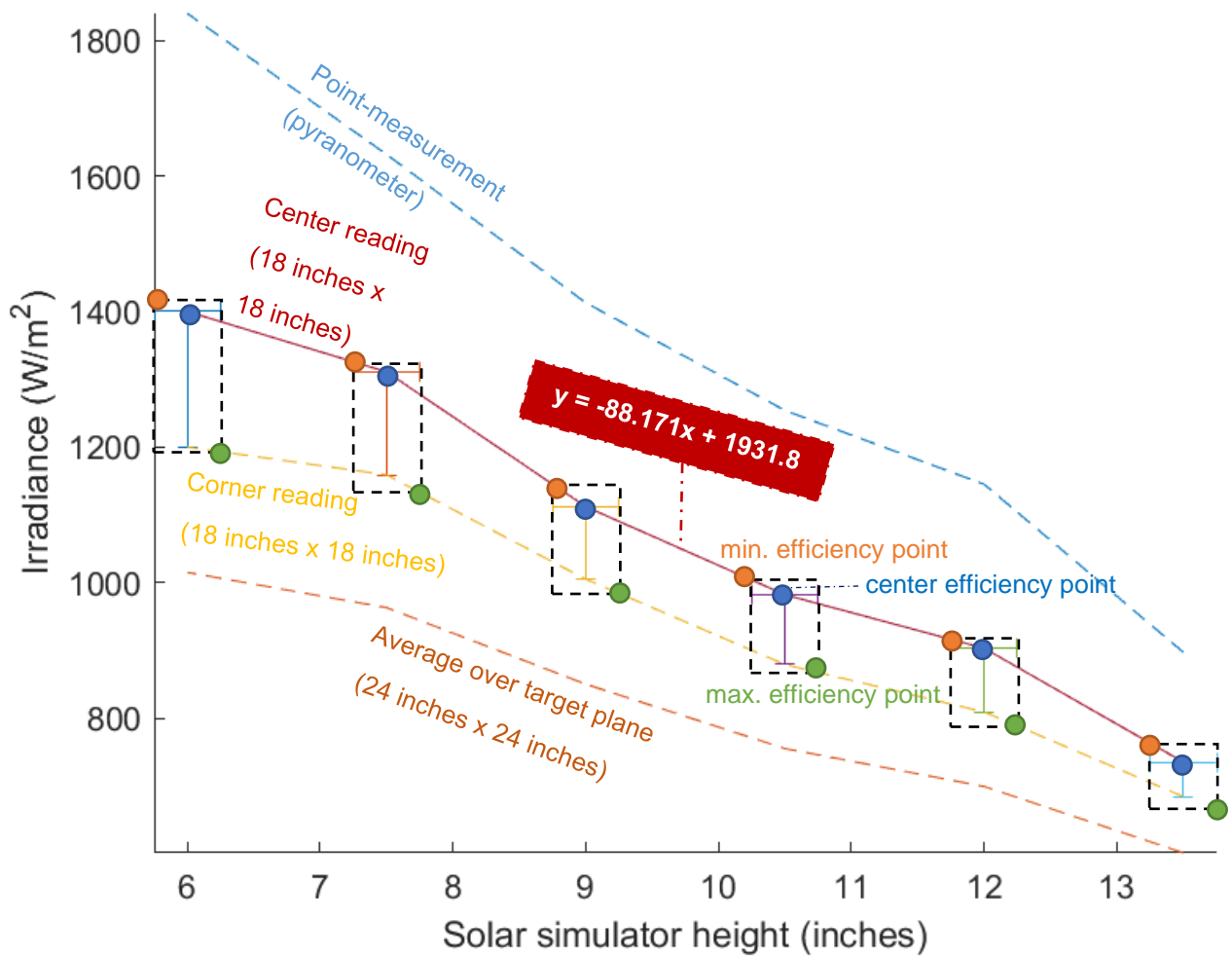


Figure 4-4: Irradiance from: point-measurement, center, corner and over plane. Plotted as a function of solar simulator height (inches) with correlation given. Minimum, maximum and center efficiency points are shown, with center efficiency taken for the present study.

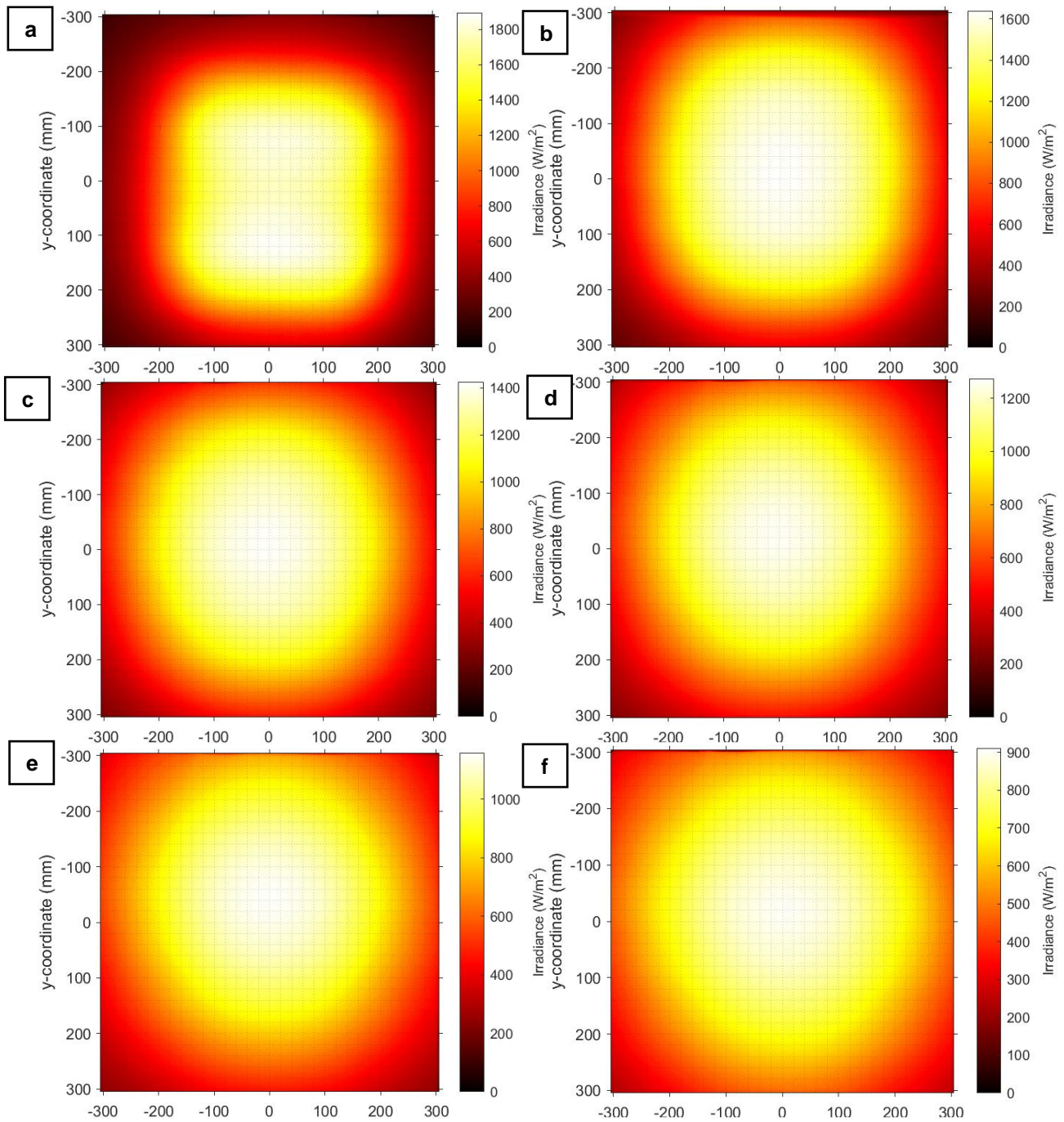


Figure 4-5: Average solar heat flux mapped over CSES aperture. Simulator height and corresponding average solar flux at center: (a) 6 inches – 1390 W/m<sup>2</sup>, (b) 7.5 inches – 1311 W/m<sup>2</sup>, (c) 9 inches – 1112 W/m<sup>2</sup>, (d) 10.5 inches – 982 W/m<sup>2</sup>, (e) 12 inches – 903 W/m<sup>2</sup>, and (f) 13.5 inches – 735 W/m<sup>2</sup>.



#### 4.1.4 Evaporation rates for conventional solar stills

Six configurations of CSES were tested for evaporation rates. The mode of mass transfer for each configuration are of particular interest to evaporation. Interestingly, the open-top design with hydrophilic layer achieved relatively high evaporation rates of ~75 g/hr under ~0.9 sun (~25% solar-to-thermal efficiency at this irradiance). This design with cloth acted as a solar absorber, as opposed to the repeated experiment without cloth showing ~20% lower evaporation rates (~60 g/hr). While the evaporation rates are impressive, the maximum temperatures of the water/absorber reached only ~ 30 °C. CSES, on the other hand, achieves a very high absorber temperature at the 1 sun range of at least ~120°C, which may be useful beyond evaporation, such as for medical sterilization, space heating, cooking, drying or other crucial tasks requiring heat. Moreover, condensation collection methods for conventional solar stills require inclined plastic sheets or glass to gravity feed condensed droplets to a collection unit. This glazing and collection unit will accompany optical losses reducing overall solar-to-thermal efficiency.

Furthermore, while the open-top designs have decent evaporation rates, fouling is an inherent problem lowering the absorptivity of the absorber (be it water or cloth). Moreover, the low efficiency of CSES illustrates the room for boosting efficiencies of this novel solar still configuration, which may be boosted to ~40% under 1.5 suns, especially with designs beyond ~20% solar-to-thermal efficiency (achieved for CSES in its 2<sup>nd</sup> generation).

The 1.5 sun range is very important for CSES, as will be shown in Section 4.3, because steam temperatures achieved with a heat exchanging effectiveness of ~60% was ~135 °C, which is beyond the minimum for the recommended temperatures for medical steam sterilization [3]. Results of the mass experiments with temperatures recorded are displayed in Figures Figure 4-6, Figure 4-7 4-12. Table 4-2 illustrates the mass details of the 6 configurations of solar stills run. Figure 4-6 and Figure 4-7 contains the mass and temperature profiles, with Figure 4-8 detailing the evaporation rates for the closed-top configuration left overnight.

*Table 4-2: Evaporation for different configurations of CSES.*

<b>Configuration</b>	<b>Irradiation (1 sun = 1000 W/m<sup>2</sup>)</b>	<b>Mode of Mass Transfer</b>	<b>Steady-state hours tested (hr)</b>	<b>Hourly mass evaporated (g/hr)</b>
Open-top	Simulator off	Convection	6	12.9
Open-top	~0.9 sun	Solar-driven evaporation	3	~60
Open-top and hydrophilic layer	~0.9 sun	Solar-driven evaporation	3	~75
Closed-top and clamped	Simulator off	Diffusion	13.5	0.37

Closed-top, clamped and outlet tube taped	Simulator off	Diffusion	12	0.33
Closed-top and clamped	~1 sun	Infrared-driven evaporation (boiling) and diffusion (sub-boiling)	3	~65

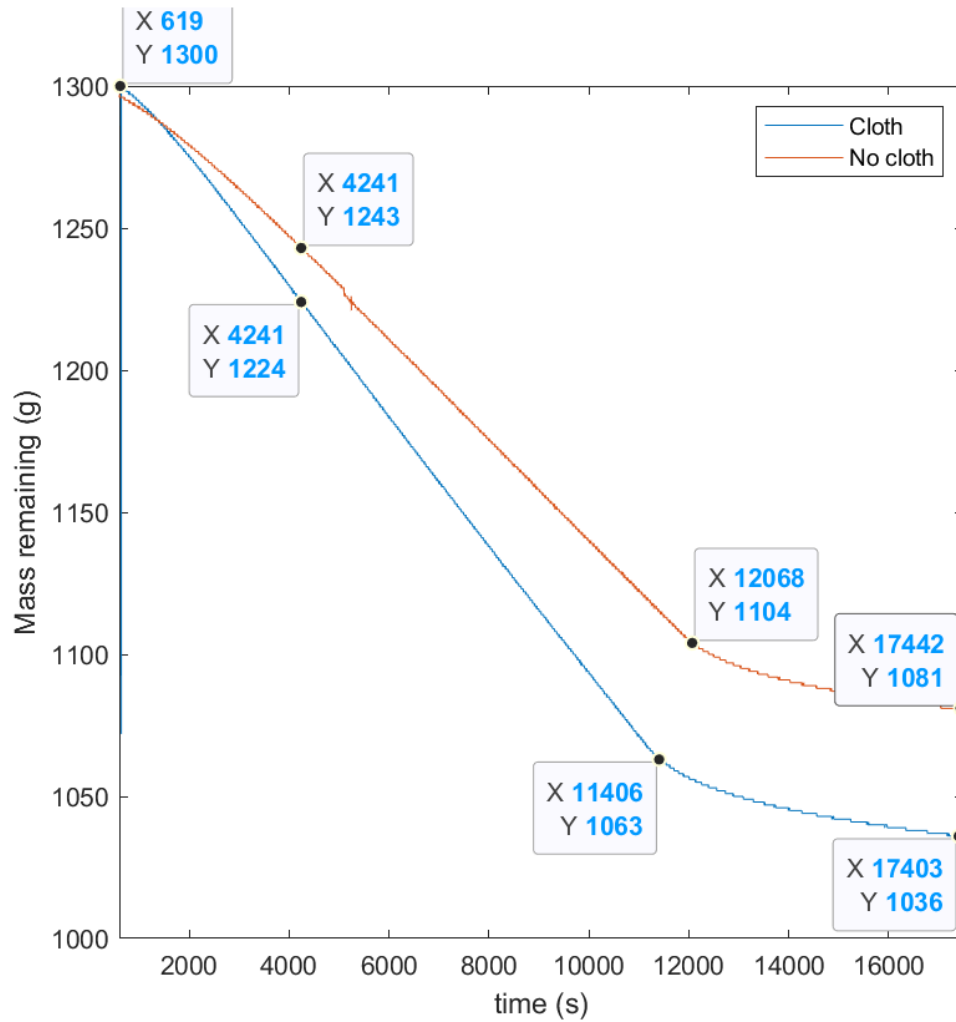


Figure 4-6: Evaporation curves for Experiment 36 (cloth) and Experiment 37 (no cloth).

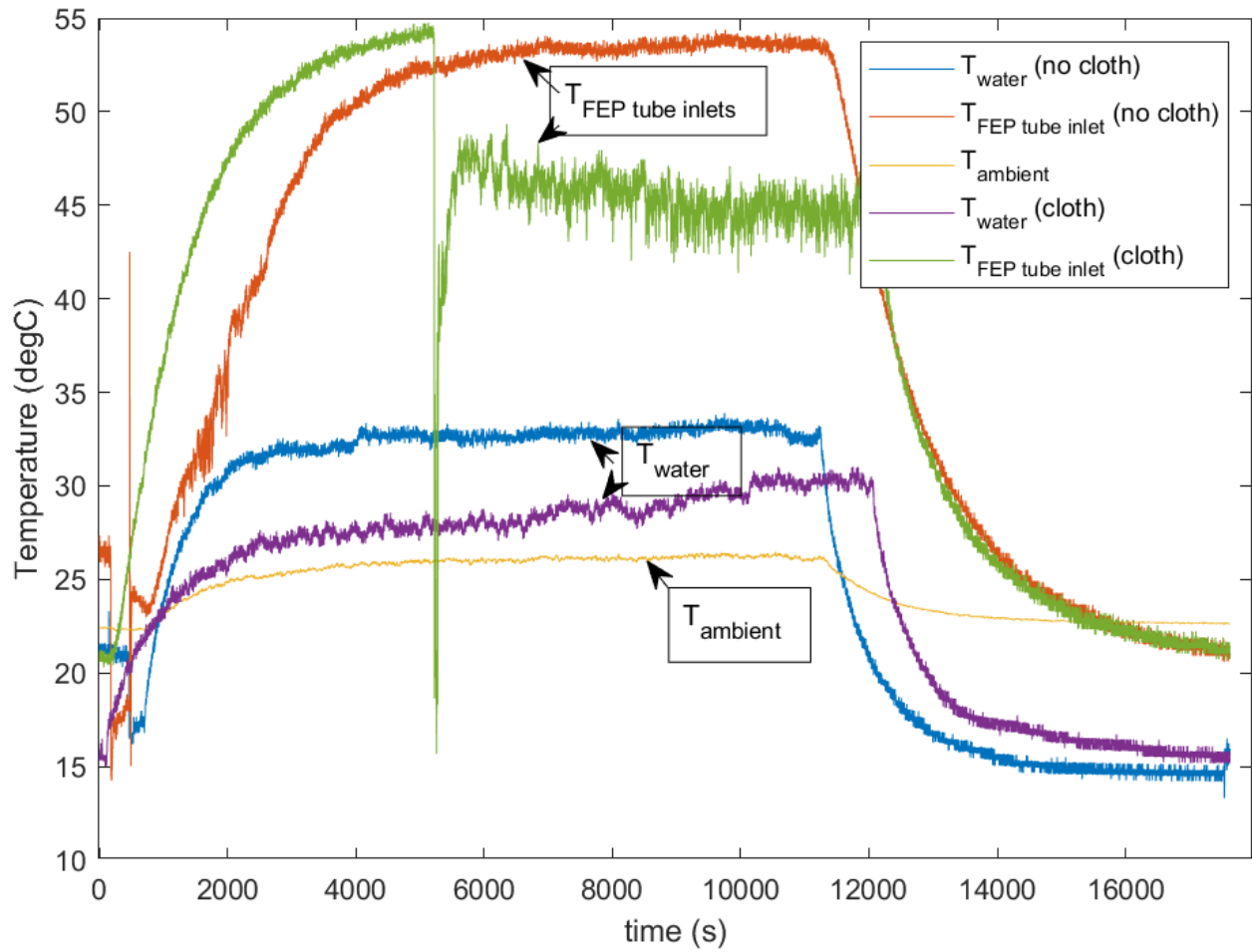


Figure 4-7: Temperature behavior of Experiment 36 (top) using cloth as solar absorber and Experiment 37 (bottom) using the water itself as solar absorber with regards to water, steam tube and ambient temperature.

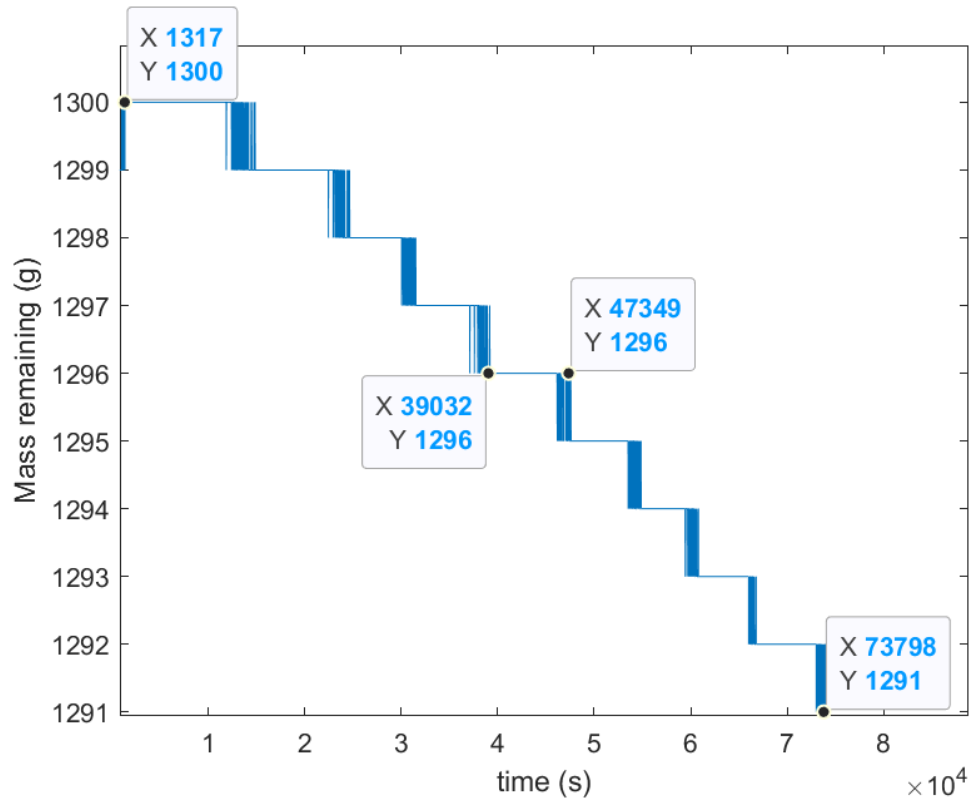


Figure 4-8: Evaporation curve for CSES left for 22 hours with closed top. Only a total of ~ 9 grams evaporated within the 22 hour time period (~0.4 g/hr).

## 4.2 Overview of main experimental performance assessment

Two figures may be used as guides throughout the results section. Figure 4-9 and Figure 4-10 illustrate the two key parameters achieved for all 41 experiments where readings were recorded (save few) for the two chief results of interest: maximum absorber temperature obtained and solar-to-thermal efficiency. The details of the 6 experiments highlighted in order and purpose are detailed:

- I. Experiment 40 represents the keynote results highlighted and used to validate the model. This experiment utilized a hydrophilic cloth which showed equivalent evaporation rates as the experiment without cloth. Using hydrophilic layers such as cloths (widely available) may be of tremendous interest for solar stills, for the practical purposes of reducing water mass (directly reducing heat-up time to boiling steady-state)
- II. Experiment 39 is a repeat of the above experiment without cloth to observe any discrepancies, for which none were found.
- III. Experiment 38 is the equivalent test (with cloth) run using seawater at ~ 35,000 ppm, finding a rise in salinity within after 4 ½ hours of testing. The resulting rise in salinity within the basin was found to be ~40,000 ppm, confirming the hypothesis that there would be no contact between salt and the absorber (i.e. SSA). This experiment was also compared with Experiment 40 to observe any effects of salinity versus tap water during operation.
- IV. Experiment 41 utilized 6 solar simulator heights (6 inches - 13.5 inches), for which the steady-state absorber temperatures and solar-to-thermal efficiencies were recorded.
- V. Experiment 35 represents a test used to investigate the absorber temperature difference from center to diagonal edge (causing a mismatch in modelling when using center absorber temperature value).
- VI. Experiment 28 represents the very successful test with the 4<sup>th</sup> Design iteration reaching ~24% solar-to-thermal efficiency, although under ~1.1 sun. This experiment demonstrated smooth readings, although at a higher solar flux than the 5 aforementioned experiments. Furthermore, this experiment did not utilize a second thermocouple at the absorber diagonal edge. This reading was crucial to ensure the model matches the correct mean temperature of the absorber for validation.

#### 4.2.1 Absorber temperatures (~0.75 to ~1.4 suns)

Throughout 41 experiments, the solar simulator was adjusted from a height of 6 inches to 13.5 inches resulting in an irradiance of between 0.75 and 1.4 suns (700 – 1400 W/m<sup>2</sup>). The maximum absorber temperatures (center reading) at steady-state were recorded for each experiment and summarized in Figure 4-9.

At the upper end are anomalous temperatures of beyond 200 °C, which denotes basin heating in earlier experiments (1 - 5b), reaching abnormally high temperatures higher than 200 °C. This is because the water had leaked in these experiments, leading to the emitter heating the basin instead. The high temperatures achieved with no water illustrate two things. Firstly, a large portion of energy from SSA goes towards heating water, without which the SSA could reach much higher temperatures under ~1.4 suns. This temperature could be useful for a wide range of applications, from cooking to space heating. Secondly, for practical purposes, materials which can resist such high temperatures in the event of basin drying should be implemented. The material used in the present study for basin (FEP), was found to perform well within up to ~160 °C. With a melting point of above 250 °C, this material is recommended to be used to contain water with any insulation material. Such basin flexibility leads to potential usage of this high-temperature plastic for inflatable solar still applications.

The absorber temperatures range from ~105 °C (0.75 sun range) at the lower end to ~ 160 °C (1.4 sun range). Under all 41 experiments, boiling temperatures were reached for the water. This is especially important to ensure high evaporation rates with the boiling state. With this observation, a linear rise in temperature could be found for higher irradiance.

Such temperature ranges are useful for a wide range of applications, and the implication from Figure 4-9 is that certain irradiance levels should be targeted using concentrators. This control over the temperature under ambient sunlight conditions is quite useful for applications requiring such heat. For example, for medical sterilization, the minimum steam temperature requirement of 132 °C suggests that the 1.5 sun irradiance be used. To achieve this, concentrators would definitely be needed.

Within the ~1 sun range (~10.5" solar simulator height) of 1000 W/m<sup>2</sup>, there was a large confidence of absorber temperature values found within ~128 °C. These represent Experiments 26, 38, 39, 40 and 41c. Higher temperatures may be accounted for by the x-y-z error of the irradiance. These irradiance errors have been illustrated with the error bars, with a very small error within the thermocouple temperatures (~1 °C based on a 0.75% accuracy from maximum absorber temperature of 160 °C).

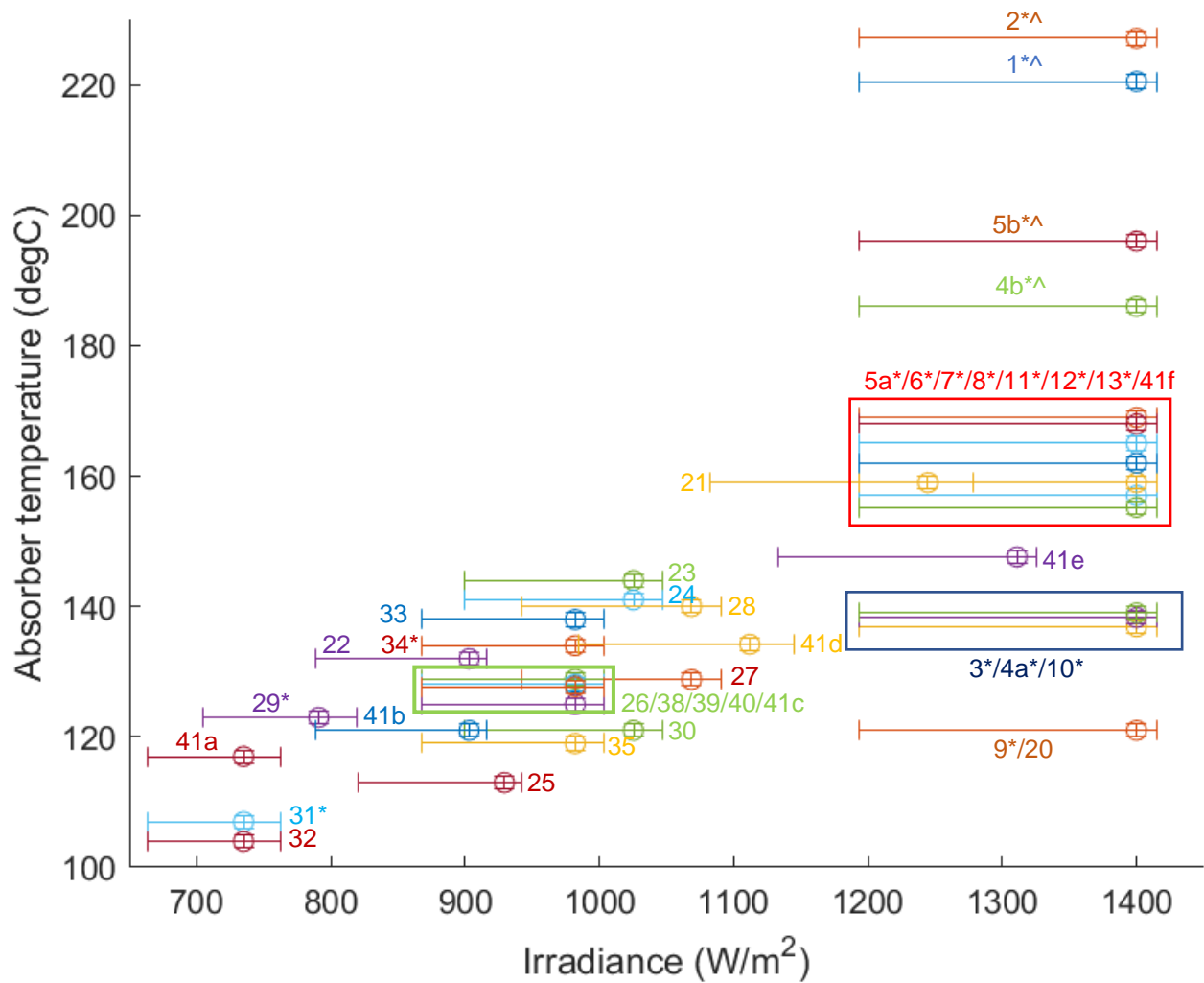


Figure 4-9: Maximum absorber temperature (center reading) achieved between 0.75 – 1.4 suns (38 experiments shown out of 41 experiments conducted). The asterisk (\*) denotes experiments conducted without hydrophilic cloth. The (^) denotes temperatures of absorber after water dries, or leaks in the very early experiments (1-5).

#### 4.2.2 Solar-to-thermal efficiency (~0.75 to ~1.4 suns)

Figure 4-10 displays the solar-to-thermal efficiency summarized for 18 experiments for which a mass balance was used to record the mass differential needed to calculate solar-to-thermal efficiency. These efficiency values were taken at steady-state and does not take heat-up times into account for evaporation rates. The hydrophilic layer used (cloth) was found to have no observable effect on evaporation rates, and therefore solar-to-thermal efficiency. This is useful because using hydrophilic cloths are not only relatively cheap to implement, but also boost performance in terms of practicality and heat-up times. Using a hydrophilic cloth may also reduce spillage of saltwater onto the absorber, leading to fouling and consequently a reduction in SSA performance.

Experiments 26, 34, 35, 38, 39 and 41c all showed similar efficiencies in the 1 sun range of ~18% to ~20% solar-to-thermal efficiency. The plot illustrates the generally linear rise in solar-to-thermal efficiency with rising irradiance. One experiment is the outlier in this trend, namely Experiment 29. This may have been due to the reflective walls along the sidewalls, increasing effective solar flux at that height.

This experiment was conducted with the solar simulator slightly above 1 sun range with the inlet of the top clamper taken as the reference plane instead of the absorber (i.e. ~3 inches higher). When calculating the efficiency for the 1 sun from absorber plane, an irradiance of ~ 775 W/m<sup>2</sup> was used. This perhaps illustrates the effectiveness of the reflective walls along the sidewalls of the CSES aperture leading up to the absorber.

It is interesting to note that the 1.4 sun range and beyond achieve efficiencies of up to 45%. Since achieving even beyond 1 sun is difficult to maintain (especially given the intermittent nature of the solar energy), concentrators are warranted to boost the solar flux to the range of ~1.5 suns and beyond. This would not only ensure that CSES stays within steady-state phase, where boiling (i.e. water at 100 °C) achieves at least triple the evaporation rates of sub-boiling temperatures. It will be shown in the breakeven analysis in sub-section 4.4.1 that the minimum flux to achieve boiling is ~700 W/m<sup>2</sup>, which is confirmed with Experiment 40 (13.5" solar simulator height resulting in ~750 W/m<sup>2</sup>, or 0.75 suns). It is extrapolated that even under 0.7 suns, CSES would have reached boiling state.

This 0.70 sun range is easily achieved during summer seasons, even in Canada. Moreover, high concentration ratios of 5 and above would unlock doors to even lower solar flux (~0.3 suns) to be utilized for high efficiencies in the realm of ~45%.

The large error range for irradiance suggest that the tuning parameters used are justified, given that the input power to the system could be quite off the mark.



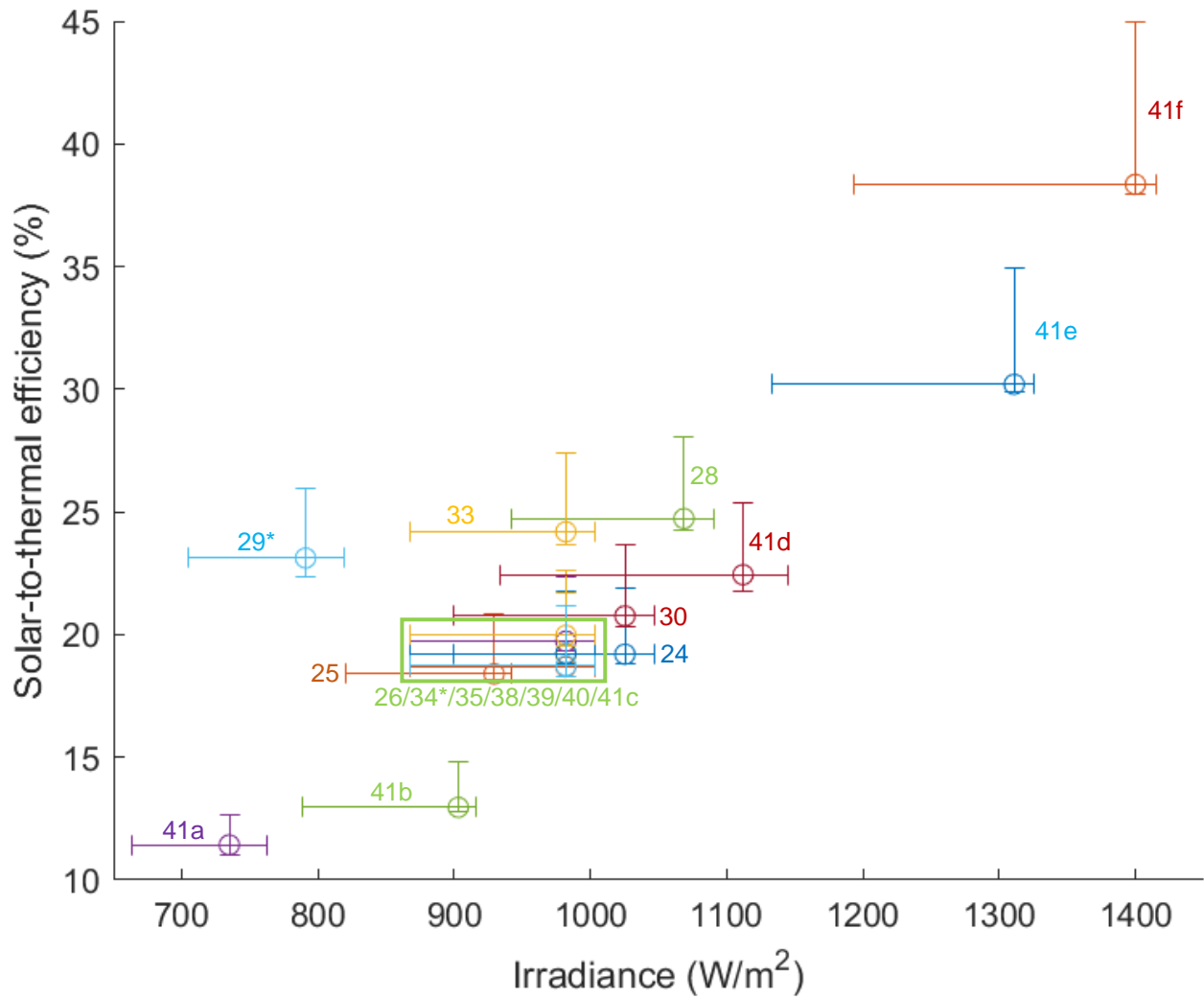


Figure 4-10: Solar-to-thermal efficiency for all experiments from ~0.75 to ~1.4 suns (18 results displayed of 41 experiments conducted). The asterisk (\*) indicates which experiments conducted without the hydrophilic cloth.

### 4.3 Experimental results

Experiment 40 was chosen as the keynote experiment for which the model was validated against. The obtained absorber temperature at steady-state was ~135 °C with a resulting heat exchanging effectiveness (1 of 3 tuning parameters) of 60%. Finally, with the water boiling at 100 °C, the steam temperature was further superheated to ~ 115 °C. It must be noted that the steam thermocouples were found to be much less accurate and consistent compared to the thermocouples for water and absorber.

A sample calculation is given to calculate the solar-to-thermal efficiency for Experiment 40. A resulting efficiency of 19.97% was found from an input solar flux of 982 W as obtained from flux mapping. To calculate this value, Equation 2-46 is invoked and re-arranged to obtain the theoretical maximum evaporation rate.

$$\begin{aligned}\dot{m}_{\text{maximum}} &= \frac{(q_{\text{solar}} \cdot A_{\text{aperture}})}{h_{fg}} = \frac{Q_{\text{solar}}}{h_{fg}} && (\text{Eqn. 4 - 1}) \\ &= \frac{982 \left(\frac{\text{W}}{\text{m}^2}\right) * 0.209 \text{ m}^2}{2,257,000 \left(\frac{\text{J}}{\text{kg}}\right)} = 327.36 \left(\frac{\text{g}}{\text{hr}}\right)\end{aligned}$$

With the theoretical maximum known, we may simply divide the obtained experimental evaporation rate (in grams per hour, g/hr) by this quantity.

$$\eta_{\text{solar,thermal}} = \frac{\dot{m}_{\text{experimental}}}{\dot{m}_{\text{maximum}}} = \frac{65.37 \left(\frac{\text{g}}{\text{hr}}\right)}{327.36 \left(\frac{\text{g}}{\text{hr}}\right)} = 19.97\% \sim 20\% \quad (\text{Eqn. 4 - 2})$$

#### 4.3.1 Experiment 40 (keynote)

Experiment 40 was conducted with a hydrophilic cloth and achieved a solar-to-thermal efficiency of ~20% (Figure 4-11 and Figure 4-12). Interestingly, condensation effects led to periodic oscillations throughout the steady-state period (~2 ½ hours), as showed in the bottom close-up graph in Figure 4-11. The yellow, red and blue transparent rectangles denote heat-up, steady-state and cool-down behavior for the water, absorber (center and diagonal) and steam thermocouples. Moreover, the remaining mass is displayed on the right y-axis. To calculate the mass flow rate, a mass differential (with respect to time) was taken by using two points on the linear slope of the evaporated mass curve. The model was found to match the steady-state temperatures, however, there were discrepancies in pre-steady-state temperatures and cool-down. Moreover, the model was able to match the experimental steady-state for a mean absorber temperature taken to be ~121.5 °C based on experimental findings (Experiment 35) of the absorber temperature being between ~128 °C and ~115 °C at edges. Thus, between this 13 °C range, ~6.5 °C was taken below the maximum absorber temperature at center, or 6.5 °C above the minimum at edges.

The solar-to-thermal efficiency achieved, as calculated above, was 19.97% as calculated in Equation 4-2.

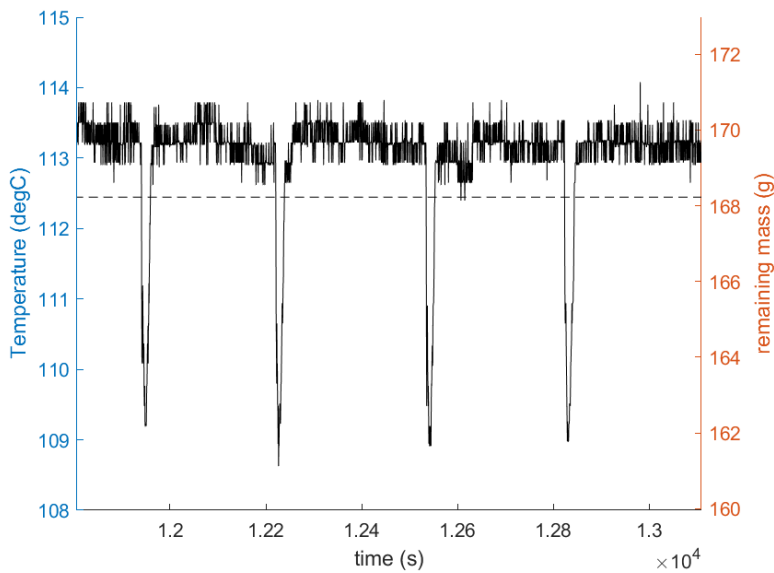
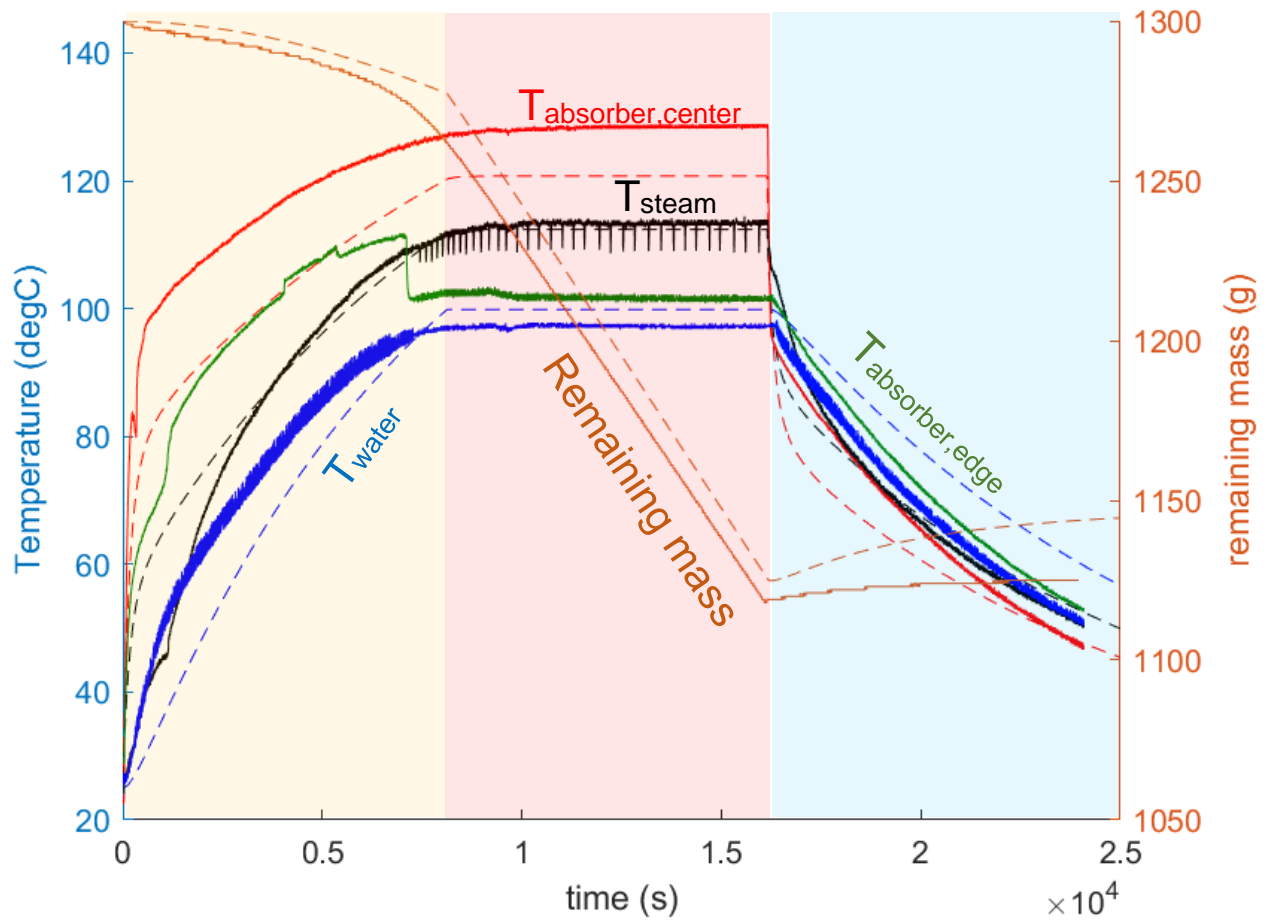


Figure 4-11: Numerical model vs. Experimental results for Experiment 40. Tuning parameters include optical efficiency (64.5%), heat exchanging effectiveness (60%) and side loss factor (3.2) (top) and close-up of steam thermocouple fluctuations due to condensation effects at outlet tube.

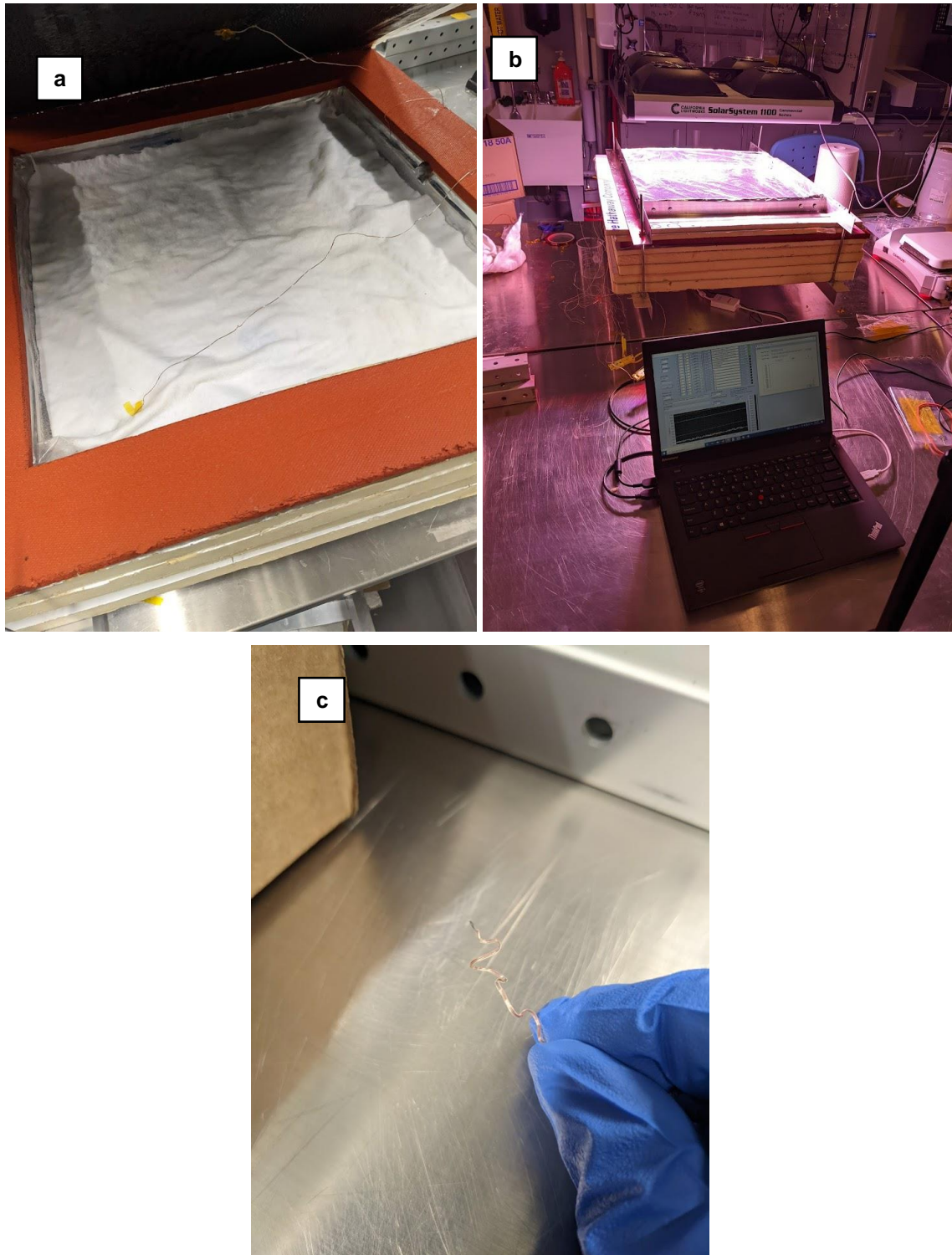


Figure 4-12: Pictures from Experiment 40 with (a) cloth, (b) setup and (c) steam thermocouple slightly bent into a spacer and also used in Experiments 35-41.

#### 4.3.2 Experiment 39 (without cloth)

Experiment 39 was run under normal conditions without a hydrophilic cloth. The comparison between the two are illustrated in sub-subsection 4.3.3. The results are shown in Figure 4-13 with accompanying pictures of setup before experiment in Figure 4-14. Experiment 39 is discussed in more detail in the following subsection, where the results are contrasted to Experiment 40 (with cloth). In this experiment, the absorber thermocouple at the diagonal edge fell into the water around 10,000 seconds in.

The solar-to-thermal efficiency achieved was 18.69%.

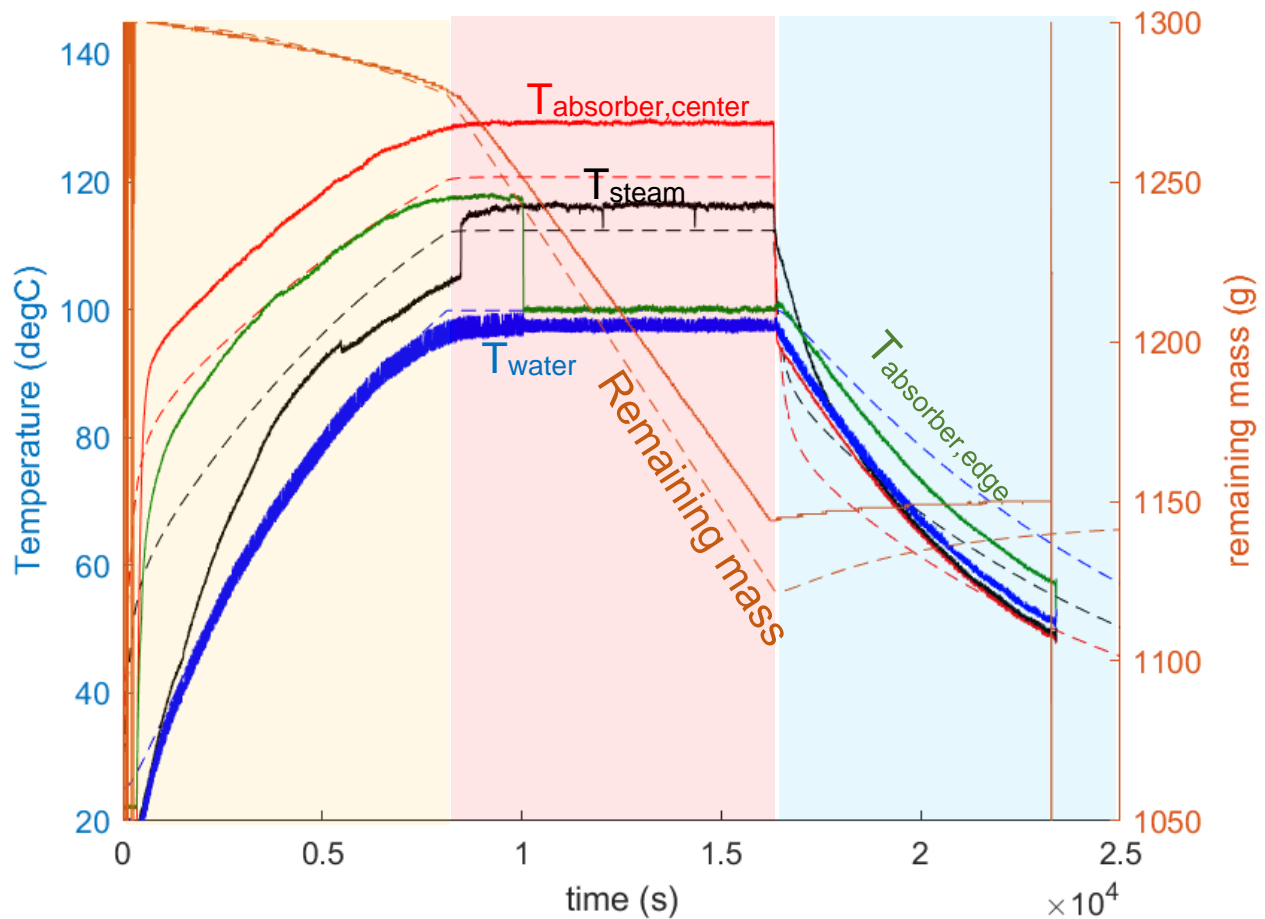


Figure 4-13: Experiment 39 with cloth, with incorrect heat-up temperature.

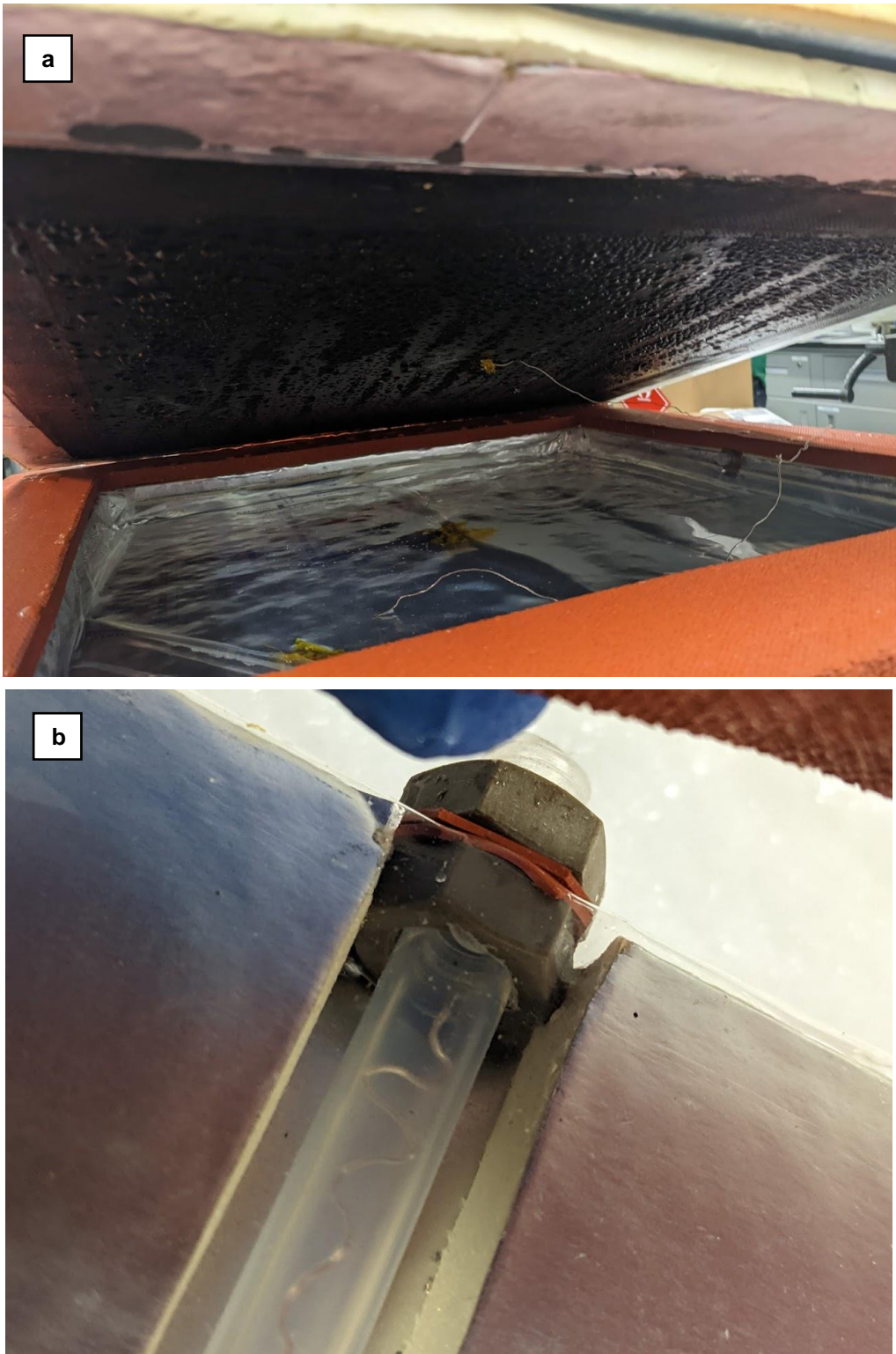


Figure 4-14: Pictures from Experiment 39 with no cloth with (a) SSA lifted showing CSES interior, and (b) steam thermocouple placement (bent into spacer).



#### 4.3.3 Experiment 39 (without cloth) vs. 40 (cloth)

From the comparison of Experiment 39 and 40, no observable difference was found in using the cloth, apart from a slightly delayed heat-up time for Experiment 39. Furthermore, the pre-steady state evaporation rates for Experiment 40 (with cloth) were found to be much higher, which at boiling point matched the evaporation rates without cloth. The water in Experiment 39 (without cloth) had a slower heat-up time by ~2,000 seconds compared to Experiment 40 (cloth). Moreover, Experiment 40 demonstrates higher evaporated mass after the 4 ½ hour test. The resulting difference between the two experiments in mass evaporated is ~ 25 g. Lastly, the absorber had a slightly slower heat-up time for Experiment 39 as well.

The remaining behavior for steam and absorber diagonal edge thermocouples showed agreement. However, for both tests, the diagonal edge absorber thermocouple had fallen into the water, reading the water temperature on top of the cloth (for Experiment 40), compared to the water thermocouple below the cloth. This slight temperature difference of ~3 °C may be accounted for by the thermal resistance through cloth.

To re-iterate, the solar-to-thermal efficiency for Experiment 39 and 40 are 18.69% and 19.97%, respectively.

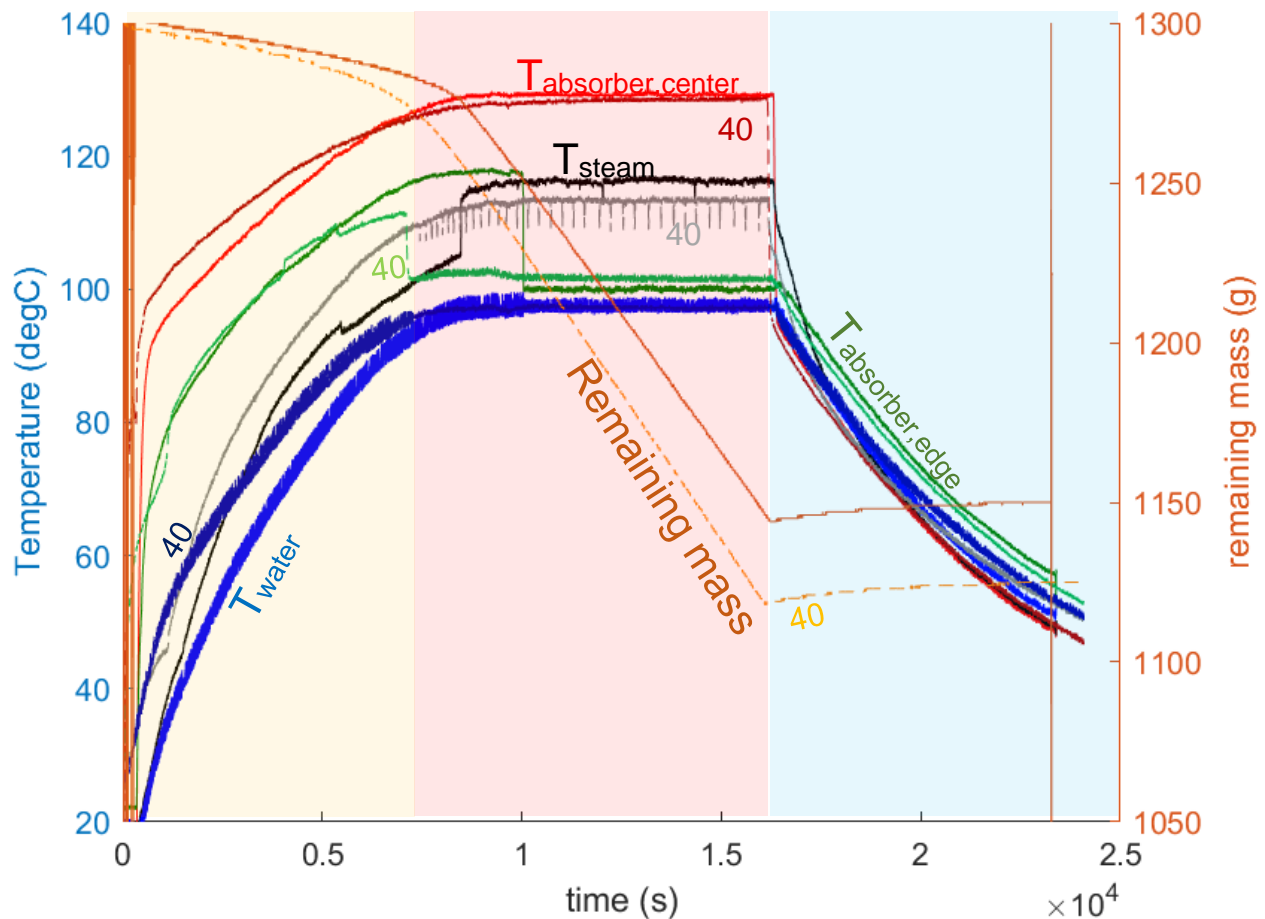


Figure 4-15: Experiment 39 (cloth) vs. Experiment 40 (without cloth).

#### 4.3.4 Experiment 38 (seawater) vs. Experiment 40 (tap water)

Figure -16 shows the results of Experiment 38 contrasted to the numerical model.

Both experiments were conducted with the cloth, with the only difference between tests being the salinity of water (~35,000 ppm for seawater and ~500 ppm for tapwater). Apart from the difference in evaporation rates prior to boiling, Experiment 40 matched the results from Experiment 38 quite closely. However, the discrepancy in heat-up time may be investigated further in order to improve the model accuracy considering salinity properties of water during operation.

It is also important to note that small salt marks were observed on the absorber, which may have been due to splashing of the water inside the enclosure. This denotes strategies (preferably passive) which could avoid splashing from the basin to emitter. Perhaps porous net structures could be used to prevent water from spilling upwards. Apart from the mechanical risk of fouling, the contactless design achieved the ability to completely avoid fouling during operation. The diagonal edge absorber thermocouple for this experiment was the only successful one from all tests outlined in this Section.

The solar-to-thermal efficiency for Experiment 38 (19.24%) closely matches Experiment 40's (19.97%).

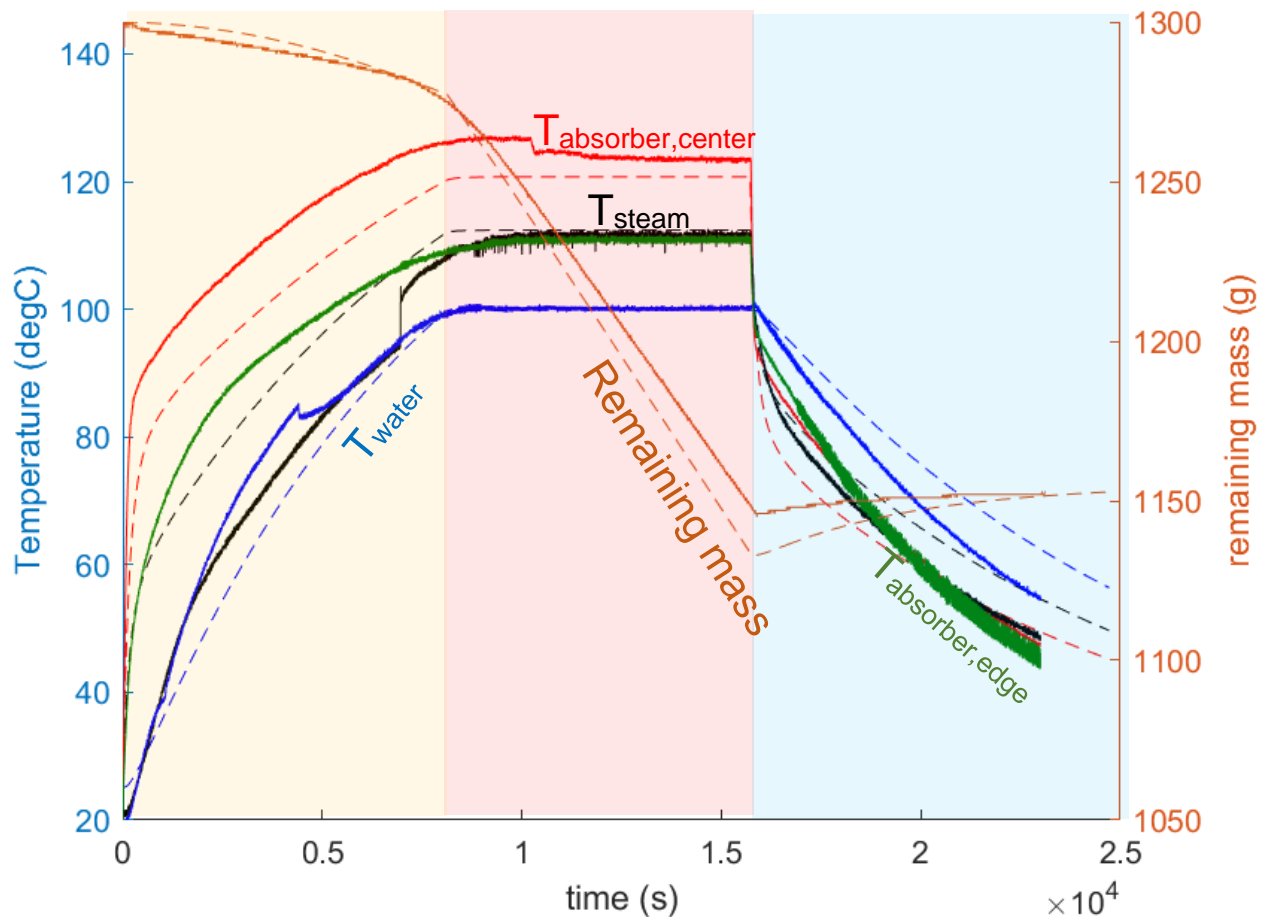


Figure -16: Experiment 38 using simulated seawater (~35,000 ppm).



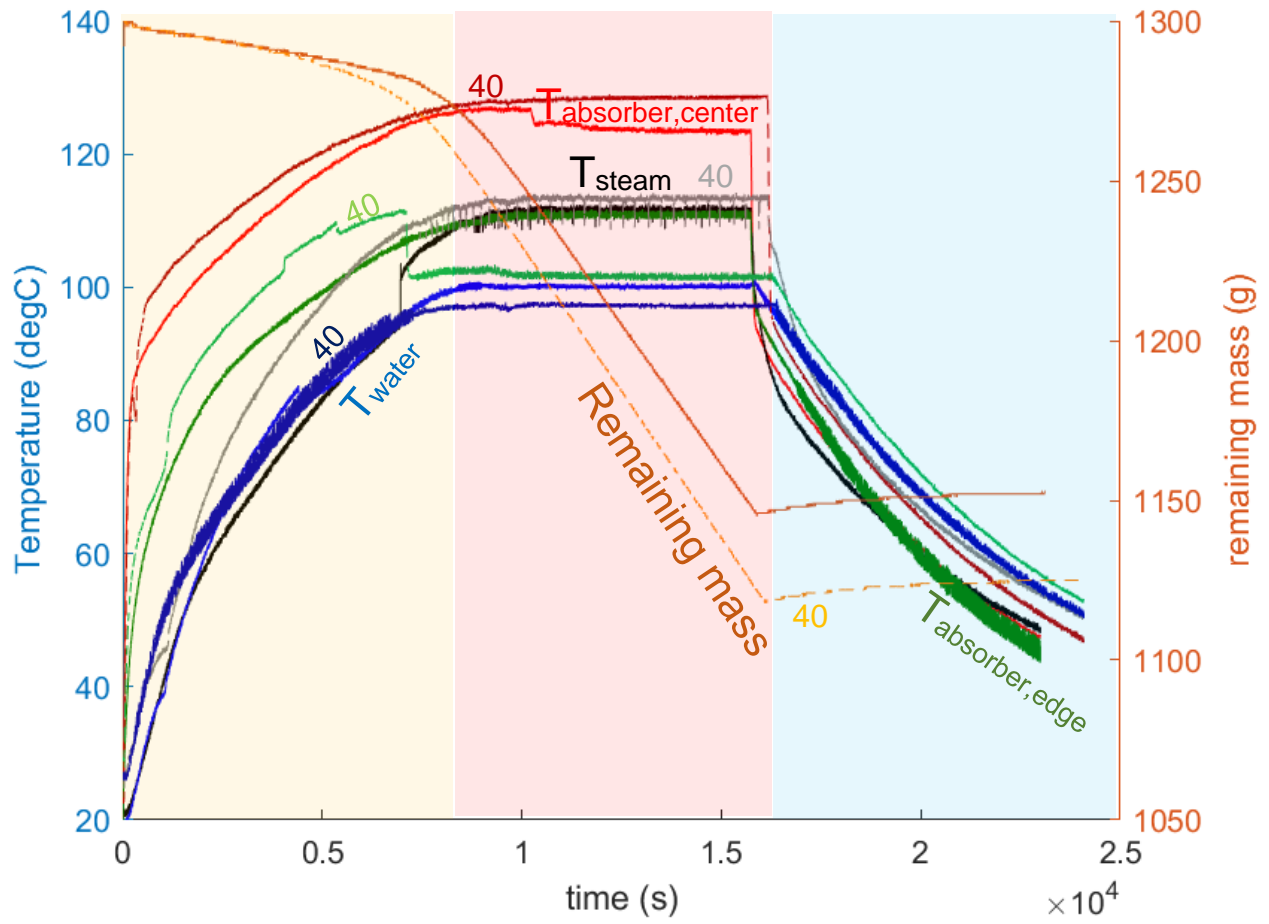


Figure 4-17: Experiment 38 (seawater) vs Experiment 40 (tapwater).

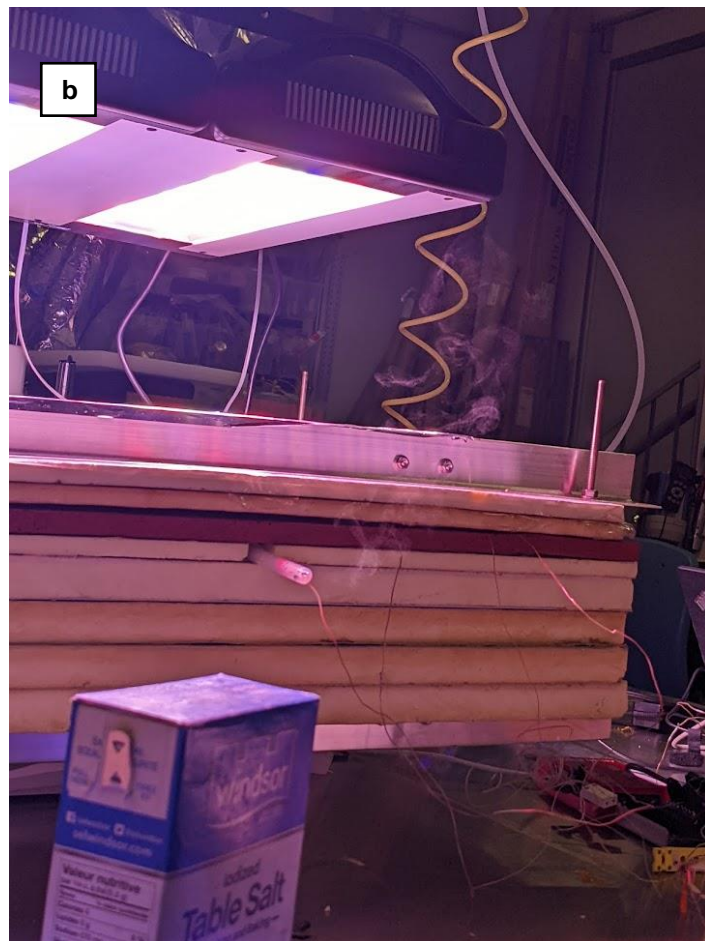


Figure 4-18: Pictures from Experiment 38 conducted with simulated seawater (~35,000 ppm). (a) Saltwater on cloth is shown, with (b) CSES operating and salt used to simulate seawater.

#### 4.3.5 Experiment 41 (Irradiance from ~0.75 Suns to ~1.4 suns)

Figure 4-19 represent the results for Experiment 41, which was run at 6 different irradiance configurations (~0.75 suns to ~1.4 suns). The resulting absorber temperatures and solar-to-thermal efficiencies are also shown in Figure 4-20. Figure 4-21 illustrates the experiment in operation with regards to temperature and mass details at each of the 6 irradiance range. The absorber edge thermocouple fell into the water since the beginning of the experiment, reading the temperature at the top of the hydrophilic cloth while the original water thermocouple read the temperature below the cloth. It should be noted that unlike previous experiments, the initial temperatures were at 50 °C compared to 25 °C in all other experiments mentioned in this Section. Thus, the heat-up times should be taken with caution for the 13.5 inch simulator height (outputting ~ 0.75 suns). The cool-down behavior is still accurate for this Experiment from ~1.4 suns. At the highest irradiance (~1.4 suns), the steam temperatures reached 136 °C, which is a very useful range for purposes of medical steam sterilization. Moreover, the efficiency at this point was upwards of 45%. The overall efficiency range for all experiments was between 11% to 45% (~0.75 suns to ~1.4 suns).

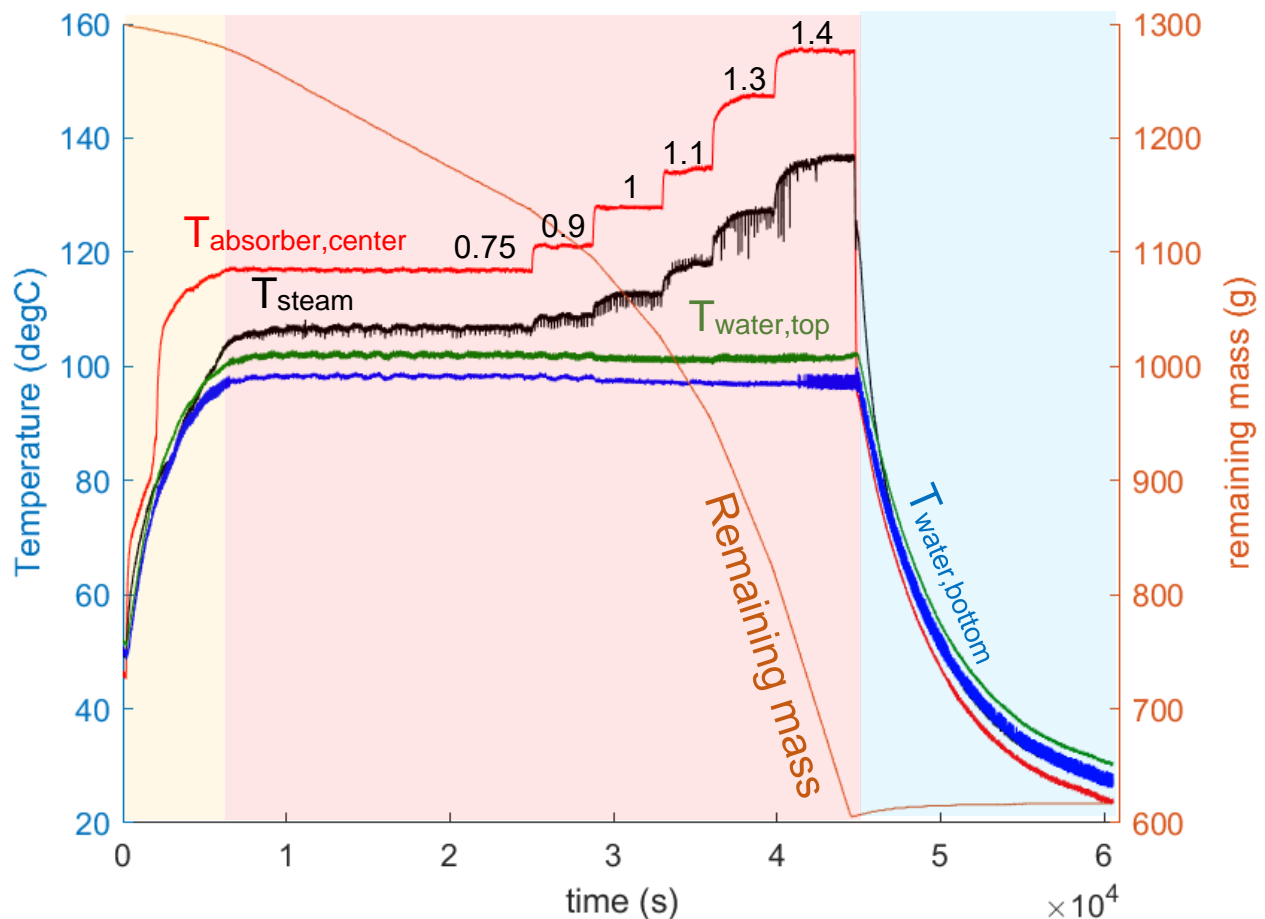


Figure 4-19: Experiment 41 adjusting the solar simulator height from 13.5 inches (~0.75 suns) down to 6 inches (~1.4 suns). The 13.5 inches height was kept for ~ 7 hours. The data labels at top indicate the irradiance (in suns, with 1 sun = 1000 W/m<sup>2</sup>) kept for ~ 1 hour at each steady-state absorber temperature.

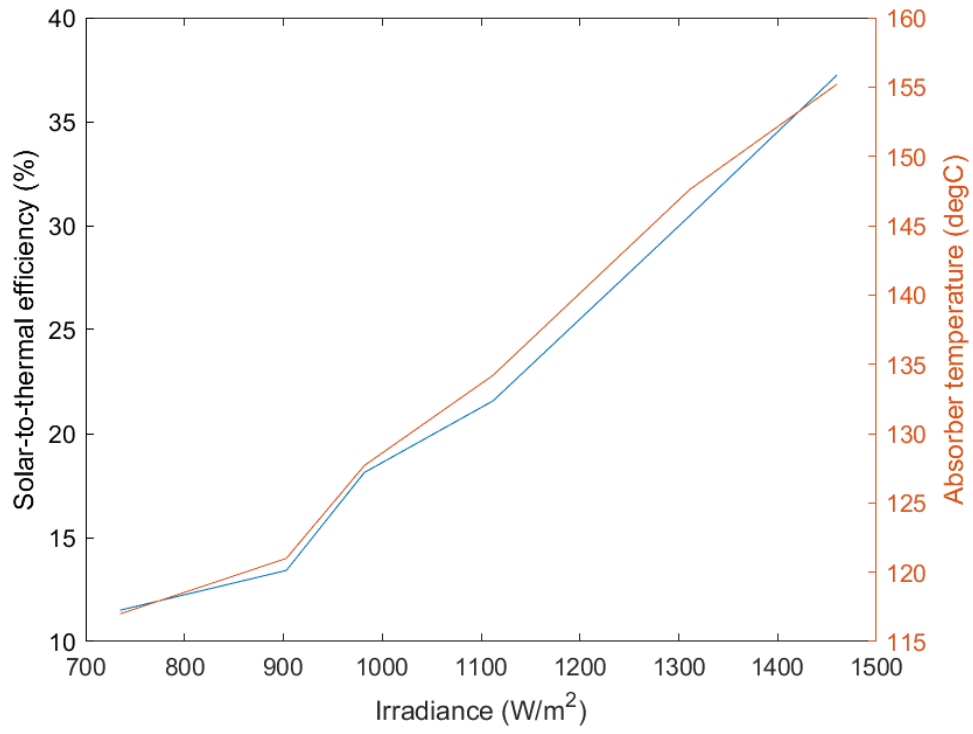


Figure 4-20: Solar-to-thermal efficiency (left y-axis) and absorber temperature (right y-axis) vs. Irradiance for Experiment 41.

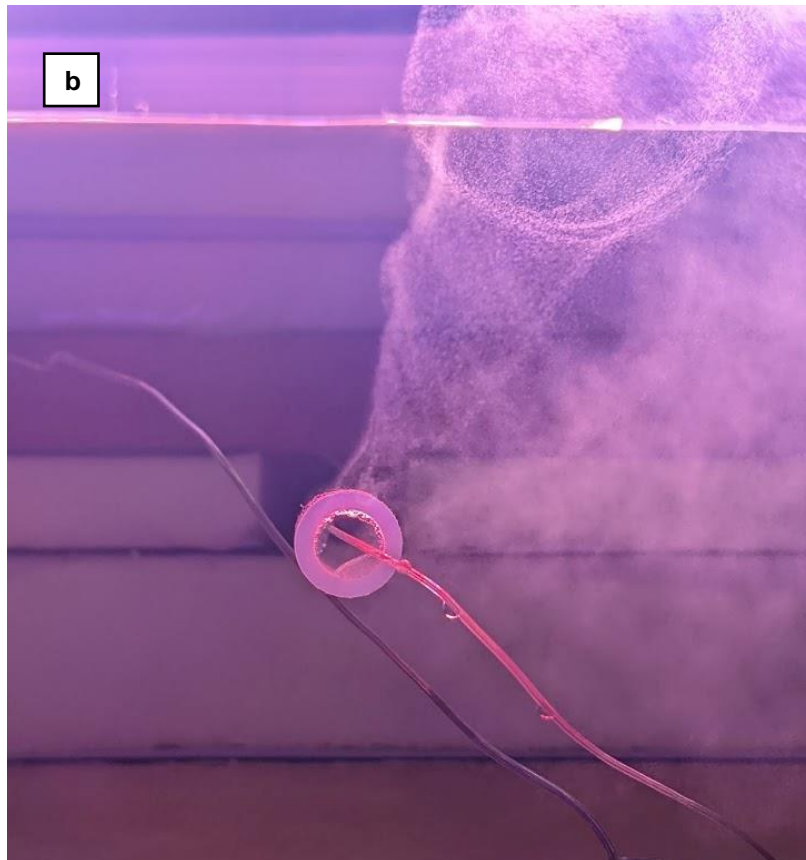


Figure 4-21: (a) Experiment 41 viewed with 6" solar simulator, with (b) close-up of steam outlet tube. Steam is transparent in the visible spectrum, so water is shown in the bottom are tiny condensed water droplets. This experiment under  $\sim 1.4$  suns achieved steam at  $136^{\circ}\text{C}$ .

#### 4.3.6 Experiment 28 (first successful run)

Experiment 28 was the first successful run since the very first experiment (Figure 4-22, with pictures in Figure 4-23). However, this test was run under  $\sim 1.1$  suns ( $1094 \text{ W/m}^2$ ) as compared to  $\sim 1$  sun ( $1012 \text{ W/m}^2$ ) in all other experiments highlighted (Experiment 35 and 38 – 41). Thus, the conditions of Experiment 28 were repeated in Experiment 39 to show, with two thermocouples (center and diagonal edge), that the mean temperature of the model adjusted between the center and diagonal readings, resulted in the model evaporates, temperatures and heat-up times matching.

The 4<sup>th</sup> thermocouple in this study was used to measure the temperature of the FEP outlet tube at the entrance. While it was intended for this thermocouple to read the steam temperature at inlet of tube, it failed to do so. Instead, it displays a different transient behavior than the other curves for absorber (center), water and steam.

The solar-to-thermal efficiency for this experiment was 24.16%.

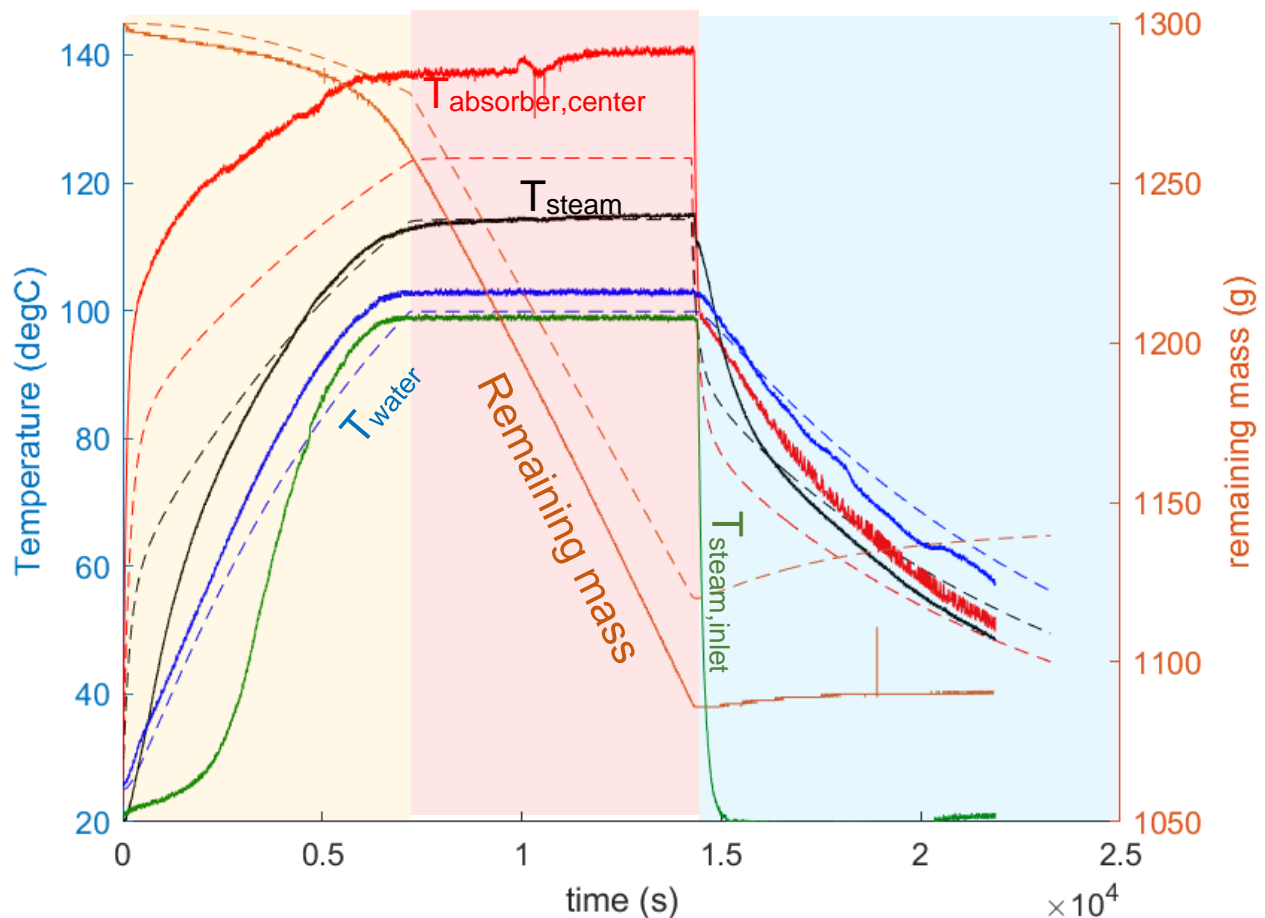


Figure 4-22: Experiment 28 was the first successful test with relatively smooth thermocouple readings, although under  $\sim 1.1$  suns.



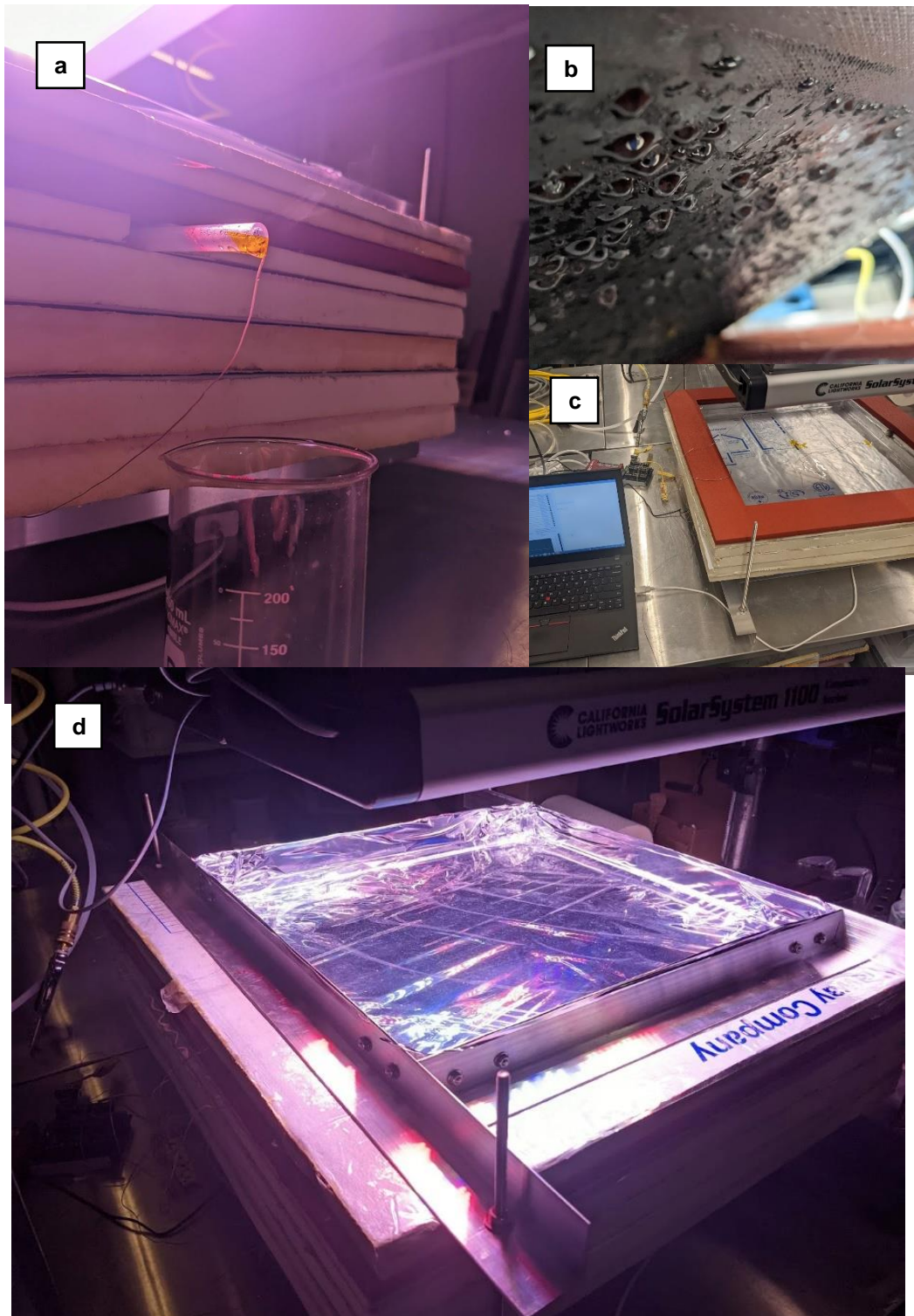


Figure 4-23: (a) Superheated steam ( $\sim 115$  °C) flow out of tube. (b) Condensation on the absorber after test. (c) The setup without the top (open-top). (d) Experiment 28 operating under 1 sun when viewed from standing height.

#### 4.3.7 Experiment 35 (2 thermocouples)

Experiment 35 was conducted to gauge the effects of uneven heating of the SSA (Figure 4-24 and Figure 4-25). The results confirmed the presumptions that the SSA was not isothermal, showing center readings of  $\sim 125\text{ }^{\circ}\text{C}$  and edge readings briefly for  $\sim 115\text{ }^{\circ}\text{C}$ . Shortly at steady-state however, the edge thermocouple fell into the water. Consequently, the thermocouple read the temperatures for water at top of cloth with slight irradiation from emitter (normally water thermocouple is placed taken under cloth).

The solar-to-thermal efficiency for this experiment was 18.13%, exactly matching Experiment 39 (without cloth).

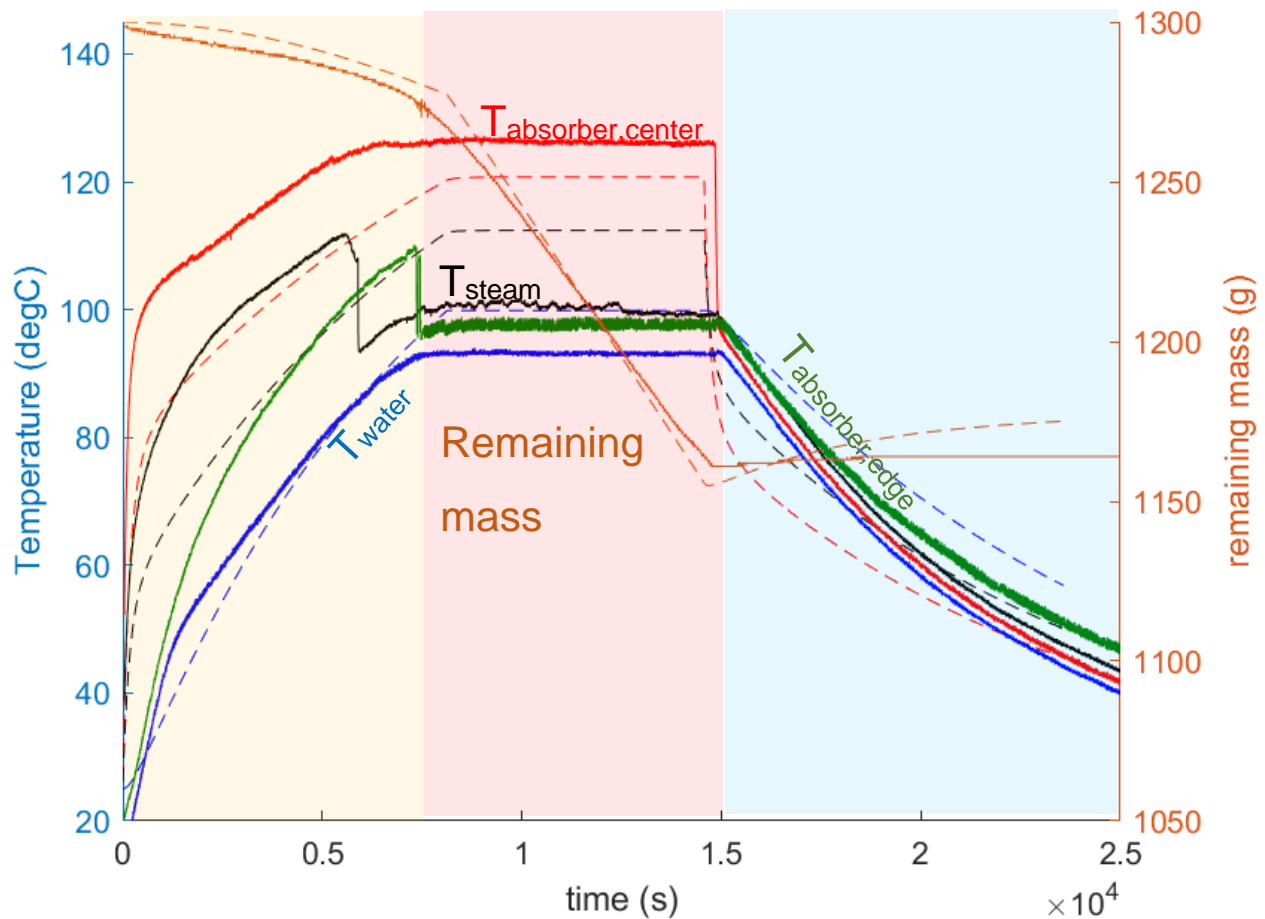


Figure 4-24: Experiment 35 was the first test using 2 absorber thermocouples (center and diagonal edge).



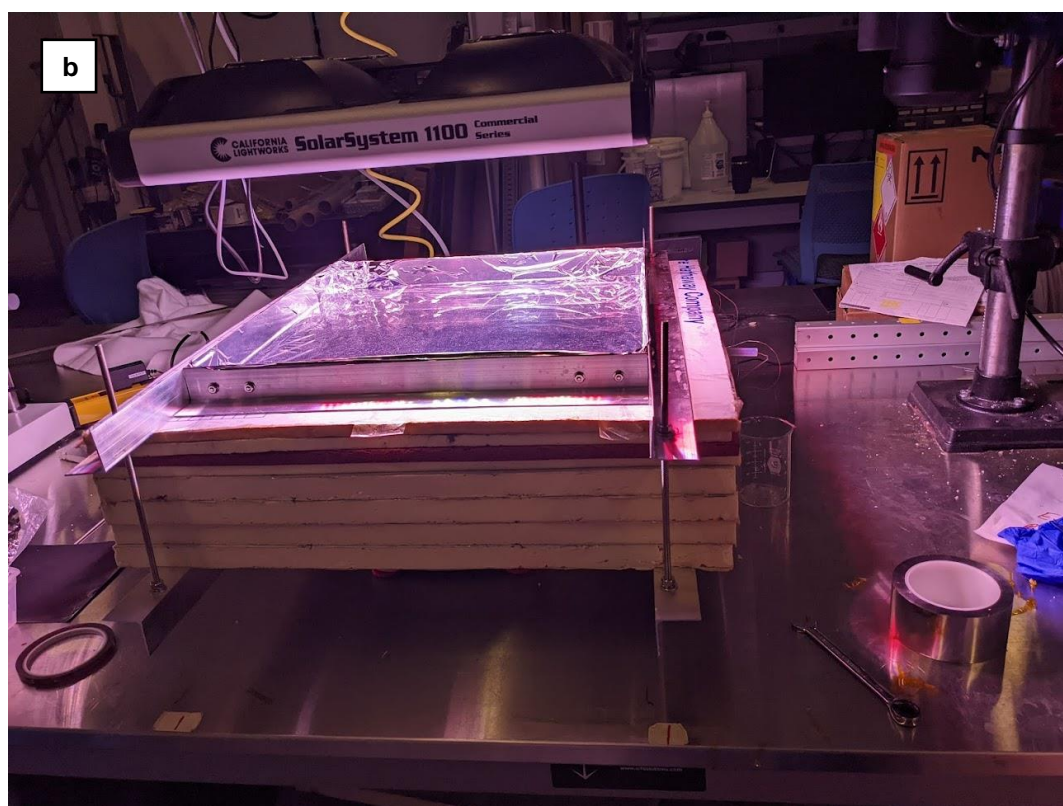
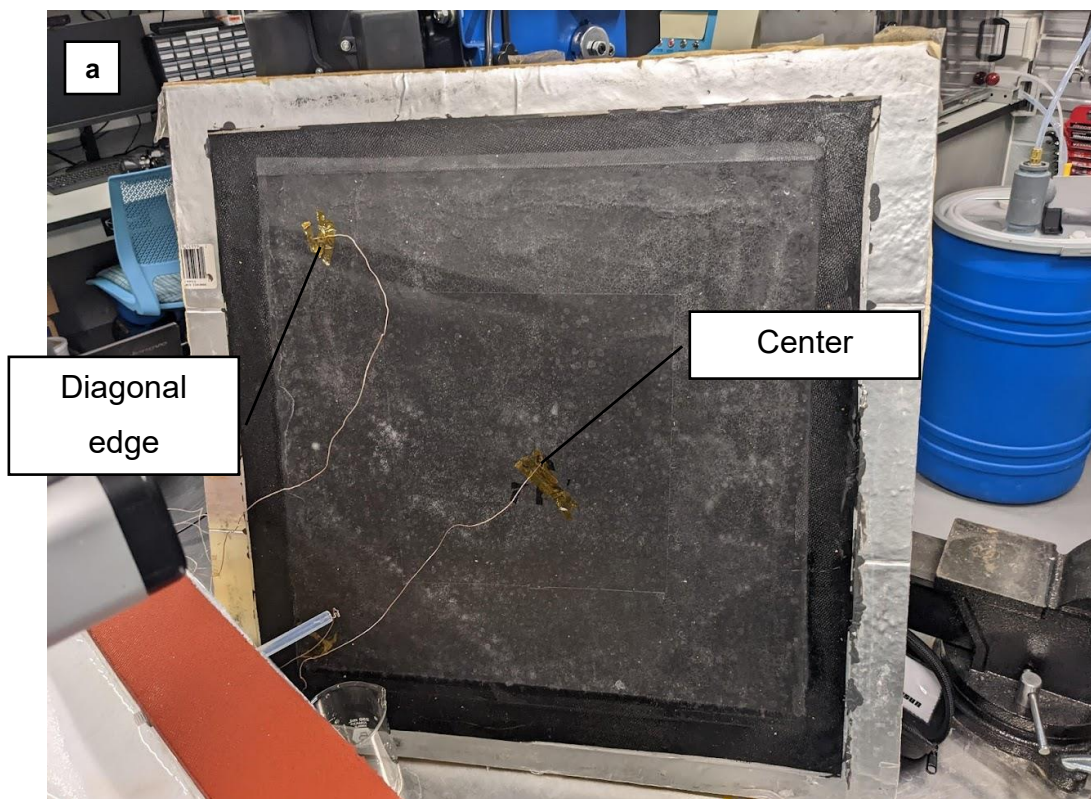


Figure 4-25: Experiment 35 run with (a) extra thermocouple and hydrophilic cloth. (b) Experiment 35 setup.

#### 4.4 Numerical results

The numerical model is quite robust as a quasi-1D transient analysis which can be run iteratively for a wide variety of operating conditions and parameters. The former is discussed in the present section, with the parametrized study conducted as a Sensitivity Analysis in Section 4.8.

Figure 4-26 to Figure 4-31 illustrate the robustness of the numerical model to operate under different irradiance conditions and observing various effects. The first plot (Figure 4-26) illustrates the conditions at minimum breakeven flux of 0.7 suns. The irradiance run for the test ranges from 0.1 suns ( $100 \text{ W/m}^2$ ) to 1.4 suns ( $1400 \text{ W/m}^2$ ) in increments of 0.1 suns ( $100 \text{ W/m}^2$ ). The most important plot is the solar-to-thermal efficiency vs. irradiance, shown in Figure 4-27.

Experimental results from Experiment 41 was used where appropriate as a benchmark for the numerical results. The most important design implication from these results is that the minimum solar irradiance required to reach boiling is  $\sim 0.7$  suns.

The numerical model is useful to model a wide variety of design alternatives in terms of materials, geometry and ambient conditions. The plots in upcoming sub-sections illustrate useful outputs which may be obtained from the model. These include the breakeven flux, at which water would boil, solar-to-thermal efficiency vs. irradiance, heat-up time vs. irradiance as well as vs. water mass, and absorber temperature vs. receiver area.

Moreover, thousands of design iterations could be simulated for the performance metrics (i.e. absorber temperature and evaporation rate) for the parametrized model. To this end, a parameter study was run using 10 key parameters of the model to gauge the sensitivity of the parameters on the aforementioned performance metrics.

#### 4.4.1 Water & absorber temperatures vs. irradiance

These results illustrate the minimum solar flux required to boil water in CSES. This breakeven flux is an important quantity, to be used as a milestone flux to aim for, as evaporation rates within CSES are increased drastically at the boiling state (less than 20 g/hr sub-boiling versus ~65 g/hr under one sun).

The numerical results (solid line) for absorber temperature are slightly below the experimental values (Experiment 41 in dashed lines). The water temperature is not plotted as it has been at boiling point since the breakeven flux (~700 W/m<sup>2</sup>) with the solar simulator at 13.5 inches was achieved.

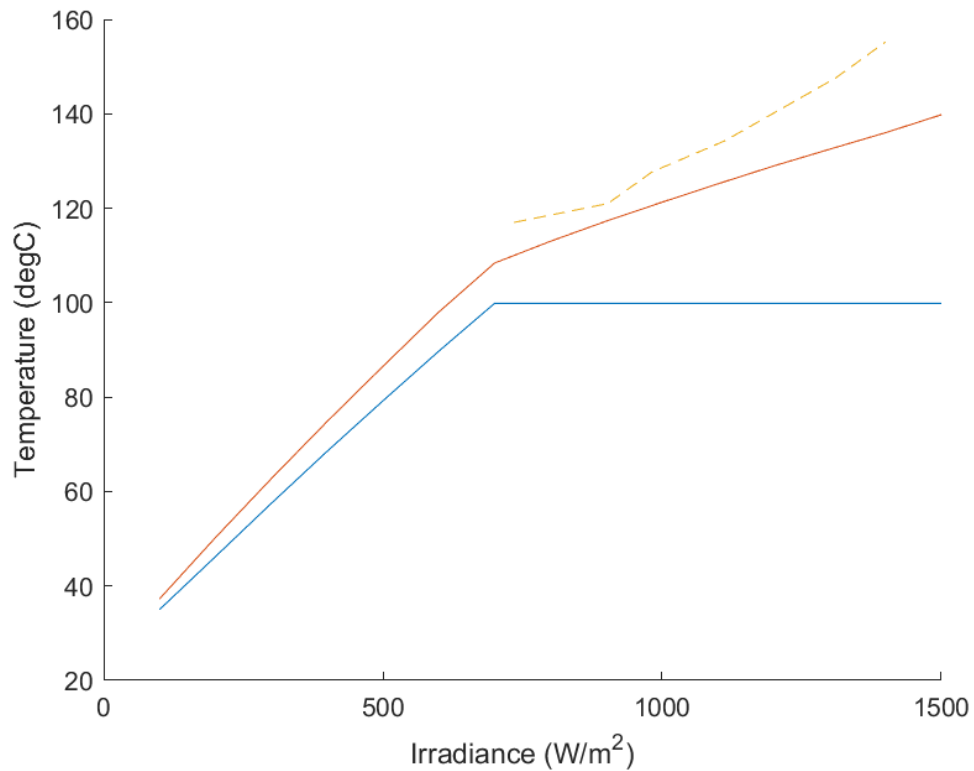


Figure 4-26: Irradiance vs. Temperatures (water and absorber reading at center).

#### 4.4.2 Solar-to-thermal efficiency vs. irradiance

The solar-to-thermal efficiency is plotted for experimental (dashed line) and numerical (solid line). The model shows agreement, with only the 6 inch simulator height image (~1.4 suns) being off point. Correcting the error at this point (of 6 experimental readings taken for flux mapping) may show better agreement of the model. As is apparent below, higher irradiance corresponds to a higher solar-to-thermal efficiency. The ~1.5 sun range represents upwards of ~40% efficiency, and with higher scales of CSES, this efficiency can be further boosted due to lower heat losses on exposed surfaces of CSES.

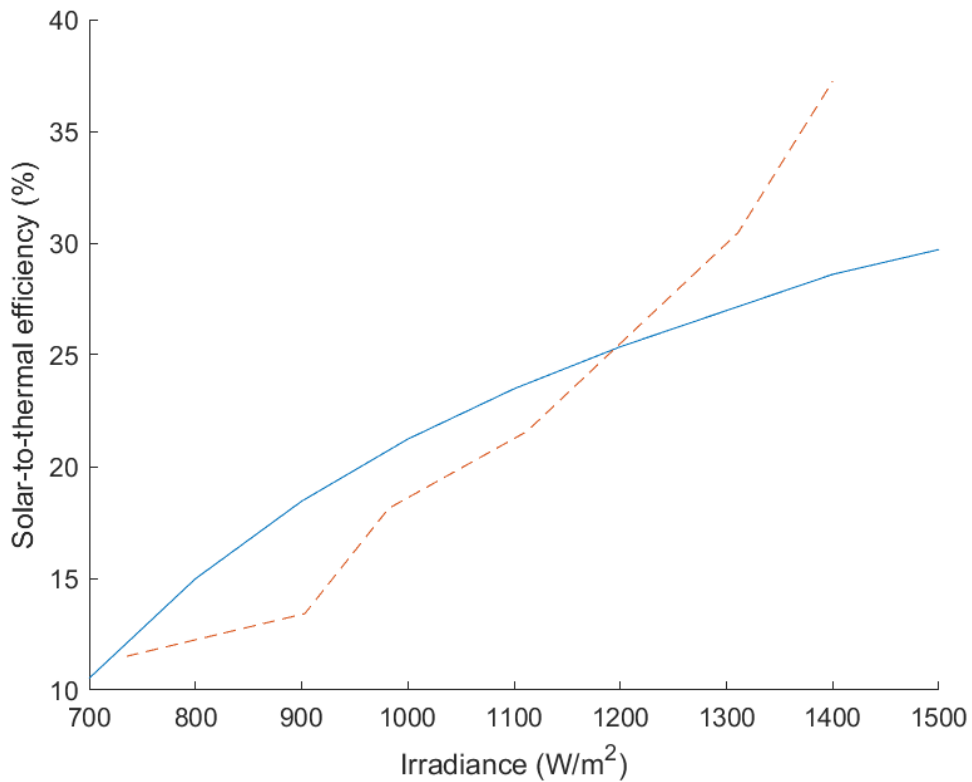


Figure 4-27: Solar-to-thermal efficiency vs. Irradiance.

#### 4.4.3 Heat-up time vs. irradiance

The heat-up time decays exponentially with higher irradiance. This further provides motivation for concentrators which can boost irradiance with concentration ratios of up to 2. A simple parabolic concentrator was tested in the 1<sup>st</sup> generation CSES by Cooper et al. [3]. Boosting irradiance on the absorber to ~1.5 suns is highly desired, as this corresponds to about half an hour of heat-up time, which is practical to utilize solar heat at boiling steady-state where evaporation rates are at least tripled. By contrast, 0.7 suns (near the average daily irradiance) takes an extremely long time to heat CSES at its current scale, taking about ~16,000 seconds, or 4 and a half hours. This is highly impractical, as more than half the day is lost to simply reach boiling steady-state.

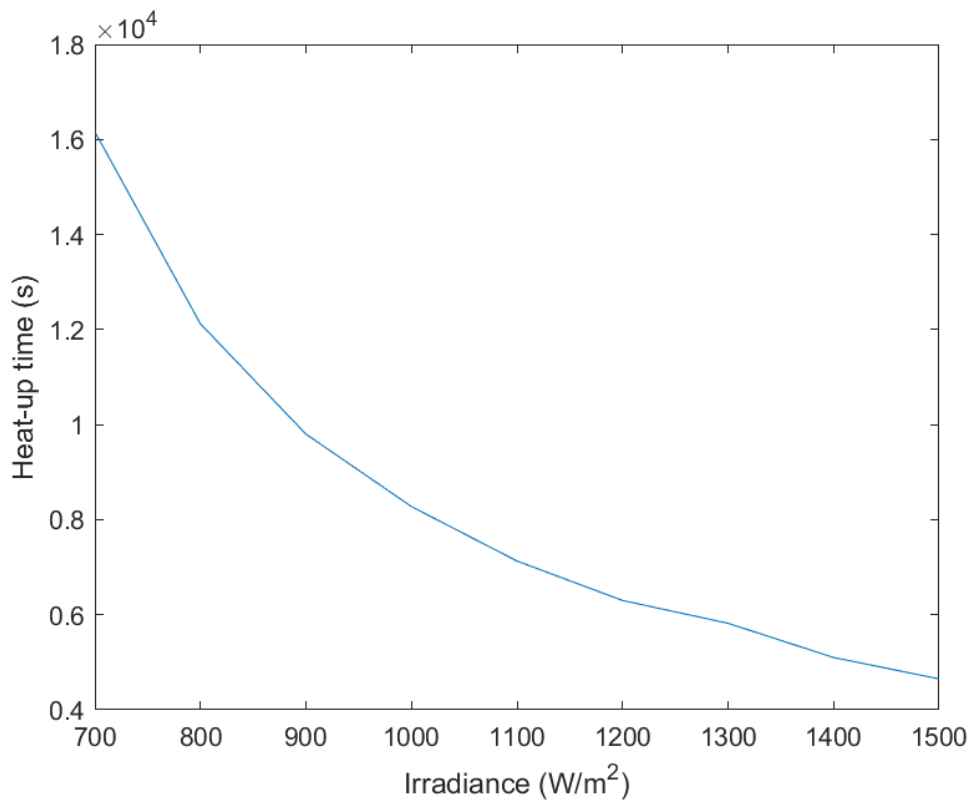


Figure 4-28: Heat-up time vs. Irradiance.

#### 4.4.4 Heat-up time vs. water mass

The heat-up time is of interest in the present study, which has utilized a hydrophilic layer (cloth) to ensure that lower amounts of water could be used in the basin. This is because unevenness of water exposed to radiation from emitter would affect evaporation rates. Figure 4-29 below illustrates a linear rise in heat-up time with more water used in the basin.

The most practical water mass to be used on cloth is ~ 500 g corresponding to 2000 s (or ~30 minutes) of heat-up time. Such a fast heat-up time would be extremely beneficial for desalination devices which rely on boiling for enhanced evaporation rates (~3x increase at least, based on experimental findings).. This also has design implications, in which future CSES designs incorporate automatic water feed intake, perhaps with wicking strategies. Ensuring a constant water supply would effectively increase water to be desalinated.

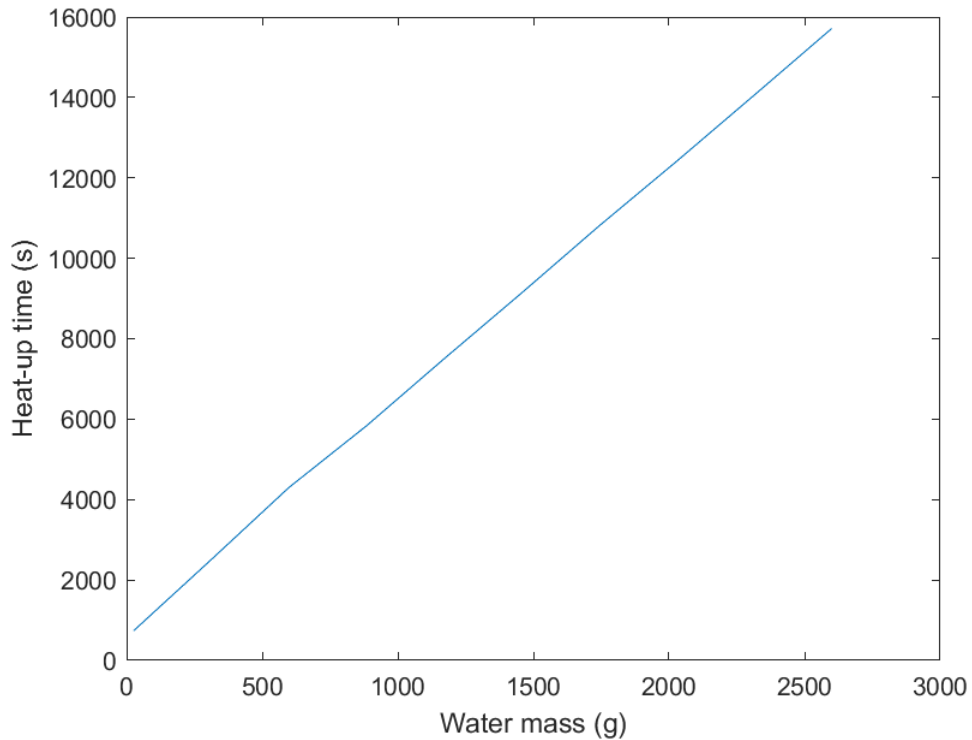


Figure 4-29: Heat-up time vs. Water mass.

#### 4.4.5 Absorber temperature vs. receiver area

The absorber temperature shows a sharp rise in temperature beyond 0.2 m<sup>2</sup> of receiver area, corresponding to the 18 inches x 18 inches used in the present CSES prototype. In the 1<sup>st</sup> generation CSES, 6 inches x 6 inches was used (~0.02 m<sup>2</sup>), which showed significant side losses. The present study, despite lower side losses from scale up, could still not achieve higher solar-to-thermal efficiency than the 1<sup>st</sup> generation of smaller scale.

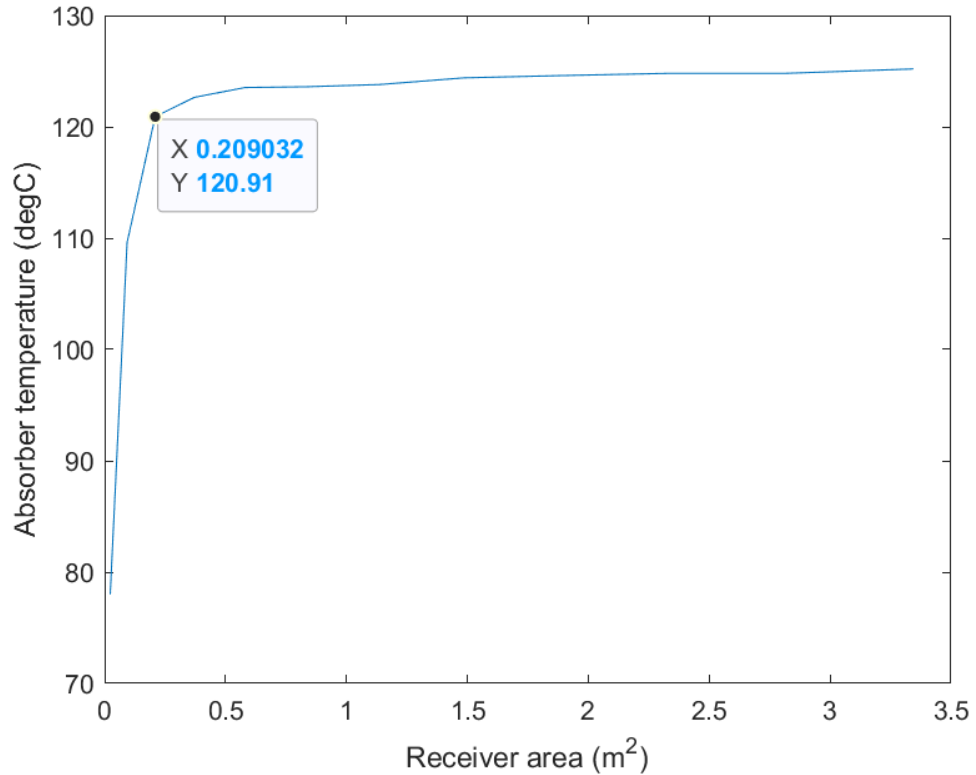


Figure 4-30: Effect of increasing receiver area (m<sup>2</sup>) on absorber temperature.

#### 4.4.6 Heat-up time vs. receiver area

The heat-up time as a function of receiver area is displayed below. It is shown below that CSES scales of 1 m<sup>2</sup> and beyond may be suitable for low heat-up times using 1.3 L of water in basin. This corresponds to ~ 2000 s of heat-up time, or slightly higher than half an hour. The half an hour heat-up time is much more practical than the current ~2 hours of heat-up time.

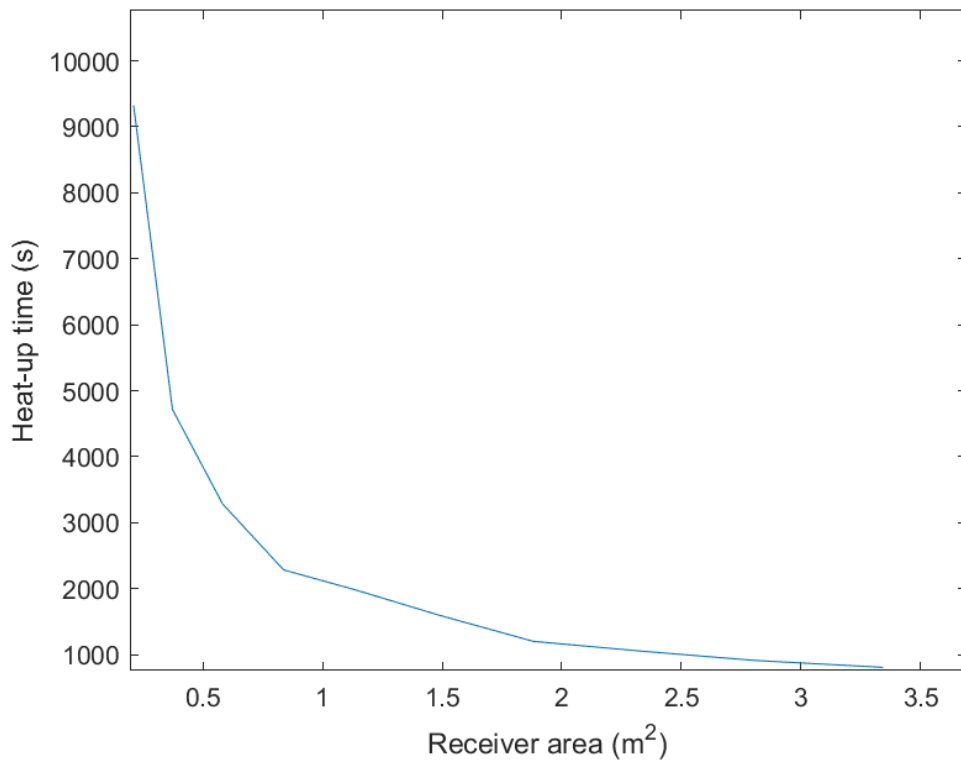


Figure 4-31: Effect of higher receiver areas on heat-up time (to steady-state boiling state).



#### 4.4.7 Parameter study

A Sensitivity Analysis was run to augment the numerical model by enabling a deeper look into parametric effects, as well as identification of the most important parameters influencing thermal performance of CSES. This plot essentially answers objective 3 (parameter tunability via sensitivity analysis and observation of potential alternate designs of CSES. It should be noted that the  $q_{\text{solar}}$  input for the parameter study was 8 hours under 1 sun. This is not practical in real-world scenarios where the sun is intermittent and only outputs near 1 sun at solar noon. Nevertheless, the model was set up in this way to allow for fair comparison to evaporation rates under 1 sun and several hours as done in in-door solar testing (~6 hours at least per experiment, not including data analysis and preparation).

Figure 4-33 illustrates the parameter influence of each of the 7 parameters. Of the material properties, the insulation thermal conductivity ( $k_{\text{insulation}}$ ) was found to be especially influential. The absorber emissivity ( $\epsilon_{\text{absorber}}$ ) at the top was also found to be influential, given that this parameter directly contributes to radiative losses of the hot absorber. The absorber emissivity at the bottom ( $\epsilon_{\text{emitter}}$ ) was not found to be as significant. With regards to the geometric properties, it is surprising that the insulation bottom thickness ( $L_{\text{insulation, bottom}}$ ) has such a large influence on the performance. The design implication of this is further investigation into the bottom losses at the current 3 inch thickness. The basin side length ( $L_{\text{side}}$ ) was also found to influence the performance, but not nearly as much as the bottom thickness. Lastly, the ambient conditions showed a strong effect of ambient temperature ( $T_{\text{ambient}}$ ) on the performance. By contrast, the ambient convection coefficient ( $h_{\text{ambient}}$ ) on non-windy to windy days were found to be not as influential, showing good insulation. These effects could be greatly reduced with more insulation for cold climates. The side loss was not taken into account for the geometric parametrization in the parameter study.

Three tuning parameters were used to tune the model, namely the optical efficiency, heat exchanging effectiveness, and side loss factor. Figure 4-32 below illustrates these results, whereby absorber temperature is to be maximized and remaining mass minimized. Thus, the results for both of these performance parameters are reversed in the plots below. The heat exchanging effectiveness was not found to affect absorber temperatures or evaporated mass, serving instead to superheat the steam. The optical efficiency, however, is an extremely sensitive parameter for the model. This is physically accurate, as losses before solar radiation heats the absorber represent a chief area of improvement for solar-thermal concentration and solar desalination applications. Lastly, the side loss factor was found to negatively affect absorber temperatures and evaporated mass.

In summary, the findings from the parameter study reveal that CSES is well optimized for this thermal layout. This is true whether in terms of geometry, materials or ambient conditions. The red rectangle in Figure 4-32 indicates the operating range of CSES in terms of maximum absorber temperature (~125 °C) and remaining mass (0.8 – 0.9 grams remaining after 8 hours, including heat-up time). Statistically, the operating absorber temperatures and evaporation rates of CSES were found to outperform most other designs. As can be observed from the frequency of designs falling within the lower absorber temperatures

( $\sim 40^\circ\text{C}$ ) and evaporated mass (most designs not boiling and evaporating less than 100 grams of water). Several correlation relationships are displayed to illustrate the parameter influence on the performance metrics: maximum absorber temperature (mean) and evaporation rates.

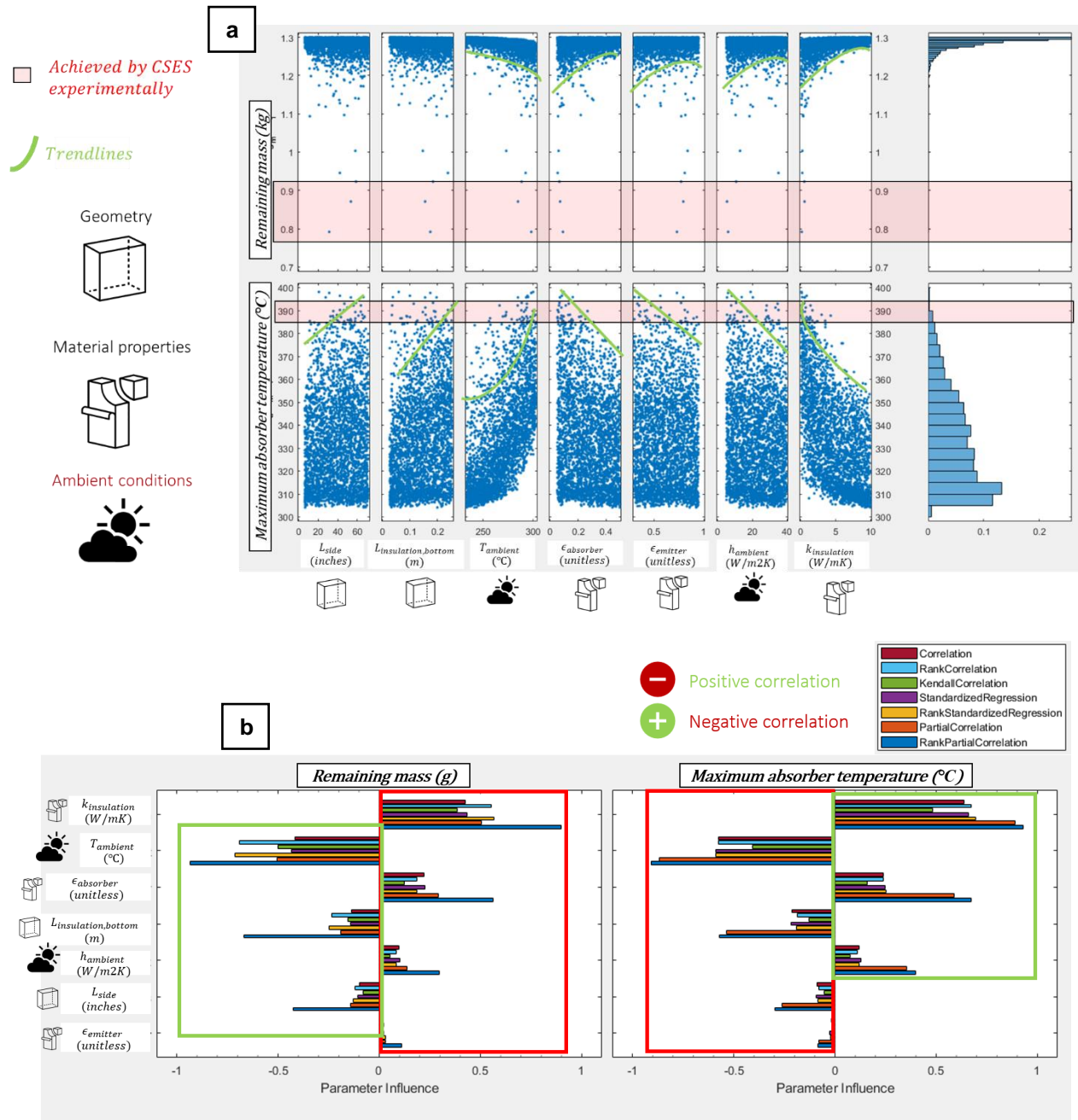


Figure 4-32: (a) Results from the sensitivity analysis of 3000 plotted design points. The red rectangle indicates the range of absorber temperature and mass evaporated by CSES experimentally. (b) Correlation matrix showing influence of 7 parameters on 2 requirements.

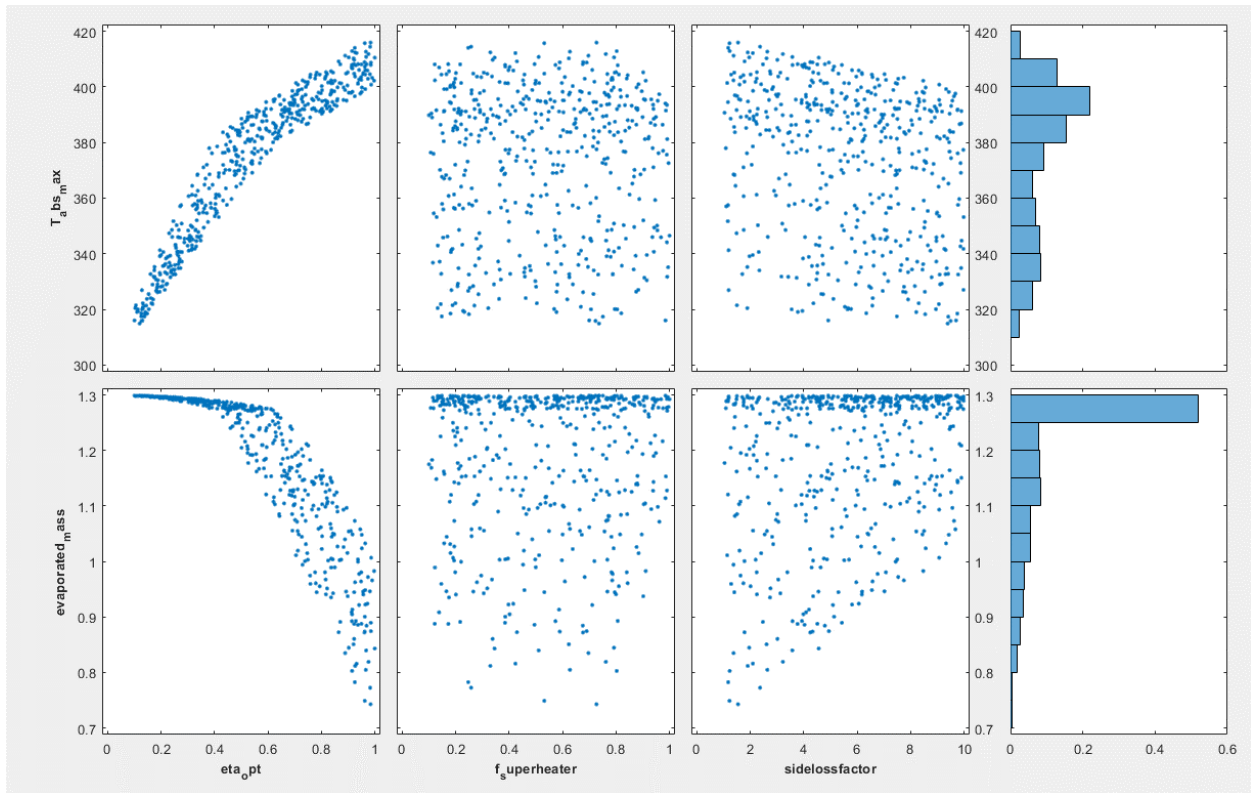
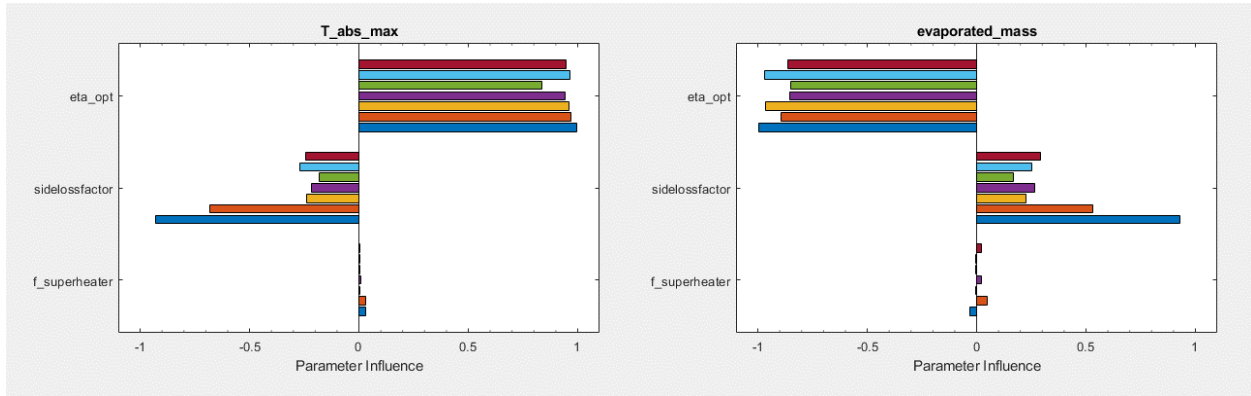
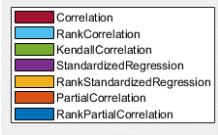


Figure 4-33: Effect of tuning parameters on maximum absorber temperature and evaporated mass (corresponding linearly to higher solar-to-thermal efficiencies).

## 4.5 Discussion Points

The following 11 discussion points are elucidated in the present section based on the results obtained from nearly 41 experiments:

- I. How could the final design help indigenous communities in Arctic Canada where there are low sunlight hours?

Regions in Northern Canada receiving only a couple of hours of sunlight during winter would simply be unable to effectively boil water with CSES. This is especially true given heat-up times, which may be reduced with lower water mass (over 2 hours for CSES). More specifically, regions such as Nunavut in Northern Canada receive an hour or so of sunshine during January and December. During the summer months, the hours of sunshine are 6 to 7 ½ hours in April (worlddata.info). To solve this issue, either concentrators with high concentration ratios (~3+) would be needed to warrant usage, as solar-to-thermal efficiency drops drastically below the boiling point (i.e. breakeven flux ~ 0.7 suns).

Moreover, the heat-up time can be reduced to less than an hour with half of the water used throughout 41 experiments in the present study. If using 500 ml of water, the numerical model predicts less than an hour of heat-up time which is more viable. Even smaller amounts can be used to reduce this heat-up time to below 30 minutes. The heat-up time can be reduced further by increasing the receiver area from 0.2 m<sup>2</sup> to high areas. With a 3m<sup>2</sup> receiver, the heat-up time predicted is in the range of 1,000 seconds.

To combat the issue further, these regions require innovative solar-thermal storage options during the summer months and stored for winter. Although given the low amount of sunlight in these regions, this would still be quite challenging without the use of effective concentrators.

- II. How accurate is the flux mapping procedure for characterizing irradiance? How accurate is it for in-door solar testing?

Two images are required for the flux mapping procedure. The first image is a meter reading (output of flux) which was taken in the present study using a pyranometer. Photodiode based power meters may also be used to similar degrees of accuracy. The second image is of the Lambertian target diffusely reflecting light. The meter reading is then scaled over the pixel values of the image (out of 256 for 8-bit images) taken of the target. The error was calculated for this procedure by taking an 18 inch x 18 inch ROI at the center as upper limit, and the same ROI area at the corners for the lower limit. The solar simulator was adjusted for experiments according to the upper limit, and thus the true solar flux may be lower. This, however, means that the true solar-to-thermal efficiency may be higher as the solar flux considered is on the upper limit. This is because the solar-to-thermal efficiency has an inverse relationship with the input flux (i.e. irradiance).

One innovation of the present study is in the setup of solar simulators and characterization of the error associated in flux mapping. This is crucial, as the irradiance influences all parameters of the thermal

performance of solar desalination systems. As the main input to the system, the solar-to-thermal efficiency is proportionally affected.

In the literature, a gap was identified in the lack of rigorous approach to characterizing solar flux impinging on the absorber (or collector) area. The present study has considered 3 spatial dimensions of human error (xyz-error). The error from the xy-plane was obtained from the flux mapping procedure, where the target (24 inch x 24 inch) was used to map the flux from simulator. Next, a center 18 inch x 18 inch ROI was placed within the target plane, and in the corners. These two readings were used to characterize the maximum and minimum xy-error. As for the z-error, the simulator height was considered to be within 0.25 inches of human error, which was accounted for in the solar-to-thermal efficiency calculations using three efficiency points. Using these three efficiency points, a box of error may be visualized for the error. While this may seem deleterious, it enables slight parameter tuning within the model to account for the large irradiance error. For example, the minimum, center and maximum efficiency points for Experiment 41 at 1.5 suns is 37.95%, 38.35%, and 45% respectively.

III. Are the evaporation rates achieved by CSES viable for real-world desalination applications? What is the resulting solar-to-thermal efficiency?

The evaporation rate achieved was ~65 g/hr for the 0.2 m<sup>2</sup> receiver area of CSES. This was calculated by taking a mass differential (with respect to time) anywhere on the linear steady-state remaining mass curve.

This equates to 330 g/hr for a 1m<sup>2</sup> design (not taking into account lower side losses due to higher scale as discussed in the side loss study). However, this 330 g/hr mass differential is taken with the input solar flux of ~ 1000 W/m<sup>2</sup>, which is rarely held in the real-world in non-desert regions. In fact, in the real world, clouds, mountains, buildings and other obstructions will directly impact available sunshine. Moreover, the solar flux of 1000 W/m<sup>2</sup> is achieved near solar noon, declining in the hours close to dawn and dusk. In real-world conditions, a concentrator is highly recommended to stay within the boiling state (at least triple the sub-boiling evaporation rate).

IV. What is the time it took to reach steady-state and is this viable for real-world desalination?

It took ~140 minutes (or ~ 8500 seconds) for the absorber, water and steam to reach steady-state (as well as the evaporation rate). This was obtained using 1.3 L of water in the basin. This really long heat-up time could be reduced by half using 650 ml of water in the basin instead. This is enabled using the hydrophilic cloth which ensures even spread of water for exposure to infrared radiation. Immediately, it is apparent that there is a large jump in evaporation rates before and after boiling point. Thus, it is very important to stay within the boiling state in steady-state.

It was shown in the numerical results that the minimum temperature to achieve boiling is ~ 700 W/m<sup>2</sup>, and thus the real evaporation rates would be much lower at these flux levels. For a 12 hour day at a solar flux of 1 sun (assuming concentration and/or non-solar sources of heat supplied to absorber), a nominal daily

evaporation rate would be 65 g/hr x 4 full sun hours (not the case for most latitudes) ~ 260 ml per day for a design of this scale. For a 1 m<sup>2</sup> design (5 times the current scale), this would equate to ~ 1 L per day. Given the recommended amount of ~ 5 L per day, this would require a 5 m<sup>2</sup> CSES scale to fulfill the needs of one person's drinking needs.

- V. How much confidence is placed on the temperature and mass readings obtained, given instrument accuracies?

The two instruments giving temperature and mass readings are three thermocouples and a mass balance, respectively. The thermocouples have accuracies of around ~1 °C based on accuracies of 0.75% based on an absorber temperature of ~ 160 °C. Moreover, the thermocouples after opening CSES post-test were observed to be in the correct spots (the absorber thermocouple would fall occasionally, or the water thermocouple peeling off the tape and floating on the water and giving same readings as emitter due to irradiation). The first issue can be solved by ensuring thermocouple wires are kept mostly straight and not curved. The second issue can be solved by applying silicone for the water thermocouple, and multiple layers of criss-crossing tape (Kapton tape used due to high temperature of the absorber) on the absorber to prevent falling. Moving around CSES attached to the LabJack (which itself is attached by USB cable to the computer) may lead to problems in thermocouple readings, and so moving CSES around while instruments are attached are not recommended.

As for the mass balance, there is one issue to be careful of, which is to ensure that there are no 'mass shorts' from CSES to the ground. To elucidate, mass shorts are similar to electric shorts (may be realized with an electric circuit) whereby a comparatively large, unwanted current is transmitted in parallel to the desired current flow, potentially leading to a circuit short. Similarly, the mass short in this situation may occur due to any component of the CSES touching the ground. To prevent such problems from happening, two 1 inch polyisocyanurate blocks were placed and tared on the mass balance to provide sufficient clearance for CSES for mass measurements.

The timesteps for measurements was 1 second, with the accuracy being within 1 g of precision (which for 1350 grams of water corresponds to an accuracy within ~ 0.1% of desired readings).

- VI. How do we improve solar-to-thermal efficiencies for future designs of different thermal layout and scale?

The three tuning parameters (heat exchanging effectiveness, optical efficiency and mass transfer coefficient) are the chief methods of better utilizing the solar heat gain and reducing losses (resulting in a higher solar-to-thermal efficiency).

Regarding the very low heat exchanging effectiveness (~ 40%), there is much room for improvement. One method of improving the superheated steam temperature is to implement copper tubes, which conductively heat up from the hot emitter at ~ 120 °C.

As for optical efficiency (~65%), there are not as many methods of improving this. The optical efficiency for the 6 inch prototype by Cooper et al. [3] was a higher value (~75%). Given the transmission of FEP of ~95% and given that two such FEP plastic films were used in the convection reducers, this corresponds to  $0.95^2$  or 90% effective transmission through both. However, this value of 95% transmission is the default given by the manufacturer. Given the progressive sagging of the FEP sheets (due to thermal expansion) at higher temperatures, this efficiency is suspected to be closer to ~80% for both convection reducers. However, there is another 25% of optical losses to account for. These may be due to the losses across sidewalls of the clamper and two convection reducers. While MYLAR reflective tape was used to reduce these losses, the reflected light may be visible when viewing the aperture of CSES, thus providing visual confirmation that the sidewalls are only partially effective at redirecting light which would have been otherwise absorbed in the sidewalls towards the absorber. A more reflective tape with a reflective bias towards a particular direction (desired to be the solar absorber and not towards ambient) may solve this issue.

#### VII. What are the Life Cycle Assessment (LCA) considerations for CSES given the current materials?

The materials used (not including smaller components such as fasteners, bolts, etc.) include polyisocyanurate foam (for insulation), FEP (air trapping and convection reduction, as well as for basin and outlet tube) solar selective surface (aluminum substrate) and aluminum (for clampers). The recyclability of the product is a lucrative feature of CSES, as there are criticisms of the LCA of large-scale RO plants which would require significant cleanup costs if a plant were to be abandoned for operation.

With regards to eco-friendliness, the author is optimistic in seeing 'green' insulation materials made from materials such as natural fibre composites (currently using a non-environmentally friendly epoxy resin for matrix). Many solar stills in the literature use a wooden basin to reduce cost and promote a usage of green materials.

Other components such as the transmissive high-temperature FEP plastic sheet will be much more difficult to produce in an eco-friendly manner but may be substituted with recycled glass panels.

Aluminum used in clampers may be substituted with any strong green material, with the most obvious choice being wood.

The hydrophilic felt may be of any cloth or cotton-based material (agriculturally available in many parts of the world, such as Bangladesh).

There are currently no 'green' solar selective absorber materials, but there is a clear motivation towards diversifying the material usage for solar absorbers to increase viability across many regions lacking access to current materials and manufacturing methods used to manufacture SSAs.

With regards to manufacturing, there are virtually no setup or manufacturing costs (not including labor costs). CSES is easy to build, setup, maintain and recycle. In short, the diversity of green materials and lack of setup costs leads CSES to be a lucrative option for many rural communities.

VIII. What were the effects of utilizing a hydrophilic layer to ensure even distribution of water on the basin (rather than pooling observed on basin made of hydrophobic material)?

We have also experimented with hydrophilic on top of hydrophobic layers, to enable water to stay flat throughout irradiation. This hydrophilic cloth is identified in the present study as a key innovation, enabling lower water mass to be used and prevent spillage on the absorber (i.e. fouling).

Unevenness on the basin (as parts dry up) atop hydrophobic layers such as flex seal or FEP basin (observed throughout the 3<sup>rd</sup> and 4<sup>th</sup> Design Iterations) leads to lower evaporation rates due to lower exposed surface area of the water. This opens doors towards using much lower water in basin (therefore lower heat-up times), and reduces chances of spillage when CSES is tilted in practical, real-world conditions. Being able to tilt CSES could potentially increase in more irradiance achieved by orienting CSES manually to face the sun. This is particularly useful for the case of indigenous communities in Canada during winter months.

Moreover, by using less water mass in the basin, heat-up times are reduced. Using 500 ml of water in the basin is predicted by the model to take ~30 minutes. This is contrasted to the 1.3 L of water used in the basin for CSES, resulting in heat-up times of close to 2 hours. This 2 hour heat-up time is highly impractical and the range of ~30 minutes of heat-up time should be targeted for future designs.

IX. From the cool-down phase, what are the implications of the thermal storage capacity of water within CSES?

Since CSES is very well insulated against heat losses, even after the solar simulator was turned off, what is first apparent is that the absorber temperature sharply drops to match the heat energy radiated from the water volume at 100 °C. From then on, it takes roughly 4 hours for the water to reach 50 °C, after which it takes a further 8 hours to reach room temperature. It is possible to reduce heat losses within CSES further but insulating the bottom, and closing off the outlet tube, which was not closed throughout the cool-down. The potential pairing of CSES with solar-thermal storage solutions represents a potentially interesting study to be investigated in the future. In this way, solar heat could be harnessed using water as a 'thermal battery' to store heat even after sun-down. Perhaps novel thermal energy storage systems using CSES itself could manage to keep the water as hot as ~50 °C even left overnight after sun-down.

X. How can CSES be adjusted to experimentally test solar-driven interfacial heating phenomena in future studies?

There is tremendous potential to investigate solar-driven interfacial phenomena using the exact setup as CSES. Essentially, CSES achieves a setup such that it is an insulated box filled with water which is



irradiated in infrared wavelengths (which can readily be determined from Planck's Law or Wien's Displacement Law for a qualitative idea of the spectral distribution). Advanced photographic equipment and accurate temperature measurements are recommended in a rigorous setup to test this natural phenomenon.

- XI. What practical considerations need to be taken into account for the deployment of CSES in real-world situations? (e.g. condensation efficiency, concentration and floatability, water feed intake, maintenance, operating)

The present study did not integrate certain system components due to lack of time. These include a condensation unit (superheated steam was simply allowed to diffuse in ambient without any collection), concentrator and water feed intake.

Importantly, 40 out of 41 experiments were conducted using potable tap water from the lab. This was done for two chief reasons. Firstly, simulating seawater for each experiment would take ~15 minutes to setup, leading to ~10 hours of dedicated time to increase salinity artificially for tests. More importantly, salt causes a mess with surfaces in contact. In particular, potential spillage may degrade performance of the absorber's emitting side.

Furthermore, due to continual rebuilding of the prototype, more details on long-time operation and maintenance are difficult to highlight. Nevertheless, the observation of build materials for 4 design iterations were found to be qualitatively quite strong and resilient. In particular, the FEP plastic sheets used for convection reduction did not puncture at all, despite some rough handling of Design 1, in particular, for over a year. Thus, FEP is not only a strong contender for a high-temperature plastic sheet which is also transmissive but also a strong one in terms of puncture prevention.

In terms of condensation, there are always condensation losses (leading to a condensation efficiency factor previously outlined in sub-section 2.5.5). These result according to the method of condensation. The method recommended by the author for condensation, while not tested, is to collect the exhaust superheated steam with a tube extension feeding into a water container. This arrangement is commonly observed in 'bubblers' for various high temperature machines, such as a tube furnace, whereby water is used as a safe heat exchanging fluid (stealing heat away from a hot surface) and heated to steam and drained in a bubbler.

Lastly, on the point of concentrators, there are challenges in pairing a concentrator if it is really tall as per design requirements of achieving at least 1.5 average concentration ratios throughout the day. Moreover, the concentrator would have to be structurally sound enough to withstand strong winds of up to 30 km/h as is common in Canada (especially during the Winter season).

## 5 Conclusion & Recommendations

### 5.1 Summary of Project & Innovations

The present project was undertaken to build the 2<sup>nd</sup> generation prototype of CSES [3]. Within the span of over 2 years, 4 design iterations were built and tested at CooperLab, York University. Within the span of a year, 41 experiments have been conducted to innovate towards an efficient 2<sup>nd</sup> generation CSES. The initial objectives of the study are first reviewed:

1. [Design and Experiment]: Experimental demonstration of a high-efficient and scaled up CSES prototype.
2. [Simulation]: Development and validation of numerical model which can accurately predict solar-to-thermal efficiency and transient temperature profiles of absorber, water and steam.
3. [Parameter Study]: Extension of the numerical model by tuning design parameters and gauging effects on evaporated mass and maximum absorber temperature.

With regards to *design*, the prototype of CSES itself was made with simple build materials which are widely available. This provides a strong motivation, despite the low efficiency achieved, for using low-cost to free junk materials for its construction. Moreover, the wide availability of solar energy on all parts of the globe prove a strong case for CSES. Thus, it is envisioned that CSES can be constructed globally to harness solar energy for useful applications. The cost of the prototype was ~\$500 USD, with a ~\$100 USD functional cost for FEP, SSA and polyisocyanurate insulation boards. The cost was found to be much more expensive than RO (~200 times cheaper), or even HD system alternatives (~20 times cheaper). However, this leads to a motivation to innovate in materials and thermal layout of CSES in future generations to be low-cost.

With regards to *experimentation*, From the 41 experiments conducted over the course of a year, Figure 4-9 and Figure 4-10 summarize the two key parameters (maximum absorber temperature and evaporation). These two figures summarize approximately 400 hours of experiments. It is very important to always accurately measure incoming radiation for all solar-testing applications, and thus  $q_{\text{solar}}$  over the average aperture inlet of CSES was also measured with a novel flux mapping technique.

With regards to the *model*, Figure 4-11 illustrates the most useful plot from this study, where the numerical model was validated against Experiment 40. The rigorous experimentation also demonstrates the mechanical and optical resilience of core components, namely the Solar Selective Absorber (SSA), Fluorinated Ethylene Propylene (FEP) and polyisocyanurate foam boards (for insulation). Useful results were generated from the numerical model, which are detailed in Section 4.4. These results have design implications for CSES, namely the benefits of using the hydrophilic cloth in reducing heat-up times by being able to use lower water mass in basin. Moreover, efficiencies are significantly boosted at the ~1.5 sun range, implying the usage of concentrators to boost solar fluxes to this range.

The design innovations will now be briefly highlighted in Table 5-1 below.

*Table 5-1: Summary of innovations.*

<b>Key Innovation</b>	<b>Explanation</b>
I. Scale-up & side losses	The 2nd generation CSES was tested with an 18 inches x18 inches collector area, which is a 10x scale up from the 1st generation (6 inches x 6 inches collector area).
II. Hydrophilic cloth	A hydrophilic cloth was used and found to have no negative impact on evaporation rates and absorber temperature. Such cloths are widely available and may be used to boost evaporation rates by preventing water pooling (given the thin water height for infrared heating). Moreover, such cloths may prevent spillage of saltwater onto the absorber (i.e. fouling). Lastly, the cloth ensures that low water masses may be used in the basin, which would tremendously boost heat-up times and therefore, overall evaporation rates throughout the day.
III. Flux mapping	A novel flux mapping procedure used to quantify solar flux and x-y-z error over an aperture. Such procedures are extremely useful for in-door solar testing to ensure an accurate solar flux characterization. From a physics modelling perspective, the solar flux is the key input determining the outputs of any solar-thermal system and should be fed into models within high confidence.
IV. In-door solar testing with LED Growlight	A solar simulator (LED Growlight for in-door agriculture applications) for in-door testing was characterized with regards to height and resulting solar flux using a Lambertian target.
V. Mass transfer physics	Model has utilized interesting mass diffusion physics in sub-boiling temperatures. Such mass diffusion is hypothesized to be driven by concentration differences of the steam within the gas gap, with the odd configuration of a hot surface at top instead of bottom in everyday scenarios. Such mass diffusion require further investigation.
VI. Model parametrization	The model has been parametrized with a sensitivity analysis which is very useful to observe effects of tuning parameters for a wide variety of ambient conditions, materials and CSES geometry.
VII. Origami-folded plastic basin	Origami-folded FEP basin, which is easy to make and does not thermally degrade at temperatures of ~150 °C (simplified glazing system from 1 <sup>st</sup> generation).
VIII. Reflective tape	Reflective tape on all exposed surfaces, increasing optical efficiency (resulting from solar heat losses from aperture to absorber).

IX. Clamping	Effective and simplified clamping mechanism from the 1 <sup>st</sup> generation, preventing steam leaks to ambient. Moreover, the simplicity of the clamping mechanism alongside the closed-cell silicone gasket demonstrate strong steam leak prevention. Such a mechanism may be used in a wide variety of applications involving steam containment within an enclosure.
X. Experimental comparison with contact solar stills	The performance of CSES was contrasted to its configuration resembling a contact solar still, whereby the water itself and cloths were used for 2 experiments. The evaporation rates were contrasted to those of CSES and found to be similar. Justification was given for CSES in light of high temperatures achieved (~120 °C compared to ~30 °C).
XI. New product development guidelines	Based on the experience gathered in the design, experimentation and model of the 2 <sup>nd</sup> generation of CSES, methods and results detailing the development of a completely new product could be extrapolated to innovative products across all disciplines.

## 5.2 Conclusion

In conclusion, the present study has detailed the design and development of the 2<sup>nd</sup> generation of a Contactless Solar Evaporation Structure (CSES), which was found to achieve absorber temperatures of ~120 °C (mean temperature), which was able to not only boil water (100 °C) through infrared radiation, but also superheat steam to temperatures of ~115 °C. The resulting system-level efficiencies were found to be ~65% optical efficiency and ~60% heat exchanging effectiveness.

The purposes of this device was ultimately desalination for clean drinking water. To this aim, evaporation details were collected as well, finding evaporation rates of ~65 g/hr. The solar-to-thermal efficiency for this evaporation rate under 1 sun is ~20%.

A model was also developed and validated against the experimental results. While 41 experiments were conducted over a year (Section 4.3), only 5 experiments (Experiments 40, 39, 38, 28 and 35, in order of discussion) were highlighted in the results section with details on transient temperature and mass profiles. Accompanying pictures of the design evolution throughout the 41 experiments were tabulated in sub-section 3.3.4.

The model was also parametrized, showing trends with respect to maximum absorber temperature and evaporation in Section 4.4. Moreover, the temperature and mass profiles of CSES with regards to different solar irradiation scenarios were found using the model. The heat-up time is especially important for CSES, given that under 1 sun and current thermal design, it would take ~2 hours to heat up. Given that the efficiency from heat-up (mass diffusion) to steady-state (boiling) is at least triple (i.e. triple the evaporation rates), it is highly desired to stay within the steady-state as much as possible.

To gain confidence in the experiment and model, preliminary experimental characterization was conducted with regards to optical properties of materials used, optical efficiency test, flux mapping and evaporation rates for 6 configurations of CSES mimicking the conventional solar still.

### 5.3 Recommendations for future work

Valuable lessons discussed in the discussion section may pave the way forward for future studies, described in point form below:

- i. The side loss model is approximately 3 times off. Thus, a deeper investigation into the side losses needs to be investigated to enable the model to be scaled accurately for any contactless solar still.
- ii. The thermal layout and materials of CSES needs to be updated with novel solutions. Both the 1<sup>st</sup> ([3]) and 2<sup>nd</sup> generations of CSES (present study) could not exceed 25% efficiency reliably, with the first generation coming close at 24.6% efficiency at one sun and the second generation only ~20% efficient.
- iii. More accurate flux mapping techniques should be explored to minimize the overall error accompanying the method. The input solar flux (i.e. irradiance) is the most influential input parameter for numerical modelling solar stills (and perhaps, by extension, all solar-thermal systems). Slight deviations in this parameter will influence the ultimate output of the model.
- iv. There is a tremendous potential for heating by infrared radiation, enabling a complete bypass of the fouling issue. Configurations of the contactless thermal layout of CSES may be translated to real-world scenarios such as under bridges, aquifers or any exposed surfaces insulated by either ground or surroundings and irradiated by the sun.
- v. There is tremendous interest in the fundamental physics of the interaction of infrared photons with water molecules at the molecular level. Thus, the radiative boiling phenomena of water should be investigated further.
- vi. Infrared radiation being able to radiatively boil water as well as superheat steam (convectively with hot emitter) which has direct benefits to the medical community, with regards to steam sterilization at temperatures ~ 130 °C.
- vii. From a practical standpoint, being able to desalinate water with concentrated solar heat (e.g. using a compound parabolic concentrator) may boost efficiencies, opening doors to utilizing hot steam for useful purposes.
- viii. Moreover, it is of interest to deploy CSES on water flotation situations, which is of practical interest to the Ocean Engineering research community, whereby CSES could be deployed at no land cost towards desalination, which is difficult to achieve with reverse osmosis and other large-scale desalination measures. To this aim, floating CSES should be investigated. One suggested idea for such a floating device are inflatable, high-temperature plastics with an SSA.

- ix. Radiation error is a key area of interest in accurate superheated steam temperature measurements for desalination. More specifically, Investigating the radiosity from tube walls of outlet tube (made of FEP in present study) to a thermocouple, resulting in radiation errors
- x. The transient mass curve needs further investigation with regards to the sub-boiling temperatures (i.e. during the heat-up phase). Moreover, the salinity properties of water need to be taken into consideration with regards to the heat-up phase.
- xi. From a materials engineering perspective, there is interest to develop the same thermal layout of CSES with eco-friendly materials (e.g. mud, ground, natural fibres, etc.) in substitution of polyisocyanurate foam for insulation, high-temperature FEP plastic sheets/film/tube, solar-selective absorber with aluminum backing, and aluminum clampers.
- xii. From an instrumentation perspective, the successful utilization of LED Solar Simulator enables further investigation as to its spectrum and any potential discrepancies with incandescent solar simulators.
- xiii. With regards to the above, there is also interest in developing efficient flux mapping procedures using consumer-grade cameras, which are widely available and cheaper than lab-grade photographic equipment.
- xiv. Given that 82% of Canada's residential energy demands go towards space and water heating, there may be tremendous scope in using hot water vapor to heat up ambient surroundings for space heating. This may potentially be done using CSES itself if perhaps superheated steam can exchange heat with surrounding air (which may be done within an insulated heat exchanger).
- xv. Investigation into a more accurate mass transfer coefficient for the thermal layout of CSES
- xvi. Many materials extensively used in the project, such as polyisocyanurate, fluoroethylene propylene (FEP) and the solar selective absorber, have not been extensively reported in the research literature on desalination. Such new materials require experimentation to retrieve valuable thermal and optical properties to be used in desalination research
- xvii. CSES should also be tested in real-world conditions within rural communities. The user design experience of such communities with the device, its operation and maintenance is of interest.

Thus, the second generation of CSES paves the way forward for the next generation of contactless solar stills, which may boil water under high temperatures (relative to ambient). The boiling steam being superheated to high temperatures (~135 °C and beyond) under one sun (typical ambient conditions) are of tremendous interest for applications beyond desalination. Rural communities globally have an active interest in pursuing such structures towards a future where such communities have decentralized technology for their basic drinking, sanitation and medical needs.

## References

- [1] "Saudi Arabia Gasoline Prices - February 2022 Data - 1995-2021 Historical." [Online]. Available: <https://tradingeconomics.com/saudi-arabia/gasoline-prices>. [Accessed: 29-Mar-2022].
- [2] X. Li, T. Cooper, W. Xie, and P. C. Hsu, "Design and Utilization of Infrared Light for Interfacial Solar Water Purification," *ACS Energy Lett.*, vol. 6, no. 8, pp. 2645–2657, 2021, doi: 10.1021/acsenergylett.1c00869.
- [3] T. A. Cooper *et al.*, "Contactless steam generation and superheating under one sun illumination," *Nat. Commun.*, vol. 9, no. 1, pp. 1–10, 2018, doi: 10.1038/s41467-018-07494-2.
- [4] Y. Tu, J. Zhou, S. Lin, M. Alshrah, X. Zhao, and G. Chen, "Photomolecular Effect Leading to Water Evaporation Exceeding Thermal Limit," 2022.
- [5] H. Ghasemi *et al.*, "Solar steam generation by heat localization," *Nat. Commun.*, vol. 5, pp. 1–7, 2014, doi: 10.1038/ncomms5449.
- [6] G. Ni, S. H. Zandavi, S. M. Javid, S. V. Boriskina, T. A. Cooper, and G. Chen, "A salt-rejecting floating solar still for low-cost desalination," *Energy Environ. Sci.*, vol. 11, no. 6, pp. 1510–1519, 2018, doi: 10.1039/c8ee00220g.
- [7] P. Tao *et al.*, "Solar-driven interfacial evaporation," *Nat. Energy*, vol. 3, no. 12, pp. 1031–1041, 2018, doi: 10.1038/s41560-018-0260-7.
- [8] L. Zhou, X. Li, G. W. Ni, S. Zhu, and J. Zhu, "The revival of thermal utilization from the Sun: Interfacial solar vapor generation," *Natl. Sci. Rev.*, vol. 6, no. 3, pp. 562–578, 2019, doi: 10.1093/nsr/nwz030.
- [9] Y. Pang, J. Zhang, R. Ma, Z. Qu, E. Lee, and T. Luo, "Solar–Thermal Water Evaporation: A Review," *ACS Energy Lett.*, vol. 5, no. 2, pp. 437–456, 2020, doi: 10.1021/acsenergylett.9b02611.
- [10] C. M. and A. Yadav, "Water desalination system using solar heat: A review," *Renew. Sustain. Energy Rev.*, vol. 67, pp. 1308–1330, 2017, doi: 10.1016/j.rser.2016.08.058.
- [11] "NEOM: Made to Change." [Online]. Available: <https://www.neom.com/en-us>. [Accessed: 10-Mar-2022].
- [12] M. M. Rahman, M. A. Hossain, M. R. Ali, Z. Ahmed, and A. H. M. Hedayatul Islam, "Assessing vulnerability and adaptation strategy of the cyclone affected coastal area of Bangladesh," *Geoenvironmental Disasters*, vol. 9, no. 1, 2022, doi: 10.1186/s40677-022-00209-2.
- [13] F. Suhr and J. I. Steinert, "Epidemiology of floods in sub-Saharan Africa: a systematic review of health outcomes," *BMC Public Health*, vol. 22, no. 1, pp. 1–15, 2022, doi: 10.1186/s12889-022-12584-4.

- [14] H. S. Munawar, A. W. A. Hammad, and S. T. Waller, "Remote Sensing Methods for Flood Prediction: A Review," *Sensors*, vol. 22, no. 3, 2022, doi: 10.3390/s22030960.
- [15] O. Awume, R. Patrick, and W. Baijius, "Indigenous perspectives on water security in Saskatchewan, Canada," *Water (Switzerland)*, vol. 12, no. 3, 2020, doi: 10.3390/w12030810.
- [16] T. Latchmore, C. J. Schuster-Wallace, D. R. Longboat, S. E. Dickson-Anderson, and A. Majury, "Critical elements for local Indigenous water security in Canada: A narrative review," *J. Water Health*, vol. 16, no. 6, pp. 893–903, 2018, doi: 10.2166/wh.2018.107.
- [17] S. Torquato and G. R. Stell, "An Equation for the Latent Heat of Vaporization," pp. 41–44, 1982.
- [18] K. A. Sharp, "Paper: Structure and properties," *Chem. Eng. J.*, vol. 37, no. 2, p. 131, 2001, doi: 10.1016/0300-9467(88)80038-8.
- [19] H. T. Do Thi, T. Pasztor, D. Fozzer, F. Manenti, and A. J. Toth, "Comparison of Desalination Technologies Using Renewable Energy Sources with Life Cycle, PESTLE, and Multi-Criteria Decision Analyses," 2021.
- [20] J. Lienhard V, M. Antar A., A. Bilton, J. Blanco, and G. Zaragoza, "Chapter 9: Solar desalination," *Int. J. Nucl. Desalin.*, vol. 2, no. 4, pp. 363–371, 2007, doi: 10.1504/IJND.2007.015802.
- [21] L. N. Nthunya *et al.*, "Fouling, performance and cost analysis of membrane-based water desalination technologies: A critical review," *J. Environ. Manage.*, vol. 301, no. September 2021, p. 113922, 2022, doi: 10.1016/j.jenvman.2021.113922.
- [22] D. Viviroli and R. Weingartner, "'Water Towers'—A Global View of the Hydrological Importance of Mountains," *Adv. Glob. Chang. Res.*, vol. 31, pp. 15–20, 2008, doi: 10.1007/978-1-4020-6748-8\_2.
- [23] "Having access to water is increasingly a matter of survival in conflict zones | ICRC." [Online]. Available: <https://www.icrc.org/en/document/having-access-water-increasingly-matter-survival-conflict-zones>. [Accessed: 24-Mar-2022].
- [24] "Day Zero: Where next?" [Online]. Available: <https://www.nationalgeographic.com/science/article/partner-content-south-africa-danger-of-running-out-of-water>. [Accessed: 24-Mar-2022].
- [25] "Water Use Statistics - Worldometer." [Online]. Available: <https://www.worldometers.info/water/>. [Accessed: 24-Mar-2022].
- [26] "Average daily residential litres per capita." [Online]. Available: <https://www150.statcan.gc.ca/n1/daily-quotidien/190611/cg-b002-eng.htm>. [Accessed: 24-Mar-2022].



- [27] A. Tiwari, M. K. Rathod, and A. Kumar, *A comprehensive review of solar-driven desalination systems and its advancements*, no. 0123456789. Springer Netherlands, 2022.
- [28] “Solar resource data available for Canada.” [Online]. Available: <https://www.nrcan.gc.ca/energy/energy-sources-distribution/renewables/solar-photovoltaic-energy/solar-resource-data-available-canada/14390>. [Accessed: 10-Mar-2022].
- [29] “Global Solar Atlas.” [Online]. Available: <https://globalsolaratlas.info/map>. [Accessed: 10-Mar-2022].
- [30] UN, “PERCENTAGE OF TOTAL POPULATION LIVING IN COASTAL AREAS Oceans, Seas and Coasts Coastal Zone Core indicator.” .
- [31] C. S. L. Mercer *et al.*, “Chapter 3 : the Coastal Challenge,” pp. 69–98, 2016.
- [32] “Populations in Coastal Zones | Resource Watch.” [Online]. Available: <https://resourcewatch.org/data/explore/Populations-in-Coastal-Zones?section=Discover&selectedCollection=&zoom=0.8041310211833178&lat=0&lng=81.25848308278115&pitch=0&bearing=0&basemap=dark&labels=light&layers=%255B%257B%2522dataset%2522%253A%2522995ec4fe-b3cc-4cf4-bd48-b89d4e3ea072%2522%252C%2522opacity%2522%253A1%252C%2522layer%2522%253A%25222e533124-3258-4ec2-a777-beed1712d1a0%2522%257D%255D&aoi=&page=1&sort=most-viewed&sortDirection=-1>. [Accessed: 10-Mar-2022].
- [33] B. Neumann, A. T. Vafeidis, J. Zimmermann, and R. J. Nicholls, “Future Coastal Population Growth and Exposure to Sea-Level Rise and Coastal Flooding - A Global Assessment,” *PLoS One*, vol. 10, no. 3, Mar. 2015, doi: 10.1371/JOURNAL.PONE.0118571.
- [34] “Home - Water Scarcity Atlas - Water Scarcity Atlas.” [Online]. Available: <https://waterscarcityatlas.org/>. [Accessed: 14-May-2022].
- [35] Y. Cengel, *Heat transfer, second edition*, 2nd Editio. 2002.
- [36] J. H. I. Lienhard and J. H. V Lienhard, “A Heat Transfer Textbook, fifth edition,” 2020.
- [37] M. F. (Michael F. . Modest, *Radiative heat transfer*. Elsevier Science, 2013.
- [38] A. Palacios, L. Cong, M. E. Navarro, Y. Ding, and C. Barreneche, “Thermal conductivity measurement techniques for characterizing thermal energy storage materials – A review,” *Renew. Sustain. Energy Rev.*, vol. 108, no. November 2018, pp. 32–52, 2019, doi: 10.1016/j.rser.2019.03.020.
- [39] “Alumina (Aluminum Oxide, Al<sub>2</sub>O<sub>3</sub>):: MakeItFrom.com.” [Online]. Available: [https://www.makeitfrom.com/material-properties/Alumina-Aluminum-Oxide-Al<sub>2</sub>O<sub>3</sub>](https://www.makeitfrom.com/material-properties/Alumina-Aluminum-Oxide-Al2O3). [Accessed: 15-May-2022].

- [40] Y. A. Cengel and A. J. Ghajar, *Heat and Mass Transfer, Fundamentals & Application, Fifth Edition in SI Units*, vol. 5th, no. 3. 2015.
- [41] M. Nauenberg, "Max Planck and the birth of the quantum hypothesis," *Am. J. Phys.*, vol. 84, no. 9, pp. 709–720, 2016, doi: 10.1119/1.4955146.
- [42] G. Kirchhoff, "Ueber das Verhältniss zwischen dem Emissionsvermögen und dem Absorptionsvermögen der Körper für Wärme und Licht," *Ann. Phys. Chemie*, vol. 109, p. 275, 1860.
- [43] "Age and Origin of the Solar System." [Online]. Available: [http://earthguide.ucsd.edu/virtualmuseum/ita/05\\_3.shtml](http://earthguide.ucsd.edu/virtualmuseum/ita/05_3.shtml). [Accessed: 26-Mar-2022].
- [44] S. Graham, "The Water Cycle," 2010. [Online]. Available: <https://earthobservatory.nasa.gov/features/Water>. [Accessed: 26-Mar-2022].
- [45] M. T. Chahine, "The hydrological cycle and its influence on climate," *Nature*, vol. 359, no. 6394, pp. 373–380, 1992, doi: 10.1038/359373A0.
- [46] P. Snow and Smithsonian Institution., *History of the world map by map*. 2018.
- [47] A. Seyfi, R. Afzalzadeh, and A. Hajnorouzi, "Increase in water evaporation rate with increase in static magnetic field perpendicular to water-air interface," *Chem. Eng. Process. Process Intensif.*, vol. 120, no. June, pp. 195–200, 2017, doi: 10.1016/j.cep.2017.06.009.
- [48] W. D. Callister and D. G. Rethwisch, *Materials science and engineering : an introduction*. 2018.
- [49] M. Morciano, M. Fasano, S. V. Boriskina, E. Chiavazzo, and P. Asinari, "Solar passive distiller with high productivity and Marangoni effect-driven salt rejection," *Energy Environ. Sci.*, vol. 13, no. 10, pp. 3646–3655, 2020, doi: 10.1039/d0ee01440k.
- [50] "What is a TDS meter and do you need one? | Aquasana." [Online]. Available: <https://www.aquasana.com/info/tds-meter-what-is-it-and-do-you-need-it-pd.html>. [Accessed: 10-Mar-2022].
- [51] D. M. Warsinger, J. Swaminathan, E. Guillen-Burrieza, H. A. Arafat, and J. H. Lienhard V, "Scaling and fouling in membrane distillation for desalination applications: A review," *Desalination*, vol. 356, pp. 294–313, 2015, doi: 10.1016/j.desal.2014.06.031.
- [52] Y. Zhang, T. Xiong, D. K. Nandakumar, and S. C. Tan, "Structure Architecting for Salt-Rejecting Solar Interfacial Desalination to Achieve High-Performance Evaporation With In Situ Energy Generation," *Adv. Sci.*, vol. 7, no. 9, 2020, doi: 10.1002/advs.201903478.
- [53] V. Belessiotis and S. Kalogirou, *Thermal Solar Desalination - 1st Edition*. .
- [54] B. Kalista, H. Shin, J. Cho, and A. Jang, "Current development and future prospect review of freeze

- desalination,” *Desalination*, vol. 447, no. September, pp. 167–181, 2018, doi: 10.1016/j.desal.2018.09.009.
- [55] S. A. Kalogirou, *Solar Energy Engineering: Processes and Systems, 2nd Edition*. Elsevier, 2014.
- [56] S. A. Kalogirou, “Solar Desalination Systems,” *Sol. Energy Eng.*, pp. 431–479, 2014, doi: 10.1016/B978-0-12-397270-5.00008-X.
- [57] A. N. Angelakis *et al.*, “Desalination: From ancient to present and future,” *Water (Switzerland)*, vol. 13, no. 16, 2021, doi: 10.3390/w13162222.
- [58] UNESCO, *Water and Climate Change (World Water Day - 2020 Report)*. 2019.
- [59] “Population served by drinking water plants.” [Online]. Available: <https://www150.statcan.gc.ca/t1/tb11/en/tv.action?pid=3810009301>. [Accessed: 09-Mar-2022].
- [60] F. Alnaimat, M. Ziauddin, and B. Mathew, “A review of recent advances in humidification and dehumidification desalination technologies using solar energy,” *Desalination*, vol. 499, no. August 2020, p. 114860, 2021, doi: 10.1016/j.desal.2020.114860.
- [61] S. Shoeibi, N. Rahbar, A. Abedini Esfahlani, and H. Kargarsharifabad, “A comprehensive review of Enviro-Exergo-economic analysis of solar stills,” *Renew. Sustain. Energy Rev.*, vol. 149, no. May, p. 111404, 2021, doi: 10.1016/j.rser.2021.111404.
- [62] T. Akinaga, S. C. Generalis, C. Paton, O. N. Igobo, and P. A. Davies, “Brine utilisation for cooling and salt production in wind-driven seawater greenhouses: Design and modelling,” *Desalination*, vol. 426, no. February 2017, pp. 135–154, 2018, doi: 10.1016/j.desal.2017.10.025.
- [63] T. Dordi, D. Henstra, and J. Thistlethwaite, “Flood risk management and governance: A bibliometric review of the literature,” *J. Flood Risk Manag.*, no. October 2020, pp. 1–18, 2022, doi: 10.1111/jfr3.12797.
- [64] H. Panchal, K. K. Sadasivuni, F. A. Essa, S. Shanmugan, and R. Sathyamurthy, “Enhancement of the yield of solar still with the use of solar pond: A review,” *Heat Transf.*, vol. 50, no. 2, pp. 1392–1409, 2021, doi: 10.1002/htj.21935.
- [65] M. R. Diab, F. A. Essa, F. S. Abou-Taleb, and Z. M. Omara, “Solar still with rotating parts: a review,” *Environ. Sci. Pollut. Res.*, vol. 28, no. 39, pp. 54260–54281, 2021, doi: 10.1007/s11356-021-15899-8.
- [66] S. Chen *et al.*, “A floating solar still inspired by continuous root water intake,” *Desalination*, vol. 512, no. May, p. 115133, 2021, doi: 10.1016/j.desal.2021.115133.
- [67] G. Sadeghi and S. Nazari, “Retrofitting a thermoelectric-based solar still integrated with an

- evacuated tube collector utilizing an antibacterial-magnetic hybrid nanofluid," *Desalination*, vol. 500, no. September 2020, p. 114871, 2021, doi: 10.1016/j.desal.2020.114871.
- [68] M. Alhaj, A. Hassan, M. Darwish, and S. G. Al-Ghamdi, "A techno-economic review of solar-driven multi-effect distillation," *Desalin. Water Treat.*, vol. 90, pp. 86–98, 2017, doi: 10.5004/dwt.2017.21297.
- [69] S. Lin *et al.*, "Seawater desalination technology and engineering in China: A review," *Desalination*, vol. 498, no. July 2020, p. 114728, 2021, doi: 10.1016/j.desal.2020.114728.
- [70] A. Naminezhad and M. Mehregan, "Energy and exergy analyses of a hybrid system integrating solar-driven organic Rankine cycle, multi-effect distillation, and reverse osmosis desalination systems," *Renew. Energy*, vol. 185, pp. 888–903, 2022, doi: 10.1016/j.renene.2021.12.076.
- [71] "Desalination for cost-effective water production - Advisian." [Online]. Available: <https://www.advisian.com/en/global-perspectives/desalination-for-cost-effective-water-production>. [Accessed: 10-Mar-2022].
- [72] "Thermal Vapour Compression - an overview | ScienceDirect Topics." [Online]. Available: <https://www.sciencedirect.com/topics/engineering/thermal-vapour-compression>. [Accessed: 10-Mar-2022].
- [73] M. Qasim, M. Badrelzaman, N. N. Darwish, N. A. Darwish, and N. Hilal, "Reverse osmosis desalination: A state-of-the-art review," *Desalination*, vol. 459, no. February, pp. 59–104, 2019, doi: 10.1016/j.desal.2019.02.008.
- [74] S. M. Shalaby *et al.*, "Reverse osmosis desalination systems powered by solar energy: Preheating techniques and brine disposal challenges – A detailed review," *Energy Convers. Manag.*, vol. 251, no. October 2021, p. 114971, 2022, doi: 10.1016/j.enconman.2021.114971.
- [75] *Reverse Osmosis: Industrial Processes and Applications - Jane Kucera - Google Books.* .
- [76] T. Arumugham *et al.*, "Recent developments in porous ceramic membranes for wastewater treatment and desalination: A review," *J. Environ. Manage.*, vol. 293, no. May, p. 112925, 2021, doi: 10.1016/j.jenvman.2021.112925.
- [77] Y. J. Lim, K. Goh, M. Kurihara, and R. Wang, "Seawater desalination by reverse osmosis: Current development and future challenges in membrane fabrication – A review," *J. Memb. Sci.*, vol. 629, no. December 2020, p. 119292, 2021, doi: 10.1016/j.memsci.2021.119292.
- [78] Y.-H. Yu and D. Jenne, "Analysis of a Wave-Powered, Reverse-Osmosis System and Its Economic Availability in the United States: Preprint," 2017.
- [79] F. E. Ahmed, R. Hashaikeh, and N. Hilal, "Solar powered desalination – Technology, energy and

- future outlook,” *Desalination*, vol. 453, no. December 2018, pp. 54–76, 2019, doi: 10.1016/j.desal.2018.12.002.
- [80] M. Freire-Gormaly and A. M. Bilton, “Design of photovoltaic powered reverse osmosis desalination systems considering membrane fouling caused by intermittent operation,” *Renew. Energy*, vol. 135, pp. 108–121, 2019, doi: 10.1016/j.renene.2018.11.065.
- [81] L. Horrigan and M. Freire-Gormaly, “Modelling the effects of ultrasonic sonification on reverse osmosis feed channel temperature,” *Desalination*, vol. 521, no. August 2021, p. 115332, 2022, doi: 10.1016/j.desal.2021.115332.
- [82] H. Saleem and S. J. Zaidi, “Nanoparticles in reverse osmosis membranes for desalination: A state of the art review,” *Desalination*, vol. 475, no. November 2019, p. 114171, 2020, doi: 10.1016/j.desal.2019.114171.
- [83] N. D. Suzaimi *et al.*, “Strategies in forward osmosis membrane substrate fabrication and modification: A review,” *Membranes (Basel)*, vol. 10, no. 11, pp. 1–42, 2020, doi: 10.3390/membranes10110332.
- [84] L. Zhu, C. Ding, T. Zhu, and Y. Wang, “A review on the forward osmosis applications and fouling control strategies for wastewater treatment,” *Front. Chem. Sci. Eng.*, 2021, doi: 10.1007/s11705-021-2084-4.
- [85] M. Bergstedt, “A Novel Forward Osmosis Draw Solution | AIChE.” [Online]. Available: <https://www.aiche.org/chenected/2014/12/novel-forward-osmosis-draw-solution>. [Accessed: 10-Mar-2022].
- [86] “Mechanical Vapor Compression - an overview | ScienceDirect Topics.” [Online]. Available: <https://www.sciencedirect.com/topics/earth-and-planetary-sciences/mechanical-vapor-compression>. [Accessed: 13-Feb-2022].
- [87] “6(h). Earth-Sun Geometry.” [Online]. Available: <http://www.physicalgeography.net/fundamentals/6h.html>. [Accessed: 03-Mar-2022].
- [88] M. Tawfik, X. Tonnellier, and C. Sansom, “Light source selection for a solar simulator for thermal applications: A review,” *Renew. Sustain. Energy Rev.*, vol. 90, no. April, pp. 802–813, 2018, doi: 10.1016/j.rser.2018.03.059.
- [89] P. M. Pattison, J. Y. Tsao, G. C. Brainard, and B. Bugbee, “LEDs for photons, physiology and food,” *Nature*, vol. 563, no. 7732, pp. 493–500, 2018, doi: 10.1038/s41586-018-0706-x.
- [90] “LED Array Light Sources.” [Online]. Available: [https://www.thorlabs.com/newgrouppage9.cfm?objectgroup\\_id=2853](https://www.thorlabs.com/newgrouppage9.cfm?objectgroup_id=2853). [Accessed: 14-Mar-2022].

- [91] C. E. Kennedy, "Review of Mid- to High- Temperature Solar Selective Absorber Materials Review of Mid- to High- Temperature Solar Selective Absorber Materials," no. July, 2002.
- [92] K. Xu, M. Du, L. Hao, J. Mi, Q. Yu, and S. Li, "A review of high-temperature selective absorbing coatings for solar thermal applications," *J. Mater.*, vol. 6, no. 1, pp. 167–182, 2020, doi: 10.1016/j.jmat.2019.12.012.
- [93] F. Cao, K. McEnaney, G. Chen, and Z. Ren, "A review of cermet-based spectrally selective solar absorbers," *Energy Environ. Sci.*, vol. 7, no. 5, pp. 1615–1627, 2014, doi: 10.1039/c3ee43825b.
- [94] M. A. Annacchino, *New Product Development: From initial Idea to Product Management*. .
- [95] K. T. Ulrich and S. D. Eppinger, *Product Design and Development*, 6th Editio. .
- [96] "Open Cell Foam vs. Closed Cell Foam - Stockwell Elastomerics." [Online]. Available: <https://www.stockwell.com/blog/open-cell-foam-vs-closed-cell-foam/>. [Accessed: 13-Mar-2022].
- [97] "How Does A Thermocouple Work? Working Principle And Operation." [Online]. Available: <https://www.omega.ca/en/resources/how-thermocouples-work>. [Accessed: 22-Feb-2022].